eman ta zabal zazu

Universidad del País Vasco
Euskal Herriko Unibertsitatea

Probing and tuning the electronic properties of low dimensional van der Waals materials

Francesco Calavalle

PhD Thesis

Supervisor: Prof. Luis E. Hueso

2022


CIC
nanoGUNE
MEMBER OF BASQUE RESEARCH & TECHNOLOGY ALLIANCE

Abstract

The investigation on the physical properties of new materials is of fundamental importance to gain understanding and knowledge on systems and phenomena which one day may be exploited for revolutionary technological applications. In this regard, probing and tuning the electronic transport properties of low-dimensional materials might represent one of the routes that can satisfy the requirements of modern electronics/spintronics advancements. Since the discovery of graphene in 2004, van der Waals (vdW) materials have been considered as the new hope for a breakthrough in the development of game changing technologies. The low dimensionality of such materials is not only of interest for scalability purposes in electronic applications, but it brings into the game new and exotic physical phenomena, which can be also combined stacking vdW materials on top of each other to form artificial systems with on demand properties, the so-called vdW heterostructures. Moreover, the single crystalline nature of this class of materials, which can be characterized by symmetry breakings dependent on the lattice configuration, leads to a very strong interplay between their atomic structure and physical properties. In the specific case of electronics and spintronics, mastering the relationship between symmetries and resultant electron and spin transport properties can be exploited to overcome some of the limitations which were imposed by symmetry constraints in more traditional materials.

Following the common thread of investigating and manipulating the transport properties of low dimensional and low symmetrical systems, this thesis will be divided in two main parts: the first concerning the molecular tuning of intrinsic physical properties of two van der Waals materials and the second focuses on the study of the relationship between spin related phenomena and the symmetry breaking in a chiral system. The manuscript will be organized as follows:

- **Chapter 1** gives a first broad overview on van der Waals materials, briefly telling their history, presenting the idea and the potential of vdW heterostructures, and introducing the interesting connection found in recent experiments between physical properties and symmetry breakings.
- **Chapter 2** describes the experimental methods employed for the fabrication and the characterization of the different systems presented in this thesis. It includes diverse fabrication methods such as, lithography, metals

and molecules growth, and 2D materials exfoliation and stamping. Moreover, it presents also the principal characterization techniques used for the different experiments: atomic force microscopy (AFM), X-ray reflectometry and multiterminal cryogenic magneto transport measurements.

Part I

- **Chapter 3** serves as an introduction to the first part of the thesis, describing the state of the art and the potentiality of molecular approaches to tune 2D materials properties. The pivotal point of this part is to demonstrate how the versatility of molecular compounds can be used to reshape a broad variety of physical properties starting from the molecule's design.
- **Chapter 4** reports a molecular tuning of $NbSe_2$ superconductivity via self-assembled molecular adlayers. It explains the growth and optimization of the self-assembly, the transport and spectroscopic measurements on MBE grown $NbSe_2$ and the mechanism behind the superconducting critical temperature modulation.
- **Chapter 5** deals with the exchange bias induced by thin molecular films on the 2D ferromagnet Fe_3GeTe_2. It introduces the materials used for the experiments and the specific method to electrically probe the magnetic properties of the 2D ferromagnet. Finally, a comparative analysis on the molecular induced exchange bias and on the underlying mechanism are presented.

Part II

- **Chapter 6** introduces charge-to-spin interconversion mechanisms in low symmetry systems, where the structural arrangement of the materials lifts the constraints imposed by symmetry in terms of directions of spin polarization, charge and spin currents allowing the generation of spin currents in unconventional directions.
- **Chapter 7** explores the magnetoelectrical properties of elemental Te nanowires (NWs). Through current-dependent magnetotransport measurements and structural analysis we study the interplay between the chirality of the material, its band structure, and the charge-to-spin interconversion phenomena occurring when electrical current is applied to the low symmetrical structure of Te NWs.

Resumen

La investigación sobre las propiedades físicas de nuevos materiales es de fundamental importancia para obtener conocimiento básico sobre sistemas y fenómenos que algún día podrían ser explotados para aplicaciones tecnológicas. En este sentido, manipular las propiedades de transporte electrónico de materiales de baja dimensionalidad podría representar una de las rutas para cumplir los requisitos para futuros avances en el campo de la electrónica y la espintrónica.

Desde el descubrimiento del grafeno en 2004, los materiales van der Waals (vdW) se han considerado la nueva esperanza para un cambio de paradigma en el desarrollo de nuevas tecnologías. La baja dimensionalidad de tales materiales no sólo es de interés para la escalabilidad de aplicaciones electrónicas, sino que introduce fenómenos físicos nuevos y exóticos. Estos fenómenos también se pueden combinar apilando materiales vdW uno encima del otro para formar sistemas artificiales con propiedades bajo demanda, llamadas heteroestructuras vdW.

Entre los materiales de van der Waals de interés para la realización de heteroestructuras, una clase que se hizo muy popular después 2004 fue la de los dicalcogenuros de metales de transición (TMDCs). Los TMDCs son típicamente semiconductores o semimetales formados por estructuras a capas del tipo MX_2, donde cada lámina está compuesta por una capa de átomos de metal de transición (M) intercalados entre dos capas de átomos de calcógeno (X). Su larga historia se remonta a 1923, cuando se determinó por primera vez la estructura. A fines de la década de 1960 se sabía que varios TMDC presentaban estructuras a capas que finalmente se exfoliaron a pocas capas a través de la exfoliación mecánica. Solo en 1986, una sola capa suspendida de MoS_2 se aisló por primera vez a través de un método químico, pero la investigación sobre TMDC siguió siendo limitada. Desde 2004, el rápido crecimiento de la investigación relacionada con el grafeno estimuló el desarrollo de técnicas adecuadas para trabajar con materiales a capas, lo que provocó un resurgimiento del interés en los TMDC y otros sistemas de van der Waals. Este renovado interés llevó al descubrimiento, alrededor de 2010, de una fuerte fotoluminiscencia en monocapa MoS_2 y la demostración del primer transistor basado en monocapa de MoS_2. En consecuencia, los TMDC se convirtieron en candidatos atractivos para nuevas aplicaciones de electrónica, optoelectrónica y fotónica.

Desde entonces, la cantidad de materiales vdW descubiertos y estudiados ha estado en continuo aumento, acelerándose en los últimos años, y se prevé que su número aumente aún más, ya que se ha estimado que más de 1800 compuestos podrían estar hechos de estructuras a capas potencialmente fáciles de exfoliar. Hoy en día, la gran familia de materiales vdW ya está cubriendo una gama extremadamente amplia de propiedades físicas, contando no solo con TMDC y grafeno, sino también con nitruro de boro hexagonal (hBN), fósforo negro, imanes 2D con propiedades metálicas (Fe_3GeTe_2), semiconductores ($Cr_2Ge_2Te_6$) y aislantes (CrI_3), otros calcogenuros metálicos del tipo: MX (InSb), M_2X_3 (Bi_2Se_3) y MPX_3 ($FePS_3$), y también materiales elementales formados por cadenas quirales 1D unidas por fuerzas vdW como el telurio.

Dada la reducida dimensionalidad de esta clase de materiales, las interfaces juegan naturalmente un papel clave en el control y la manipulación de sus propiedades. La importancia de las interfaces se reconoció desde el principio, cuando se descubrió que reduciendo el efecto del sustrato en la superficie del grafeno con encapsulación h-BN, era posible lograr movilidades de los portadores de carga enormemente altas. Esto tuvo grandes implicaciones en la forma en que los científicos comenzaron a manipular las propiedades de los materiales vdW, interconectándolos, no solo con otros materiales vdW, sino también con otros compuestos de baja dimensión, como moléculas orgánicas (0D) o nanocables semiconductores y nanotubos, así como polímeros orgánicos (1D). El advenimiento de las heteroestructuras vdW amplió aún más el horizonte de fenómenos y propiedades que pueden explorarse con sistemas de baja dimensión.

El apilamiento de dos o más capas atómicas de diferentes materiales vdW reúne una rica variedad de sistemas electrónicos 2D en los que la correlación de electrones con espines, fonones y otros electrones se puede aumentar considerablemente. Esto resulta en la aparición de fenómenos cuánticos colectivos que afectan el transporte de espín y carga, entropía y energía en el límite cuántico, lo que lleva a implicaciones fundamentales para aplicaciones prácticas. Por ejemplo, se utilizaron dos láminas de grafeno separadas por una película delgada de h-BN para sondear una transición metal-aislante en grafeno debido a la localización de Anderson a bajas temperaturas, se acoplaron grafeno y TMDC semiconductores para obtener transistores atómicamente delgados de alto rendimiento, la transferencia de huecos ultrarrápido se midió en heteroestructuras MoS_2/WSe_2, y se descubrió una transferencia de carga de excitón degenerado en $MoSe_2/WSe_2$ y $MoSe_2/WS_2$. Además, los picos de fotoluminiscencia adicionales que emergen en la heteroestructura acoplada

$WS_2/MoSe_2$ se atribuyeron a la recombinación de triones formados por los excitones en las capas WS_2 y electrones en las capas $MoSe_2$. Otra forma profundamente investigada de abordar y combinar las propiedades de los materiales vdW, con el objetivo de explotar la mejor característica de cada componente de heteroestructura, es aprovechar los efectos de proximidad. Con los apilamientos oportunos, por ejemplo, se puede "transferir" el acoplamiento de espín y órbita de un TMDC a una porción localizada de un canal de grafeno, para generar corrientes de espín que luego pueden transportarse a largas distancias en la región restante no proximitizada del canal. Recientemente, también se ha demostrado que la interacción de intercambio magnético inducida por la proximidad ocurre cuando los imanes 2D se acoplan al grafeno o a las monocapas de TMDC. Todos estos fenómenos raramente vistos abren nuevas vías para el desarrollo de nuevas aplicaciones electrónicas y optoelectrónicas, así como dispositivos fotovoltaicos y memorias.

Como se mencionó anteriormente, existen métodos para actuar sobre las propiedades de los materiales 2D que van más allá de las heteroestructuras 2D-2D. Uno atractivo se basa en el uso de pequeños compuestos orgánicos para funcionalizar los materiales vdW de una manera similar a como se hace con efectos de proximidad. Las moléculas diseñadas para tener funcionalidades específicas se pueden acoplar a capas individuales de materiales vdW para diseñar nuevos compuestos con la funcionalidad deseada, o para ajustar las propiedades que ya posee el material mismo. Las moléculas ofrecen una perspectiva distintiva para ampliar el horizonte de las heteroestructuras vdW. Mientras que las propiedades de los materiales inorgánicos 2D están definidas por la disposición atómica de la estructura de una sola capa, los compuestos moleculares pueden diseñarse para tener características específicas predeterminadas en la etapa de síntesis. Esta flexibilidad química permite la síntesis de un número casi infinito de moléculas posibles con grupos funcionales que llevan propiedades electrónicas, ópticas y magnéticas que pueden activar interacciones atómicas/moleculares específicas con materiales vdW.

Por otro lado, la naturaleza monocristalina de esta clase de materiales, que se caracteriza por roturas de simetría dependientes de la configuración del cristal, resulta en una conexión íntima entre estructura atómica y propiedades físicas. Entre la plétora de fenómenos exóticos observados en materiales vdW y sus heteroestructuras están los efectos non lineales ópticos y de Hall, la física de contraste de valles, la física de espín y órbita, las cuasipartículas quirales, la piezoelectricidad, la superfluidadez y la superconductividad. La mayoría de éstos revelaron estar dictados por simetrías rotas, como ruptura de inversión, espejo, rotación, inversión de tiempo y simetrías de gauge. Las roturas de

simetría pueden ocurrir tanto por la disposición estructural de los átomos del cristal como por factores externos, como la tensión, el dopaje, los acoplamientos entre capas o los campos magnéticos y eléctricos.

En el caso específico de la electrónica y la espintrónica, el conocimiento de la relación entre las simetrías y las propiedades de transporte electrónico y de espín puede explotarse para superar algunas de las limitaciones presentes en materiales más tradicionales. En particular, la falta de simetría de inversión proporciona los requisitos previos para la aparición del acoplamiento espín-órbita Rashba-Dresselhaus, que ha sido ampliamente estudiado para explicar configuraciones no convencionales de procesos de interconversión de espín a carga, y es interesante para nuevas aplicaciones de espín-orbitrónica.

Siguiendo el hilo conductor de investigar y manipular las propiedades de transporte en sistemas de baja dimensionalidad y simetría, esta tesis se divide en dos partes principales: la primera, que trata sobre la manipulación por medio de moléculas de las propiedades físicas intrínsecas de dos materiales vdW y la segunda, que se centra en el estudio de la relación entre los fenómenos de espín y la ruptura de la simetría en un sistema quiral.

El manuscrito se organiza de la siguiente manera:

- **El capítulo 1** ofrece una primera visión general de los materiales vdW, contando brevemente su historia, presentando la idea y el potencial de las heteroestructuras vdW, así como introduciendo la conexión, encontrada en experimentos recientes, entre propiedades físicas y rupturas de simetría.
- **En el capítulo 2** se describen los métodos experimentales empleados para la fabricación y caracterización de los diferentes sistemas presentados en esta tesis. Se incluyen varios métodos de fabricación como litografía, crecimientos de películas moleculares y metálicas, así como la exfoliación y transferencia de materiales 2D. Además, el capítulo presenta también las principales técnicas de caracterización utilizadas: microscopía de fuerza atómica (AFM), reflectometría de rayos X y medidas criogénica de magneto transporte.

Parte I

- **El capítulo 3** describe el estado del arte y la potencialidad de las películas moleculares para manipular las propiedades de los materiales 2D. El punto fundamental de esta parte es demostrar cómo la versatilidad de los compuestos moleculares se puede utilizar para remodelar una amplia

variedad de propiedades físicas a partir del diseño de las moléculas individuales.

- **El capítulo 4** presenta resultados experimentales sobre la modulación de la superconductividad de $NbSe_2$ a través de capas moleculares auto ensambladas. Se explica el crecimiento y la optimización del autoensamblaje, el transporte y las medidas espectroscópicas en $NbSe_2$ crecido epitaxialmente y el mecanismo detrás de la modulación de la temperatura crítica del superconductor.
- **El capítulo 5** trata del "exchange bias" inducido por películas moleculares delgadas en el material ferromagnético 2D Fe_3GeTe_2. Se presentan los materiales utilizados para los experimentos y el método específico para medir eléctricamente las propiedades magnéticas del material 2D. Finalmente, se introduce un análisis comparativo sobre el "exchange bias" inducido por moléculas y el mecanismo subyacente.

Parte II

- **El Capítulo 6** introduce los mecanismos de interconversión de carga a espín en sistemas de baja simetría, donde la estructura cristalina levanta las restricciones impuestas por simetría en términos de direcciones de polarización de espín y de corrientes de carga y espín, permitiendo la generación de corrientes de espín en direcciones no convencionales.
- **El capítulo 7** explora las propiedades magnetoeléctricas de los nanohilos de Te. A través de mediciones de magnetotransporte dependientes de la dirección de corriente y análisis estructurales, estudiamos la interacción entre la quiralidad del material, su estructura de banda y los fenómenos de interconversión de carga a espín que ocurren cuando se aplica corriente eléctrica a una estructura con simetría reducida.

Acknowledgements

Here, I would like to thank all the people which made this experience a wonderful and fulfilling journey. First, to Luis and Fèlix who gave me the opportunity to work with them and to join the nanodevices family; you have been an all-around guidance to deal not only with scientific stuff, it has been a real pleasure, thank you! A special thank you goes to Marco (…and Maider!!) who "adopted me" following my work closely and helping me to not give up after some initial struggles. To Roger (a.k.a. "calzone"), I learned so much stuff and had so much fun with you and Battiato! To the whole nanodevices group for the fantastic working environment, support, and collaborations.

This work would have been impossible to be realized without all the collaborators spread around the world. I feel very lucky to have had the possibility to work with all of you and to learn something from you. Thank you! A thank you note goes also to QuESTech and the whole group of people with whom I shared this international network.

To the whole nanoGUNE and the city of Donostia, which have been amazing places to form amazing relationships with which I shared this experience. To the group of friends that filled my life in the last four years and became my new family: los dos enanitos calvos (Josu y Juanma), la polpettina (Neri), the supercool guy aka Alvin, il crucco Franz, Sandrino el portuguesh, la prof (Marta), Lebron Sanchez, Eva, Jakob, Edurne, Mr. loudvoice (Elias), Mr. nano (Tuong), Paz, I poveri migranti and many others. Thank you, boys and girls! To Inge, who became more than just a friend, I feel extremely lucky to have met you! Thank you for still standing me!! To all the people who came and went away during these four years, but who will be never really gone.

Ai regaz dell'università in giro per il mondo (e non), con i quali ci vediamo sempre quando torno a Bolo, e con i quali si finisce sempre a discutere delle cose più assurde a ore inverosimili fuori dal Punto, grazie per essere un porto sicuro in cui tornare ogni volta e per il divertentissimo Garbage Time!

Ai miei Bro di Urbania, siete come la mia seconda famiglia e non potrei sperare di avere un gruppo di amici migliore. Grazie per continuare ad essere lì ogni volta che torno a passare le serate insieme come se il tempo non fosse mai passato e come se non fossi mai partito.

Infine, alla mia famiglia e al supporto/libertá datemi durante questi anni, senza la quale nulla di tutto questo sarebbe mai stato possibile. Grazie!

Table of Contents

Abstract **i**

Resumen **iii**

Acknowledgements **ix**

Table of Contents **xi**

1 Van der Waals materials: a low-dimensional and low-symmetrical playground **1**

1.1 Van der Waals materials 2

1.1.1 The discovery of Graphene 2

1.1.2 Transition metal dichalcogenides and other van der Waals materials 4

1.2 A playground in low dimensions and low symmetry 5

1.2.1 Mixed-dimensional vdW heterostructures 5

1.2.2 Symmetry breaking in vdW materials 7

2 Experimental techniques **9**

2.1 Fabrication techniques 9

2.1.1 Lithography 9

2.1.1.1 Shadow masking 9

2.1.1.2 Laser writing and Electron-beam lithography 10

2.1.2 Materials growth 11

2.1.2.1 Electron-beam evaporation 11

2.1.2.2 Thermal evaporation 12

2.1.2.3 Magnetron Sputtering 12

2.1.2.4 Vapor-Phase deposition 13

2.1.3 Exfoliation and delamination of vdW materials 14

2.2 Characterization techniques 17

2.2.1 Atomic force microscopy 17

2.2.2 Electrical transport measurements 20

2.2.2.1 PPMS 20

2.2.2.2 Oxford Heliox III 22

2.2.3 X-ray reflectivity 22

PART I

3 Hybrid van der Waals heterostructures **27**

3.1 Molecules as building blocks for hybrid vdWHs 28

3.2 Molecules on 2D materials: doping effects 29

3.2.1 Microscopical origin of molecular doping 30
3.3 Beyond doping: 2D materials molecular decoration 34
3.4 Review of relevant experiments 37
3.4.1 Deterministic control of the SAM to control the dipole-induced doping 38
3.4.2 Molecular tunability of magnetic exchange bias 41

4 Tailoring superconductivity of $NbSe_2$ via self-assembled molecular adlayers 45
4.1 $NbSe_2$: a 2D superconductor 45
4.2 Molecular decoration of $NbSe_2$ 46
4.2.1 Epitaxially grown monolayer $NbSe_2$ 46
4.2.2 Self-assembly formation and characterization 48
4.3 Dipole induced modulation of $NbSe_2$ work function 49
4.4 Tuning of $NbSe_2$ critical temperature 52
4.5 Air stability improvements 54
4.6 Results discussion 55
4.7 Conclusions 56
4.8 Appendices 57
A. Growth of $NbSe_2$ monolayers 57
B. Photoelectron spectroscopy 58
X-ray photoelectron spectroscopy (XPS) 58
Ultraviolet photoelectron spectroscopy (UPS) 58
C. Mechanism of growth of silane-based molecular films 59
D. Additional electrical characterization 61
E. Comparison with previous works 62

5 Exchange Bias in Fe_3GeTe_2/CoPc heterostructures 65
5.1 Fe_3GeTe_2: a vdW ferromagnetic metal 65
5.2 CoPc/Fe_3GeTe_2 heterostructures 68
5.3 Spinterface induced exchange bias 70
5.4 Exchange bias dependence on layers thicknesses 73
5.5 Conclusions 76
5.6 Appendices 77
A. CoPc morphological characterization 77
B. Raman Characterization 78
C. Control experiments 79
Field cooling of FGT/hBN 79
Effect of oxidation 80
D. Comparison with other work 81

PART II

6 Introduction on spin-to-charge interconversion in low-symmetry systems 85
6.1 Brief notes on the history of spintronics 85
6.2 The electron spin 88
6.3 Charge and Spin currents 89
6.4 Spin-Orbit coupling 91
6.5 Spin to charge interconversion in systems with broken inversion symmetry 92
6.5.1 Rashba effect 92
6.5.2 3D systems with bulk inversion asymmetry 94
6.5.2.1 Dresselhaus effect 94
6.5.2.2 The case of chiral crystals 95
6.5.3 Edelstein Effect 96
6.6 Unidirectional Magnetoresistance 98

7 Gate-tunable and Chirality-dependent Edelstein effect in Tellurium nanowires 101
7.1 Tellurium: a prototypical chiral material 101
7.1.1 Band structure and spin texture of Te 102
7.1.2 Tellurium nanowires 104
7.2 Magnetoelectrical characterization 105
7.3 Chirality dependent Unidirectional Magnetoresistance (UMR) 108
7.4 Electrical modulation of UMR 112
7.5 Conclusions 115
7.6 Appendices 116
A. Chemical Synthesis of Te NWs 116
B. Additional crystallographic analysis 116
C. Field-effect mobility 119
D. Additional magnetoelectrical characterizations 120
Extended magnetoresistance measurements 120
Evaluation on the presence of UMR extra components 121
On the origin of the unusual UMR angular dependence 123
E. Reproducibility of UMR in different samples 126
F. Theoretical Calculations on the Edelstein effect 127

Conclusions and future perspectives 131

Bibliography 133

List of Publications and Contributions 157

1 Van der Waals materials: a low-dimensional and low-symmetrical playground

"What could we do with layered structures with just the right layers? What would the properties of materials be if we could really arrange the atoms the way we want them? They would be very interesting to investigate theoretically. I can't see exactly what would happen, but I can hardly doubt that when we have some control of the arrangement of things on a small scale, we will get an enormously greater range of possible properties that substances can have, and of different things that we can do."

Richard Feynman, *There's Plenty of Room at the Bottom,* 1959

More than 60 years ago, Richard Feynman delivered some of the ideas that lead to the development of nanoscience and nanotechnology, a field that has changed radically all aspects of human life. His main idea was based on the manipulation of condensed matter at an atomic level with the perspective of discovery new phenomena, a plethora of new materials properties and potential ways to exploit them for the advances of knowledge and progress. In his famous lecture [1], *"There is Plenty of Room at the Bottom"*, he foreseen somehow what today is well-known to be nanofabrication techniques, scanning probe microscopy techniques and nanoscale machines.

With the help of these amazing developments, nowadays we are getting closer to fulfill Feynman's vision. Whereas technology relied for several decades on the downscaling of structures and devices reaching the nanoscale, more recently researchers learned how to obtain uniform, atomically thin layers and how to manipulate them into novel solids with a broad range of tunable physical properties.

1.1 Van der Waals materials

Van der Waals materials are characterized by long range periodic crystalline structures kept together by strong in-plane covalent bonds and weak out-of-plane van der Waals forces. Due to these characteristics, single layers can be separated by breaking the van der Waals bonds, causing little damage either to the remaining structure or to the extracted layer.

Lowering the dimensionality of a system has been linked with exceptional electronic, optical, and magnetic properties as the reduction of available phase space and diminished screening lead to enhanced quantum effects and increased correlations. Two-dimensional (2D) materials have been extensively investigated as theoretical toy models even before the discovery of stable ones and after the discovery of graphene, they have become a pivotal class of materials for multidisciplinary scientific research [2].

1.1.1 The discovery of Graphene

Graphene is an allotrope of carbon, made by a single layer of atoms tightly arranged in a 2D honeycomb lattice and it is the fundamental component of any graphitic materials of other dimensionality (Figure 1.1a) such as 0D fullerenes (wrapped) or 1D nanotubes (rolled). Whereas it has been widely studied for many years [3,4] to describe the properties of carbon-based materials and as a condensed matter analogue of (2+1)-dimensional quantum electrodynamic systems [5,6], for a long time self-standing 2D crystals were well-accepted to be unstable and impossible to isolate for experiments [7], so that graphene was considered just as an "academic" material [8].

Finally, in 2004 after many failed attempt, scientists Andre K. Geim and Konstya S. Novoselov, during one of their famous "Friday afternoon experiments", managed to isolate single sheets of graphene [9,10] employing an as rudimental as effective mechanical cleaving technique that will pass to history as the *"scotch tape method"*. Starting from bulk crystals of graphite and scotch tape pieces, they discovered that it was possible to thin down graphite to its monolayer form by peeling repeatedly the initial crystal with the adhesive tape. Then, they could transfer the cleaved material from the tape to different substrates. The result was a dispersion of "flakes" of different dimensions and thicknesses among which they could identify the thinnest ones to be single atomic layers (Figure 1.1b,c).

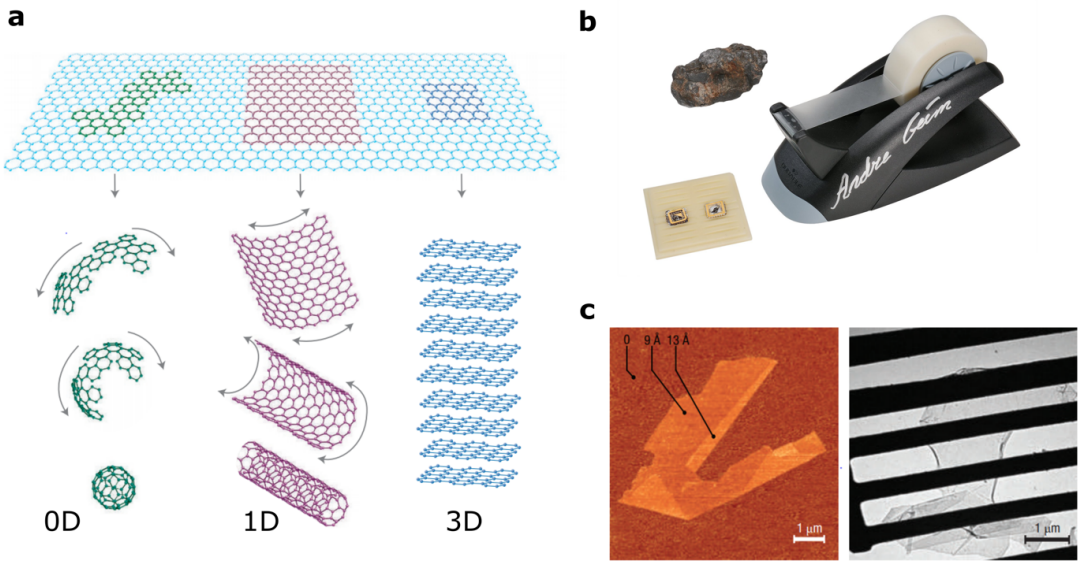

Figure 1.1| The discovery of graphene. a, Allotropes of carbon starting from the 2D graphene structure (image adapted from Ref. [11]) . **b**, Graphite, tape roll and graphene transistors donated by Novoselov and Geim to the Nobel Museum (photo by: Gabriel Hildebrand, The Nobel Museum). First isolations of single layers identified via atomic force microscopy (AFM) and transmission electron microscopy (TEM), image adpted from Ref. [10].

Exfoliated graphene flakes of several micrometers square were found to be continuous and to have an incredibly high crystal quality, that together with its 2D nature results in exceptional charge and spin transport properties [12,13], optical [14] and thermal [15] conductivity, and high mechanical strength [16]. In particular, one of the earliest observations, revealed that graphene shows an ambipolar electric field effect through which the charge carriers can be tuned continuously between electron and holes with concentrations up to $n \approx 10^{13}$ cm^{-2} and that their mobilities can exceed $\mu = 15000$ cm^2 V^{-1} s^{-1} in ambient conditions [9]. These are key features that made graphene a very appealing candidate for next-generation electronic applications. Moreover, the long mean free path of the charge carriers and their unique relativistic nature, being massless Dirac fermions, has been exploited also to observe quantum phenomena [17–21].

For these reasons, graphene has been the subject of a real "gold rush", that has led to the publication of an uncountable amount of experimental and theoretical works since its discovery, awarded with the Nobel Prize in 2010.

1.1.2 Transition metal dichalcogenides and other van der Waals materials

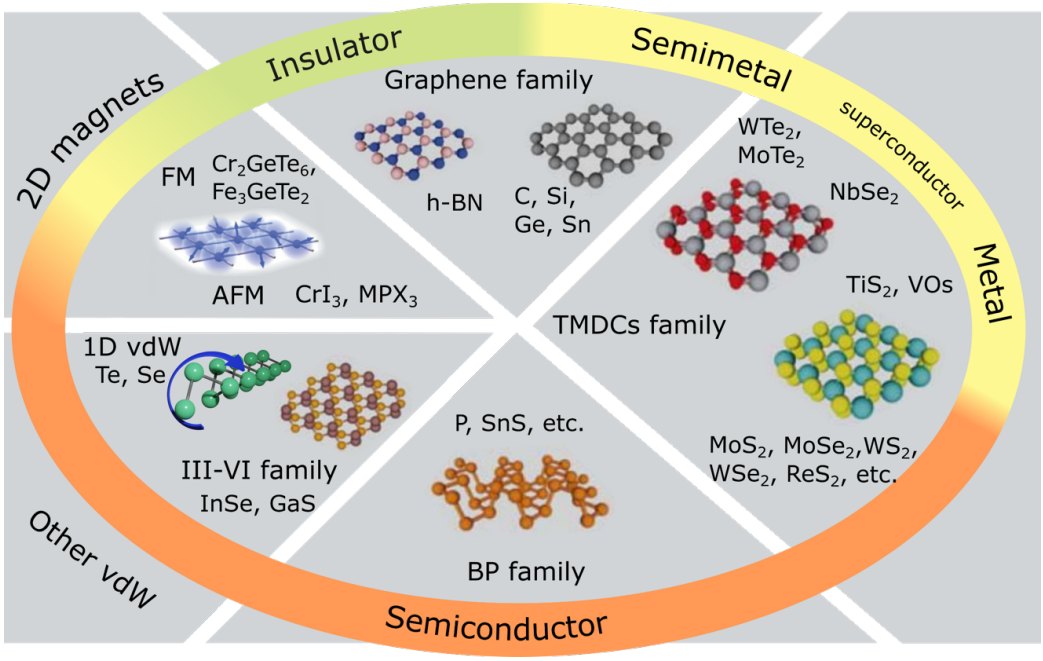

Figure 1.2| VdW family. Scheme representing the different main classes of vdW systems covering almost the whole spectrum of physical properties (image adapted from Ref. [2]).

Transition metal dichalcogenides (TMDCs) are typically semiconductors or semimetals formed by layered structures of the type MX_2, where each sheet is composed by a layer of transition metal atoms (M) sandwiched in between two layers of chalcogen atoms (X). Their long story goes back to 1923, when the structure was first determined [22], then by the end of 1960s several TMDCs were known to present layered structures [23] that were eventually exfoliated down to few layers via mechanical cleaving [24]. Only in 1986, a suspended MoS_2 single layer was isolated for the first time via chemical method [25], but the research on TMDCs remained limited. Since 2004, the rapid growth of graphene-related research stimulated the development of techniques suited for working with layered materials, triggering a resurgence of interest in TMDCs and other van der Waals systems [26]. This renovated interest led to the discovery, around 2010, of strong photoluminescence [27,28] in monolayer MoS_2 and the demonstration of the first monolayer MoS_2 based transistor [29]. Consequently, TMDCs became appealing candidates for new electronics [29,30], optoelectronics [31] and photonics applications [32].

Since then, the amount of discovered and studied vdW materials has been growing continuously with increasing speed in the last few years, and their

number is predicted to further increase since it has been estimated that more than 1800 compounds could be made of potentially easy to exfoliate layered structures [33]. Today, the large family of vdW materials is already covering an extremely wide range of physical properties (see Figure 1.2), counting not only on TMDCs and graphene, but also on hexagonal boron nitride (h-BN) [34], black phosphorus [35], 2D magnets with metallic (Fe_3GeTe_2) [36], semiconducting ($Cr_2Ge_2Te_6$) [37] and insulating (CrI_3) [38] properties, other metal chalcogenides of the type: MX (InSb) [39], M_2X_3 (Bi_2Se_3) [40], and MPX_3 ($FePS_3$) [41], and also elemental materials formed by chiral 1D chains held together by vdW forces such as Tellurium [42].

1.2 A playground in low dimensions and low symmetry

1.2.1 Mixed-dimensional vdW heterostructures

Given the reduced dimensionality of this class of materials, interfaces naturally play a key role in the control and manipulation of their properties. The importance of the interfaces was recognized early on when it was found that, reducing the substrate effect on the surface graphene with h-BN encapsulation, it was possible to achieve extremely high charge carrier mobilities [34]. This had major implication on the way with which scientists started to manipulate vdW materials properties [43,44], interfacing them, not only with additional vdW materials, but also with other low dimensional compounds such as small organic molecules (0D) or semiconducting nanowires and nanotube as well as organic polymers (1D). The advent of the so called vdW heterostructures further expanded the horizon of phenomena and properties that can be explored with low-dimensional systems (see Figure 1.3).

Stacking two or more atomic layers of different vdW materials brings together a rich variety of 2D electronic systems in which electrons' correlation with spins, phonons, and other electrons can be greatly increased. This results in the emergence of collective quantum phenomena which affects the transport of spin and charge, entropy, and energy at the quantum limit, thus leading to fundamental implications for practical applications. For instance, two graphene sheets separated by a thin film of h-BN were used to probe a metal-insulator transition in graphene due to Anderson localization at low temperatures [45], graphene and semiconducting TMDCs were coupled to obtain high-performance atomically thin transistors [46], ultrafast hole transfer was measured in MoS_2/WSe_2 heterostructures [47], and a degenerate exciton charge

transfer was discovered in $MoSe_2/WSe_2$ and $MoSe_2/WS_2$ systems [48,49]. Moreover, additional photoluminescence peaks emerging in the coupled $WS_2/MoSe_2$ heterostructure were attributed to the recombination of trions formed by the excitons in the WS_2 and electrons in the $MoSe_2$ layers [50]. Another deeply investigated way to address and combine vdW materials properties, with the objective of exploiting the best feature of each heterostructure component, is to take advantage of proximity effects [51]. With opportune stackings, for instance, one can "transfer" spin orbit coupling (SOC) from a TMDCs to a localized portion of a graphene channel, to generate spin currents that then can be transported for long distances in the remaining non-proximitized region of the channel [52–54]. Recently, it has been also demonstrated that proximity-induced magnetic exchange interaction occurs when 2D magnets are coupled to graphene [55] or to TMDCs monolayers [56]. All these rarely seen phenomena open up new avenues for developing novel electronic and optoelectronic applications as well as photovoltaic devices and memories.

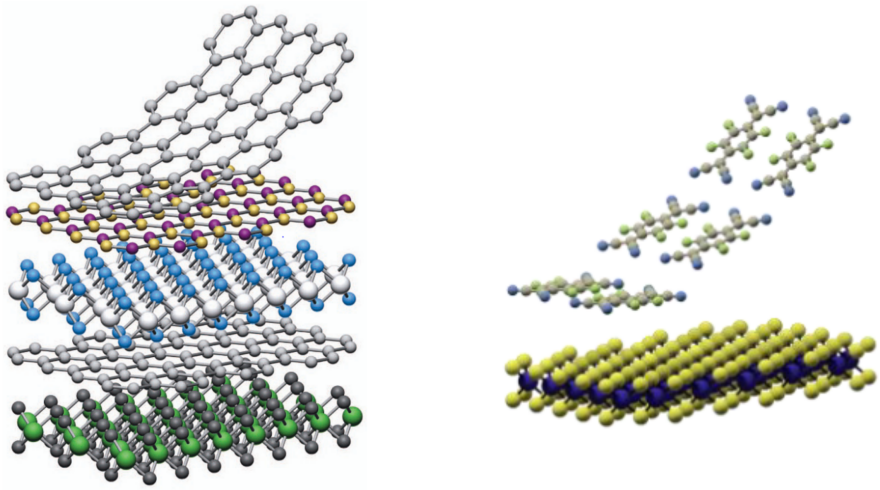

Figure 1.3| Mixed dimensional vdW heterostructures. Illustration of two typical methods to tailor the properties of vdW materials, on one hand the stacking of layers one on top of the other to exploit interlayer couplings and proximity effects, on the other a molecular chemistry approach that relies on the surface modification. Image is partially adapted from Ref. [43]).

As mentioned above, there are methods to tackle the properties of 2D materials that go beyond the 2D-2D heterostructures. An appealing one relies on the use of small organic compounds to functionalize vdW materials in a similar way as it is done with proximity effects. Molecules designed to have specific functionalities can be coupled to single layers of vdW materials in order to engineer novel compounds with desired functionality, or to tune the properties

already possessed by the material itself. This molecular approach will be discussed more in depth in Chapter 3, as it is a fundamental ingredient that led to the results presented in Part I of this thesis.

1.2.2 Symmetry breaking in vdW materials

Among the plethora of exotic phenomena observed in vdW materials and their heterostructures, such as nonlinear optics [57–59], Hall effects [60,61], valley-contrasting physics[62,63], spin-orbit physics [64–66], chiral quasiparticles [67], piezoelectricity [68], superfluidity and superconductivity [69,70]; the majority of them revealed to be dictated by broken symmetries namely, breaking of inversion, mirror, rotational, time-reversal and gauge symmetries. The symmetry breakings can occur both because of the structural arrangement of the crystal's atoms or due to external factors, such as strain, doping, interlayer couplings or magnetic and electric fields [71].

In particular, the lack of inversion symmetry provides the prerequisites for the appearance of Rashba-Dresselhaus spin-orbit coupling [72], that has been widely studied to explain unconventional configurations of spin to charge interconversion processes, interesting for novel spin-orbitronics applications. The interplay between symmetry breakings and spin related effects will be discussed further in chapter 6, to give a solid background on the topic that will be at the basis of the findings reported in Part II of this thesis.

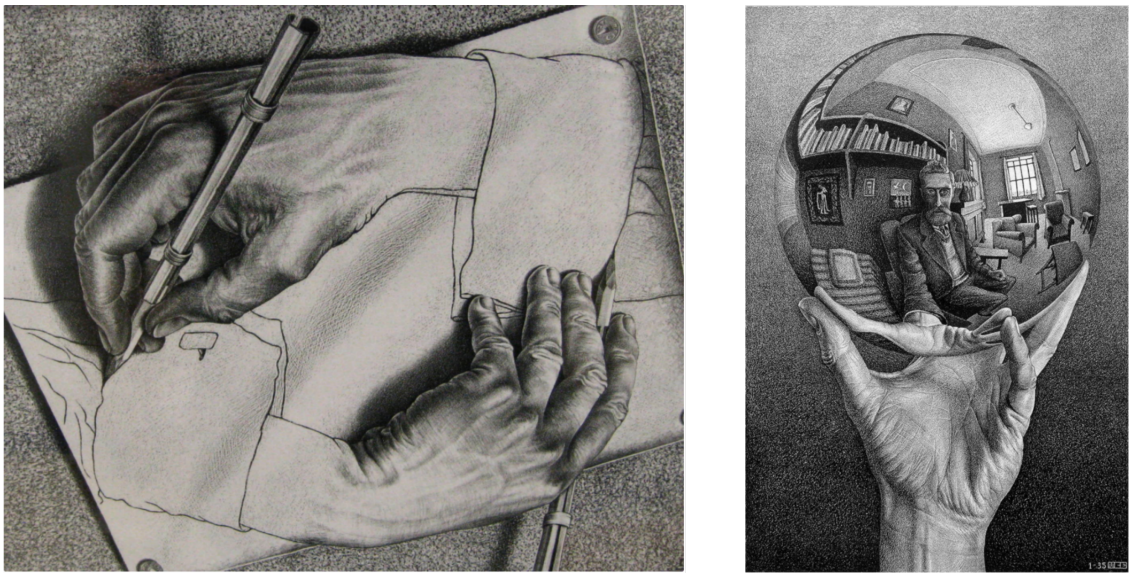

Figure 1.4| Artistic representations of broken symmetries. Lithographs from Maurits Cornelis Escher; left "Drawing Hands", 1948 and right "Hand with reflecting sphere", 1935.

2 Experimental techniques

In this chapter, the experimental techniques employed for the realization of the experiments presented in this thesis, will be explained. The chapter is divided in two parts, the first gives a general explanation of the fabrication techniques and the second goes through the characterization methods. Additional experimental methods, carried out by collaborators, will not be presented here, but are directly inserted as Appendices at the end of each Chapter.

2.1 Fabrication techniques

2.1.1 Lithography

Lithography has been employed to define the patterns of the metallic contacts used to measure electrically the samples. In general, it consists of three steps:

1. preparation of a mask in which the desired design is defined as openings in a layer
2. deposition of a material (in our case a metal) through the masked region
3. removal of the mask to obtain the metallic contacts, patterned as imposed by the apertures on the mask.

2.1.1.1 Shadow masking

Shadow masking is a form of stencil lithography. A shadow mask is a thin sheet of metal with precisely prepatterned features etched completely through the material. Typically, the shadow mask is placed in close contact with the substrate's surface such that a desired material (in our case a metal) is only deposited on the substrate through the apertures in the mask. Due to mechanical limitations, such as the minimum aperture that one can define in a metallic plate with laser cutting or the shadows effects coming from the non-ideal contact between mask and sample, this technique is characterized by a poor resolution in terms of minimum feature size (~ 100 μm) and alignment of subsequent patterns. Nevertheless, it brings the huge advantage of not requiring any heat or chemical treatment of the substrate (like baking, developing, and removing the resist). For this reason, it is a very useful tool to work with clean

and sensitive surfaces that doesn't require extreme precision in terms of dimensions and alignments. For the experiments presented in Chapter 4, a metallic plate with four to six squared apertures was used as a shadow mask to define Au contact pads on the samples.

2.1.1.2 Laser writing and Electron-beam lithography

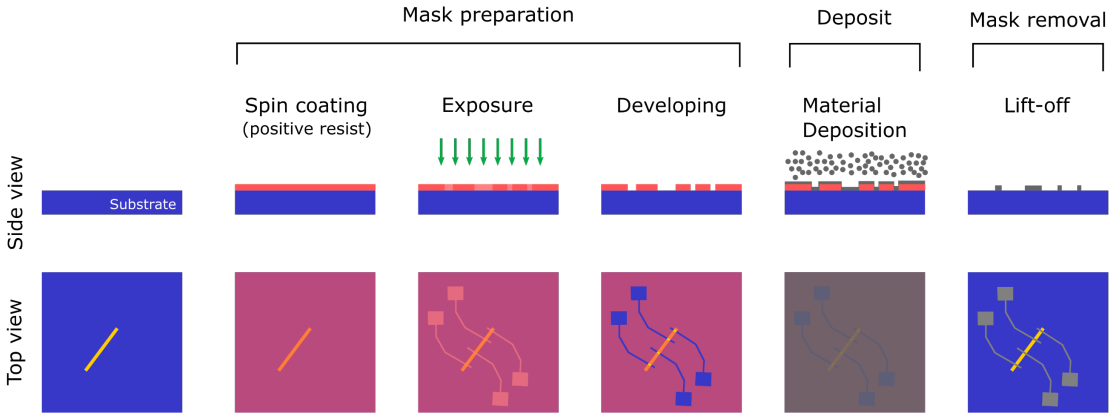

Figure 2.1| EBL and LW lithography procedure. Sketch of the different steps followed to prepare metallic contacts with a positive resist.

In micro- and nanofabrication to overcome the alignment and resolution problems of the previous method, ultraviolet (UV) or electron-beam sensitive polymers (also called resists) are deposited in direct contact with the substrate and used to precisely prepare the mask.

First, a smooth and continuous layer of resist is spin coated on top of the surface of a clean substrate. After this, the substrate is baked to remove residual of solvents and cure the resist. During the writing process, a customized design is transferred to the resist either through UV laser (LW) or a beam of electrons (EBL). At this point, the resist is weakened by the exposure to localized high energies, and it can be "developed" using a particular solvent that etches away only the polymer regions exposed to the writing beam (in the case of a negative resist the unexposed regions would be the one etched away). Once the mask is ready, the metal of choice is deposited on the substrate, and finally the resist is removed during the lift-off step employing another solvent (also called remover), which dissolves all the remaining resist leaving on the substrate a metallic pattern correspondent to the exposed design (see Figure 2.1).

While these techniques involve chemicals and heating of the samples, the resolution that can be achieved exceeds the one of shadow masking of several orders of magnitude making it a very powerful tool to create micro- and

nanostructures. In this case, the maximum resolution is given by the resist properties and by the minimum dimension of the beam spots, so in the case of a laser is diffraction limited, while in the case of an electron beam it depends on how well the beam is focused (minimum feature size for LW ~ 1 μm, for EBL ~ 10 nm). In this thesis, LW has been used to fabricate prepatterned Hall bar shaped contacts on which to delaminate exfoliated Fe_3GeTe_2 (Chapter 5), and EBL to create top contacts on Te nanowires (Chapter 7).

In the first case, the material was very reactive, but the flakes were too small to be contacted with shadow masking, so LW was a good choice to quickly produce micrometer sized prepattern bottom contacts. The exposure step was performed with a Direct Laser writer (DLW) from Heidelberg instruments.

In the second case, EBL in combination with alignment markers and microscopic optical images was necessary to define contacts, precisely aligned to the nanowires. The exposure step was performed with two different EBL systems: *Raith 150-TWO* and *Raith e-Line*.

2.1.2 Materials growth

2.1.2.1 Electron-beam evaporation

Electron-beam evaporation is a physical vapor deposition (PVD) method, and it has been employed to deposit Au contacts in high vacuum conditions (pressure $< 10^{-7}$ mbar). Highly energetic electrons, thermionically emitted from a W filament, are employed to heat up the source material placed in a crucible, until reaching its melting point. The electrons are guided to the crucible through a magnetic field that can be controlled in order to bend the electron beam. Increasing the current in the filament, and thus the number of electrons reaching the source, vapors of the material can be deposited on a substrate facing the source.

Two different systems have been used to deposit the Au contacts. One with a shadow masking system (Theva UHV dual chamber system) for the $NbSe_2$ samples presented in Chapter 4. The system is characterized by an ultra-high vacuum (UHV, base pressure $\sim 10^{-9}$ mbar), since it has a separate load lock chamber for loading the samples and to preserve the base pressure of the main chambers. The deposition of 30 nm thick Au contacts was performed directly on top of $NbSe_2$ through a shadow mask at a rate of ~ 1 Å/s.

The other system (by Kurt J. Lesker), placed in our cleanroom, presents a rotating sample holder for a uniform distribution of the metal film on a larger

area. This was used for the deposition of Ti/Au prepatterned contacts on 4" wafers of Si/SiO_2 (300 nm thermal oxide), that were successively cut into the chips (with Hall bard shaped contacts) on which we delaminated exfoliated flakes for the experiments of Chapter 5. The deposition of a thin Ti (2 nm) film served as adhesion layer for the Au to stick properly on the substrate surface and improve the lift-off process. The overall thickness of the contacts (Ti (2nm)/Au (11 nm)) was optimized to preserve good conductive properties, but at the same to minimize the difference in height with respect to the substrate plane. In this way, when delaminating thin flakes on the contacts, the harmful stress induced by the height steps at the contacts edges was minimized. For both metals the deposition rate was ~ 0.8 Å/s.

2.1.2.2 Thermal evaporation

This technique is again a PVD method, but that relies on the evaporation of a material via Joule effect. The crucible, hosting the compound to be evaporated, is wrapped in a current-carrying metallic filament which produces sufficient heat to melt and evaporate the source material.

Thermal evaporation has been employed to sublimate and deposit thin films of CoPc molecules used in the experiments of Chapter 5, using a Knudsen cell and quartz cylindrical crucibles placed in the Theva UHV dual chamber. A thin layer of molecules (~ 5 nm at 0.1 Å/s) was evaporated on the prepatterned chips before the delamination of Fe_3GeTe_2 flakes (see Chapter 5). The thickness was optimized to ensure a homogeneous coverage of the substrate, but being thin enough to not compromise the electrical contacts between the flakes and the Ti/Au electrodes.

2.1.2.3 Magnetron Sputtering

Another PVD method is magnetron sputtering. The difference with respect to the other methods regards the way in which the source material is removed from the target, to then be deposited on a substrate. Instead of warming up a crucible, in this case the target is a flat disc made of a certain material (in our case Pt) which is bombarded with ions of an inert gas (in our case Ar). The Ar atoms are injected in the chamber through a gun, and they get ionized and accelerated to the target by an electric field generated between the sample holder (acting as anode) and the magnetron (hosting the target and acting as cathode). In this way, the Ar+ ions create a plasma in the proximity of the magnetron, where a magnetic field is used to increase the plasma density. The

target gets strongly struck by the Ar+ and when the deposited energy overcome the binding energy of the target atoms, the latter are extracted from the target generating a vapor that will deposit on the substrate.

For the experiments presented in Chapter 7, it has been used a UHV Magnetron Sputtering system by *AJA* containing seven targets and a sample holder equipped with a rotator. The choice of using sputtered Pt to contact Te NWs has been taken for two reasons. First, Pt sticks better than Au on Si/SiO_2 substrates and doesn't require the deposition of a Ti adhesion layer. This significantly improved the quality of the contacts with Te (ohmic with Pt), most likely because of cleaner films and a better energy level alignment between Pt (high work function) and Te rather than Ti (low work function) and Te. Second, in our sputtering system the magnetron faces the sample with an angle, while the sample rotates. Hence, Pt is evenly distributed on the sample surface and can even attach to the side of thick structures, guaranteeing a good contact with the material under probe. In Chapeter 7 (Figure 7.9), we will see that were able to contact a 300 nm thick Te NWs with just 50 nm of Pt (deposited at 1.2 Å/s).

2.1.2.4 Vapor-Phase deposition

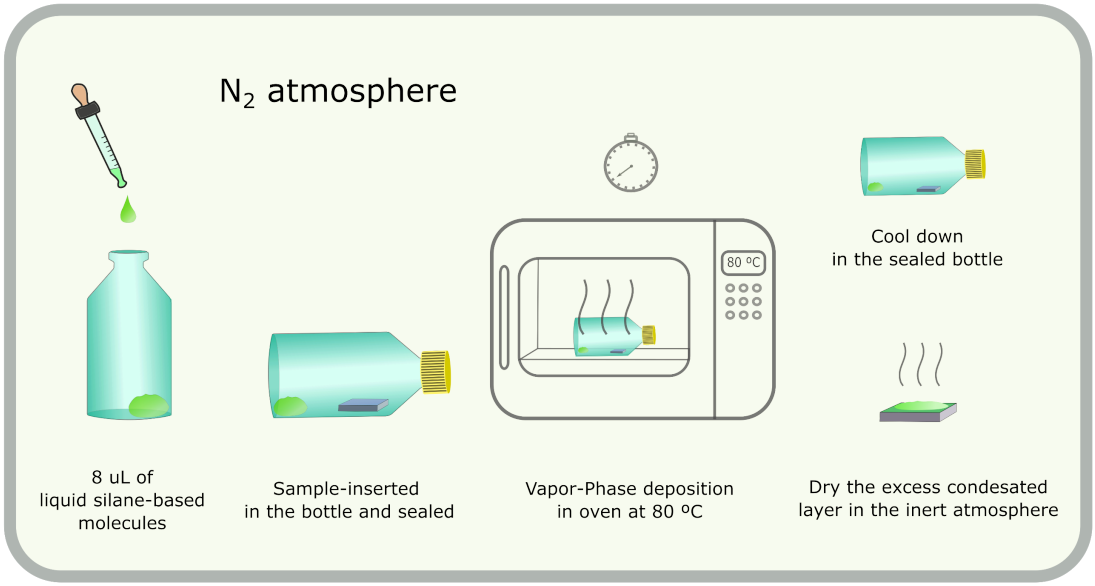

Figure 2.2| Vapor-Phase deposition. Illustration showing the step-by-step procedure followed to grow the molecular adlayers.

Vapor-phase deposition was employed to grow self-assembly adlayers on the surface of $NbSe_2$. A sketch representing the step-by-step procedure is illustrated in Figure 2.2, the whole process was done in a nitrogen glovebox. The sample was placed and sealed in a 20 mL vial together with a droplet of 8 µL

of molecules. AHAPS (*N*-[3-(Trimethoxysilyl)propyl]ethylenediamine (97%)), PFS (Trichloro(1*H*,1*H*,2*H*,2*H*-perfluorooctyl)silane (97%)) and OTS (Trichloro(octadecyl)silane (≥90%)) were purchased from Sigma Aldrich. Then, the sample was carefully positioned in the vial to avoid touching the droplet. At this point, the vial was inserted in an oven at 80 °C for 40 min (AHAPS) and 50 min (PFS and OTS). During the heating process, vapors of the liquid molecules saturate the atmosphere inside the vial driving the growing process. After taking out the vial from the oven, we left it to cool down while maintaining it sealed. Finally, the sample was extracted and kept for at least one hour in the N_2 atmosphere to let dry eventual condensed excesses of molecules.

HOPG was used as surface to optimize coverage and quality of the films on large areas. In particular, the growth recipes were optimized carefully controlling the deposition parameters: volume of molecules, volume of the vial, temperature, and time. The volumes of molecules and vial don't play a crucial role, as far as the atmosphere in the vial is fully saturated, so they were maintained constant. The other two parameters defined coverage and quality of the adlayers and were tuned by mapping the morphology of the HOPG surface after each growth process with atomic force microscopy (AFM, see below).

2.1.3 Exfoliation and delamination of vdW materials

In fundamental research, the standard technique to isolate high quality and few layers thick flakes from bulk vdW materials relies on the mechanical exfoliation of a source layered crystal with adhesive tapes. In this thesis, mechanical exfoliation of Fe_3GeTe_2 (FGT) and hexagonal boron nitride (hBN) has been employed together with all-dry deterministic stamping [73], for the fabrication of the devices used for the experiments of Chapter 5.

The whole process was carried out in an Ar-filled glovebox to prevent the oxidation of the very reactive FGT flakes. In Figure 2.3 are displayed the different steps involving this fabrication process. First, Nitto tape (also known as blue tape) is used to cleave several times an FGT bulk crystal until obtaining a clean dispersion of exfoliated material on one of the tape stripes (Figure 2.3a). Then, the FGT flakes, randomly dispersed on the Nitto tape, are transferred onto a piece of the transparent and viscoelastic polymer Polydimethylsiloxane (PDMS), previously attached on a glass slide (Figure 2.3b). To do this, the Nitto tape is pressed against the PDMS, taking care of having a uniform adhesion and the absence of bubbles, and then it is quickly peeled away. During this step is very important to peel away quickly the Nitto tape from the PDMS, to increase the amount transferred material. At this point,

with the microscope installed inside of the glovebox, the PDMS is inspected to find uniform and thin flakes (Figure 2.3c).

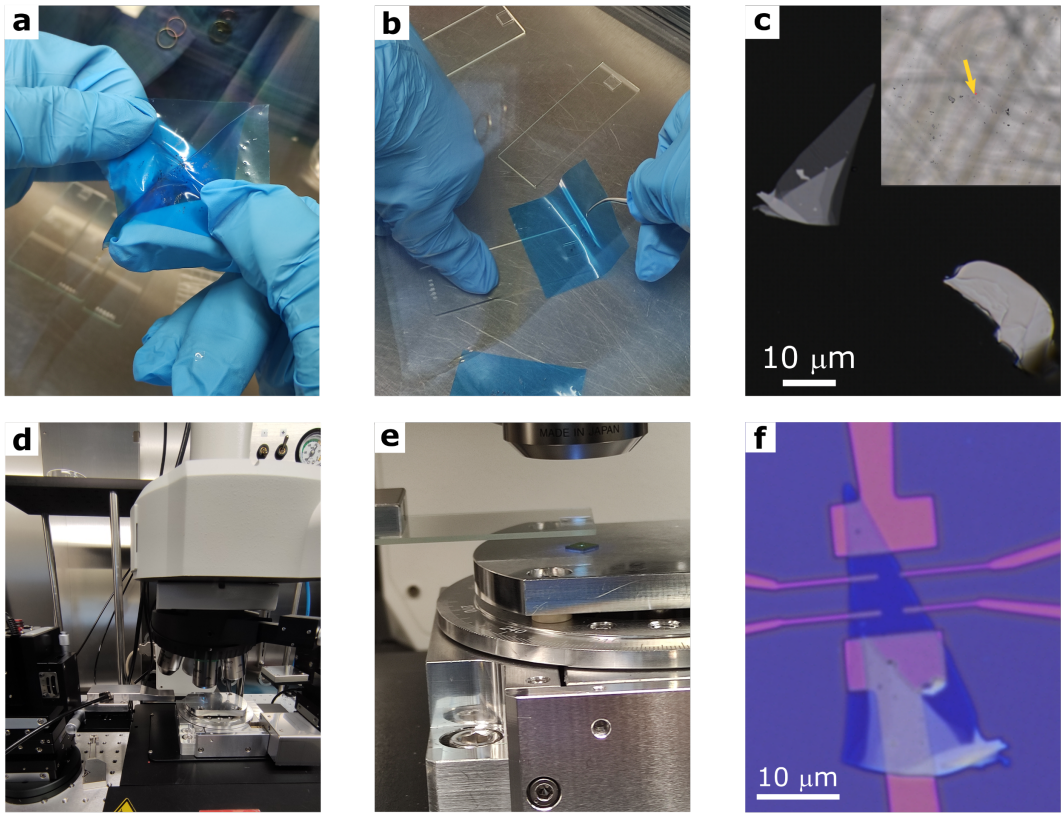

Figure 2.3| Exfoliation and delamination procedure. a, Mechanical exfoliation with Nitto Tape is repeated with several stripes. **b**, Nitto tape is pressed against a piece of PDMs attached to a glass slide that will serve as a transparent support. **c**, Optical image displaying how the FGT flakes look on the PDMS. **d**, Delamination system placed inside the Ar-glovebox. The system is composed by a microscope; a sample holder equipped with a heater, which can rotate, and move in *x, y,* to adjust the position of the substrate; micromanipulators capable to move in *x, y, z*, to align and transfer the flakes onto the substrate. All the system is controlled remotely. **e**, Approach step, the glass slide with PDMS is brought in contact with the substrate. **f**, Microscope image of the FGT flake in **c**, successfully aligned and transferred onto prepatterned electrodes.

The thickness can be roughly estimated from the optical contrast, after calibration with atomic force microscopy (AFM, see below for more details). Once the flake is identified, the glass slide is mounted on a support, placed in the microscope vicinity, which can be remotely manipulated with micrometric precision (see Figure 2.3d). After that, a prepatterned substrate is placed underneath the microscope light, and the support with the glass slide is roughly placed in between the microscope objective and the substrate. Thanks to the transparency of the PDMS, it is possible to look through the glass slide and

the PDMS, to precisely align flake and electrodes using the micromanipulators and rotating the sample holder. Once the alignment is established, the PDMS is gently approached to the substrates until reaching adhesion (Figure 2.3e). Finally, the glass slide is carefully retracted from the substrate leaving the flake attached to the substrates and contacts (Figure 2.3f). During this last step, it is possible (but not necessary) to heat up the microscope plate to improve the transfer from PDMS to SiO_2.

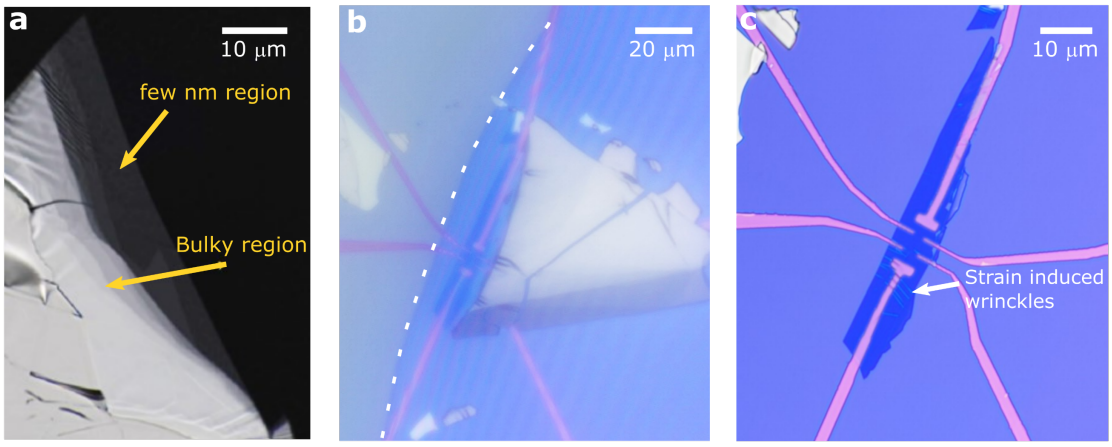

Figure 2.4| Tearing flakes. a, Optical image of a typical FGT flake on PDMS. The not ideal exfoliation properties of FGT often result in flakes with non-uniform thickness. In this specific case a desirable lobe few nm thick is attach to a big bulky region. **b**, Another multilayered flake is shown in this optical image during a transfer process. The PDMS is partially attached to the sample (dashed line indicates the adhesion border). By tilting the micromanipulator support, and thus the glass slide, one can decide from which direction the adhesion is coming. In this way, only the thin part of the flake could be selectively brought in contact with the substrate. Once the adhesion was achieved, the glass slide was gently pulled in x, y, inducing enough stress to break the flake exactly at the step with the bulky part. **c**, As a result, only the desired part of the flake is transferred on the substrate, avoiding potential short circuits of contacts with the thicker part, which may affect the current paths during the transport measurements. Notice that this procedure can induce sometime strain and wrinkle in the flakes, which may cause undesired effects depending on the experiment.

During the last step, it is very important to take care of the possible sources of strain induced by the structures on the substrates and by the deformation of PDMS, which can cause the flake to break during the transferring. At the same time, this dangerous strain can be also exploited thanks to the elasticity of PDMS to deterministically rip off sections of thin flakes connected to unwanted bulky parts of the exfoliated material (see Figure 2.4).

In general, this deterministic transfer of flakes can be repeated to form van der Waals heterostructures, stacking subsequent flakes on top of each other. In our case, we repeated the process with hBN, just to cap the FGT flakes and protect them from the exposition to atmosphere.

The direct use of PDMS may seem unusual for a reader who worked with atomically thin graphene, but in our case, it allowed to avoid any other fabrication process involving solvents, the presence of air, or heat, which could harm the very reactive FGT flakes. The drawback of this technique is mainly the difficulty in finding flakes thinner than ~ 10 nm, because of the characteristic of FGT, which does not exfoliate easily, and the transparency of PDMS, which doesn't provide for a very nice contrast of flakes with very low thickness. Nevertheless, for the purpose of our experiments, it revealed to be the best compromise possible.

2.2 Characterization techniques

2.2.1 Atomic force microscopy

Atomic force microscopy (AFM) is a scanning probe technique used to characterize the surface topography of a wide range of materials. The working principle of this method relies on atomic interactions that develops between the probe and sample surface. The probe is typically an atomically sharp tip placed at the edge of a cantilever and controlled with a piezoelectric actuator. The standard way to detect the interaction between tip and sample consists in shining a laser light on top of the cantilever which reflects the beam on a position sensitive photo detector (PSPD), while scanning the tip in close contact to the sample surface. Due to the interactions between the tip and the topography encountered, the cantilever can be deflected, causing the laser beam to change its position on the PSPD, and inducing a voltage signal which can be translated in height information. More precisely, the image is formed through a feedback loop which maintains constant the interaction between tip and sample. Depending on the mode used, namely contact, alternated-contact, or non-contact the way in which the interaction is kept constant is rather different. In contact mode the tip is in direct contact with the sample and the setpoint parameter given to the feedback loop is a force, defined by the initial deflection imposed to the cantilever. The interactions are positive repulsive forces. In alternate and non-contact mode, the cantilever oscillates at a high frequency at or close to resonance, and in proximity to the sample surface. In

this mode van der Waals attractive interactions modify the cantilever oscillation, while the feedback loop receives as setpoint parameter either amplitude or frequency of oscillation.

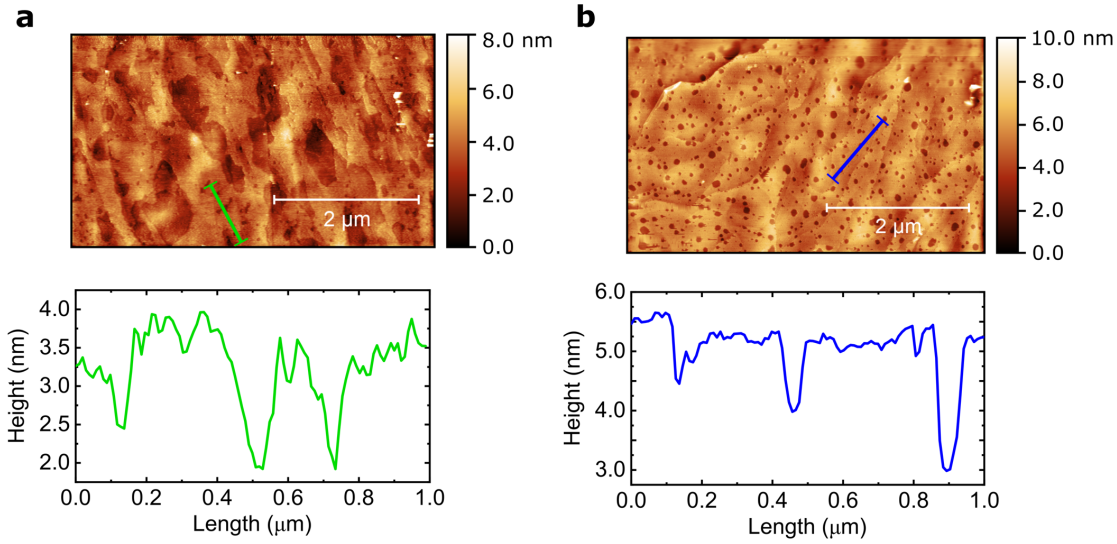

Figure 2.5| Optimization of the self-assembly adlayers. Examples of AFM images and relative cross sections used to optimize the growth of **a**, Trichloro(1H,1H,2H,2H-perfluorooctyl)silane (PFS) and **b**, N-[3-(trimethoxysilyl)propyl]ethylenediamine (AHAPS) molecular adlayer on top of HOPG substrates. HOPG was used to optimize coverage and quality of the films on large areas.

In this thesis, AFM imaging, it has been employed for several purposes: to characterize the surface of $NbSe_2$, to optimize the quality of growth of self-assembly adlayers, to control the roughness of CoPc thin films, and to evaluate the thickness of FGT exfoliated flakes. The equipment employed was an *Agilent 5500 SPM*.

Figure 2.5 shows an example of image taken for the optimization of the self-assembly molecular adlayers employed in the experiments of Chapter 4. For the specific case of molecules, alternate contact mode was employed with a relatively soft cantilever (RTESPA-150 tips, elastic constant ~ 5 N/m) to avoid damages on the soft molecular materials. The images show a background topography relative to HOPG, which was used as a substrate, and the self-assembled adlayer on top of it, following the background morphology. To evaluate the thickness of the molecular adlayers, we optimized the growth recipes to leave uncovered some areas on the substrate, which are imaged as "holes" in the molecular adlayer. Measuring the profiles across these holes, we were able to estimate the thickness of the molecular adlayers. Here, the substrate coverage was in the range of 80-90%. Adjusting the parameters of vapor phase

deposition and taking subsequent AFM images we were able to define the optimal growth conditions.

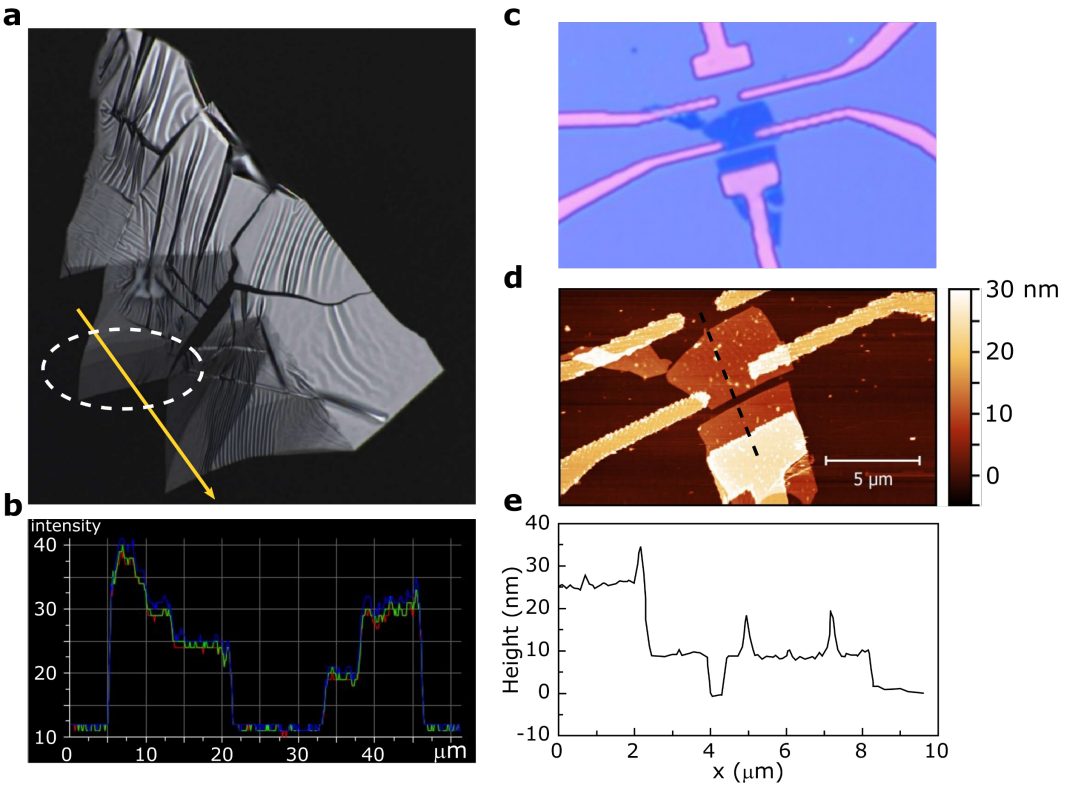

Figure 2.6| Calibration of FGT thickness matching contrast information and AFM topography. a, Optical image of an FGT flake exfoliated on PDMS. The flake presents several steps indicating the presence of a different number of layers. **b**, Light intensity profile correspondent to the yellow arrow in **a**. Sharp steps of light intensity results from the changes in thickness. **c**, Optical image of the flake in **a**, ripped during the stamping process. The piece transferred to the substrate correspond to the portion of FGT flake in the white dashed ellipsis. **d**, AFM image of the same flake, obtained in contact mode. **e**, The cross section extracted from the black dashed line in **d**, shows a flake thickness of $\sim$ 10 nm.

In Figure 2.6, the procedure to roughly calibrate the thickness of exfoliated FGT flakes with their optical contrast on PDMS is presented [74]. First, an optical image of a flake with multi layered regions was taken on specific condition of magnification (100×), and light exposure time (6 ms). The image was then analyzed with the microscope software, to extract the light intensity profile of flakes portions with different thicknesses (Figure 2.6a,b). The light intensity presents descrete steps of minimum intensity $\sim$ 5 (a.u) in correspondence to the thickness steps of the exfoliated flake. Transferring several flakes on different substrates (Figure 2.6c is an example of a broken one) and measuring with AFM in contact mode the actual thickness, one can calibrate the light intensity profiles to give information on the FGT thickness

at the exfoliation stage, before even transferring the flakes. In this case, contact mode was employed because we didn't care much about damages on the flakes. Already from the information reported in Figure 2.6, we can see that the broken part of the flake transferred on the substrate (Figure 2.6c), which was showing intensity of ~ 25 on a ~ 10 background intensity, was measured to be ~ 10 nm thick. This procedure has been particularly useful to have an idea about the flakes' thicknesses without needing to characterize them with AFM before performing the transport experiments on FGT (Chapter 5), avoiding so the harmful exposition to atmosphere. However, as mentioned before, it is a rather rough approximation, since the light intensity is not strictly linear with the thickness of FGT, especially when it becomes bulky (> 50 nm). For this reason the flakes' thicknesses were confirmed in every sample with AFM, after the transport measurements.

2.2.2 Electrical transport measurements

The main results reported in this thesis come from transport experiments. In Chapter 4, the superconductivity of $NbSe_2$ was probed with four-probe measurements at low temperature (T). In Chapter 5 and 7, magneto transport measurements at low T were employed to measure the anomalous Hall effect (AHE) in FGT and the unidirectional magnetoresistance (UMR) in Te nanowires.

2.2.2.1 PPMS

All the transport measurements performed in nanoGUNE were carried out in a Quantum Design PPMS (Physical Property Measurement System), a practical cryostat for magnetotransport measurements with a temperature range of 1.9 – 400 K, and a maximum magnetic field of 9 T. The PPMS stick, hosting the chip carrier, is equipped with a rotator which allows also to perform magnetotransport measurements dependent on the angle of applied magnetic field. The samples are glued to the chip carrier and electrical contacts are formed via wire bonding (*West Bond*). Since the magnetic field direction is fixed by the axis of the superconducting coil in the cryostat, to change direction of magnetic field with respect to the sample directions, two different chip carriers, also known as *pucks*, are employed. Thanks to the combination between rotator, type of pucks and mounting direction, one can decide to scan the field angle in three different planes. The N-puck allows for measurements with magnetic field that can vary from in-plane to out-of-plane direction with respect to the sample. The T-puck allows for rotating the field in the plane of the sample.

In Chapter 5, to measure the AHE of FGT, the magnetic field needed to be oriented in the out-of-plane direction, so normally the N-puck was used and maintained perpendicular to the magnetic field direction. In Chapter 7, we performed both field dependences with fixed angles and angular dependences in all the three planes available, so the samples were mounted and dismounted from both pucks to obtain the desired magnetic field configuration (see Appendices of Chapter 7 for more details).

The electrical measurements were performed employing a current source (*Keithley 6221*), a nanovoltmeter (*Keithley 2128A*) and a source measure unit (*Keithely 2636*). The four-probe measurements were carried out using the pair of Keithleys 6221 and 2128A, employing the so-called *delta mode* to improve the signal to noise ratio and suppress potential thermal effects. Delta mode is a d.c. reversal technique, which consists in injecting alternated positive and negative currents and measuring the voltage each time that the polarity of the current changes. For each measurement point the voltage reading is extracted form the following equation:

$$\Delta V = \frac{V(I_+) - V(I_-)}{2} \tag{2.1}$$

where $V(I_+)$ and $V(I_-)$ are the voltages for the positive and negative charge current polarity, respectively. The process is repeated for a set number of times (e.g., 16 or 32 counts) to then average on all the obtained ΔV values. This method works in linear regime of current and voltage and removes any contribution dependent on the current direction. Delta mode is equivalent to measure the 1st harmonic signal when using an a.c. lock-in measurement, and it has been employed for the measurements of FGT AHE in Chapter 5, and for the measurements of what we call R^{avg} in Chapter 7. In both cases, the voltage signals have been translated into resistances, dividing by the current applied.

The delta mode can also be employed in an asymmetric way, which allows also extracting the values of voltage dependent on the current direction. To do this, instead of changing the polarity of the d.c. pulses, one can set the delta to jump between $I_{+/-}$ and $I = 0$ A. The difference between the signals ($\Delta V_{+/-}$) obtained from the asymmetric delta mode was taken to analyse the current-dependent resistance ($R^{\text{diff}} = (R(I_+) - R(I_-))/2$). This takes into account the nonlinear contributions coming from different current directions, and the signals obtained are the equivalent of 2nd harmonic signals when using an a.c. lock-in measurement. In this case, we had to discard all the measurements with currents which were causing heating effects on the samples.

For the gate dependence measurements, a Keithley 2636 source meter was used to apply a constant voltage between the Si doped substrates and the ground connected to the sample under probe, in order to form a kind of field effect transistor configuration. The leakage current through the SiO_2 dielectric was constantly proved with the source meter to be smaller than 10 nA.

Asymmetric delta in combination with gate dependence have been used to measure the UMR characteristic of the Te NWs presented in Chapter 7.

2.2.2.2 Oxford Heliox III

An Heliox VL ^{3}He insert from Oxford, was used to perform the four-probe measurements of Chapter 4, down to 0.29 K. The use of such system was necessary because the lowest temperature reachable with our PPMS in nanoGUNE, was not low enough to fully observe the superconducting transition of $NbSe_2$. Moreover, the reasonably fast loading and unloading procedure, made it the ideal choice to measure many samples in a reasonable amount of time. It was used with the help of Ananthu Surendran, Thilo Bauch and Floriana Lombardi, during a secondment in Chalmers university.

The sample was placed in the insert and immerged in the cryostat to perform four-probes R vs T measurements while cooling down to 290 mK. To go below the liquid ^{4}He temperature, we pumped on ^{4}He, collected in the so-called 1K-pot, bringing the T to around 2 K. In this way, the ^{3}He available in a small reservoir, embedded in the insert, could condensate. A certain amount of liquid ^{3}He accumulates in the 300mK-pot located in the vicinity of the sample, providing for enough cooling power to lower T until the base temperature. The base temperature could be kept constant for about 90 mins. For the electrical measurements, an *Agilent* wave form generator was used to apply current to the sample, which was wire bonded to a chip carrier and probed through a bias circuit characterized by a bias resistor and a sampling resistor. The voltage was measured across the sample and the sampling resistor to get respectively voltage and current, which were then amplified and readout with multimeters and data acquisition system.

2.2.3 X-ray reflectivity

X-ray reflectivity (XRR) measurements have been employed to extract the thickness of thin films, and calibrate the deposition rates of metals and molecules, in order to have a good control on the films' thickness. These measurements were performed in a *X'Pert PRO* by *PANalytcal*. The X-ray tube of

this system has a wavelength $\lambda = 0.154$ nm that corresponds to CuK_α radiation, as the anode of the X-ray generator is made of Cu. As crystals consists of regularly spaced atoms, depending on the optical path of the X-rays into the crystal, the reflected rays will interfere constructively or destructively (see scheme in Figure 2.7).

The spatial variation of the intensity forms a diffraction pattern that contains information of the crystallographic structure of the material. Bragg's law describes the condition for constructive interference:

$$n\lambda = 2dsin(\theta). \tag{2.2}$$

where n is the interference order, λ is the wavelength of the incident wave, d is the distance between the atomic planes and θ is the scattering angle respect to the surface plane.

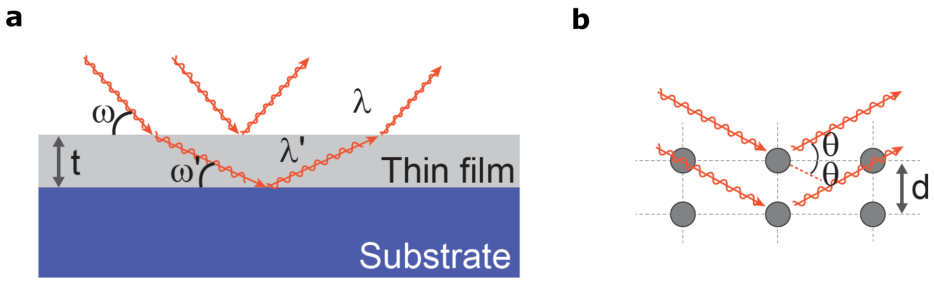

Figure 2.7| X-ray reflectometry working principle. a, Schematic of X-ray reflectivity beam configuration, where ω is the incident angle of the X-rays, λ and λ' are respectively the wavelengths in air and in the film, and t is the film thickness. **b**, Schematic illustration of X-ray scattering in crystalline samples. Figure adapted from [75].

The x-ray incident beam angle and detection angle have the same grazing incidence value during the scan. The interference is generated at the top and the bottom surface of the film, giving rise to the Kiessig fringes in the measured intensity. From the periodicity of the fringes, we can calculate the thickness of the material [76]. The thin films made of metals and molecules characterized with this technique were typically polycrystalline, but nevertheless were giving enough reflected intensity to be able to analyze the Kiessig fringes. With such measurement, it was possible to determine with nanometric precision thicknesses between 5 and 100 nm. The limiting factor for this measurement method is the roughness of the films, i.e. if it exceeds 5 nm the reflected intensity is strongly damped and the fringes cannot be observed, making impossible to determine the thickness.

PART I

3 Hybrid van der Waals heterostructures

The fabrication of materials with on-demand electronic, optical and magnetic properties lies at the heart of materials science. Efforts in the quest for materials by design have produced exquisite results in basic research and technology, which have influenced a number of research fields directly linked to applications (communications, information, mobility). A strong connection exists between basic research in materials science and electronics, since the design of ultimately all electronic components relies on peculiar material capabilities. In this regard, the demonstration of new materials with unconventional properties could inspire novel device concepts which could go beyond conventional micro-electronics. The discovery of two-dimensional (2D) materials [10] and the possibility of forming layered heterostructures [43], gave a further push to the search for novel customized materials. Speaking about the role of heterostructures in device applications, in the 2000 Nobel Lecture [77], Herbert Kroemer coined the famous phrase "*the interface is the device*". When describing 2D materials, one could say similarly that "*the surface is the material itself*", thus implying the presence of an ultra-high sensitivity to surface modifications, which is intrinsically connected to their low dimensional nature. For instance, it has been demonstrated that electric fields effectively modulate several physical properties of 2D materials. The initial breakthrough work on graphene reported an electric field effect modulation of the electrical conductance of graphene [78] by a gate terminal in a field effect device. After few years, it was realized that even the optical properties of 2DMs, such as the photoluminescence, are gate-tuneable [79,80]. Recently, electric field effect was found to modify also superconductivity [81,82] and magnetism [83–85] of 2D materials, opening an intriguing path for understanding electron-electron correlations in reduced dimensionality, and offering the possibility to design novel devices for spintronics and quantum information.

Following these examples, hybrid vdW heterostructures (vdWHs), where molecules are coupled to 2D materials, have been studied with two distinct goals, i.e., demonstrating novel device architectures for electronic and optoelectronic applications and modifying fundamental physical properties of 2D materials [86]. While nowadays a rather vast literature exists about molecular

doping on 2D materials for the improvement of the performance of optoelectronic devices, their full potential is far from being completely explored. In the following sections we will go through the mechanisms behind the doping effects, how they can be indirectly exploited to tailor also intrinsic properties of 2D materials and finally, we will go through a review of previous experiment that represented a fundamental background for the findings that will be reported in the next chapters.

3.1 Molecules as building blocks for hybrid vdWHs

Molecules offer a distinctive prospect to enlarge the horizon of vdW heterostructures. Whereas the properties of inorganic 2D materials are defined by the pristine atomic arrangement of the single layer structure [87], molecular compounds can be designed to have specific characteristics pre-determined at the synthesis stage. This chemical flexibility allows for the synthesis of a quasi-endless number of possible molecules with functional groups carrying electronic, optical, and magnetic properties that can activate specific atomic/molecular interactions with 2D materials [88–90].

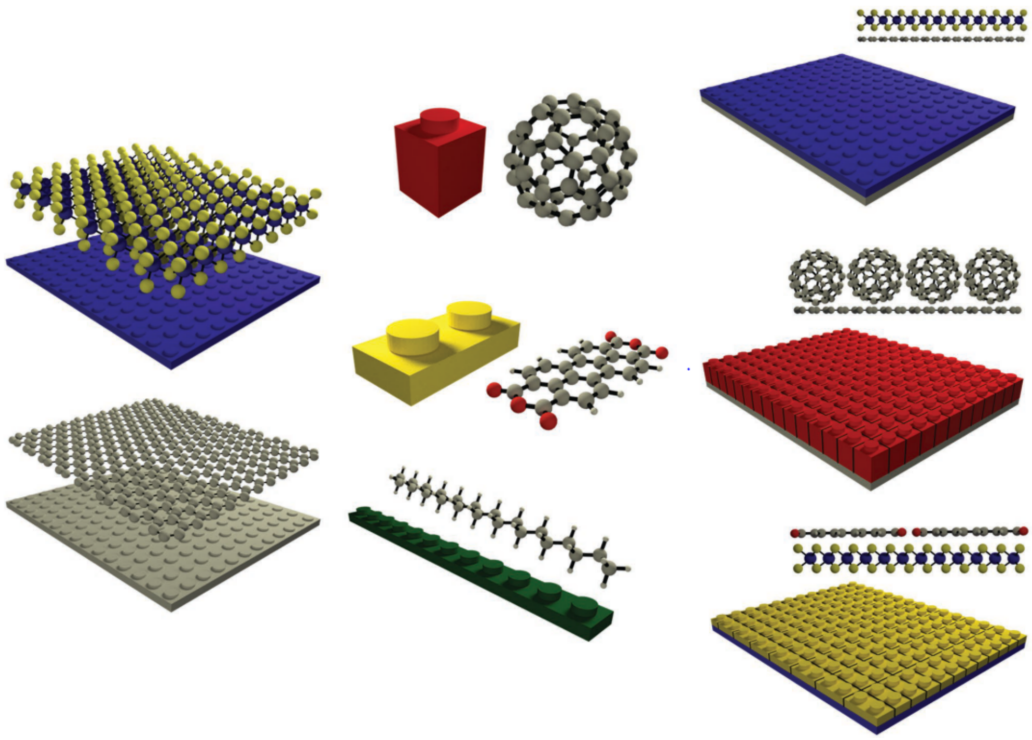

Figure 3.1| Molecules as building blocks with function by design. Small molecules with different functionality defined by their design that can be used as 0D or 1D building blocks to form hybrid vdW heterostructures. Figure adapted from Ref. [86].

Similarly to the original visual concept that depicts inorganic 2DMs as flat building blocks [43], one can consider small molecules as dot-like quasi-0D building blocks, which aggregate in continuous layers onto the inorganic 2D materials surfaces with thicknesses ranging from that of a monolayer up to tens of nanometers (Figure 3.1). Within the organic layers, molecules stick together through weak noncovalent interactions such as vdW, dipole–dipole, or electrostatic forces [91–94]. The control of such supramolecular interactions can be employed to generate self-assembled long-range ordered organic films that can grow over large areas at the surface of inorganic 2D materials [95]. In a similar way, the single components of the molecular layers can be organised to assume certain orientations along a given direction, providing further control on the formation of the assembly. Thanks to the crystalline ordering that can be obtain in such molecular layers, the periodically recurrent local interactions between the 2D materials and each molecular site collectively sum-up to induce a spatially homogeneous surface modification on a mesoscopic scale that results in nonlocal macroscopic effects influencing the properties of the new system. The interactions keeping together the stacks composed by the 2D materials and molecular layers are generally weak van der Waals forces as in inorganic 2D-2D heterostructures [96]. For this reason, the interface environment is similar in the two cases and organic/inorganic architectures can be seen as the hybrid equivalent of fully inorganic vdW heterostructures. Following this analogy, one can easily understand that crystalline molecular monolayers can be grown on 2D materials [97–101] that can be further integrated in complex multilayered heterostructures composed of alternating organic/inorganic single layers [86].

3.2 Molecules on 2D materials: doping effects

From the early experiments on graphene, it became clear that the interaction of gas molecules with its surface was responsible for significant changes on the electrical transport properties of graphene itself. It was soon demonstrated that this effect was induced by the molecular species acting as donors/acceptors and introducing an effective carrier density variation in the material [102,103]. After these first reports, molecular (or chemical) doping of graphene established as a steadily growing field, and many other studies exploiting molecules to tune the work function of graphene were produced in the next years [104–108]. Following this approach and applying well-established concepts inherited by organic electronics to select or design p- or n-type molecular dopant [109], the field expanded towards mono- and few-layers TMDCs [110–115] and

black phosphorous [116] demonstrating that controllable doping have implications not only on the electrical properties, but also on the optical ones. Moreover, one of the beauties of this doping approach is the possibility of upscaling it to large areas for potential industrial purposes [111].

3.2.1 Microscopical origin of molecular doping

Molecular doping is typically described in two ways (see Figure 3.2), charge transfer [106] or molecular-dipole-induced shift in work function [108]. The case of charge transfer involves the energy level alignment between the 2D material and the molecular layer which makes energetically convenient for electrons or holes to move from one material to the other, at the interface. For instance, when the electrochemical redox potential of a given molecular dopant lies below (above) the Fermi level of the 2D material, holes (electrons) transfer can take place from the molecules to the 2D sheet, inducing electron depletion (accumulation) namely p-type doping [110] (n-type doping [117]).

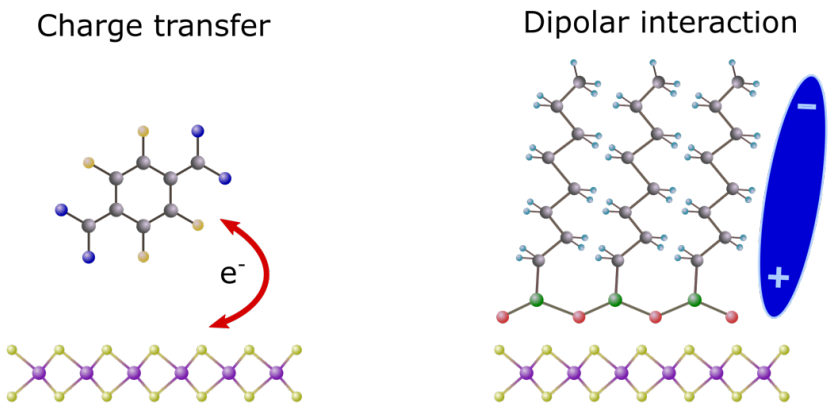

Figure 3.2| Interactions and doping mechanisms at molecules – 2D interfaces. Schematic representation of the two main processes responsible for doping effects in hybrid vdW heterostructures, namely charge transfer (left) and dipole induced doping.

On the other hand, dipole-mediated doping can potentially occur whenever polar molecules are physisorbed on the surface of 2D materials. In this case, the mechanism relies on the emanation of an electric field by the molecular dipole moment, that modulates the local charge carrier density as a nanoscopic equivalent of a fixed electrostatic gate in field-effect devices. When several physisorbed molecules order and align to form a continuous layer, the local gating can sum up leading to a macroscopical modification on the 2D material work function and thus inducing doping [118]. The field effect strength depends on the orientation of the dipolar groups with respect to the surface

(maximum when perpendicular) and it can even change sign depending on which side of the dipole approaches the interface, resulting in p- or n- type doping [113,119]. While the two mechanisms are often contributing together to the doping effects and they are difficult to discern, it is important to understand their practical differences to design customized experiment for each specific purpose and material. Here to have a further insight, we will briefly analyse special cases in which either contribution is dominant for the doping of few-layer TMDCs.

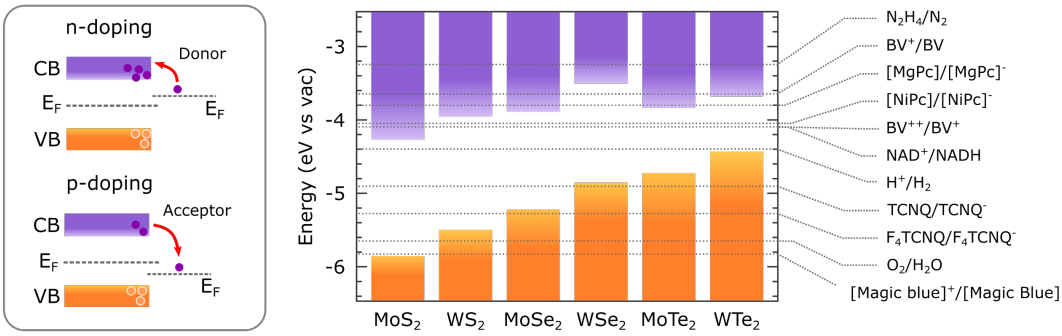

Figure 3.3| Charge transfer mechanism and chart showing electrochemical redox potentials of various molecular dopants and band edges of group-6 TMDs. Molecular species act as acceptor or donors depending on their energy level alignnt with the TMDCs conduction band (CB) or valence band (VB). The chart on the left was adapted from Ref. [120].

Figure 3.3 shows a comparison between the reduction potentials of several molecules and the electron affinity (conduction band minimum) and ionization potential (valence band maximum) of group-6 TMDCs. The diagram can be used as guideline to select opportune 2D material/molecule pair in which charge transfer take place as main doping effect. Since the charge transfer is regulated by the energy level alignment at the interface between molecules and 2D materials, we can consider a situation in which there is a large difference between the reduction potential of the molecule and either the conduction band (for n-type semiconductors) or the valence band (for p-type semiconductors) edge of the 2D material. For instance, in the case of MoS_2, an n-type semiconductor, the charge transfer occurs at the conduction band edge since the Fermi level is closer to it than to the valence band, and two good choices to induce n- and p-doping are respectively, Benzyl-viologen (BV) as electron donor and 2,3,5,6-tetrafluoro-7,7,8,8- tetracyanoquinodimethane (F_4TCNQ) as electron acceptor (see Figure 3.3). Benzyl-viologen has a very low reduction potential, so that when it is coupled to electron acceptors the offset between conduction band and reduction potential makes it favourable for the electrons

to be transferred from the molecule to the 2D material. This effect has been demonstrated in MoS_2 based transistors as an increase in the concentration of free electrons available for charge transport that changes the transfer characteristic of the doped device as shown in Figure 3.4a,b [117].

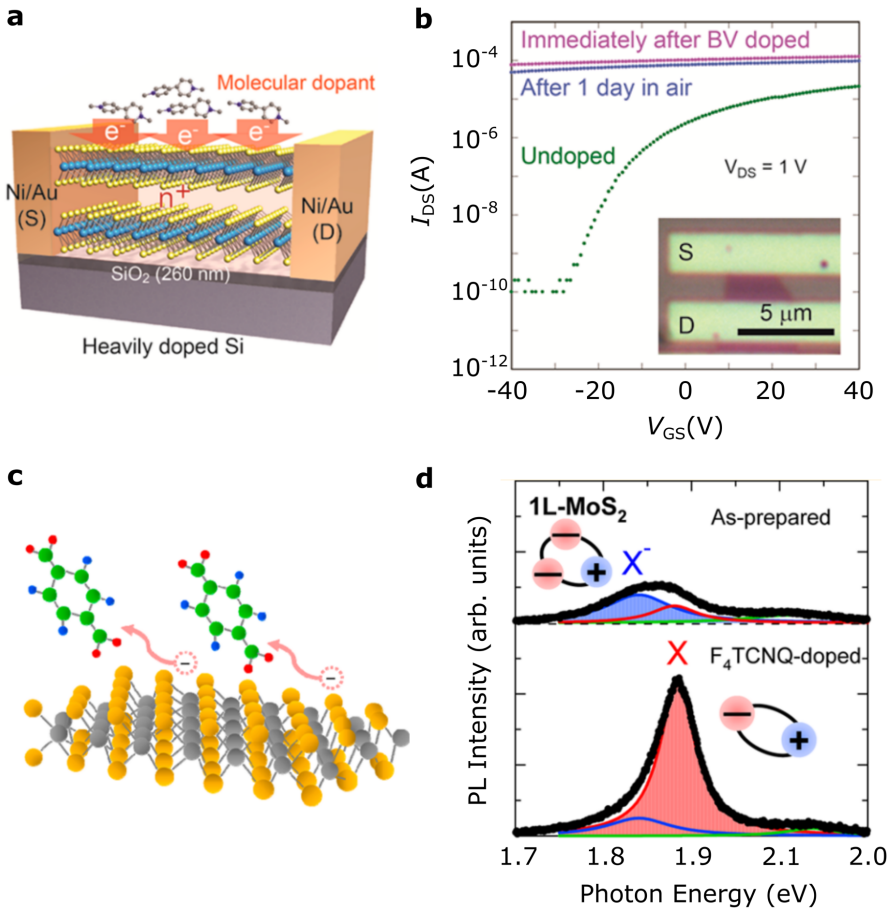

Figure 3.4| Experiments on molecular doping of MoS_2 in which n- and p-doping via charge transfer changes transport and optical properties of the material. a, Schematic illustration of a back-gated MoS_2 device used for neutral benzyl viologen (BV) surface charge transfer doping studies. **b**, Transfer characteristic curves of the device before doping (green), right after BV doping (purple), and after the doped device was kept in air for 1 day (blue) at $V_{DS} = 1$ V. The inset shows an optical microscope image of the device, consisting of trilayer MoS_2. **c**, Illustration of F_4TCNQ molecules acting as electron acceptors when brough in contact with single layer MoS_2. **d**, Analysis of the PL spectral shapes for as-prepared and F_4TCNQ-doped MoS_2. The peaks were fitted with trion (X^-) and neutral exciton (X) contributions. The images are adapted from Refs. [110,117]

Conversely, F_4TCNQ it has been widely studied as p-dopant for MoS_2, since the reduction potential lays well below the conduction band edge and electrons are taken by the molecule, depleting the MoS_2. Interestingly, changes in photoluminescence were recorded due to the change of the recombination process

taking places in the band gap. In particular, in pristine MoS_2 the trion intensity was found to be higher than the neutral exciton intensity, while in the depleted material the situation reverses (see Figure 3.4b,d) [110]. These findings suggest that solution processed molecules can provide for an alternative method to enhance the efficiency of injection and extraction of electrons in optoelectronics applications.

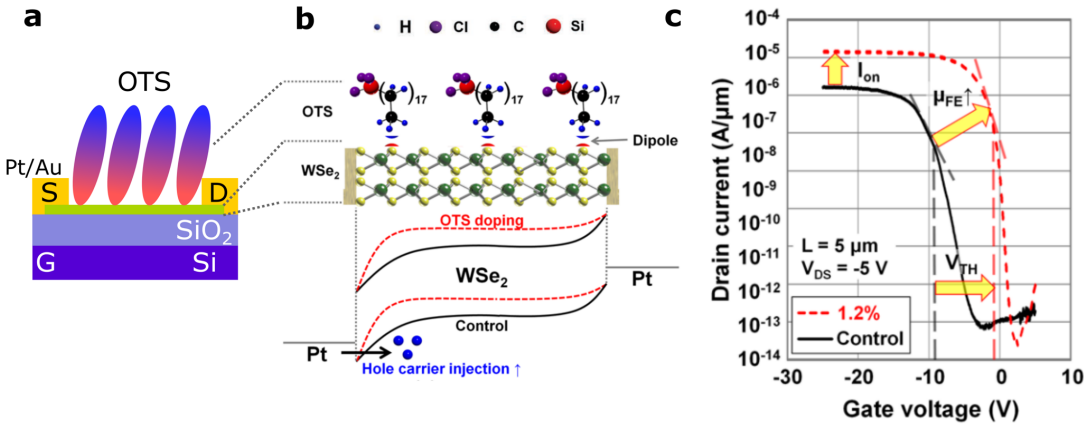

Figure 3.5| Dipole induced p-type doping on WSe_2 via octadecyltrichlorosilane (OTS) adlayer. a, Device scheme illustrating the field-effect transistor configuration and the aligned OTS molecules forming the adlayer. **b**, The doping mechanism is represented as an induced dipole at the interface that causes a shift in the WSe_2 work function. **c,** Effect of the OTS layer onto the field-effect response of WSe_2. The shift of the threshold voltage toward more positive values is indicative of p-type doping. Figure adapted from Ref. [113].

The doping effect attributed to molecular dipoles can be isolated and understood considering molecular species with very wide bandgaps, i.e., insulators, since their energy level configuration typically prevents an efficient charge transfer to 2D semiconductors. For instance, octadecyltrichlorosilane (OTS) was demonstrated to induce p-type doping on WSe_2 [113]. The effect was observed in a field-effect device where, after the deposition of the molecular film, the threshold voltage of the device transfer characteristic decreased showing a shift towards positive voltages, as if p-doping was induced by the molecules. Excluding charge transfer processes, the explanation was ascribed to a shift in the work function of WSe_2 induced by a global electric field generated from all the aligned molecular dipoles forming the molecular layer. Such alignment and long-range ordering are dictated by a self-assembly process that is fundamental to determine the orientation of the molecular dipole, and thus the polarity of the effective electric field experienced by the 2D material. Even though in the case of results represented in Figure 3.5, the role of the molecular

orientation was only a posteriori inferred on the basis of the electrical results, it revealed that a precise control over the self-assembly would allow another deterministic way to control efficiently the doping of 2D materials, expanding the range of possible molecular compounds to be used for such purposes.

3.3 Beyond doping: 2D materials molecular decoration

The reliability and reproducibility of doping effects in hybrid vdW heterostructures led to the tendency of researchers to use molecular compounds on 2D materials almost exclusively to boost or optimize the performances of electronic and optoelectronic devices. Despite this approach granted excellent results, it also limited the exploration of the molecules' full potential. In fact, recent experiments indicate not only that carrier density variations can have indirectly an impact on intrinsic properties of 2D materials, but also that doping is only one among the possible effects taking place at the organic/2D material interfaces. In particular, experiments adopting the so-called "molecular decoration" demonstrated that it is possible to open a bandgap in bilayer graphene and even to modify the superconducting properties of a 2D In layer as well as the ones of $NbSe_2$. These are among the earliest works aiming to tailor the fundamental properties of 2D materials with molecules and, in both cases, there was no particular control over the molecular assembly since it was not playing a fundamental role in the specific experiment. At the end of this chapter, we will see how, having full control on the molecular arrangement, one can achieve similar manipulations of 2D materials properties in a more programmable manner.

The first example is presented to demonstrate how doping can be indirectly used in more creative ways, as for the case of bilayer graphene, in which a bandgap can be opened with an out-of-plane electric field that breaks spatial inversion symmetry [121]. While a straightforward way to achieve this is to employ dual gate configurations [122,123], it has been demonstrated also that molecular dopants can exert strong statical electric fields and provide for the same bandgap opening in graphene without the need of particular fabrication processes [124–126]. In one specific case [126], a chemical engineering approach was employed to maximize the efficiency of the molecular layers. Bilayer graphene was mechanically exfoliated onto a SiO_2 substrate that was previously functionalized with a self-assembled monolayer (SAM) possessing an n-doping amino group (NH_3). Subsequently, a layer of F4-TCNQ (p-dopant) was evaporated on the top graphene surface, forming a sandwich structure in which a

strong electric field developed perpendicularly to the bilayer graphene due to the nature of the top and bottom layers, effectively opening a bandgap. With the electrical characterization, it was confirmed that the amino-SAM introduced n-doping resulting in a shift of the Dirac point toward negative values. With the addition of the F4TCNQ a further shift of the Dirac cone was observed, this time towards positive values confirming the p-doping introduced by the top layer. Moreover, the presence of the molecular layers enlarged progressively the I_{ON}/I_{OFF} ratio in the bilayer graphene, demonstrating the widening of the bandgap as a consequence of an enhanced perpendicular electric fields across the sandwich structure (Figure 3.6). From further electrical and optical characterization the bandgap was estimated to be between 100 and 200 meV, revealing that significant variation in the band structure of a 2D material could be achieved thanks to molecular decorations.

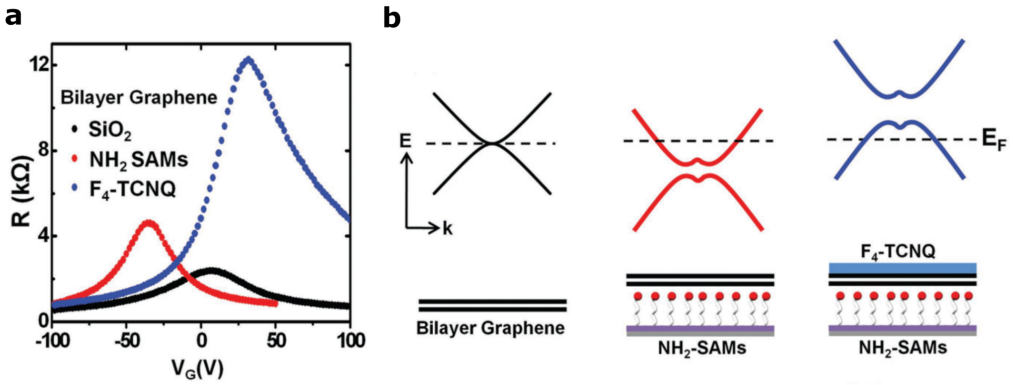

Figure 3.6| Chemical-engineering approach to open a bandgap in bilayer graphene. a, Transfer characteristics of bilayer graphene on SiO_2, on an amino SAM and covered by a F_4TCNQ layer. The resistance change induced by the presence of the molecules, indicates the opening of a bandgap in the bilayer graphene/organic systems. **b**, Scheme of the mechanism displaying the role of the molecules that introduce a significant electric field across the bilayer graphene capable to break inversion symmetry and open a bandgap. Figure adapted from Ref. [126].

In a more recent study [127], Yoshizawa et al. reported that the superconductivity of a 2D material was affected by molecular adlayers, demonstrating the existence of molecular related effects beyond doping. Epitaxial monolayers of In grown on Si were used as a platform to compose heterostructures with two phthalocyanine (Pc) molecules with different coordinating metal ions (MnPc, CuPc) and to study the effect of the molecules on the superconductivity of In. Increase or decrease of superconducting transition temperature (T_C) were observed due the interaction of In monolayers with adlayers of CuPc or MnPc respectively (Figure 3.7). Using a combination of different techniques,

including STM, angle-resolved photoemission spectroscopy, X-ray magnetic circular dichroism, and ab initio calculations the authors were able to address the mechanism behind the suppression or enhancement of the superconductivity. In the case of MnPc, the decrease in T_C was ascribed to the magnetic pair breaking effect induced by the magnetic momentum of the d-molecular orbital extending to the In monolayer. Conversely, the d-orbitals of CuPc are confined within the molecule and the same suppression effect was not observed in this situation. On the other hand, the resistance vs temperature plots show a small increase in T_C that it has been explained by a molecular induced p-type doping.

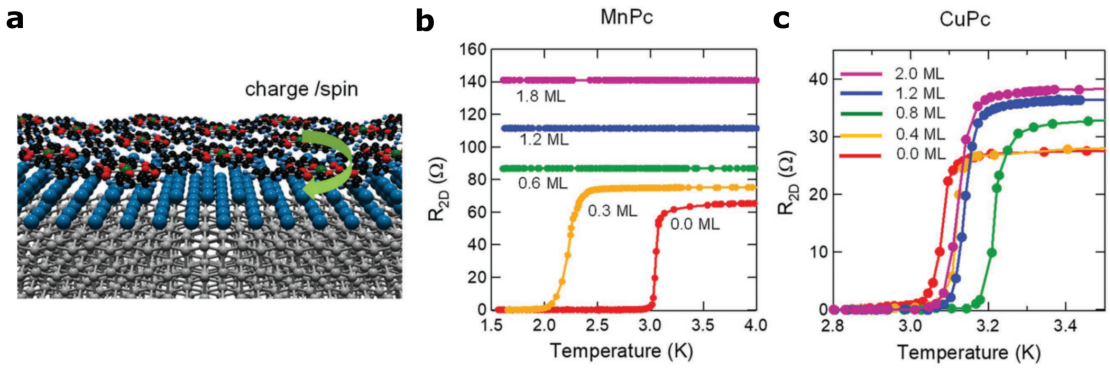

Figure 3.7| Molecular tuning of superconductivity in epitaxially grown monolayer In. a, Representation of the multilayer composed by In, grown on a Si substrate with metal phthalocyanines deposited on top (Mn, Cu are the coordination metals). In the case of MnPc, **b**, the superconductivity is largely suppressed, while in the case of CuPc, **c**, the transition temperature is increased. Figure adapted from Ref. [127]

The results of these studies show the possibility to tune fundamental parameters of 2D materials and highlight the importance of a comprehensive understanding of the effects occurring at the inorganic/organic interface. On the specific case of modulation of superconductivity, for example, Kezilebieke et al. performed a fundamental study on the interaction of single CoPc molecules on the superconductive states of $NbSe_2$ [128]. Due to the Co metallic center and their structure, CoPc possess a non-zero magnetic moment ($S = 1/2$), and it behave like a magnetic impurity on the surface of $NbSe_2$ having a dramatic impact on its superconductivity. In particular, the effect of magnetic impurities is to break time-reversal symmetry and to induce low energy bound states within the superconducting gap called Yu—Shiba—Rusinov states (YSR). Using low-temperature scanning tunneling microscopy (STM) and spectroscopy, YSR states were observed on single CoPc molecules deposited on the $NbSe_2$ surface (Figure 3.8). Moreover, since YSR states spatial extent

is greatly enhanced in 2D systems, the formation of coupled states is facilitated and through STM lateral manipulation the authors created controlled CoPc dimers demonstrating the formation of YSR coupled states. Strong variations of the coupling strength were found depending on the detailed geometry of the CoPc dimer, which are ascribed on the details of the wave function overlap of the two impurity states. This work demonstrated, through a fundamental study, a promising path to realize novel topological phases or to design magnetic lattices on superconductors.

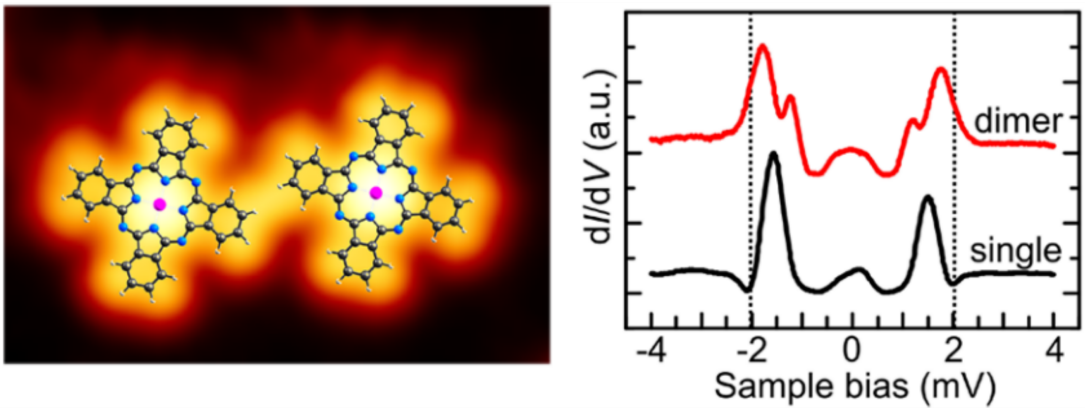

Figure 3.8| Coupled Yu-Shiba-Rusinov states in molecular dimers on $NbSe_2$. STM image of a Cobalt phthalocyanine molecular dimer deposited on the surface of $NbSe_2$ and comparison of the $\mathrm{d}I/\mathrm{d}V$ spectra between the molecular dimer, showing split YSR states (red line), and the single molecule (black line). Figure adapted from Ref. [128].

Finally, it should be now clear that molecular compounds provide for unique functions which could be coupled to 2D materials for the exploration of more advanced phenomena, beyond static doping. However, there are still only few examples in which molecular decoration is exploited to confer unique molecular capabilities to 2D materials [129–135].

3.4 Review of relevant experiments

As mentioned in one of the previous sections here we will review, in more detail, two experiments that represented respectively the main background for Chapters 4 and 5.

3.4.1 Deterministic control of the SAM to control the dipole-induced doping

The precise control over the ordering of molecular layers, allows to periodically extend over a large area, the otherwise local interactions between single molecules and the surface of 2D materials. The connection between the quasi zero dimensionality of molecules and the two-dimensionality of layered materials, can be realized via spontaneous yet controllable self-assembly that can be designed specifically to create highly ordered molecular lattices on the surface of 2D materials. The process of self-assembly at surfaces has been initially studied in graphene samples [136–138], and it is driven by molecule–molecule and molecule–substrate vdW interactions, which are similar also for most layered materials, including TMDCs [139–141]. Therefore, well-established concepts inherited by research in supramolecular chemistry at the surfaces [142] can be exploited to controllably arrange molecular functional groups on 2D materials.

In a recent work of Stoeckl et al. [143], for instance, silane molecules containing different functional groups were used to form self-assembled monolayers on the surface of WSe_2 with the objective of boosting in a controlled manner the mobility of either electron, holes or of both simultaneously. WSe_2 is a semiconducting TMDC of great interest for electronic applications since it can transport both electrons and holes. However, WSe_2 based transistors are typically characterized by poor charge injection if fabricated with standard Au contacts, and while unipolar transistor properties can be improved via contact engineering, the ambipolar transport is prevented by the limited injection of either electrons or holes. In their experiments, the authors employ particular silane-based molecules, made of two different functional group, to create self-assembled monolayers at the surface of WSe_2 that would induce a dipole mediated n- or p-doping, capable of improving at will the injection and mobility of electron or holes, respectively (see Figure 3.9). The efficient doping is mediated by a shift in Work Function (WF) of WSe_2 caused by the global electric field emanated from the long range ordered molecular layer with all the dipoles aligned perpendicularly to the surface of the 2D material. Depending on the choice of functional group, being amine based in N-[3-(trimethoxysilyl)propyl]ethylenediamine in AHAPS or fluorinated in Trichloro(1H,1H,2H,2H-perfluorooctyl)silane PFS, it is demonstrated that one can control the orientation of the dipole and thus, the type of doping (Figure 3.9a,b). Therefore, the molecular design allows for a programmable tuning of the 2D material, where on one hand, the functional group define the orientation of the dipole, and so the

type of doping, while on the other, the anchoring group is crucial for the formation of a well-ordered self-assembly in which perfectly aligned dipoles add up their contributions on a macroscopic scale to ensure an efficient doping.

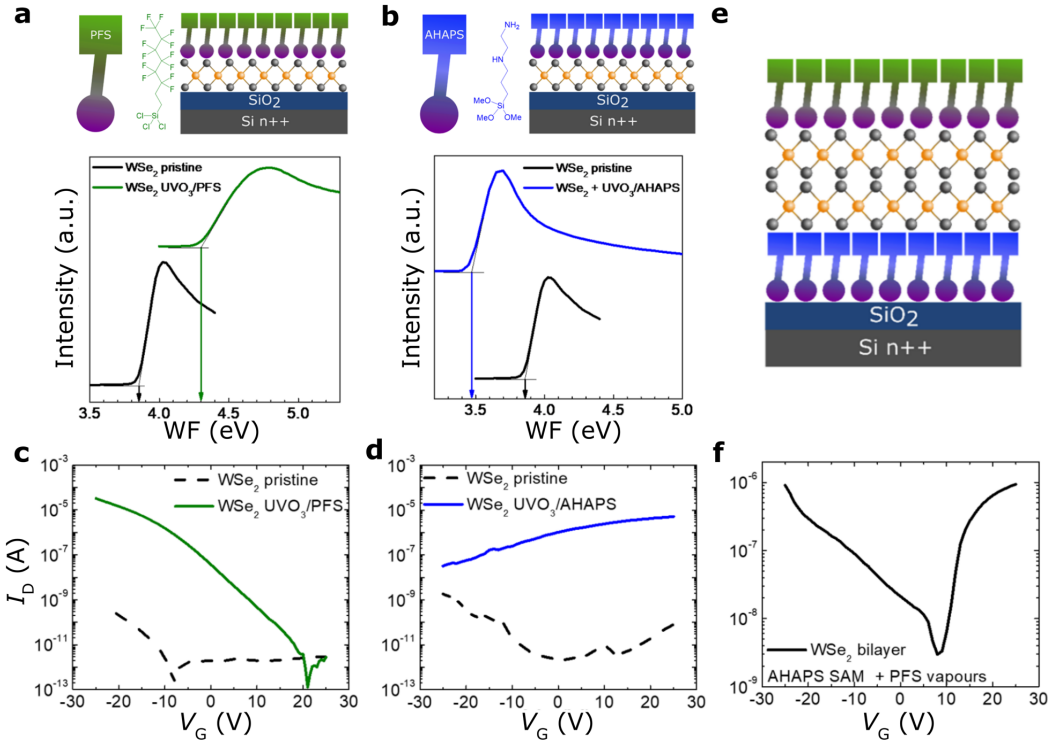

Figure 3.9| Analysis on the dipole induced doping dependent on the SAMs functional groups and demonstration of ambipolar transport in WSe_2. Device scheme and secondary electron cutoff of **a**, AHAPS-treated and **b**, PFS-treated WSe_2 surface, compared to the corresponding pristine surface. Transfer characteristic of single layer WSe_2 flakes before (dashed lines) and after (solid lines) the treatment with **c**, PFS and d, AHAPS. **e**, Scheme of a WSe_2 double layer sandwiched in between the two SAMs. **f**, Transfer characteristic of the device obtained from the sandwiched structure showing ambipolar transport. Figure adapted from Ref. [143].

These two degrees of freedom are analyzed in detail, starting from the role of the functional group. Measuring the transfer characteristic of field effect transistors based on single layer WSe_2, it was observed that the samples treated with AHAPS and PFS were showing respectively an opposite conductivity dependence to the gate voltage, demonstrating that the two SAMs induce respectively n- and p-doping (Figure 3.9c,d). The ultraviolet photoemission spectroscopy UPS measurements confirms that the WF of WSe_2 is modulated consistently with the doping observed by the presence of the SAMs (Figure 3.9a,b). Moreover, in a final experiment, the ambipolar transport was demonstrated in a bilayer-based transistor built in between a sandwich of the two SAMs, one used to functionalize the substrate and the other grown on top

of the 2D material (Figure 3.9e,f). The realization of this device demonstrates once more the power and versatility of molecular decoration.

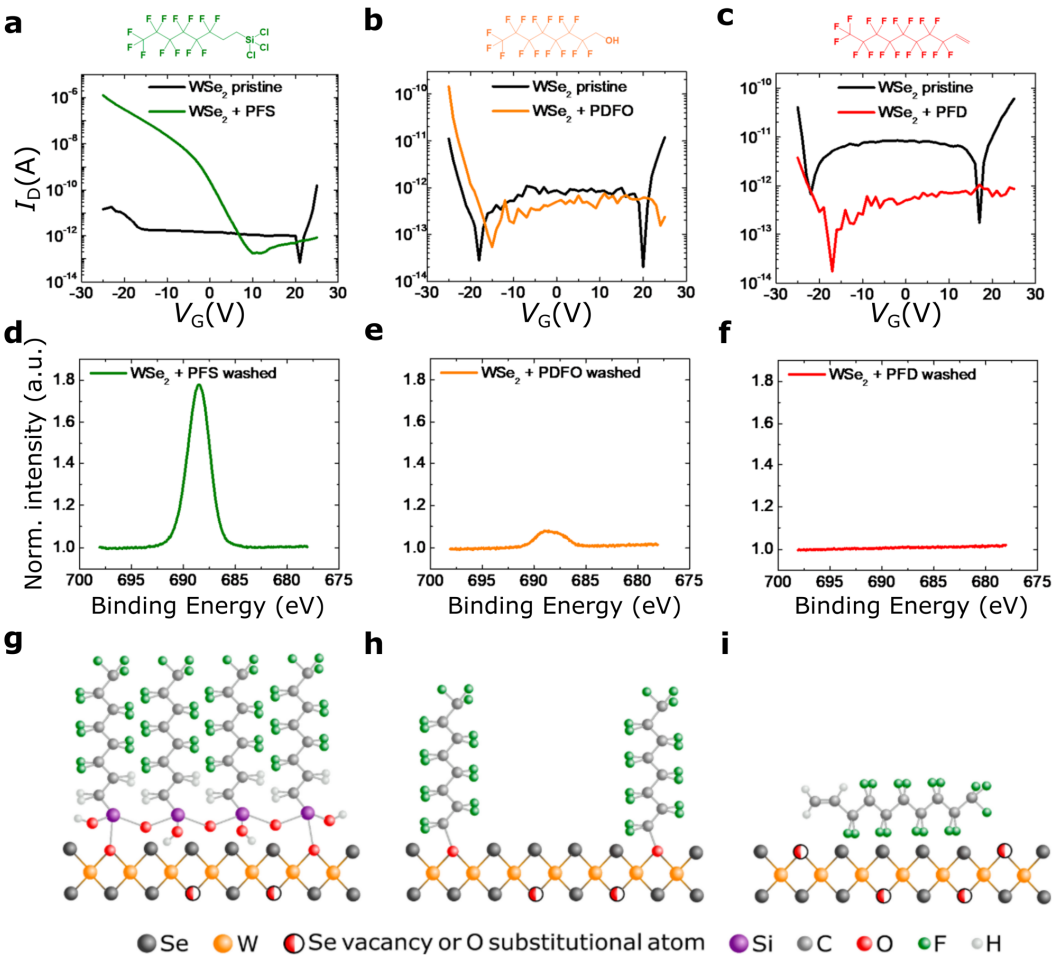

Figure 3.10| Analysis on the role of the anchoring group to the formation of a long range ordered self-assembly. a-c, Transfer curves of WSe_2 single layers on untreated SiO_2 substrates (black lines), and comparison with the same samples exposed to **a**, PFS, **b**, PDFO, and **c**, PFD vapor (colored lines). The chemical structures of PFS, PDFO and PFD are shown above. **d-f**, Fluor 1s core level spectra of WSe_2 bulk crystal after exposure to **d**, PFS, **e**, PDFO, and **f**, PFD vapor and subsequent sonication in ethanol and toluene. **g-i**, Schematic illustration of the proposed anchoring mechanism/adsorption on defective WSe_2 (exhibiting vacancies or oxygen substitutional atoms) for each molecule. Figure adapted from Ref. [143].

The importance of the molecular design in terms of control on the self-assembly is shown in Figure 3.10, where the effects of three different molecules with the same fluorinated group, bearing the dipole necessary to induce p-doping, but different anchoring groups, were tested on the surface of WSe_2. The three molecules, namely PFS, PDFO and PFD are terminated respectively with a trichloro silane group, an alcohol group and an alkane group. After exposing WSe_2 flakes to vapor of the three molecules and washing away

the excesses, electrical and spectroscopical measurements were performed to cast light on the role of the anchor group. The electrical measurements in Figure 3.10a,b,c show that PFS has the best impact on the performance improvements of the three transistors, PDFO leave the situation unchanged while PFD degrade even further the already poor performances of WSe_2, demonstrating already that the anchoring group plays a role in the strength of the doping effect. The spectroscopic analysis of the samples (Figure 3.10d,e,f) on both the molecules and WSe_2, suggests that the mechanism behind the formation of PFS ordered layers relies on the formation of few strong bonds between silanol groups and Se vacancies or oxygen substitutional atoms at the surface of WSe_2 [144–146], that subsequently act as polymerization sites for the growth of the SAM composed by aligned and ordered neighbouring molecules (Figure 3.10g) [147]. In contrast, the alcohol group of PDFO, which might bind to defects in WSe_2 as well, does not have additional binding sites for polymerization; hence, most molecules, simply physisorbed on the WSe_2 surface (see Figure 3.10h), are removed by the washing procedures. Similarly, the alkene head of PFD prevents any covalent interaction with WSe_2 nor alignment of the dipole (Figure 3.10i), and the molecules are easily desorbed.

The results reviewed in this section will be a partial foundation for the work that will be presented in the next chapter of this thesis.

3.4.2 Molecular tunability of magnetic exchange bias

Following the example of some of the works performed on hybrid inorganic/organic interfaces [148–156], an intriguing direction for the research on hybrid vdW heterostructures, is the modulation of intrinsic magnetic properties of 2D materials by proximity of molecular adlayers with peculiar spin textures. Long-range magnetic order was found in a molecular assembly on graphene [137], and a claim of molecular induced magnetism in $NbSe_2$ has been reported [157], but whether or not (ferro) magnetism can be manipulated or induced in a 2D material by proximity effect to a molecular assembly is still a rather unexplored field. Here, to have a deeper understanding on the so-called "spinterfaces" [158], we will review a recent study [155], demonstrating the control of magnetism in Co ultra-thin films via exchange coupling mediated by adlayers of molecules carrying a nonzero spin and arranged with an antiferromagnetic ordering.

The hybridization of orbitals in metal–organic interfaces, also known as the formation of "organic spinterfaces" can lead to several effects of great interest for spintronic applications, such as spin-selective tunnel barriers [148,149],

modified magnetic anisotropy of ferromagnetic films [151] and tuning of interfacial magnetic coupling . The "on surface" configuration of molecules with ferromagnetic thin films provides an archetype platform for studying couplings between molecular spins and their environment. For instance, planar organometallic complexes [159–161] have been shown to couple their individual unpaired spins antiferromagnetically when stacked in multiple layers [162]. This means that if coupled to ferromagnets, organometallic molecular films can induce exchange bias to a ferromagnetic layer in their proximity. The exchange bias, induced by the AFM/FM coupling, strongly pins the magnetization of the FM layer leading to broadenings and shifts in the magnetic hysteresis loop of the entire film, providing for the fundamental features required in magnetic reading units and non-volatile memory devices.

In their work, Jo et al. performed a fundamental study that demonstrate the emergence of a tuneable molecular magnetic exchange bias at the hybrid interface between metalloporphyrin and FM cobalt layers [155]. They fabricated bilayers composed of Co and organic paramagnetic octaethylporphyrin (MOEP, M = Ni, Cu, and Zn) molecules and compared the magnetic properties of the bilayers to the ones of pure Co films. The magnetic properties were observed both through magnetometry and through magnetoresistance measurements at 10 K and after cooling down the samples under applied magnetic fields (± 2 T). The observed hysteresis loops showed significant broadening in all Co/MOEP systems and an asymmetry with respect zero field, indicating the presence of exchange bias at the interface (Figure 3.11). Consistent results were obtained from anisotropic magnetoresistance (AMR) and planar Hall resistance (PHR) measurements performed on Hall bar made of the same layers used for magnetometry. The results obtained from the system Co/NiOEP are shown in Figure 3.12 as a representative example also for the other bilayers. In particular, the exchange bias recorded by the authors is the largest measured in hybrid systems and it is dependent on the sign of the magnetic field applied during the field cooling, since it sets the AFM configuration of the molecular layers that pins the FM state on one of the two in-plane directions. Further experiments show temperature dependences, training effects and thicknesses dependences from both molecular layer and metallic layer, giving further insight on the interface coupling and confirming the presence of exchange bias.

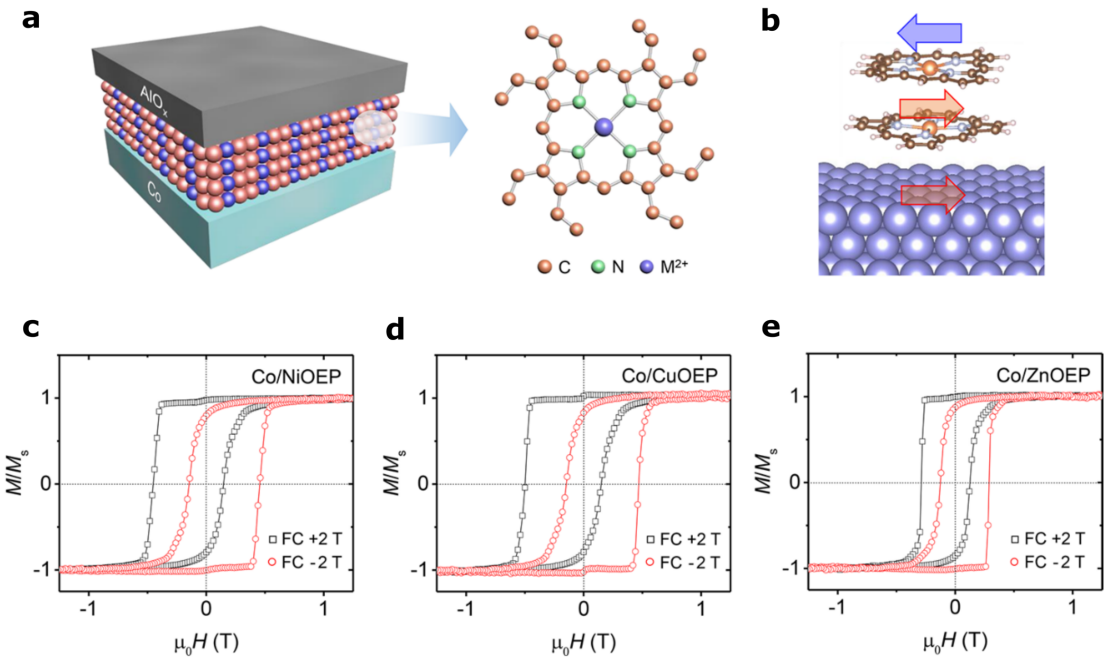

Figure 3.11| Magnetic exchange bias at the hybrid interfaces of Co/MOEP systems (M = Ni, Cu, or Zn). a, Schematic illustration of the Co/MOEP bilayer and chemical structure of the MOEP molecules. **b**, Representation of the magnetic ordering inducing exchange bias at the hybrid interface. **c-e**, Normalized magnetic hysteresis loops at $T = 10$ K of the heterostructures with Co (4 nm) and respectively NiOEP(8 nm), CuOEP(8 nm), and ZnOEP(8 nm). Each system displayed exchange bias characterized by a unidirectional shift in the hysteresis loop from the center. Figure adapted from Ref. [155].

Moreover, theoretical calculations have been used to model the interaction between molecules and metal at the interface (Figure 3.12c). While the overall magnetic configuration of AFM/FM was found to be consistent, since the interaction between subsequent layers of molecules also favours AFM ordering, the interfacial interactions between the FM and the molecular layers were ascribed to an indirect coupling. In fact, the MOEP central metallic atoms are rather far from the Co surface and besides the influence of the latter, the magnetic ordering of the molecules is found to be mediated mainly by N p-orbitals, leading to superexchange interaction. This indicates the N atoms of MOEP play a critical role for the formation of the spinterface, and thus, that the interfacial magnetic interaction can be controlled at the molecular level through the design of the metal–organic hybrid interfaces, since the orbital hybridization is determined by molecular structure and orbital symmetry. Once more, molecular design would allow for the enhancement of the exchange bias and to extend the use of such systems above room temperature.

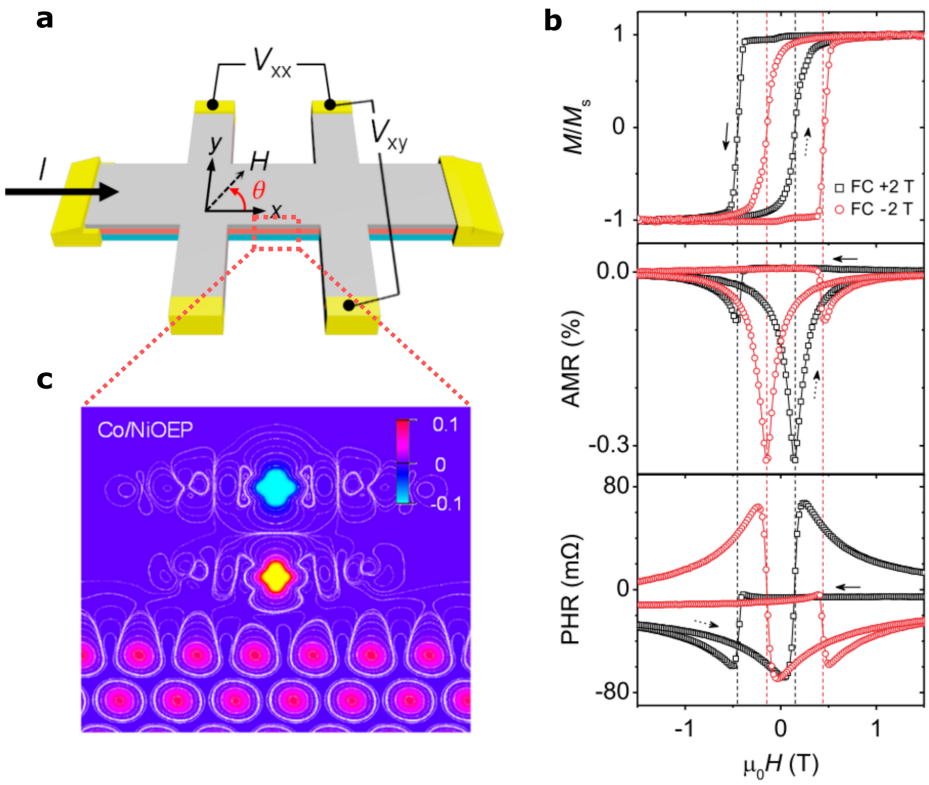

Figure 3.12| Magnetoresistance in a Co/NiOEP Hall Bar for the in-plane field sweep and simulation of the spin density contour plot at the interface. a, Schematic illustration of the Co/NiOEP Hall bar with magnetic field and electrical configuration. **b**, Comparison between magnetization, AMR and PHR measured at 10 K for a sample that went through field cooling (FC) with ±2 T. **c**, Cross-sectional contour plots of the spin density at the Co/NiOEP interface. Solid lines represent density contours. The red (bright blue) region indicates that the density of spin-up (spin-down) electrons dominates the density of spin-down (spin-up) electrons. The first molecules favor FM ordering with respect to the Co substrate and AFM alignment with the second molecular layer. Figure adapted from Ref. [155].

4 Tailoring superconductivity of $NbSe_2$ via self-assembled molecular adlayers

As explained in the previous section, 2D transition metal dichalcogenides (TMDCs) represent an ideal testbench for the search of materials by design, since their properties can be manipulated through surface engineering and molecular functionalization. However, the impact of molecules on the 2D superconductivity, observed in van der Waals (vdW) systems, remains largely unexplored. In this work, the critical temperature (T_C) of large-area $NbSe_2$ monolayers is manipulated employing ultra-thin molecular adlayers. Spectroscopic evidence indicate that aligned molecular dipoles within the self-assembled layers act as a fixed gate terminal, collectively generating a macroscopic electrostatic field on $NbSe_2$. This results in a $\sim 55\%$ increase and a $\sim 70\%$ decrease in T_C depending on the electric field polarity, which is controlled via molecular selection. The reported functionalization, which also improves the air stability of $NbSe_2$, is efficient, practical, up-scalable and suited to functionalize large-area TMDCs. Our results indicate the potential of hybrid vdW heterostructures as a novel platform for tunable superconductivity.

4.1 $NbSe_2$: a 2D superconductor

$NbSe_2$ is a hole conducting metal and superconductor [163] of the TMDC family which attracted a lot of interest in the last decade because it exhibits intriguing electronic correlated phases [69,164–168]. In particular, the hexagonal stacked phase 2H presents superconductivity and charge density wave ordering from bulk to monolayer form [69,165]. The superconductivity is conserved, but suppressed when reducing the number of layers, with a superconducting critical temperature T_C that varies from 7.2 K in bulk to ~ 1 K in the monolayer. Despite its limited air stability [164], this makes $NbSe_2$ a prototypical material to study the interplay between dimensionality, superconductivity and correlated electronic phases. Due to the low dimensionality, the 2D superconducting state has been demonstrated to be gate tunable [81,82,164], and can be modified by molecular functionalization [128,169,170].

4.2 Molecular decoration of $NbSe_2$

A schematic representation of our approach is shown in Figure 4.1. We employed single-layer $NbSe_2$ grown by molecular beam epitaxy over mm-sized areas. To characterize the effect of molecules on the superconducting transition, we measured the $NbSe_2$ T_C before and after functionalizing its surface with silane-containing molecules. The functionalization of the exposed surface of 2D materials with molecules containing silane groups holds a great potential, since their self-assembly generates ultrathin and ordered films firmly attached to the 2D surface [113,114,143,147,171].

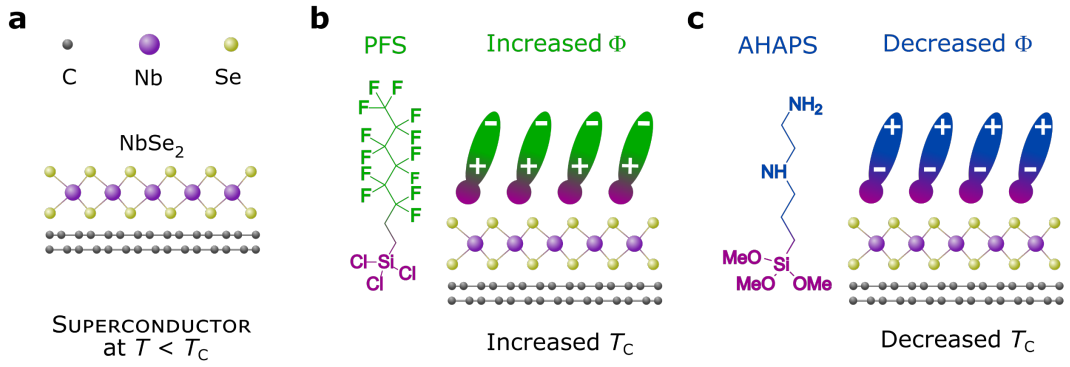

Figure 4.1| Schematic representation of our approach to manipulate the critical temperature T_C of $NbSe_2$. a, $NbSe_2$ monolayer grown on a large area by molecular beam epitaxy on bilayer graphene ($NbSe_2$/BLG/SiC). Molecular functionalization of the $NbSe_2$ monolayer with **b**, trichloro(1H,1H,2H,2H-perfluorooctyl)silane (PFS) and **c**, N-[3-(trimethoxysilyl)propyl]ethylenediamine (AHAPS). The direction of the PFS (AHAPS) molecule's permanent dipole moment leads to an increase (decrease) of the work function (Φ), which in turn causes an increase (decrease) of T_C, due to hole (electron) accumulation. Figure adapted from our publication (Ref. [172]).

4.2.1 Epitaxially grown monolayer $NbSe_2$

Single-layer $NbSe_2$ was grown on epitaxial bilayer graphene (BLG) on 6H-SiC(0001), denoted as SiC/BLG/$NbSe_2$, for the electrical measurements and on the chemically analogous surface of highly oriented pyrolytic graphite (HOPG), denoted as $NbSe_2$/HOPG, for the spectroscopic measurements (see Appendix A and B for details). The quality of the $NbSe_2$ films was characterized by atomic force microscopy (AFM) and X-ray photoemission spectroscopy (XPS). Figure 4.2a shows the typical morphology of a $NbSe_2$/BLG/SiC sample, as imaged by AFM. In this case, the $NbSe_2$ monolayer covers almost completely the terraces of epitaxial graphene on SiC. We note that, even if the

coverage is not complete, long-ranged charge carrier percolation is achieved in these $NbSe_2$ layers, as proved by the fact that we measure a superconducting state with zero resistance (see below).

The samples grown on HOPG (Figure 4.2b) present a similar morphology, i.e., a nearly full monolayer although decorated with scattered islands of bilayer. In both cases, the thickness of $NbSe_2$ layer is 0.6 ± 0.1 nm (see insets), in agreement with the reported thickness of TMDC monolayers [163].

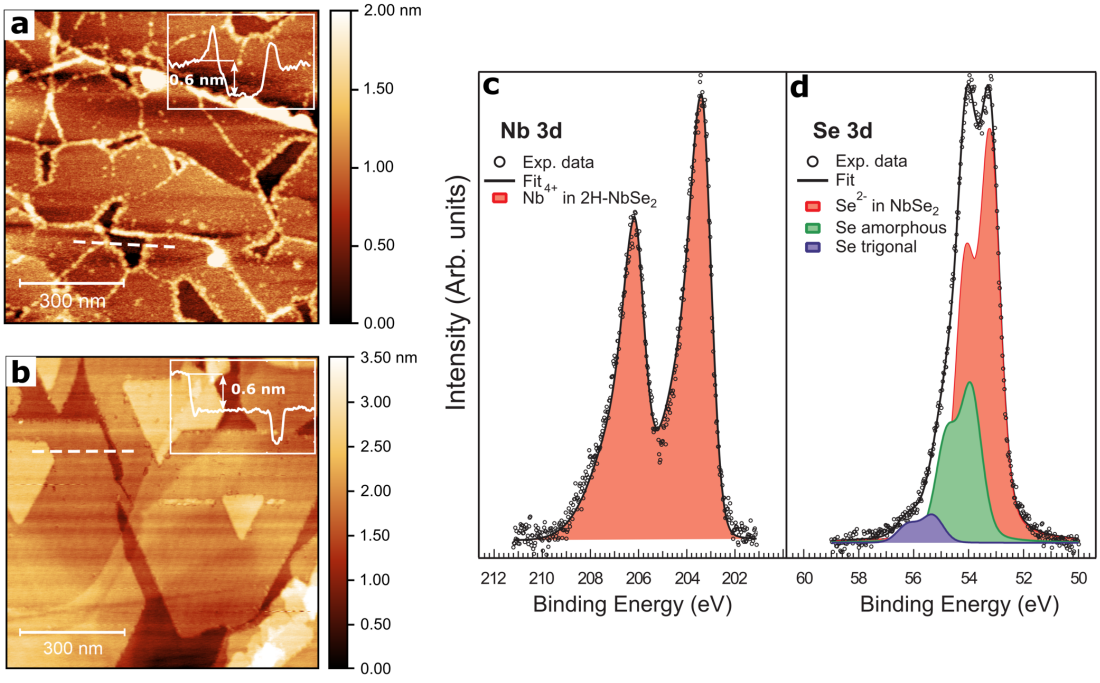

Figure 4.2| Morphological and spectroscopic characterization of $NbSe_2$ thin films grown by molecular beam epitaxy. a,**b**, AFM images of $NbSe_2$ grown on BLG/SiC and on HOPG, respectively. The insets show height profiles along the white dashed lines. **c**, Fitted Nb 3d and **d**, Se 3d core level XPS spectra of $NbSe_2$/BLG/SiC. The Se 3d core level spectrum in **d**, can be deconvolved into three components, with the main component corresponding to Se^{2-} in $NbSe_2$ ($Se\ 3d_{5/2}$ peak at 53.25 eV, red component). The two minor components can be ascribed to residual amorphous Se (green component at 53.95 eV) and trigonal Se (blue component at 55.35 eV). Figure adapted from our publication (Ref. [172]).

Chemical analysis of the $NbSe_2$/BLG/SiC substrate was conducted by XPS. The fitted Nb 3d and Se 3d core level are displayed in Figure 4.2c and d, respectively. The spectral features of the Nb 3d peak indicate that Nb has a 4+ oxidation state, as expected for the Nb coordinated with 6 Se atoms in the $NbSe_2$ 2H hexagonal phase. In particular, the Nb $3d_{5/2}$ and $3d_{3/2}$ peaks stemming from Nb^{4+} in the 2H phase of $NbSe_2$ (red components in Figure 4.2c) are located at BE = 203.40 and 206.15 eV, respectively. The Se 3d core level

spectrum in Figure 4.2d can be deconvolved into three components, with the main component stemming from Se^{2-} in $NbSe_2$ [173,174]. The fitting procedure resulted in an atomic ratio Se/Nb of 2.1, in good agreement with the expected ratio of 2.0, corroborating the high quality of the $NbSe_2$ monolayers. The other two minor components can be ascribed to residual amorphous Se and trigonal Se, which form as clusters on the surface that are imaged as bright protrusions in the AFM maps.

4.2.2 Self-assembly formation and characterization

We selected two linear molecules containing a silane group as anchoring group and a polar functional group, which are Trichloro(1H,1H,2H,2H-perfluorooctyl)silane (PFS) and N-[3-(trimethoxysilyl)propyl]ethylenediamine (AHAPS), see Figure 4.3a,b for the chemical structure. While PFS incorporates a fluorinated chain as polar functional group, AHAPS contains two amino groups. To functionalize the $NbSe_2$ monolayers with self-assembled molecular adlayers, we simply exposed the $NbSe_2$ surface to vapors of PFS and AHAPS (see Chapter 2 for more details). A similar method was employed to functionalize the chemically similar van der Waals surface of other micron-sized 2D Materials with PFS, AHAPS and other silane-based molecules [113,114,143,147,171].

In Figure 4.3, we present AFM images of $NbSe_2$/HOPG after functionalization with PFS (Figure 4.3a) and AHAPS (Figure 4.3b). The functionalized substrates display a markedly different morphology. $NbSe_2$ islands characterized by 0.6-nm-thick step edges can be discerned also after functionalization with AHAPS and PFS, but in both cases they are covered by thin and smooth molecular films characterized by a roughness of 0.3 ± 0.1 nm (Figure 4.3a,b). A similar morphology was also recorded in AFM images measured in different regions of the samples and separated by a few millimeters, indicating that the molecular adlayers extend homogenously over the entire substrate area. Vapor phase deposition is therefore ideal to functionalize large-area TMDs with homogeneous molecular adlayers.

The growth parameters of the molecular adlayers shown in Figure 4.3a,b were intentionally optimized to achieve a homogeneous but non-complete substrate coverage (adjusting the parameters of the vapor phase deposition). In this way, AFM profiles measured across the uncovered areas were used to obtain information on the molecular layer thickness. Instead, the spectroscopic and electrical characterization (see below) was performed on fully covered samples to maximize the effect of the molecular adlayers on $NbSe_2$.

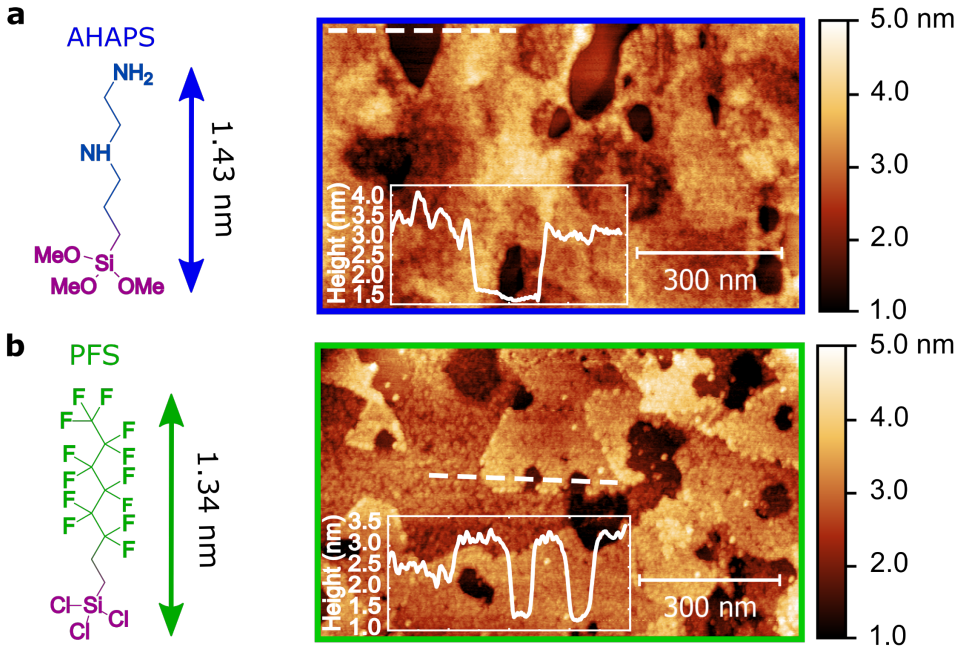

Figure 4.3| Morphological characterization of AHAPS and PFS self-assembled adlayers on $NbSe_2$ monolayers on HOPG. a,**b**, AFM images of $NbSe_2$ treated with **a**, AHAPS, and **b**, PFS, adlayers. The insets show the thickness of the molecular adlayers, as extracted from the AFM profiles correspondent to the dashed white lines, which can be compared with the length of the molecules. Figure adapted from our publication (Ref. [172]).

We estimate a thickness of 1.8 ± 0.5 nm for the AHAPS layer and of 1.5 ± 0.3 nm for the PFS layer (inset in Figure 4.3a,b); both values are in good agreement with the reported length of the two linear molecules [175]. This finding suggests that AHAPS and PFS self-assemble generating ultrathin adlayers in which individual molecules are preferentially aligned in a direction roughly perpendicular to the $NbSe_2$ surface, in agreement with the reported formation of ordered assembly of silane molecules on WSe_2 and graphene (see Chapter 3, [143,147]). Further evidence confirming the reported formation of the assembly come from the spectroscopic characterization, as discussed in Appendix C.

4.3 Dipole induced modulation of $NbSe_2$ work function

The molecular ordering in the self-assembled adlayer implies that the permanent dipoles of AHAPS and PFS are aligned and possess a component in the direction orthogonal to the surface, which introduces a field effect on $NbSe_2$ [114,143,147]. The effect of the molecular electric fields on $NbSe_2$ was charac-

terized by means of ultraviolet photoemission spectroscopy (UPS, see Appendix B) [176]. Initially, we characterized how the presence of monolayer $NbSe_2$ affects the work function (Φ) of the HOPG substrate. As can be seen in Figure 4.4, the secondary electron cut-off (SECO) position of the bare HOPG surface yields a typical Φ of 4.48 eV, whereas for HOPG/$NbSe_2$, Φ is slightly reduced to 4.32 eV.

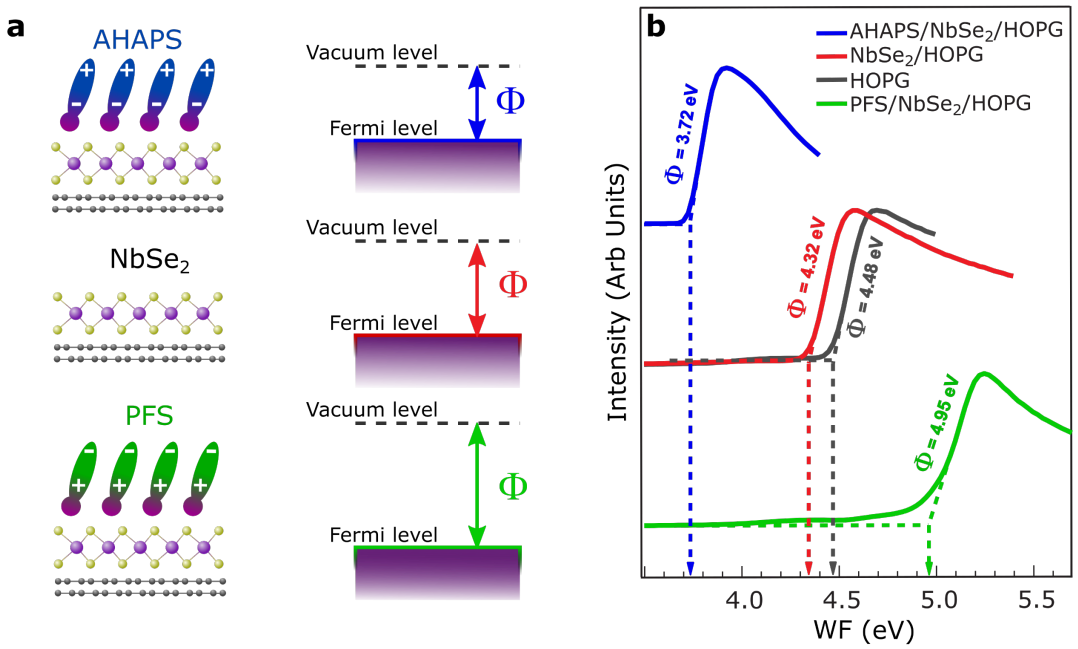

Figure 4.4| AHAPS and PFS, dipole-induced work function (Φ) shift on $NbSe_2$ monolayers. a, Sketch representing the doping effect induced by the self-assembled adlayers on $NbSe_2$. **b**, Work function of bare HOPG (black line), untreated $NbSe_2$ monolayers (red line), AHAPS-treated $NbSe_2$ (blue line) and PFS-treated $NbSe_2$ (green line), as extracted by the secondary electron cutoff (SECO) spectra. Figure adapted from our publication (Ref. [172]).

Afterwards, we investigated how the Φ of single-layer $NbSe_2$ is modified after functionalization with PFS and AHAPS. Remarkably, the functionalization with PFS increases Φ by +0.63 eV, whereas AHAPS decreases it by –0.60 eV. Such a change of Φ originates from the electric field generated by the superposition of the permanent molecular dipoles in AHAPS and PFS, which are aligned in the direction perpendicular to the surface due to the preferential out-of-plane molecular orientation framed by self-assembly. The negligible changes in the position of the Nb and Se core level after functionalization (Table 4.1 in Appendix C) excludes significant charge transfer from the molecular adlayer to $NbSe_2$.

The recorded Φ shifts provide further evidence of the presence of long-range structural order within the self-assembled adlayer. The fact that Φ increases or decreases after functionalization with PFS or AHAPS indicates that the polarity of the field effect is opposite in the two cases, implying that the molecular dipoles possess an opposite orientation in the two self-assembled adlayers. This finding further confirms the scenario in which the silanol groups in AHAPS and PFS lie close to the $NbSe_2$ surface [143,147].

A shift in the Φ of 2D materials corresponds to a change in their charge carrier density [177]. In our case, the increased Φ in PFS-functionalized $NbSe_2$ corresponds to an increase in the hole density, while the electric field effect generated by the AHAPS adlayer introduces electron accumulation in $NbSe_2$, or a decrease in the hole density. From the Φ shift values we can provide a rough estimation of the density of charge carriers Δn induced by molecular gating using a simple parallel-plate capacitor model in which the molecular adlayer acts as dielectric, using the following formula:

$$\Delta n = \varepsilon_0 \varepsilon_{eff} \frac{\Delta \Phi}{et} , \tag{4.1}$$

where ε_0 is the vacuum permittivity, ε_{eff} is the effective dielectric constant of the molecular adlayer, $\Delta\Phi$ is the work function shift, t is the thickness of the molecular adlayer and e the electron charge. Employing the values of $\Delta\Phi$ and t measured through UPS and AFM, and $\varepsilon_{eff} = 3 - 4$ as a typical value for the effective dielectric constant of a molecular adlayer [178,179], we can estimate that the PFS and AHAPS adlayers introduce a hole and electron accumulation in the range of $\Delta p \sim \Delta n \sim 5 \times 10^{12} - 1 \times 10^{13}$ cm^{-2}. Remarkably, such induced charge carrier density is close to the typical maximum value that can be achieved through electrostatic gating employing SiO_2 as a dielectric, indicating that the field effect generated by our ultrathin molecular film or gating across significantly thicker SiO_2 are comparable, thereby demonstrating the high efficiency of our molecular gating.

4.4 Tuning of $NbSe_2$ critical temperature

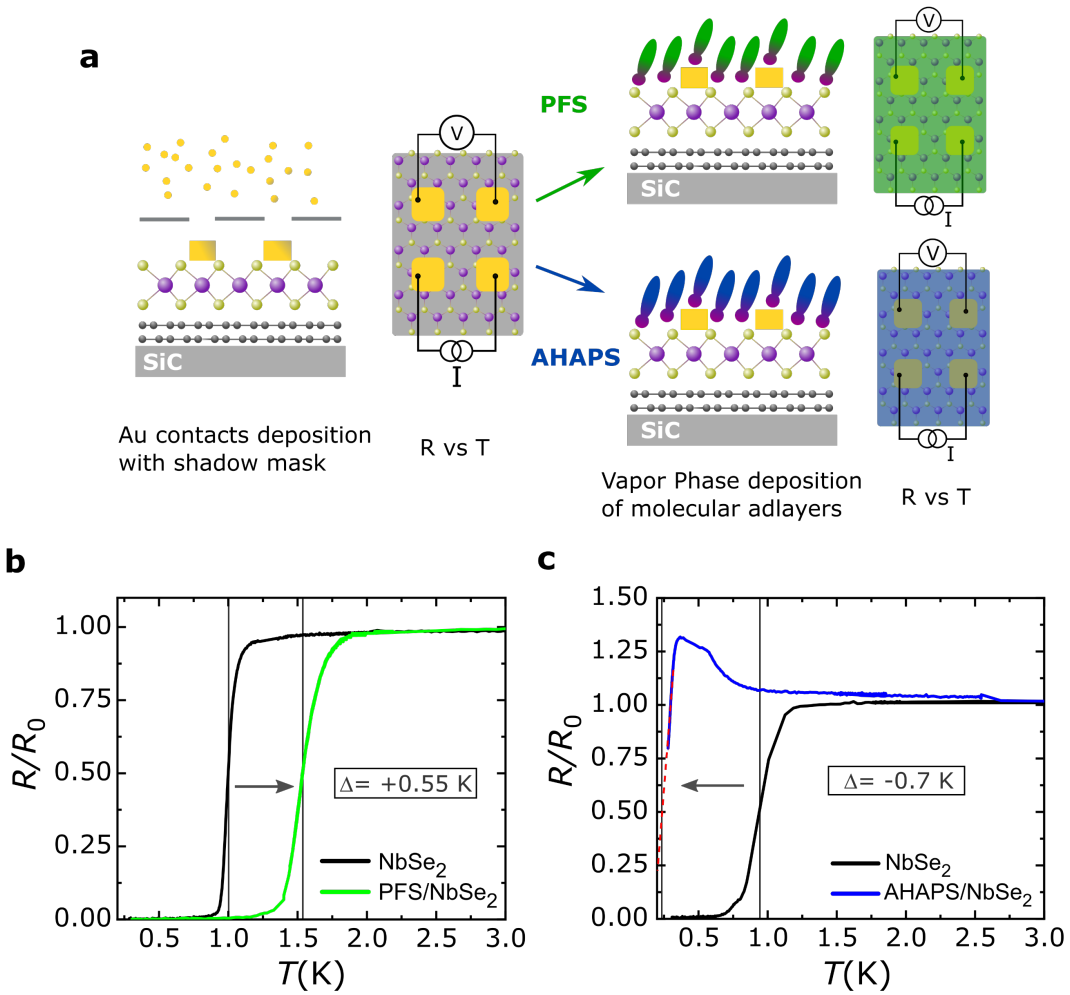

Figure 4.5| Modulation of $NbSe_2$ critical temperature. a, Scheme showing the experimental procedure employed to perform the electrical characterization. We first deposited four macroscopic gold electrodes by evaporation through shadow masks, and then we grew the molecular adlayer. The four-probe resistance was measured before and after the molecular functionalization. **b**,**c**, Normalized R vs T measurements of $NbSe_2$ samples before and after the deposition of **b**, PFS and **c**, AHAPS thin layers. In **b**, the T_C increase from 1.00 K to 1.55 K while in **c**, the T_C decreased from 0.90 K to a value lower than the limit of the measurement (0.29 K). Figure adapted from our publication (Ref. [172]).

Previous works on $NbSe_2$ field-effect devices showed that a change in the charge carrier density of $NbSe_2$ translates in a variation of the electron-phonon interaction, crucial for the formation of the Cooper pairs and the superconductive state [82]. As a result, the T_C is tunable by electrostatic gating. To explore the variation in T_C introduced by our molecular gates, we performed transport measurements on large-area $NbSe_2$ monolayers on epitaxial graphene

down to 0.29 K. Figure 4.5 show the temperature dependence of the resistance measured in two different samples before and after functionalization with PFS and AHAPS, respectively. The resistances are normalized to the value of the resistance state above the critical temperature (R_0), and we defined T_C as the value of temperature corresponding to $\frac{R_0}{2}$. Figure 4.5b,c show that the pristine $NbSe_2$ adlayers displayed the same T_C before functionalization ($T_{C0} = 1.0 \pm 0.1$ K). The broadened width of the superconducting transition is a manifestation of the two-dimensional character of the superconductor, which is described by a Berezinskii–Kosterlitz Thouless-type (BKT) transition [165].

After functionalization with the p-type PFS self-assembled adlayer, T_C increased to 1.55 K, corresponding to a $\Delta T_C = +\ 0.55$ K. In the case of functionalization with the n-type AHAPS adlayer, the T_C decreased to 0.2 K ($\Delta T_C = -0.7$ K). Note that in this case, the T_C suppression allows us to observe an upturn in the resistance, which is normally not observed due to the onset of superconductivity. While a detailed explanation on the physical origin of such phenomenon goes beyond the scope of this work, we highlight that molecular functionalization provides access to conductance regimes that cannot be otherwise reached. The reproducibility of these results was confirmed by measurements performed on other two samples (see Appendix D). These results are in agreement with previous studies on $NbSe_2$ field-effect devices, where p-type (n-type) doping was reported to increase (suppress) T_C [82], reinforcing the similarity between the molecular adlayer and a fixed gate terminal.

To verify whether the recorded T_C shifts were due to the electric fields generated by the molecular adlayers and to further exclude the role of the anchoring group, we exposed another sample to vapors of trichloro(octadecyl)silane (OTS), a molecule widely used to generate hydrophobic self-assembled monolayers. Since OTS does not feature a strong permanent dipole, it is not expected to induce strong electric fields on $NbSe_2$. Even though this specific sample showed signs of degradation (see the superconducting transition), the experiment revealed that the change in the T_C of $NbSe_2$ before and after OTS functionalization is significantly lower than what measured for PFS and AHAPS ($\Delta T_C \sim 0.1$ K, see Figure 4.6). This change is less significant with respect to the one induced by PFS and AHAPS, but not negligible.

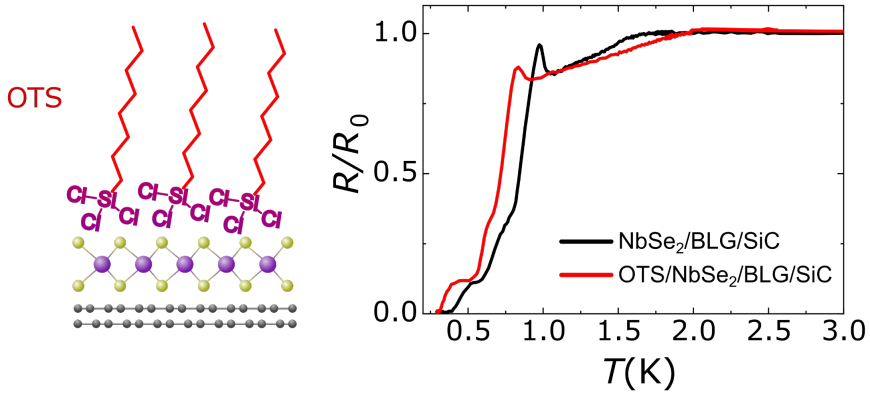

Figure 4.6| Effect of Trichloro(octadecyl)silane (OTS) molecular adlayer on $NbSe_2$ T_C. Schematic illustration of the OTS self-assembled adlayer on $NbSe_2$, and four probe R vs T measurement of the sample before and after the functionalization. Minimum variation can be observed before and after the OTS growth. Figure adapted from our publication (Ref. [172]).

The causes could be related to i) the molecular layer introducing some disorder which alters T_C due to the multifractal nature of the electron wavefunctions in $NbSe_2$ [166], ii) permanent dipoles present at the $NbSe_2$/adlayer interface, arising from the Si-O-Si produced by the condensation of the silanol groups, which might introduce minor field effects in $NbSe_2$. Nevertheless, these data indicate that ΔT_C scales with the sign and strength of the molecular permanent dipoles, not only supporting the molecule-induced electrostatic effect as the main cause of variation in T_C, but also providing a rational route to molecular design. In particular, by employing silane as anchoring groups and polar functional groups as source of electric fields, it is possible to modulate the T_C of $NbSe_2$ in a deterministic way, thanks to the ordered nanoscale arrangement of silane-based molecules on TMDs.

4.5 Air stability improvements

As a final experiment, we tested the air stability of an uncapped and a PFS-treated $NbSe_2$ by measuring the temperature dependence of their four-point resistance before and after exposing them to air for 60 hours. For the uncapped sample, we measured a 50% resistance increase, indicative of a significant degradation of $NbSe_2$ in air. On the contrary, the resistance of the PFS-treated $NbSe_2$ increased only for a factor 3%, demonstrating that the molecular adlayer acts as a capping layer and improves the air stability of $NbSe_2$ (Figure 4.7). Additionally, the effect of PFS on T_C is only minimally modified by storing the sample in air for 60 hours (Figure 4.7b). These results fully exploit the

potential of silane- functionalization of TMD, demonstrating that they are ideal molecules not only to improve the performances of electronic devices, but also to engineer the intrinsic properties of atomically thin TMDs extending over large areas.

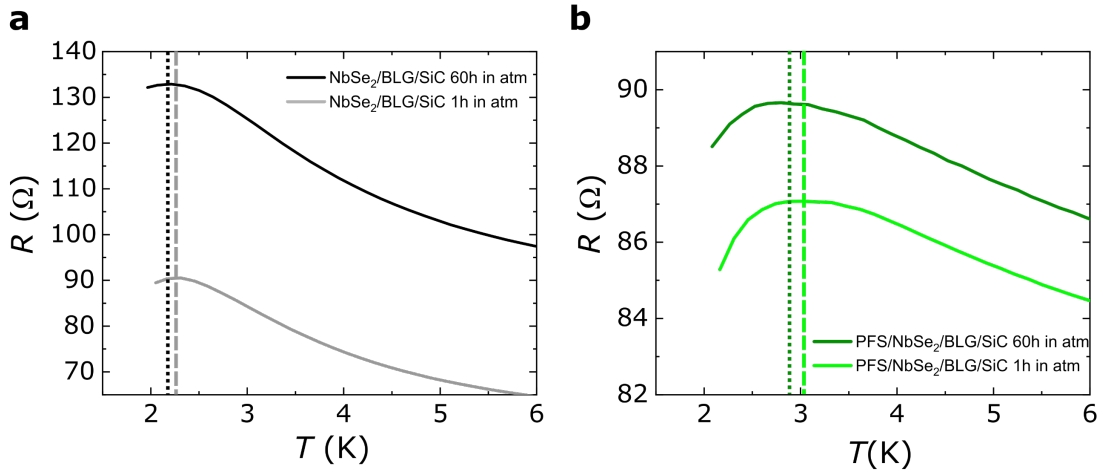

Figure 4.7| Silane-based capping as passivation layer. a,**b**, Comparison between the degradation over time of the conduction properties of two $NbSe_2$ samples grown in the same conditions, but keeping one sample uncapped (**a**) and the other functionalized with PFS (**b**). The prolongated exposition to atmosphere significantly increases the resistance of the uncapped sample implying oxidation of the $NbSe_2$, while it does barely affect the functionalized sample. Figure adapted from our publication (Ref. [172]).

4.6 Results discussion

To evaluate the efficiency of the molecular adlayer in the manipulation of the T_C of $NbSe_2$, we compare the shift measured in this work with that previously obtained in field effect devices [82]. Employing strontium titanate/hBN as a gate dielectric [164], a ΔT_C of approximately 50 mK was reported in bilayer $NbSe_2$, which amounts to approximately one tenth of the ΔT_C measured in our work. Additionally, employing the p-type PFS adlayer we recorded an increase in T_C, $\Delta T_C = 0.55$ K, which is close to the $\Delta T_C = +0.7$ K measured using ionic liquid gating, which accumulates approximately a ten-times-larger charge carrier density (see Table 4.2 in Appendix E) [82].

The large T_C modulation reported in this study can be partly explained by the fact that, unlike previous studies focusing on $NbSe_2$ multi-layers ($\geq$ 2 layers), we employ monolayers which minimize screening effects and are thus more sensitive to any changes in their environment. In addition, our results

indicate that while the molecular adlayers introduce an electrostatic effect on $NbSe_2$, they do not merely act as a gate dielectric, as they introduce other physico-chemical modification at the $NbSe_2$ surface which enhance the field effect. For instance, the modified chemical environment of defect states which accompanies the silane functionalization affects the T_C shift, and likely contributes to improve the efficiency of molecular functionalization. Our results show that the electrostatic effect plays a primal role in the determination of the recorded shifts, but we anticipate that mastering the other simultaneous phenomena will permit a higher control on the intrinsic physical properties of TMDs.

4.7 Conclusions

In conclusion, we were able to tune the superconductive transition in monolayer $NbSe_2$ employing ultrathin self-assembled molecular adlayers. In particular, the $T_C \sim 1$ K characteristic of pristine $NbSe_2$ monolayers could be lowered to 0.2 K and increased to 1.55 K by functionalization with self-assembled adlayers composed of two silane-based molecules with different dipolar substitutions. The T_C variation is explained as a consequence of opposite electrostatic field effects generated by the aligned molecular dipoles in the ultrathin molecular adlayers, which act as a fixed gate terminal. Remarkably, the overall relative variation in T_C, which is above 120%, is larger than what was achieved in field-effect devices based on multilayer $NbSe_2$, highlighting the high efficiency of molecular functionalization and the importance of using high quality TMD monolayers for the engineering of their intrinsic properties. Our chemical functionalization, which does not require any expensive vacuum evaporator nor any high temperature process, is practical, scalable and perfectly suited to tune the physical properties of technologically relevant TMD monolayers extending over large areas. We also highlight that molecular functionalization is fully compatible with further gating in field-effect transistors. In this regard, our molecular functionalization provides a new controllable starting environment for $NbSe_2$, which can be programmed by molecular design and eventually further finely manipulated with a gate terminal. Therefore, by combining electrostatic gating and our molecular functionalization, one could in principle engineer precisely the material properties, and investigate doping regions that cannot be explored using conventional solid-state dielectrics.

4.8 Appendices

A. Growth of $NbSe_2$ monolayers

Monolayers of $NbSe_2$ were grown on epitaxial bilayer-graphene on 6H-SiC(0001) by molecular beam epitaxy (MBE) at a base pressure of $\sim 5 \times 10^{-10}$ mbar. SiC wafers with resistivities $\rho \sim 120\,\Omega\,\mathrm{cm}$ were cleaned using an isopropyl solution in the ultrasonic bath, before they were outgassed in the vacuum chamber at a temperature of 650°C for 1 h, until a pressure of at least $\sim 5 \times 10^{-9}$ mbar could be stabilized at that temperature. Then, in an automatized cycling mechanism the temperature on the surface was ramped from 600°C to 1350°C at a defined time of 30 s. The high temperature setpoint was kept for another 30 s, before it was ramped down again to 600°C where it was kept for 10-15 s to recover the pressure in the chamber, which can raise up to $\sim 1 \times 10^{-7}$ mbar during the first cycles. In total 80 cycles are conducted, which took about 3 h and lead to uniform bilayer-graphene on the surface.

For the growth of $NbSe_2$, high purity Nb (99.99%) and Se (99.999%) are evaporated using an electron beam evaporator and a standard Knudsen cell, respectively. The growth rate is 1:25 at a pressure inside of the chamber of $\sim 2 \times 10^{-8}$ mbar (Se atmosphere). The substrate is kept at 570°C during the evaporation time of 48 min. The evaluation of the layer formation is monitored in situ using reflective high energy electron diffraction (RHEED). After 48 min of growth time the Nb evaporation is shut down, but the Se evaporation is kept for 5 consecutive minutes in order to fill atomic vacancies and achieve smooth layers. After such post-annealing, the heating power is ramped down within a minute, and the sample temperature decreases in a slower way, reaching ambient conditions in approximately 10-15 minutes.

The same parameters were used for the growth of $NbSe_2$ on HOPG, which was exfoliated in air and immediately inserted into the UHV chamber, where it was subsequently outgassed at 580°C prior to growth.

B. Photoelectron spectroscopy

The photoemission spectroscopic experiments were carried out by M. V. Nardi, M. Timpel and R. Verrucchi. Here are presented more details on the procedures.

X-ray photoelectron spectroscopy (XPS)

The bare and functionalized samples (i.e., HOPG, HOPG/$NbSe_2$, HOPG/$NbSe_2$/PFS, HOPG/$NbSe_2$/AHAPS) were characterized by X-ray photoelectron spectroscopy (XPS) using a non-monochromatized Mg Kα X-ray source (i.e., emission at 1253.6 eV). The photoelectrons were collected with a VSW HSA100 hemispherical analyzer equipped with PSP electronic power supply and control. The total energy resolution is ~ 0.8 eV. All core level binding energies (BEs) were referred to the Au $4f_{7/2}$ core level signal (BE = 84.0 eV) obtained from a clean Au surface. The Nb 3d and Se 3d core levels of the substrate were analyzed through a combination of Doniach Sunjic and Voigt function line shape deconvolution, accounting for the semi-metallic character of $NbSe_2$, after background subtraction of a Shirley function. The typical precision for the energy position of each peak is $\pm$ 0.05 eV.

Ultraviolet photoelectron spectroscopy (UPS)

The work function Φ of the samples was derived from ultraviolet photoelectron spectroscopy (UPS) by collecting the secondary electron cutoff (SECO) spectrum. The impinging photons were generated from a He lamp (i.e., He' photon energy of 21.21 eV). The SECO spectra were measured with a sample bias of -7.0 V. The x-axis of the SECO spectra is expressed in work function (WF) by subtracting the applied sample bias from the measured kinetic energy (KE) of the photo-emitted electrons. The total energy resolution is ~ 0.05 eV.

C. Mechanism of growth of silane-based molecular films

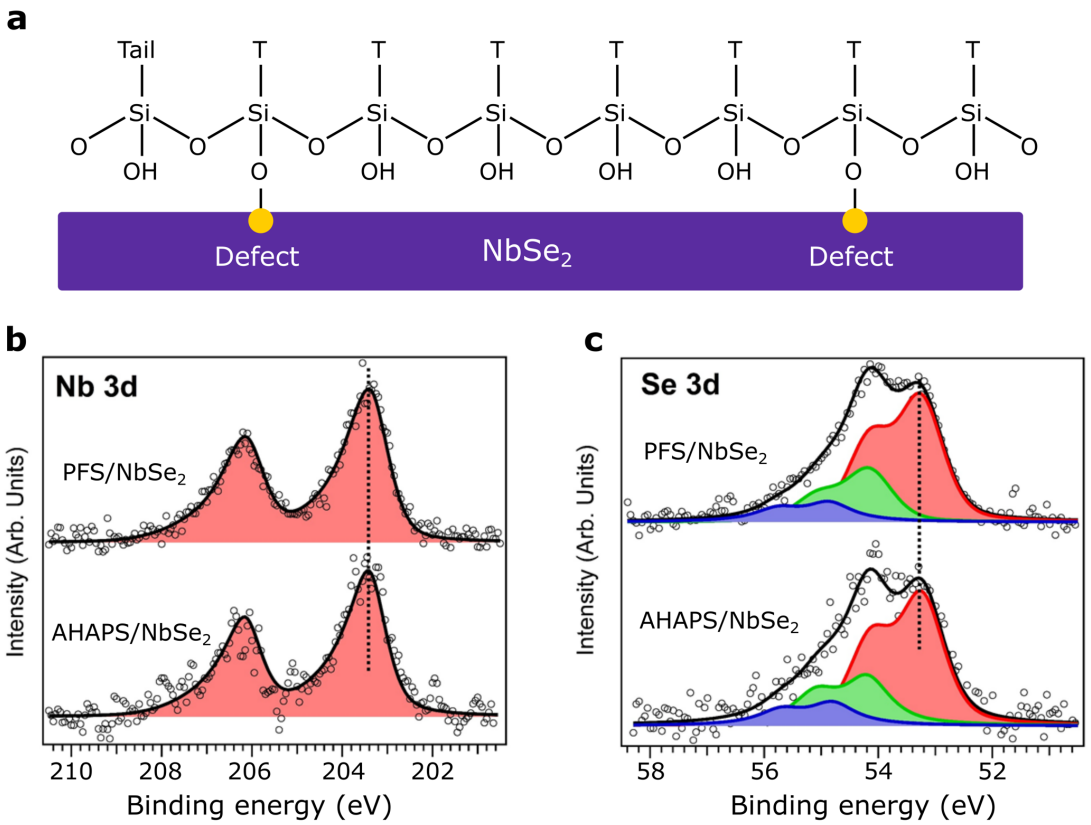

Figure 4.8| Self-assembly of silane molecules on TMDCs. a, Mechanism of formation of self-assembled adlayers of molecules containing silane groups on TMDCs. **b**,**c**, Spectroscopic characterization of $NbSe_2$ grown on HOPG and functionalized with **b,** AHAPS, and **c**, PFS. Figure adapted from our publication (Ref. [172]).

As explained in Chapter 3, the structural motifs generated by molecular self-assembly on surfaces are determined by molecule-molecule and molecule-substrate interactions. In the specific case of silane-based molecules and TMDCs, as shown in Figure 4.8a, the hydrolysis of the silane groups (trichlorosilane and trimethoxysilane in PFS and AHAPS) generates silanol groups, which bind covalently to defects in TMDs. Additionally, covalent bonds between silanol groups belonging to different molecules lead to the formation of an ordered adlayer on the surface, in which the silanol groups lie close to the TMD surface, and the functional groups are aligned in a direction perpendicular to the surface. In our case, T is the fluorinated chain in the case of PFS, the alkyl chain in the case of OTS and it contains two amino groups in AHAPS. There is an important difference in the case of self-assembly on SiO_2 and van der Waals surfaces: in the first case, ideally every silane group is covalently attached to the substrate; in the second case, covalent bonds are

sparse, and take place between silane groups and defects on the van der Waals surface such as oxygen substitutional atoms. In this regard, the spectroscopic measurements confirms the proposed mechanism (Figure 4.8b,c). The Nb 3d and Se 3d core level positions are not affected by the different functionalizing molecule, ruling out a massive covalent interaction between silanol groups and Nb/Se, in agreement with previous reports [143].

Table 4.1| Binding energy position of Nd 3d and Se 3d components of bare $NbSe_2$, AHAPS/$NbSe_2$ and PFS/$NbSe_2$.

	$NbSe_2$	$NbSe_2$ + AHAPS	$NbSe_2$ + PFS
$Nb3d_{5/2}$ BE (eV)	203.35	203.40	203.38
$Se3d_{5/2}$ (1) BE (eV)	53.30	53.27	53.31
$Se3d_{5/2}$ (2) BE (eV)	54.29	54.21	54.23
$Se3d_{5/2}$ (3) BE (eV)	54.89	54.84	54.89

Moreover, the Nb 3d and Se 3d core level binding energies of the bare $NbSe_2$ on HOPG and the one functionalized with AHAPS and PFS are basically the same within the intrinsic measurement uncertainty. This finding strongly supports the scenario reported in the previous sections, in which the electrostatic effect of the aligned molecular dipoles introduces the extra charge carriers, while there is no direct charge transfer from the molecules. Generally, efficient charge transfer from a molecular specie to a given material requires a proper energy level alignment, wherein the molecular HOMO or LUMO are respectively above or below the Fermi energy of the target material. For this reason, efficient electron (hole) dopants are typically designed to possess a high HOMO level (low LUMO). The molecules employed in this study possess a wide bandgap, wherein neither the HOMO nor the LUMO are well matched to the $NbSe_2$ Fermi energy.

D. Additional electrical characterization

The temperature dependences of the sample resistances are characterized by different transport regimes. Since we employed heavily doped SiC substrates, the high-temperature electrical conduction is dominated by the SiC substrate at T above 100 K. Since SiC is a semiconductor, its thermally activated conductance drops abruptly at low temperatures, so its contribution can be neglected in the temperature region below approximately 100 K, which is the interesting region for our measurements. Below approximately 100 K we observed that, while the resistance of the BLG/SiC substrates kept increasing when decreasing in temperature, below 50 K the R vs T of the sample with $NbSe_2$ flatten and starts to decrease, indicating the dominant metallic contribution of $NbSe_2$ to the overall conductivity. At the superconducting transition, most of the current flows through the $NbSe_2$. This behavior was already observed in previous works [180].

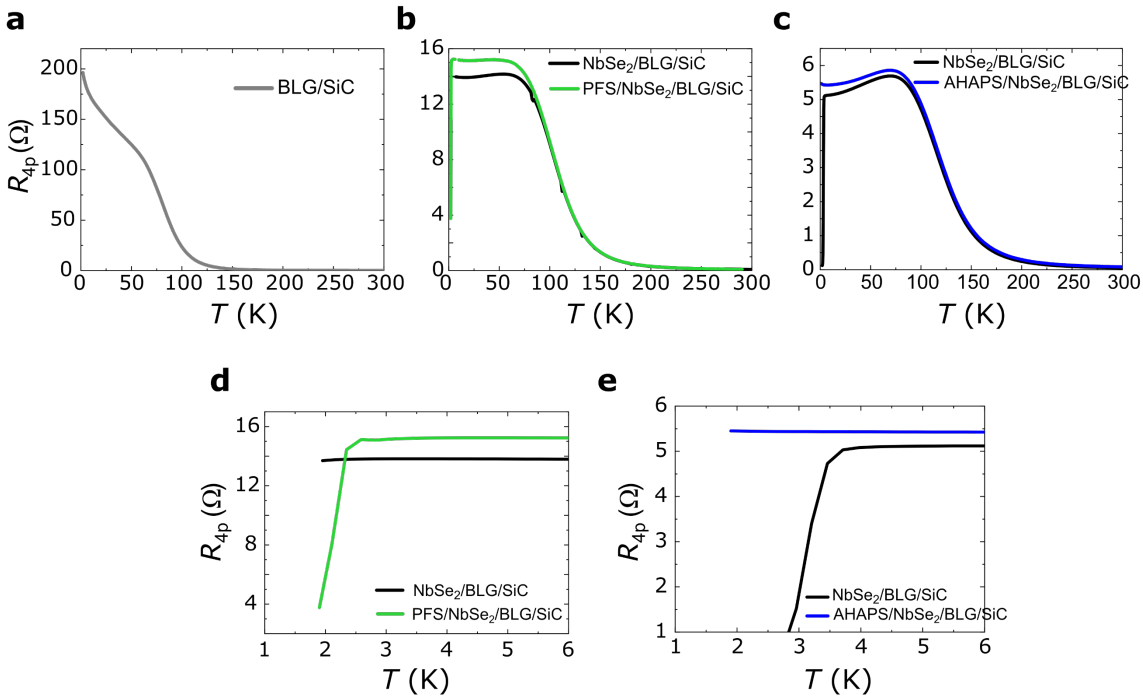

Figure 4.9| Comparison of typical full range temperature dependences of four probes resistance between **a**, BLG/SiC substrate; **b,** a $NbSe_2$/BLG/SiC sample before and after PFS deposition; **c**, a $NbSe_2$/BLG/SiC sample before and after AHAPS deposition. **d**, and **e** are zoom in of the low temperature region of panels **b**, and **c**, respectively. Figure adapted from our publication (Ref. [172]).

The results shown in Figure 4.9d,e, confirm the data displayed in Figure 4.5. In particular, while the superconducting transition in pristine monolayer $NbSe_2$ could not be observed since it was below the minimum temperature

achievable in the employed cryostat (1.9 K), after the functionalization with PFS we were able to observe the onset of the superconductive transition around 2 K, as shown in panel b,d.

To prove the opposite behavior, we fabricated thicker $NbSe_2$ films (nominally 2 layer) to achieve higher T_C in the pristine sample ($T_C = 3.1$ K, panels c,e). After the treatment with AHAPS (n-dopant), the transition to the superconducting state could not be recorded to the lowest temperature available in the system.

Importantly, we should highlight that the bilayer sample used in this study is very different from a bilayer exfoliated flake. The MBE growth does not allow us to obtain perfect bilayer samples covering homogeneously the entire substrate area. While almost ideal monolayers were grown, the growth of thicker layers resulted in a first monolayer covering homogeneously the substrate onto which a second layer locally nucleated; the nucleation of layer would start before the completion of the second layer. Therefore, the sample measured in c,e is a mixture of single, bi- and tri- layers, and the shift recorded in this case is the result of the interplay between the effect of molecules on (mostly) single- and bi-layer.

E. Comparison with previous works

In Table 4.2, we compare the results obtained in this work with the previous literature on the T_C modulation by electrostatic gating. In particular, we focus on the initial critical temperature of the $NbSe_2$ layers T_{C0}, the modification achieved through electrostatic gating ΔT_C, the charge carrier density of the pristine samples n_0, and the change in charge carrier density Δn which causes the T_C shift. According to the weak-coupling Bardeen-Cooper-Schrieffer theory, these quantities are related, as the relative change $\Delta T_C / T_{C0}$ is proportional to $\Delta n / n_0$. Table 4.2 shows how, in our case, a relatively small Δn generates a large ΔT_C. We highlight three aspects which contribute to explain the large ΔT_C.

First, in our $NbSe_2$, n_0 is smaller than the nominal hole density, as demonstrated by spectroscopic evidence. The work function value determined for the $NbSe_2$ monolayer on HOPG is 0.31 eV lower than the one recorded for a $NbSe_2$ bulk crystal, which indicates n type doping, or hole depleted $NbSe_2$. While a precise estimation of n_0 on the basis of these data is not trivial, we can confidently conclude that n_0 in our case is not higher than the nominal value, hence increasing $\Delta n / n_0$ as compared to other works. Second, the weak-coupling Bardeen-Cooper-Schrieffer theory fails to describe the rich physics of ultrathin

$NbSe_2$ layers, and the discrepancy is highest for single layers [81,82]. And third, molecular adlayers do not merely act as a gate dielectric, as they introduce other physico-chemical modifications at the $NbSe_2$ surface. For instance, the modified chemical environment of defect states, which accompanies the silane functionalization, affects ΔT_C and likely contributes to improve the efficiency of molecular functionalization.

Table 4.2| Comparison between the modulation in the $NbSe_2$ critical temperature T_C obtained by electrostatic gating in field effect devices (Ref[29,34,35]) and through molecular functionalization (this work). $\Delta T_{C,up}$ and $\Delta T_{C,d}$ are respectively the maximum increase and decrease in T_C reported in each work. n_0 is the charge carrier density for the pristine $NbSe_2$ flake in each case; between parenthesis we detail the method used for its estimation. The nominal value is typically extracted by dividing the bulk charge carrier density by the thickness of single layers; this returns approximately 9.5×10^{14} holes/cm^2 in each layer. Δn_{up} (Δn_d) is the increase (decrease) in hole density induced by electrostatic gating and molecular functionalization; between parenthesis we detail the method used for the estimation of Δn, where ppc is a parallel plate capacitor model, and Hall is the measurement of the Hall effect.

	T_C (K)	$\Delta T_{C,up}$ (K)	$\Delta T_{C,d}$ (K)	n_0 (cm^{-2}) [method]	Δn_{up} (cm^{-2}) [method]	Δn_d (cm^{-2}) [method]
SiO_2 dielectric	2-2.5	0.1	0.1	1.8×10^{15} [nominal]	4.2×10^{12} [ppc]	4.2×10^{12} [ppc]
STO/hBN dielectric	5.25	0.05	0.05	4×10^{15} [nominal, Hall]	1.3×10^{13} [ppc, Hall]	1.3×10^{13} [ppc, Hall]
Ionic liquid gate	4.5	0.5	1.0	1.9×10^{15} [nominal, Hall]	1×10^{14} [ppc, Hall]	2×10^{14} [ppc, Hall]
Molecular adlayers [Our work]	1.0	0.55	0.7	$\leq 0.95 \times 10^{15}$ [nominal, UPS]	1×10^{13} [ppc]	1×10^{13} [ppc]

5 Exchange Bias in Fe_3GeTe_2/CoPc heterostructures

In the previous chapter we demonstrated that, with the right choices of molecules and van der Waals materials, one can tailor the physical properties of the latter in a controlled manner. In this regard, another intriguing class of vdW materials, which represent an ideal playground to explore physical properties in reduced dimensions, is the one of 2D magnets [181,182]. The exfoliation of layered magnetic materials yields ultrathin single crystalline flakes characterized by extremely high surface sensitivity which makes their properties tunable via external stimuli [83]. The coupling between molecules and ferromagnetic materials, leads to hybridized interfaces with peculiar magnetic properties [158], called spinterfaces (see section 3.4.2). However, the effect of spinterfaces on 2D magnets remains rather unexplored.

Here, we demonstrate the emergence of spinterface effects at the interface between the prototypical layered magnetic metal Fe_3GeTe_2 and a thin film of paramagnetic Co-phthalocyanine (CoPc). Magnetotransport measurements show that the molecular layer induces a magnetic exchange bias in Fe_3GeTe_2, indicating that the unpaired spins in CoPc develop antiferromagnetic ordering by proximity and pin the magnetization reversal of Fe_3GeTe_2. The effect is strongest for a Fe_3GeTe_2 thickness of 20 nm, at which the exchange bias field reaches – 840 Oe, and it is measurable up to a temperature of approximately 110 K. This value compares very favorably with previous exchange bias fields reported for Fe_3GeTe_2 in all-inorganic van der Waals heterostructures, indicating that molecule/2D magnet heterostructures represent an advanced materials platform for spinterface research towards multifunctional low-dimensional devices.

5.1 Fe_3GeTe_2: a vdW ferromagnetic metal

Fe_3GeTe_2 (FGT) is a very promising vdW itinerant ferromagnet, which exhibit a strong perpendicular magnetic anisotropy, and, in its bulk state, a Curie temperature $T_C \sim 220$ K [183]. The magnetic properties of FGT are preserved when it is reduced to the few layers limit (150 K $< T_C <$ 190 K), and they strongly depend on the material thickness [36,184].

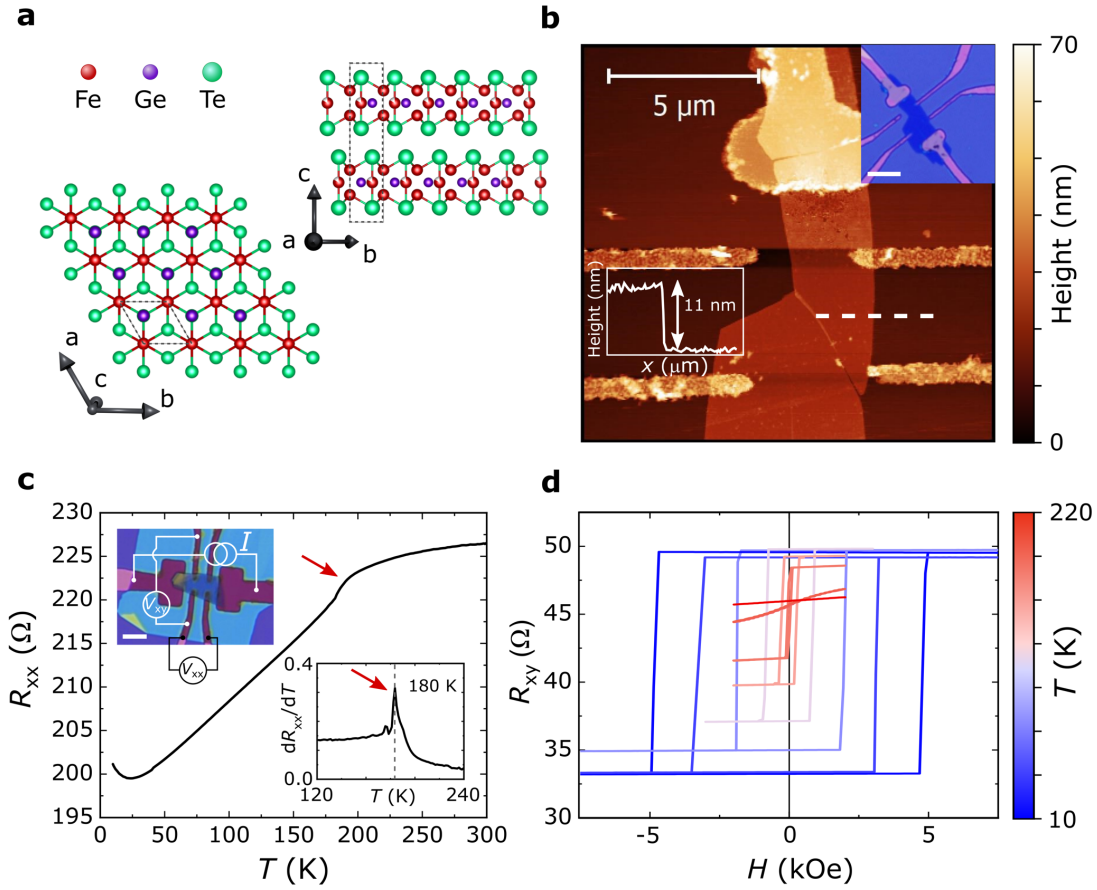

Figure 5.1| Structure and transport characterization of thin FGT flakes. **a**, Sketch illustrating the crystal structure of bilayer FGT. The dashed boxes denote the lattice unit cell. **b**, AFM map and optical image (upper right inset) of a typical thin FGT flake delaminated on 300 nm SiO_2 with prepatterned Ti/Au contacts. The lower-left inset shows the thickness of the flake. **c**, Temperature dependence of the longitudinal resistance (R_{xx}) of a FGT device (∼15 nm thick). The upper-left inset display an optical image of a Hall bar device capped with hBN, with a schematic of the contacts used to characterize the transport properties. The bottom-right inset shows the first derivative of R_{xx} as a function of temperature. The red arrows indicate the paramagnetic-ferromagnetic transition. **d**, Magnetic field (out-of-plane) sweeps of the Hall resistance (R_{xy}) measured on the same device of **c**, at $I = 5$ μA and for different temperatures. The anomalous Hall effect serves as a probe of the magnetic hysteresis loops.

Despite the relatively low T_C, not ideal for technological applications, FGT attracted a lot of interest in the scientific community, because it represents a valuable case to study magnetism in low dimensions and at the two sides of the magnetic phase transition. Moreover, its layered hexagonal crystal structure (see Figure 5.1a) makes it an ideal candidate for the exploration of vdW heterostructures.

To electrically characterize FGT, few nanometers thick flakes are exfoliated from a bulk source, to be then transferred on top of Ti/Au, Hall bar shaped, prepatterned contacts (see Figure 5.1b and Chapter 2 for more details). In Figure 5.1c, we first examine the temperature dependence of the longitudinal resistance (R_{xx} vs T) of a representative FGT Hall bar device capped with hBN to protect the material from oxidation (optical micrograph in upper-left inset, (t_{FGT} ∼15 nm)). Lowering T, at ∼ 180 K, it can be observed a kink in the R_{xx} trend that marks the transition from paramagnetism to ferromagnetism. To better appreciate such feature, dR_{xx}/dT is also plotted against the T in the bottom right inset.

Interestingly, the strong magnetic anisotropy, which fixes the magnetization perpendicularly with respect to the flake surface, can be exploited to characterize the magnetic properties of FGT via magnetotransport experiments, thanks to the anomalous Hall effect (AHE) [185]. In a FM, the transversal Hall voltage generated by a current flow and an out-of-plane magnetic field (H_z), presents the following relation with H_z:

$$R_{xy} = R_0 H_z + R_s M_z, \tag{5.1}$$

where R_{xy} is the Hall resistance resulting from the transversal voltage, which is composed of an ordinary Hall resistance (the first term in Eq. (5.1)) and an anomalous Hall resistance (the second term in Eq. (5.1)). H_z and M_z are the applied magnetic field and the sample magnetic moment perpendicular to the sample surface, and R_s is the saturation resistance. The anomalous Hall resistance is proportional to M_z. Thus, as FGT is a metallic ferromagnetic material, the normal Hall resistance is negligible compared with the anomalous Hall resistance in the magnetic field range of interest, and the shape of the R_{xy} vs H loop is equivalent to the one of the M_z vs H loop.

The Hall resistance, R_{xy} (Figure 5.1d) shows rectangular hysteresis loops with near vertical jumps when H is swept perpendicularly to the sample plane, with the coercive field reaching 5 kOe at 10 K. This indicates the domination of the AHE with a single magnetic domain over the entire flake. Together with the large remanent R_{xy} at zero field, these are hallmarks of the aforementioned strong out-of-plane magnetic anisotropy. The remanent R_{xy} and coercive field vanish at around 180 K, consistently with the kink in Figure 5.1c.

5.2 $CoPc/Fe_3GeTe_2$ heterostructures

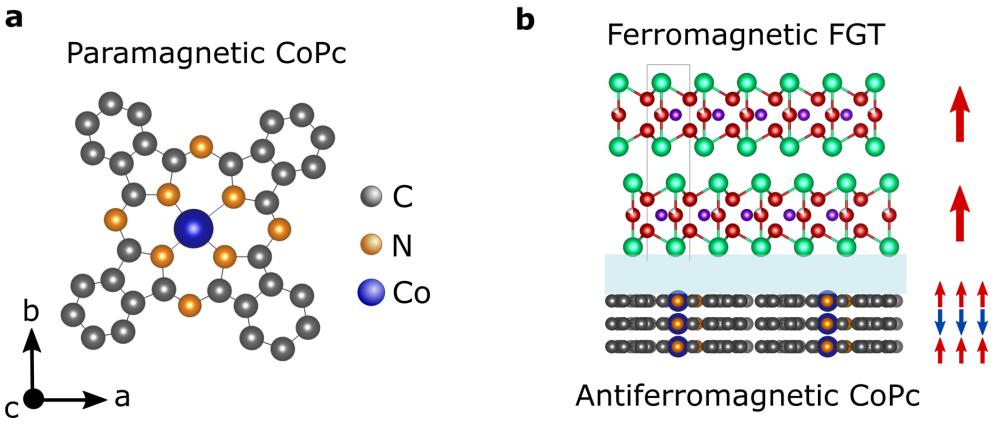

Figure 5.2| Schematics of the CoPc/FGT hybrid vdW heterostructure. a, Chemical structure of the planar, paramagnetic molecule CoPc (top view). **b**, Illustration of the hybrid CoPc/FGT heterostructure side view. The emerging spinterface mechanism is also sketched: the ferromagnetic FGT flake (red arrows in the picture) interfaced with the CoPc layers activate the antiferromagnetic molecular ordering (red/blue arrows), which in turn pins the FGT magnetization introducing exchange bias.

Metallo-phthalocyanine (MPc) are a versatile class of planar semiconducting molecules widely utilized in research and industry (Figure 5.2a). The metal ion (M2+) at the center of the molecule, usually a transition metal such as Co, Cu, or Zn, provides diverse energy levels, charge mobility, and spin states [186–188]. For the formation of the vdW heterostructures, we used CoPc, a paramagnetic molecule with a spin of $S = \frac{1}{2}$. Importantly, it was reported that the CoPc spins are prone to develop antiferromagnetic ordering at relatively high temperature ($J/k_B \sim 107$ K), higher than other MPc molecular layers [189,190]. MPc molecules deposited on conventional ferromagnetic metals [191], can induce the hybridization of the interface giving rise to the so-called spinterfaces (see section 3.4.2 of Chapter 3). Similarly, we expect the emergence of a spinterface at the CoPc/FGT interface in which the FGT layer activates an antiferromagnetic ordering in CoPc molecule layers (Figure 5.2b).

To explore this scenario, we first deposited CoPc molecules on a Si/SiO_2 substrate with the prepatterned Hall bar electrodes (see Chapter 2 for details, and Appendix A for the layers topography), and successively delaminated exfoliated FGT flakes onto the substrates. The obtained CoPc/FGT structure was also encapsulated with a hBN flake. Figure 5.3a shows the optical image

of a fabricated CoPc/FGT device. The CoPc layers covered the whole area observed in this image, while the FGT and hBN layers are highlighted by a red and black line.

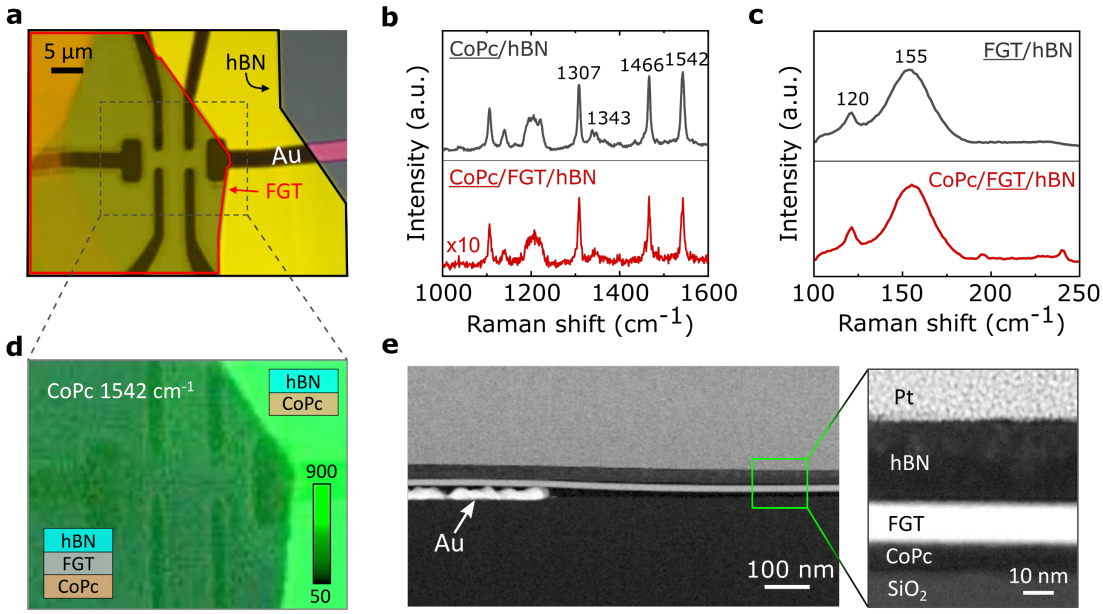

Figure 5.3| Structural characterization of a hybrid CoPc/FGT heterostructure. a, Optical image of a CoPc/FGT structure capped with hBN. The CoPc layer is deposited in the whole substrate area (including the contacts). The red and black lines indicate respectively, the FGT and the hBN flakes. **b**, Raman spectra for CoPc with and without FGT layers. Raman peaks representing intra-molecular vibrations (1300 cm^{-1} to 1600 cm^{-1}) are similar in both the CoPc/hBN and CoPc/FGT/hBN regions of the sample. **c**, Raman spectra for FGT with and without CoPc layers. The typical FGT peaks at 120 cm^{-1} and 155 cm^{-1} appear unaltered in both FGT/hBN and CoPc/FGT/hBN structures. **d**, Raman map image for CoPc (1542 cm^{-1}) in the white dotted line region of Figure 2a, displaying the formation of a homogeneous CoPc molecular layer. The region covered by FGT shows a lower Raman intensity due to the screening from the opaque FGT. **e**, STEM images of a CoPc/FGT/hBN cross-section, taken form one of the measured samples. The interface is flat and homogeneous.

The effect of the stamping procedure on the integrity of the CoPc film was proved through microRaman spectroscopy (Appendix B). Figure 5.3b shows a comparison of the Raman spectra measured in different regions of the CoPc film, either covered by hBN (CoPc/hBN) or by FGT (CoPc/FGT/hBN). In both regions, the spectra display the typical features of MPc molecules. In particular, the peaks of 1466 cm^{-1} and 1542 cm^{-1} represent the B_{1g} and B_{2g} mode of the CoPc molecule and correspond to the C-N stretching directly

associated to the central Co ion [192]. These Raman features were also observed in an uncovered thin film of CoPc molecules, indicating that the stamping process does not significantly alter the molecular layer condition.

Figure 5.3c shows the Raman features of an hBN-capped FGT flake transferred on a CoPc film or on a bare SiO_2 substrate. The two flakes displayed the two dominant Raman peaks of FGT at 120 cm^{-1} and 155 cm^{-1} associated to A_{1g} and E_{2g} vibrations [193]. Even in this case, there was no significant change in the spectra for FGT in contact with CoPc or SiO_2. In addition, we mapped the intensity of the CoPc peak at 1542 cm^{-1} in the area denoted by a white dotted line in Figure 5.3a. The homogeneity of the intensity in the map implies that the CoPc molecules are uniformly distributed in the CoPc/hBN and CoPc/FGT/hBN regions (Figure 5.3d). We note that the lower intensity of the CoPc features in the CoPc/FGT/hBN region is caused by screening from the not transparent FGT flake. These data confirm once more that the delamination of flakes on the molecular layer is gentle enough to not compromise the uniformity of the latter.

To gain additional insights on the CoPc/FGT interface, we performed scanning transmission electron microscopy (STEM). Figure 5.3e displays a cross-section of a CoPc/FGT/hBN heterostructure obtained by STEM. An image in low magnification provides overall information on the CoPc/FGT/hBN heterostructure, showing that the CoPc molecules constitute a compact film on SiO_2 which forms a homogeneous interface with the FGT flake stamped on the top. One can also appreciate how the FGT flake is just slightly bent by the small substrate step at the contact region. Moreover, it is clear that the very thin and rough Au electrodes are not fully covered by the CoPc layer, leaving room for a direct contact between FGT and Au, and ensuring an efficient charge injection. Finally, the high-resolution STEM image in the right section of Figure 5.3e highlights the formation of a flat and uniform CoPc/FGT structure, which is a crucial factor to generate a spinterface effect between CoPc and FGT layers.

5.3 Spinterface induced exchange bias

To investigate the molecular spinterface effect in CoPc/FGT heterostructures, we analyze the magnetic hysteresis of FGT flakes through magneto transport measurement, by recording the anomalous Hall effect (AHE). A specific procedure was developed to identify the magnetic interaction at the FGT/CoPc interface. First, a field-cooling (FC) process was employed to align the spin in

the system. During this phase the ferromagnetic/molecular Hall bar device was cooled down from 300 K to 10 K under an out-of-plane magnetic field ($H_z = \pm 10$ kOe). Then, measuring the AHE in such devices, we were able to study the relationship between the magnetic response of this new system and the presence of an FGT/CoPc spinterface (see Figure 5.4a for the measurement schematic).

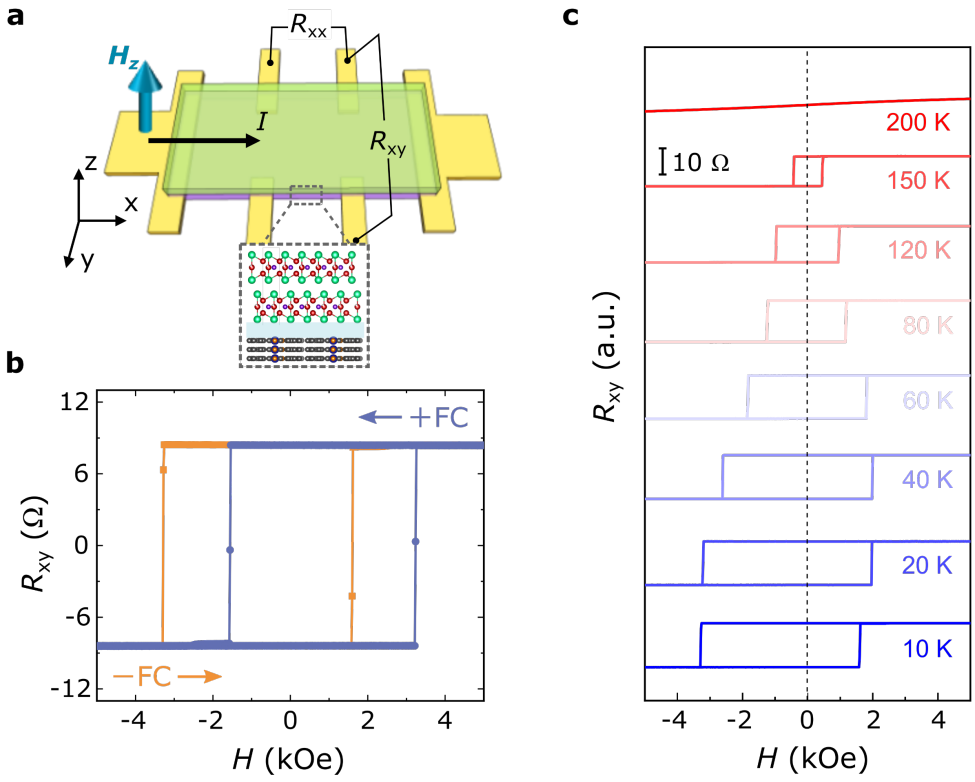

Figure 5.4| Exchange bias in a CoPc(6)/FGT(20) heterostructure. a, Schematic image of a CoPc/FGT Hall bar device. The AHE is obtained from measurements of the transversal voltage (along y) induced by a current (applied along x) and an out-of-plane magnetic field (H_z). **b**, AHE measurement at 10 K after a field cooling (FC) with +10 kOe (+FC) and -10 kOe (-FC). The hysteresis is shifted to opposite directions depending on the polarity of the FC, and the magnitude of the shifts is similar. **c**, Temperature-dependent AHE after FC with +10 kOe. The asymmetry of the hysteresis loop decreases as temperature increases.

Figure 5.4b shows the magnetic hysteresis in a CoPc(6)/FGT(20) (thickness in nm) heterostructure measured at 10 K after field cooling at +10 kOe and −10 kOe. After field cooling, the measured hysteresis loops display a large exchange bias. Specifically, for a field of +10 kOe, the magnetic hysteresis loop was significantly shifted of $H_{EB} = -840$ Oe at 10 K. Here, the exchange bias field is defined as $H_{EB} = (H_{C+} + H_{C-})/2$, where $H_{C+/-}$ indicate the coercive field at a positive and negative H. When the FC procedure was repeated with

a magnetic field of –10 kOe, the AHE at 10 K showed a reversed behavior, with the hysteresis loop shifted towards a positive field direction, and of the same amount as in the case of the positive FC. This negative exchange bias, where the direction of a hysteresis loop shift is opposite to the direction of the FC field, is typically found when a ferromagnetic interfacial coupling develops at the interface between a ferromagnet and an antiferromagnet. The asymmetry in the hysteresis loops, indicating the presence of exchange bias, was measured at different temperatures after a FC process with +10kOe. From Figure 5.4c one can see that the asymmetry decreases with increasing temperature until 80 K, where it becomes negligible.

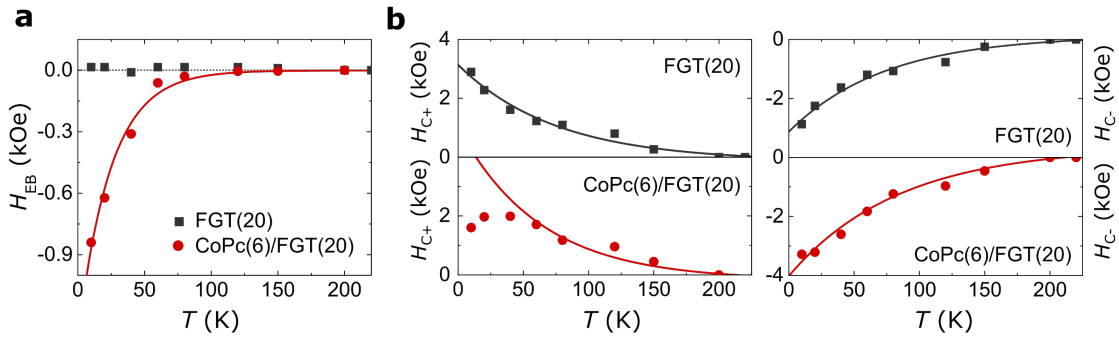

Figure 5.5| Temperature dependence of exchange bias and coercivity. a, Exchange bias field H_{EB} as a function of temperature in a CoPc(6)/FGT(20) and in a FGT(20) structures. The exchange bias in the CoPc/FGT follows an exponential behavior with an estimated blocking temperature of 110 K. No exchange bias is recorded in the control sample of FGT. **b**, Temperature-dependence of the positive and negative coercive fields $H_{C+/-}$ after FC with +10 kOe in the CoPc(6)/FGT(20) and in the FGT(20) structures. The control sample of FGT follows an exponential behavior for both positive and negative coercive fields, while the CoPc/FGT heterostructure displays an asymmetric deviation on a positive and negative field when lowering T, which represents the emerging of exchange bias.

Two control experiments were conducted, to ensure that the measured exchange bias originates from the magnetic interactions between the layered magnetic materials and the molecular film. Firstly, we fabricated a control sample, FGT(20) without CoPc molecules, and performed the same FC procedure. This sample clearly showed a symmetric hysteresis loop without any exchange bias (Figure 5.5a, and Appendix C). Secondly, although our CoPc/FGT structures were encapsulated by hBN in a Ar-filled glovebox, we could not ignore the possibility of oxidation during transferring the sample to the measurement chamber, which could induce the formation of oxidized layers with different magnetic properties and hence exchange bias [194]. To exclude this effect, we tested a FGT(25) flake intentionally exposed to air 15 minutes

without any encapsulation film. In this case, we could not detect any exchange bias nor any noticeable coercive field enhancement (see Appendix C). The control experiments confirm that the exchange bias recorded at the FGT/CoPc interface is a purely spinterface effect arising at the FGT/CoPc interface.

To understand the origin of the negative exchange bias at the FGT/CoPc interface, we put forward a mechanism according to which (i) the spins in the CoPc layer acquire long range antiferromagnetic ordering and (ii) a ferromagnetic coupling establishes between the spins of the two layers in contact, causing the negative shift in the hysteresis loop. This situation, which was previously described for other spinterfaces between conventional magnetic materials and different phthalocyanines, is further validated by analyzing the temperature dependence of the exchange bias.

Figure 5.5 shows the exchange bias field and $H_{C+/-}$ at different temperatures, collected from the data in Figure 5.4c. The exchange bias follows an exponential relation $H_{EB} = H_0\, e^{-\frac{T}{T_1}}$, where H_0 is the extrapolated value to zero temperature and T_1 is a constant. Using this fitting, the estimated blocking temperature (i.e. the starting point of $H_{EB} = 0$) of a CoPc(6)/FGT(20) structure is 110 K. This value is analogous to the critical temperature in other molecular exchange bias systems based on CoPc [195], and it also corresponds well to the estimated exchange energy for antiferromagnetic ordering of CoPc molecular layers [190]. This agreement with previous results indicates that the exchange bias in FGT indeed arises from the same physical mechanism, i.e. antiferromagnetic order in CoPc and the interfacial coupling.

5.4 Exchange bias dependence on layers thicknesses

The thickness of both the ferromagnet and the antiferromagnet are critical factors on which the intensity of exchange bias depends. Figure 5.6a displays the hysteresis loops measured at 10 K after FC with +10 kOe in different CoPc(6)/FGT(t) heterostructures in which the thickness of the CoPc layer was kept constant (6 nm), and the thickness of the FGT was varied from $t =$ 10 nm to $t = 80$ nm. Here, to focus on the coercive field change we plot the transverse resistance R_{xy} normalized to the resistance at saturation. Figure 5.6b shows the dependence of the exchange bias on the FGT thickness. For thin flakes ($t < 20$ nm), the exchange bias field increases from $H_{EB} =$ – 62.5 Oe at 10 nm to a maximum $H_{EB} = -840$ Oe at 20 nm of FGT. Above 20 nm, the exchange bias field decreased gradually down to a value of $H_{EB} =$

−145 Oe for 80 nm of FGT. In conventional exchange bias systems, the magnitude of exchange bias is inversely proportional to the thickness of a ferromagnet as $H_{EB} \sim 1/t_{FM}$ [196]. Our CoPc(6)/FGT(t) system follows this relation in the FGT thickness range from 20 nm to 80 nm (red line in the inset of Figure 5.6b). Below 20 nm the exchange bias diminishes again, as if 20 nm is the ideal thickness to maximize the effect. This divergence from the conventional trend of H_{EB} vs t could arise from the lower volume magnetization of FGT compared to metallic ferromagnets such as Co and Fe [36,194], which might be insufficient to fully activate the antiferromagnetic ordering in the interfacial CoPc layers. Regardless of the thickness of FGT, all the structures exhibit negative exchange bias which highlights the favorable ferromagnetic coupling at the interface between the FGT and CoPc layers.

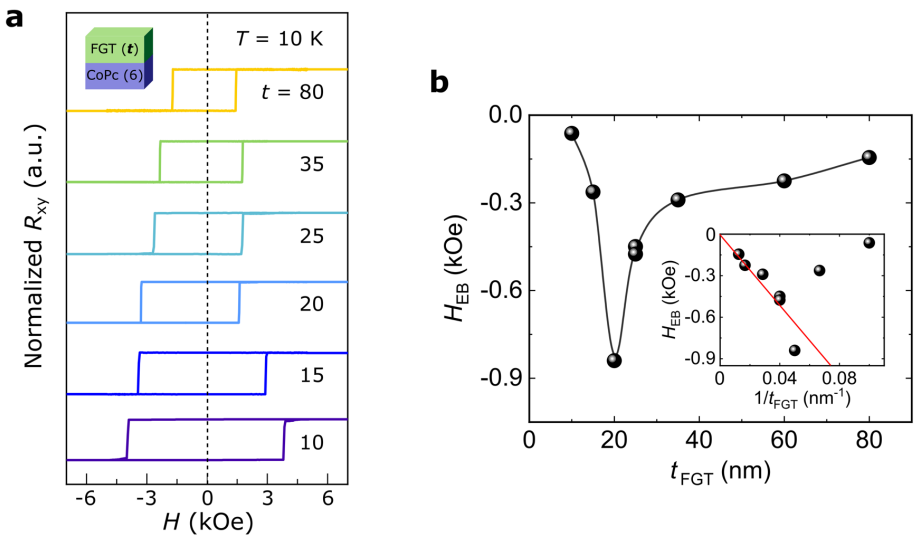

Figure 5.6| Exchange bias dependence on FGT thickness. a, Anomalous Hall effect measured in different CoPc(6)/FGT(t) heterostructures composed of a 6-nm-thick CoPc film and an FGT flake of varying thickness (in the range from 10 to 80 nm). **b**, Dependence of the exchange bias field H_{EB} in the CoPc(6)/FGT(t) heterostructures as a function of the FGT thickness t_{FGT}, as extracted from the curves in **a**. Inset: the same data plotted as a function of $1/t_{FGT}$ highlights the proportional relation between H_{EB} with the inverse of the FGT thickness from 20 nm to 80 nm. These data were measured at 10 K after a FC procedure with +10 kOe.

As FGT is a highly crystalline layered material, the magnetic proximity effects at the FGT/CoPc interface are primarily determined by the quality of the CoPc surface. Therefore, after having inspected the dependence of the exchange bias on the FGT thickness, we explore its change as a function of the CoPc thickness. Figure 5.7a displays the hysteresis loops measured at 10 K and after FC with +10 kOe in different CoPc(t)/FGT(20) heterostructures, composed of a FGT flake of approximately 20 nm and different thicknesses of

the CoPc layer (respectively $t = 2$, 4, 6 nm). In the same panel, we also show the hysteresis of a FGT flake directly transferred on a SiO_2 substrate without CoPc (corresponding to t = 0 nm), characterized by a coercive field of approximately 3 kOe without exchange bias. The presence of CoPc underneath the FGT flakes, induces primarily a magnetic hardening for low t, i.e. for the 2-nm-thick CoPc layer a small exchange bias and larger coercive field are observed. An increase in coercive field is often observed for ferromagnetic/antiferromagnetic interfaces in which the antiferromagnetic coupling is not fully developed. Increasing the t of the molecular layer to 4 nm, an even larger coercive field is obtained, and a stronger exchange bias field start to develop. Finally, a maximum exchange bias field and a reduced coercive field are observed for a CoPc thickness $t = 6$ nm. We interpretate this finding considering that the antiferromagnetic ordering is fully formed only starting from CoPc layers 6 nm thick, and that only at this point efficient pinning of FGT takes placw, resulting in maximum exchange bias and lower magnetic hardening. Figure 5.7b displays the increase in the exchange bias field with the CoPc thickness from $H_{EB} = 0$ Oe (without CoPc) to $H_{EB} = -840$ Oe (with 6 nm thick CoPc).

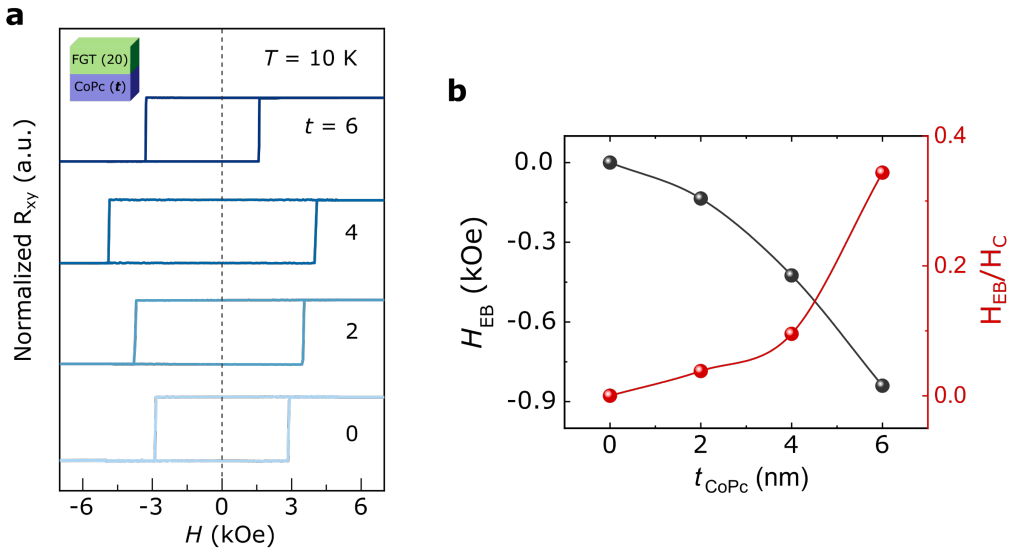

Figure 5.7| Exchange bias dependence on CoPc thickness. a, Anomalous Hall effect measured in different CoPc(t)/FGT(20) heterostructures composed of a 20-nm-thick FGT flake and a CoPc film of varying thickness (in the range from 0 to 6 nm, where 0 corresponds to no CoPc layer). **b**, Dependence of the exchange bias field H_{EB} in the CoPc(t)/FGT(20) heterostructures as a function of the CoPc thickness t_{CoPc}, as extracted from the curves in **a**. The H_{EB}/H_C ratio is also shown, where H_C is the coercive field in the FGT hysteresis loops.

The quality of a magnetic heterointerface at a ferromagnet/antiferromagnet structure can be evaluated by the ratio between the exchange bias and the

coercivity fields (H_{EB}/H_C) [197,198]. Figure 5.7b also shows the H_{EB}/H_C ratio in the CoPc(t)/FGT(20) structures. The H_{EB}/H_C ratio reaches a remarkably large maximum value of 0.34, which is the highest among the reported exchange bias structures based on FGT [194,199–203] (see Appendix D for a comparison with other systems), indicating the high quality of the magnetic CoPc/FGT spinterface.

5.5 Conclusions

In this study, we demonstrated the emergence of spinterface effects in hybrid van der Waals heterostructures composed of a CoPc film interfaced with a flake of the layered ferromagnet FGT. The formation of a homogeneous CoPc layer and of a flat and sharp CoPc/FGT interface, confirmed through Raman spectroscopy and STEM, are ideal for the emergence of magnetic interactions between the unpaired spins in CoPc and FGT. Magnetotransport measurements performed following a FC procedure indicate that the interfacial magnetic interaction induces an exchange bias in FGT persisting up to 110 K. This blocking temperature is analogous to the reported exchange energy of antiferromagnetic ordering of CoPc layers, suggesting that the CoPc layer develops an antiferromagnetic ordering which couples ferromagnetically to the FGT surface, pinning its magnetization. This is corroborated by analyzing the magnetic response of CoPc/FGT heterostructures with different CoPc thicknesses, which evolves from an increase in coercive field for thin CoPc layers to a fully developed exchange bias for thicker layers. The exchange bias field $H_{EB} = -840$ Oe, recorded for a 20-nm-thick FGT flake, is the strongest reported so far for layered magnetic materials, highlighting the superior quality of the CoPc/FGT spinterface. Our results show that hybrid van der Waals heterostructures composed of layered magnetic material interfaced to organic molecules represent the ideal materials platform to develop high quality spinterface effects, which might be a key ingredient in atomically precise multifunctional structures for practical device application.

5.6 Appendices

A. CoPc morphological characterization

The quality of the CoPc thin films growth was studied via atomic force microscopy (AFM, see Chapter 2 for details). Figure 5.8a-c displays AFM maps of CoPc films grown in the same conditions (see Chapter 2 for details), but with different thicknesses (ranging from 2 to 20 nm). The surface topography of the films indicate that CoPc grows in amorphous and relatively flat layers composed by small molecular aggregates $\sim$ 100 nm wide. The roughness of such films, estimated from the maps, and plotted against the thickness it is reported in Figure 5.8d. The roughness slightly increases with the CoPc thickness, but it remains $<$ 1 nm at the t employed for this work. The smoothness and uniformity of the CoPC films is fundamental for the formation of the studied spinterfaces.

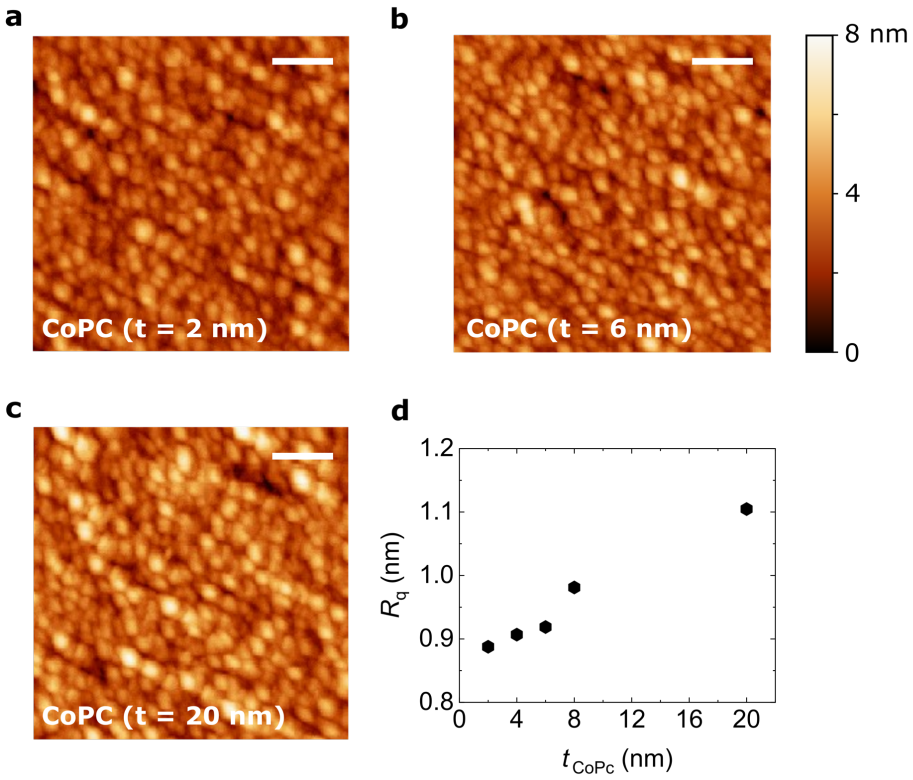

Figure 5.8| CoPc thin films surface morphology and roughness. a-c, Atomic force microscopy maps showing of the CoPc layers grown on Si/SiO_2 substrates, and with thicknesses ranging from 2 to 20 nm. The films were grown in the same condition of pressure ($\sim 10^{-8}$ mbar) and growth rate ($\sim$ 0.3 Å/s). The scale bars correspond to 500 nm. **d**, CoPc roughness as function of the layer thickness. The roughness increases with increasing thickness.

B. Raman Characterization

Raman measurements (Renishaw InVia Raman Microscope) were carried out in high vacuum (10^{-6} mbar) at 300 K. Lasers with a 532 nm and 633 nm wavelengths were used for FGT and CoPc, respectively. The laser beam was focused on the sample by a 100× lens objective in a microscope and the scattered light was collected by the same objective. A step size of 0.2 μm × 0.2 μm was used for Raman mapping. J. Jo and B. Martín García performed the measurements.

C. Control experiments

Field cooling of FGT/hBN

The complete data obtained from the control experiment described in section 5.3 are presented in Figure 5.9. After positive and negative field cooling, no asymmetry was observed in the AHE measurements representing the hysteresis loop of pristine FGT capped with hBN. This confirms no artifact coming from the measurements or from FGT itself.

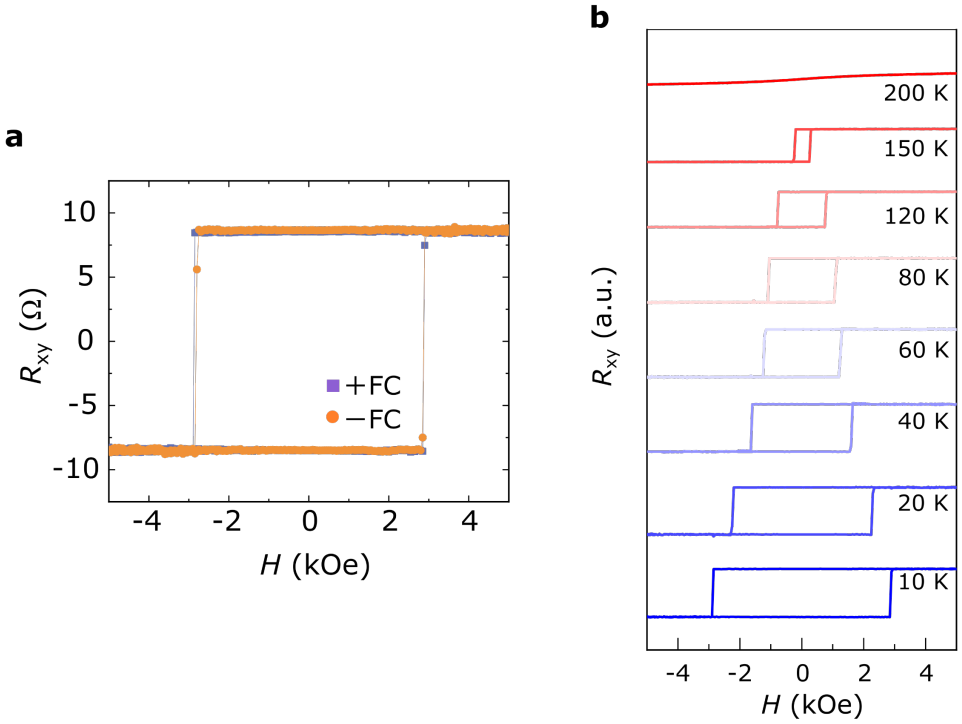

Figure 5.9| AHE measurement on hBN-capped FGT(20 nm) after field cooling. a, Hysteresis loop measured at 10 K after field cooling (FC) with ±10 kOe. Without the CoPc layer, no asymmetry was observed for positive and negative coercivity field. **b**, AHE measured at different temperatures (10 K – 200 K) after FC with +10 kOe. Exchange bias is not observed in any of the loops.

Effect of oxidation

Even though the whole stamping process (including the hBN encapsulation), was carried out in an Ar-filled glovebox, partial oxidation of the FGT may have occurred during the transferring to the measurement cryostat. Since oxidized FGT (O-FGT) was demonstrated to induce pinning effects on the magnetization of pristine FGT [194], we measured AHE after FC also on a flake that was on purpose exposed to atmosphere for a brief time ($\sim$ 15 min) to simulate an unwanted exposure to atmosphere. The result of this experiment is presented in Figure 5.10. The absence of asymmetry in the hysteresis loops obtained after positive and negative FC demonstrate that, in our experiments, O-FGT was either absent or it was not giving significant effects that may had compromised the AHE measurements.

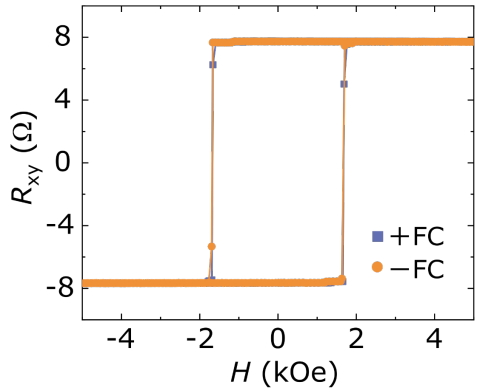

Figure 5.10| AHE measurement on a FGT(25)/O-FGT(x) structure. The measurement was performed at 10 K and after FC with $\pm$ 10 kOe applied. The flake was left intentionally exposed to air for 15 mins before encapsulating it with hBN. No signature of exchange bias is detected.

D. Comparison with other work

In the following table, we compare the H_{EB}/H_C ratio obtained from our hybrid vdW heterostructure with other works, all employing FGT as ferromagnetic material.

Table 5.1| H_{EB}/H_C ratio in FGT based exchange bias systems. The ratio is calculated with recorded data in the reference papers.

Structure (unit : nm)	H_{EB}/H_C	T (K)	AFM type	Ref.
FGT(30)/$CrCl_3$(15)	0.2	10	uncompensated	[201]
FGT(30)/$CrCl_3$(45)	0.1	10	uncompensated	[201]
FGT(17)/O-FGT(3)	0.15	70		[194]
FGT(17)/O-FGT(3)	0.28	70		[194]
FGT(20)/CoPc(6)	0.34	10	uncompensated	This work
FGT(25)/IrMn(2)	0.04	2	compensated	[203]
FGT(23)/$MPSe_3$(23)	0.04	10	compensated	[202]
FGT(23)/$MPSe_3$(23)	0.05	10	compensated	[202]
FGT(9)/$MPSe_3$(19)	0.05	10	compensated	[199]

PART II

6 Introduction on spin-to-charge interconversion in low-symmetry systems

Spin-to-charge interconversion phenomena are one of the key ingredients for the development of modern spintronics. This discipline, through the study and manipulation of the spin-charge coupling in materials brought new perspectives in terms of potential technological progress. In this Chapter, we will first see the milestones that marked the rise of spintronic, to then introduce the fundamental notions regarding spin, spin transport and spin-to-charge conversion phenomena in the specific case of systems with broken inversion symmetry.

6.1 Brief notes on the history of spintronics

Spintronic has been thriving since the first discovery of a revolutionary spin-dependent effect: the giant magnetoresistance (GMR), observed simultaneously and independently by the groups of Grünberg [204] and Fert [205] for the first time in 1988, and later awarded with the Noble prize in Physics in 2007. The GMR effect is based on the spin dependent scattering of electrons travelling across a metallic junction (composed by a normal metal (NM) sandwiched between two ferromagnets (FMs)), which induces a change in resistance depending on the mutual orientation of the magnetic states of two FMs (see Figure 6.1a). Such revolutionary discovery led, in the following years, to a breakthrough in the magnetic memory industry driven by the fast development of sensitive magnetic reading heads capable of accessing higher density of information stored in magnetic hard drives (HDD) [206].

Since the GMR discovery, spintronics, also known as "spin transport electronics", flourished as a very fruitful research field (see Figure 6.1d). This discipline aims to control and manipulate the spin degree of freedom of electrons with the objective of achieving an energy efficient storage and processing of information. The motivations driving the research on spintronics are related to the increasingly higher demand of storage and computing power, which will eventually become impossible to satisfy just with the progress of traditional CMOS (Complementary Metal Oxide Semiconductor) based electronics [207].

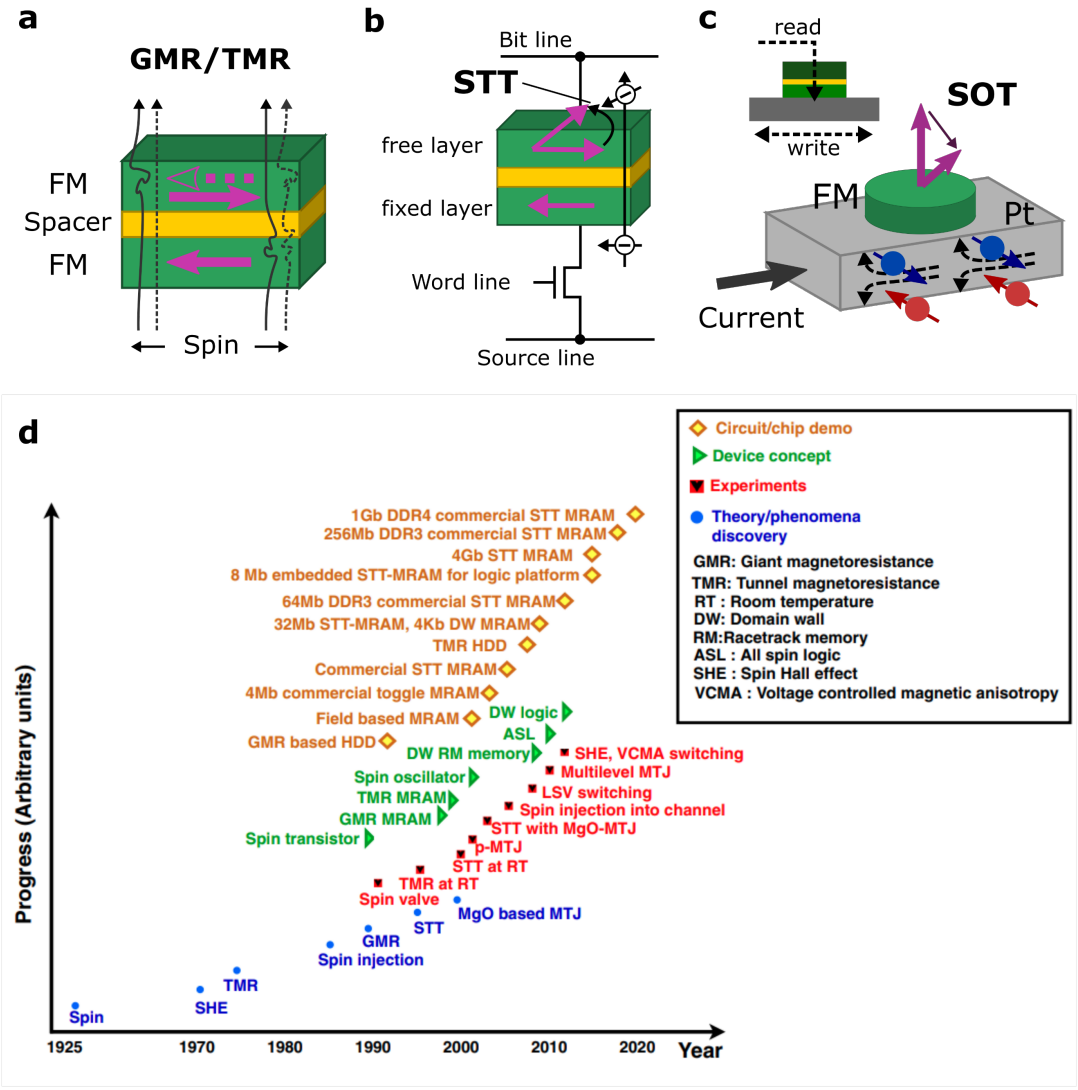

Figure 6.1| Hystory of spintronics. Important effects that marked some of the milestones of spintronics, **a**, GMR **b**, STT, and **c** SOT. **d**, Progress timeline of spintronic research and developments (adapted from Ref. [208]).

As mentioned above the discovery of GMR can be seen as the starting point of spintronics. After that, with the optimization in fabrication of magnetic tunnel junctions (MTJs), it was quickly possible to exploit an already known effect (since 1975) similar to GMR, to substantially improve the efficiency in sensing information. Tunneling magnetoresistance (TMR) is a strong magnetoresistive behaviour (up to 600%) caused by the spin-dependent tunneling of spin polarized electrons [209], travelling through a thin insulator layer used as spacer in MTJs. The outstanding progress brought by TMR in terms of sensitivity and so, reduction in bit dimensions in the HDD, made soon TMR based devices to become the state of the art in the production of memory devices [210,211]. As today, MTJs are the fundamental building blocks, not

only for the magnetic reading heads of the common hard drives, but also for non-volatile magnetic random-access memories (MRAM).

These advancements were mostly focusing on the reading of the spin information. The magnetoresistive states, in fact can be associated to "ones" and "zeros" as binary bit of information. Hence, the next bottleneck that had to be addressed by the spintronic community was the writing of information, i.e., the control of magnetization of the smallest FM elements. The traditional way to produce local magnetic fields, and so to switch the magnetic bits, was based on the induction of Oersted fields through the application of currents in opportunely designed metallic wires. However, this method revealed to be the limiting factor for the downscaling of memories, since the localization of the Oersted fields was defining the smallest switchable FM element. In MRAM, this problem has been overcome employing the so-called spin transfer torque (STT) [212,213], marking a second milestone in the spintronic field (see Figure 6.1b). The idea behind this concept is to exert a torque on the magnetization of the targeted FM element in order to switch its state, by transferring the angular momentum carried by spin polarized electrons. In STT-MRAMs, high current densities, flowing through the MTJs, get spin polarized by a fixed FM layer, to then induce the switching on the free FM layer, hence writing the information. By measuring the resistance state of the MTJ after every writing event, one can read the bit of information. In this way the scalability problem was solved, and STT-technologies beyond 28 nm nodes hit the market with chip capacities larger than 1 Gb. However, the high writing current (potentially harmful for the MTJs) and the relatively high switching latency characteristic of STT-MRAMs, still remain a matter of concern [208].

To overcome this shortcoming, the spintronic community started more recently to focus their study on spin to charge interconversion phenomena, with which the generation and manipulation of spin currents can be achieved without the need of flowing a charge current through a FM. In this regard, the spin Hall effect (SHE), predicted by D'Yakonov and Perel in 1971 [214] and revived by Hirsch in 1999 [215], attracted renewed interest in the scientific community, after its demonstration in Pt at room temperature [216]. The SHE is a relativistic effect that produces, in systems with strong spin-orbit coupling (SOC), an asymmetric deflection of electrons based on their spin orientation. Thus, the application of a charge current through an opportune medium can spontaneously generate pure spin currents and it can be used to switch the magnetization state of memory devices (see Figure 6.1c). This concept, also known as spin-orbit torque (SOT) [217–219], has been demonstrated to provide unmatched switching speed and endurance with respect to STT [220,221],

and it is expected also to hit the market with a new generation of memories, SOT-MRAMs. The discovery of SOT represents another milestone for spintronic, giving birth to the modern field of spinorbitronics.

More recently, the investigation on the interplay between the structural properties of materials and the spin/charge interactions led to the understanding that also in low symmetry systems, charge to spin interconversion processes can be observed [222]. The lack of certain symmetries in crystals enables the presence of otherwise forbidden spin to charge conversion phenomena which are of huge interest for spinorbitronics, such as non-linear Hall effects [60,61], Rashba-Edelstein effect [223–225], valley magnetoelectricity [226] and magnetochiral anisotropy [227,228]. Mastering this interconnection between material structural properties and the resulting physical effects can be the key for the realization of the next generation of spintronic applications, such as the spin transistor [134] and all spin logic devices [229], or even for the design entirely new devices concepts.

In this chapter, we will introduce the fundamental notions on spin transport and on spin-to-charge conversion in the specific case of low symmetry materials, connecting the structural properties of a system with a specific spin-to-charge interconversion mechanism, the Edelstein effect. Moreover, we will review some relevant experiments that represented the foundation for the study that will be reported in the next chapter.

6.2 The electron spin

Spin is an intrinsic form of angular momentum characteristic of elementary particles. In quantum mechanics, the description of a particle, such as an electron, can be given through its total angular momentum $\boldsymbol{J}$, composed of the orbital momentum $\boldsymbol{L}$, and the spin $\boldsymbol{S}$. The notion of spin was first inferred by the Stern-Gerlach experiment, which showed, in 1922, that a beam of silver atoms directed through an inhomogeneous magnetic field would be forced into two beams despite having no orbital angular momentum. Mathematically, spin is described as a vector or a spinor that follows the same laws as quantized angular momenta, with the addition of some peculiar properties:

- Spin quantum numbers may take half-integer values
- The spin of a charged particle is associated with a magnetic dipole moment.

The spin expectation values are given by projecting the vector $\boldsymbol{S}$ on one of the space axes, normally being the z-axis, obtaining $S_z = \hbar m_s$, where $\hbar$ is the reduced Planck constant and m_s is the spin quantum number. In the specific case of electrons, being fermions (e.g. they follow the Fermi-Dirac statistics), the spin quantum number m_s can assume only two discrete values, $\pm\frac{1}{2}$, usually called "spin-up" and "spin-down". Fermions also obey the Pauli exclusion principle, and the description of the spin angular momentum can be generalized as [230]:

$$\boldsymbol{S} = \frac{\hbar}{2}\boldsymbol{\sigma}, \tag{6.1}$$

where $\boldsymbol{\sigma}$ are the Pauli spin matrices:

$$\sigma_x = \begin{pmatrix} 0 & 1 \\ 1 & 0 \end{pmatrix}, \qquad \sigma_x = \begin{pmatrix} 0 & -i \\ i & 0 \end{pmatrix}, \qquad \sigma_x = \begin{pmatrix} 1 & 0 \\ 0 & -1 \end{pmatrix} \tag{6.2}$$

These matrices are related to an angular momentum operator, and they are a powerful tool to treat the electron spin in quantum mechanics without the need of picturing it in normal 3D space.

Moreover, since the description of the electron can be given in terms of $\boldsymbol{L}$ and $\boldsymbol{S}$, orbital and spin magnetic moment can be associated to each quantity as follow:

$$\boldsymbol{\mu_o} = -\frac{e}{2m_e}\boldsymbol{L}, \tag{6.3}$$

$$\boldsymbol{\mu_s} = -g\frac{e}{2m_e}\boldsymbol{S}, \tag{6.4}$$

where e is the electron charge, m_e is the electron mass, and g is a dimensionless quantum mechanical correction, also known g-factor, that for electrons takes approximately the value of 2.

Starting from this basic picture, it is easy to understand how electrons carry information both through charge and spin, and that to the motion of electrons can be associated the concept of spin current.

6.3 Charge and Spin currents

The non-trivial definition of spin current has been discussed intensively in the last decades [231,232]. Here, to understand the idea of spin current, we will

follow the two spin-channel model approach, introduced for the first time by Mott in 1936 to explain the dependence of electrical conductivity on the magnetization state of ferromagnetic metals [233].

If we consider a charge current as a flow of electrically charged carriers, such as electrons, for what explained before, we can easily think about the current as divided in two types of flows, one with "spin-up" and another with "spin-down" electrons. Hence, two separate charge current densities can be defined as $j_\uparrow = -en_\uparrow v_\uparrow$ and $j_\downarrow = -en_\downarrow v_\downarrow$, where $n_{\uparrow\downarrow}$ and $v_{\uparrow\downarrow}$ are respectively the carrier density and the velocity of electrons with spin up or down. As the charge current is a flow of charges $(-e)$, a spin current can be expressed as a flow of angular momentum $(-\frac{\hbar}{2})$. The sum between the contributions of the two spin channels leads to the following expressions for charge and spin currents:

$$j_c = \ j_\uparrow + j_\downarrow = -e(n_\uparrow v_\uparrow + n_\downarrow v_\downarrow), \tag{6.5}$$

$$j_s = \tfrac{\hbar}{2}(n_\uparrow v_\uparrow - n_\downarrow v_\downarrow) = -\tfrac{\hbar}{2e}(j_\uparrow - j_\downarrow). \tag{6.6}$$

From these equations, it is possible to define three types of situations, as illustrated in Figure 6.2.

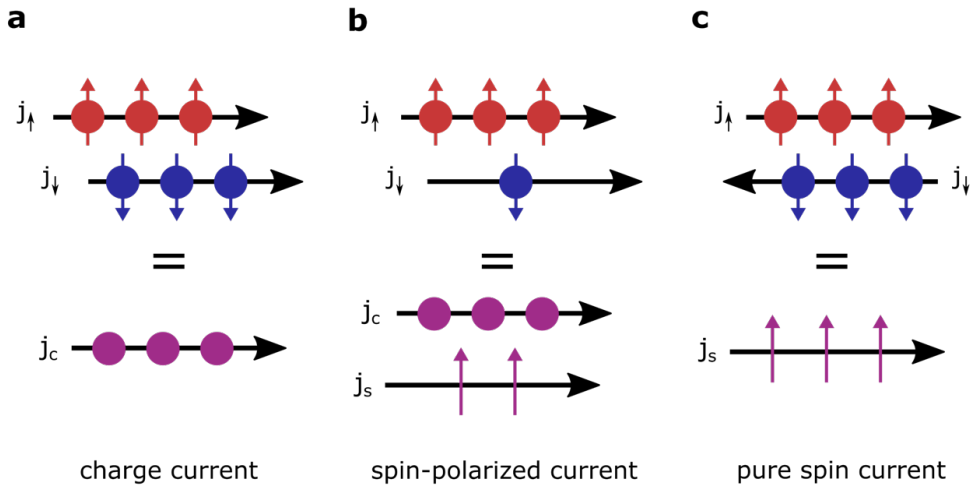

Figure 6.2| Illustration of different types of currents. a, A flow of electrons with the same amount of spin-up and spin-down give rise to a charge current. **b**, A spin-polarized current is produced in the presence of an unbalance of spin populations. **c**, The flow of electron with opposite spin polarization in opposite directions defines a current strictly composed of spin angular momentum (adapted from Ref. [234]).

In the first case (Figure 6.2a), usually observed in paramagnetic conductors, the current densities of the two spin states are equal and result in $j_s = 0$. This corresponds to a charge transport without spin transport, called pure charge current. The second situation (Figure 6.2b) can be encountered typically in ferromagnets (FMs), where an energy split of the band structure induces an unbalance of spin-up and spin-down giving $j_{\uparrow(\downarrow)} > j_{\downarrow(\uparrow)}$, and thus $j_c, j_s \neq 0$. This so-called spin-polarized current carries both charge and spin information. Finally, in special circumstances, a flow of spin angular momentum without any associated net charge transport can be created, e.g., by injection from a FM in non-local spin valves. This is called a pure spin current (Figure 6.2c), and it is characterized by $j_\uparrow = -j_\downarrow$.

6.4 Spin-Orbit coupling

The next step to understand the role of spin in transport is to evaluate its interaction with the environment surrounding the electrons. In particular, the spin-orbit coupling (SOC) is the relativistic interaction between spin and motion of a particle immerse in a potential. Since it originates from special relativity, SOC can be included in a non-relativistic Hamiltonian as a correction term. To do this, relativistic equations are employed to derive the spin-orbit coupling contribution in the non-relativistic Hamiltonian. Using the Dirac equation for free particles to describe a relativistic system, one finds out that the orbital ($\boldsymbol{L}$) and spin ($\boldsymbol{S}$) angular momentum interact together leading to a correction extra term which enters in the Hamiltonian as:

$$H_{SOC} = \frac{e\hbar}{4m_e^2c^2}\boldsymbol{E}\cdot(\boldsymbol{k}\times\boldsymbol{\sigma}) = \xi\boldsymbol{L}\cdot\boldsymbol{S}, \tag{6.7}$$

where the spin-orbit coupling constant is defined by $\xi = \frac{e}{2m_e^2c^2}\frac{1}{r}\frac{dV(r)}{dr}$ (r being the distance of electron from the nucleus), the static spherical electric field $\boldsymbol{E} = -\nabla V(r) = (\frac{\boldsymbol{r}}{r})\frac{dV(r)}{d(r)}$, the orbital angular momentum $\boldsymbol{L} = \boldsymbol{r}\times\boldsymbol{k}$ and the spin angular momentum $\boldsymbol{S} = \frac{\hbar}{2}\boldsymbol{\sigma}$.

Equation (6.7) can already give us a qualitative idea of which systems are characterized by a strong SOC. In fact, in first approximation, we can neglect the electron-electron interactions and consider the nucleus being the dominant contribution to the electric field, obtaining as a spin-orbit coupling constant $\xi \sim -\frac{Z|e|}{r^3}$ (Z is the atomic number). This implies that the spin-orbit interaction should be stronger in heavy elements (it increases with Z) and with the

distance of electrons from the nucleus. Moreover, since it depends on the orbital angular momentum, the SOC will not affect s-electrons ($L = 0$), it will be largest for p-electrons due their proximity to the nucleus, and increasingly small for d and f orbitals.

As a final remark, one should keep in mind that in a solid, the potential V acting on the electron is given by several contributions: the periodic potential related to the lattice, non-periodic potential associated to impurities or boundaries, external applied fields, and even internal ones caused by the lack of crystal inversion symmetry. Therefore, spin-orbit phenomena can have different origins and give rise to different spin to charge interconversion processes such as anomalous Hall effect (AHE), spin Hall effect (SHE), or Edelstein effect (EE), also known as inverse spin galvanic effect.

6.5 Spin to charge interconversion in systems with broken inversion symmetry

In systems with strong spin-orbit coupling and broken inversion symmetry, the band structure is split in two branches characterized by different spin orientation. In such systems, the band structure can be characterized by particular spin textures that can be exploited, according to the Edelstein effect, to generate, or detect, spin densities oriented in certain directions.

6.5.1 Rashba effect

The Rashba effect, discovered by Vas'ko [235], Bychkow and Rashba [236], appears at the surface or interface of 3D crystals and in two-dimensional electron gases (2DEG), where inversion symmetry is broken by the macroscopic structure. In such systems, a potential gradient $\partial V/\partial \boldsymbol{n}$ is present, with $\boldsymbol{n}$ the local surface normal, and for a planar surface (with $\boldsymbol{n}$ constant), a spin-orbit coupling Hamiltonian term is defined as follows:

$$H_R = \alpha_R(\boldsymbol{n} \times \boldsymbol{k}) \cdot \boldsymbol{\sigma}, \tag{6.8}$$

where α_R is the Rashba coefficient quantifying the strength of the splitting. Due to the broken inversion symmetry, the Kramers spin degeneracy is lifted, and for each value of k, the two spin-split bands with opposite spin orientations have energies defined as:

$$\varepsilon_{\uparrow,\downarrow}(k) = \frac{\hbar^2 k^2}{2m_e} \pm \alpha_R k, \tag{6.9}$$

where the first term is coming from the free-electron dispersion and the second from the Rashba term. As shown in Figure 6.3 (for $\alpha_R > 0$), two spin sub bands arise with a momentum-dependent splitting given by $k_R = \pm \frac{\alpha_R m}{\hbar^2}$. Now, performing a cut in the band structure at an arbitrary energy, we will observe that the spin splitting produces two Fermi contours with inequivalent spin textures, both with spin locked to its momentum, but with spin rotating clockwise and anticlockwise with respect to the k_x, k_y plane.

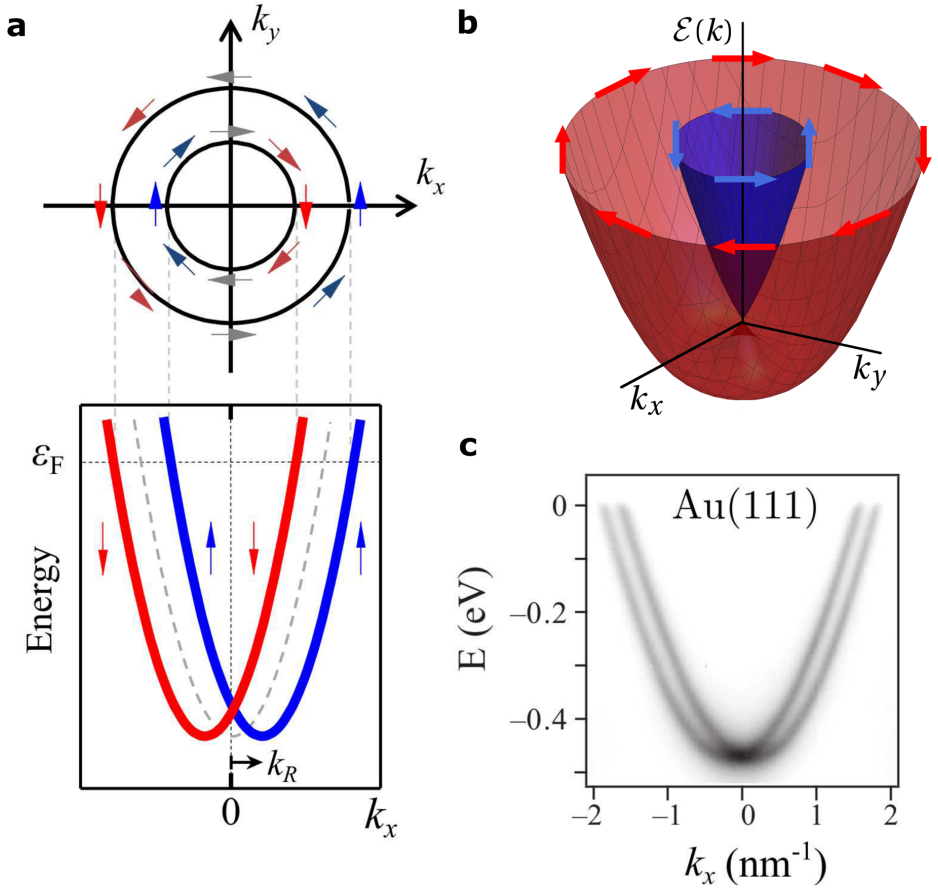

Figure 6.3| Band structure of a Rashba system with broken inversion symmetry. a, Energy dispersion for Rashba-split bands with opposite spin configurations (bottom). At the Fermi energy two contours with different sizes and helicity of the spin textures are observed (top). **b**, 3D illustration of the band structure. **c**, Rashba-split bands at the Au(11) surface, observed experimentally with angle-resolved photoemission spectroscopy. Figure adapted from Ref. [234,237,238].

An interesting feature of the Rashba spin-orbit coupling is that α_R can be easily modulated with an external electric field. From this, Datta and Das

proposed the idea of the spin transistor, a device in which the spin transport, occurring for instance in semiconductor quantum wells, could be controlled via electrostatic gate voltages [239].

6.5.2 3D systems with bulk inversion asymmetry

6.5.2.1 Dresselhaus effect

Besides the case of 2D Rashba systems, a band spin-splitting leading to unique band structure properties can occur also in 3D systems with bulk broken inversion symmetry. The first discovery of such an effect was made by Dresselhaus, which realized that in zinc-blende structures, such as GaAs and InSb, the spin degeneracy can also be lifted, leading to a spin-splitting of the band structure. Zinc-blende structures are the paradigm of non-centrosymmetric systems, in which the bulk inversion symmetry is broken due to the presence of nonequivalent atoms inside the unit cell [240]. The Dresselhaus effect leads to a spin-orbit k^3-Hamiltonian term [241], in cubic momentum space, that reads:

$$H_D = \frac{\hbar}{2}\frac{\beta_D \hbar^2}{\sqrt{2m_e^3 \varepsilon_g}}\kappa(\boldsymbol{k})\cdot\boldsymbol{\sigma} \tag{6.10}$$

where ε_g is the band gap, β_D is a material dependent parameter quantifying the strength of the spin-orbit coupling and $\kappa(\boldsymbol{k}) = [k_x(k_y^2 - k_z^2),\ k_y(k_z^2 - k_x^2),\ k_z(k_x^2 - k_y^2)]$ with k_i the momentum component along the main crystal directions.

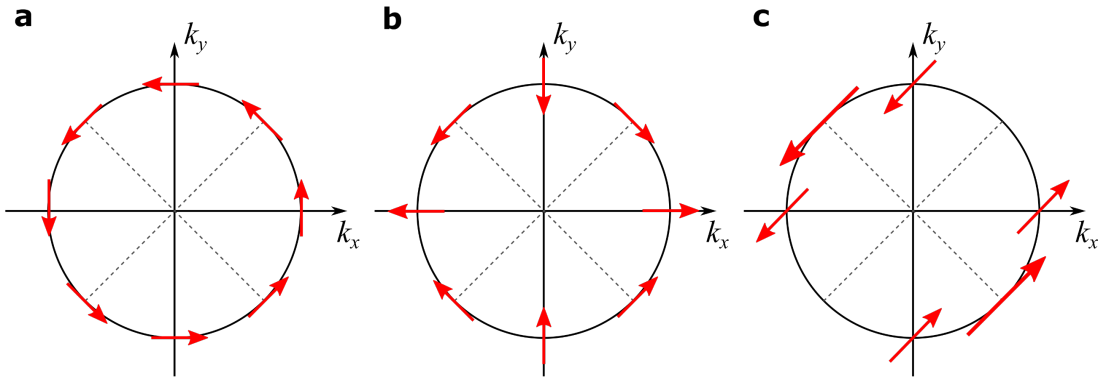

Figure 6.4| Spin textures at the Fermi surface in systems with broken inversion symmetry. a,**b**, Spin texture due to Rashba (**a**) and linear (**b**) Dresselhaus SOC. **c**, Spin texture resulting from the coexistence of both type of SOC with equal magnitude. The arrows represent the spin orbit field. Figure adapted from Ref. [72]

As in the Rashba case, also the Dresselhaus spin-orbit coupling lock the spin to its momentum and split the spin sub-bands in energy, but with a different spin configuration given by the bulk inversion asymmetry. The resulting spin texture is illustrated in Figure 6.4b. At surfaces and interfaces, the Rashba and Dresselhaus terms coexist, and depending on the symmetry point group of a system and the ratio between Rashba and Dresselhaus SOC, unconventional spin textures can show up (Figure 6.4).

6.5.2.2 The case of chiral crystals

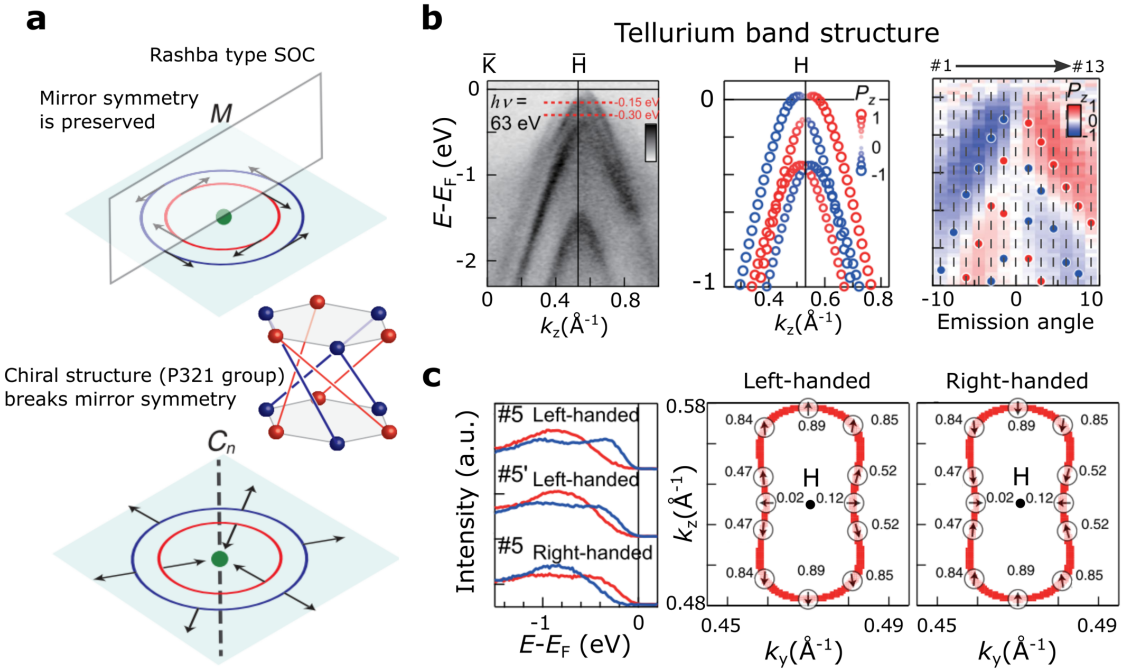

Figure 6.5| Radial spin texture in chiral systems. a, Top: sketch of the helical spin texture in momentum space for a Rashba system; due to the mirror symmetry M, the spin vector circulates around the high-symmetry point (green dot). Bottom: radial spin texture in a chiral crystal; the screw rotational axis C_n imposes a radial configuration in a plane passing through a high-symmetry point. **b**, Spin-split valence bands around the highly symmetric H-point of a chiral tellurium crystal, measured with spin- and angle- resolved photoemission spectroscopy ((S)ARPES) and matched to theoretical calculations. The z direction is defined to be parallel to the chiral axis. **c**, Spin-resolved energy distribution curves (left panel) of left- and right-handed Te crystals measured around the H-point, showing a reversed spin orientation dependent on the handedness. Calculated Fermi surfaces around the H-point for left- and right-handed crystal, respectively (right panels). Figure adapted from Ref. [242–244].

A peculiar case, of special interest for this thesis, is the one of chiral crystals with a helical structure (with point group P321). This class of materials is

characterized by the lack of inversion and mirror symmetry and by the possibility of appearing in two enantiomeric structures, being left- or right-handed. We already discussed that the lack of bulk inversion symmetry and the presence of SOC, results in a band spin-splitting giving rise to two sub bands with opposite spin orientations. However, the additional mirror symmetry breaking, characteristic of chirality, does not allow the spin vectors to be locked in the perpendicular direction to their momentum, thus preventing the appearance of a helical spin texture. Instead, around highly symmetric $\boldsymbol{k}$-points of the Brillouin Zone, where rotational symmetries are preserved, a radial spin texture is imposed (Figure 6.5a). The spin polarization points inwards/outwards in the two spin-split sub bands and reverses depending on the handedness of the crystal.

While a general tight-binding toy model, developed for generic helical systems, predicted such spin-split of the band structure with a radial spin texture [242], a SOC Hamiltonian term for this complex 3D case is non-trivial and complex to derive. Nevertheless, by spin- and angle- resolved photoemission spectroscopy experiments and *ab-initio* calculations, it has been recently confirmed that, the spin texture of a chiral system like Te is radial and dependent on its chirality (see Figure 6.5b,c) [243,244]. In the last chapter, we will see how this can have major implications in terms of electronic transport.

6.5.3 Edelstein Effect

Also called current-induced spin polarization or inverse spin galvanic effect [245], the Edelstein effect was first predicted to occur in 2DEG in the presence of SOC [223], and it consists in the generation of a non-equilibrium spin density by the application of a charge current in nonmagnetic systems. For simplicity and historical reasons, here we will analyze the most studied case, occurring in Rashba systems.

A constant current applied through a system in a certain direction x, it is driven by an electric field $\boldsymbol{E} = E_x\boldsymbol{x}$ that accelerates the electrons in the opposite direction, inducing changes in all k-dependent energy states. According to the Boltzmann equation [246], in a single-band picture, the application of an electric field produces a shift of the Fermi contour in k-space by an amount:

$$\Delta k_x = \frac{e\boldsymbol{E}\tau}{\hbar} = \frac{\boldsymbol{j}_c m_e}{n_s e\hbar}, \tag{6.11}$$

where $\boldsymbol{j}_c$ is the charge carrier density, n_s the sheet carrier density of the 2DEG, and with Δk_x in the opposite direction with respect to the electric field.

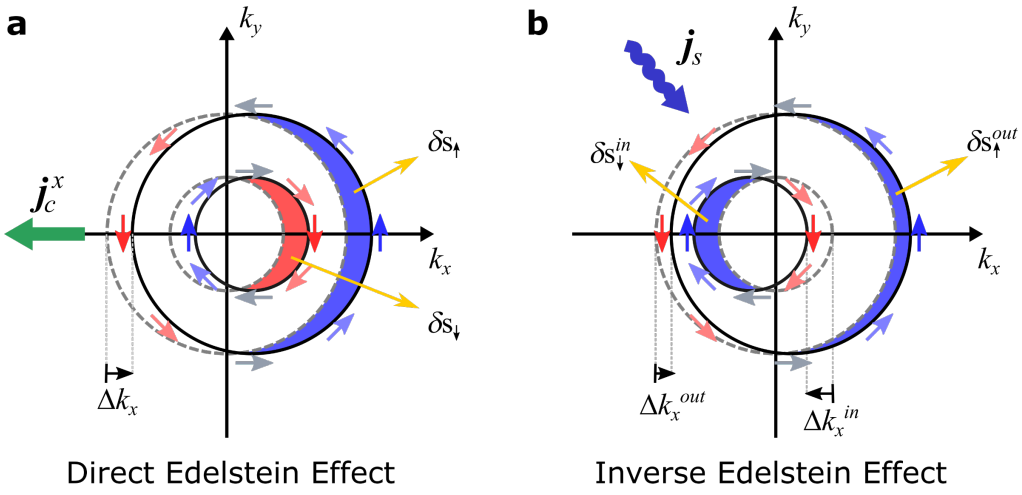

Figure 6.6| Illustration of the spin to charge interconversion in 2D Rashba systems. a, Direct Edelstein effect. In the presence of a charge current applied along $-x$ (electrons flow along x), both split Fermi contours are shifted by the same amount and in the same direction, yielding two uncompensated spin densities, thus a finite spin polarization. **b**, Inverse Edelstein effect. The injection of a steady non-equilibrium spin density with spin oriented along y, induces an uneven displacement of the Fermi circles in opposite directions, resulting in the generation of a finite charge current. Figure adapted from Ref. [234].

As discussed above, in systems with SOC and broken inversion symmetry the electron spins are forced to stay oriented orthogonally to their momentum, as if each momentum state k would "feel" a different effective magnetic field interacting with the spins. In other words, due to this spin-momentum locking, electrons in $\pm k_x(\pm k_y)$ have their spins aligned along $\pm y(\mp x)$. Hence, a shift of the Fermi contours induced by an external electric field leads to an excess of spin density $\delta s_{\uparrow(\downarrow)}$ dependent of the orientation of Δk_x. In the specific case of a Rashba 2DEG (Figure 6.3), two bands are occupied and two Fermi contours, with different radius k_F^{in} and k_F^{out}, are shifted by the same amount Δk_x, yielding two non-equilibrium spin densities $\delta s_\uparrow$ and $\delta s_\downarrow$ (see Figure 6.6a). The coloured areas representative of these two spin densities are proportional to $(k_F^{out}\Delta k_x)$ and $(k_F^{in}\Delta k_x)$, respectively, given that the Rashba constant α_R is small and τ is approximately the same for both contours. Thus, the two resultant spin densities are not equivalent, and they do not cancel each other, leading to a finite spin polarization. This current-induced spin polarization is a type of charge to spin conversion, and it is labelled as *direct Edelstein effect*.

Consistently, if a spin current (polarized along y) is injected in the system, the two Fermi contour will be displaced by Δk_x in opposite directions to compensate the excess spin population (see Figure 6.6b). In this situation, the displacements $(\Delta k^{in}, \Delta k^{out})$ will not be the same for the two Fermi circles, since the radius of the contours are different, so that Δk_x^{total} is non-zero, and a finite charge current is produced. This mechanism represents a spin to charge conversion called *inverse Edelstein effect*.

The Edelstein effect has been observed not only in Rashba interfaces [224,247–249], but also in bulk materials [250] and topological insulators [225,251,252], attracting a lot of interest because of its tunability, efficiency and appearance in low dimensions.

Finally, note that applying the same reasoning, current-induced spin polarization processes can be justified in every system characterized by spin polarized bands, resulting in charge to spin conversion phenomena where the directions of charge currents and the spin orientations are given by the type of spin texture at the Fermi surfaces. Once more, a profound understanding on the role of the structural properties of a material on its physics, is of fundamental importance to engineer the spin to charge interconversion processes that may allow spintronics to reach the next milestone.

6.6 Unidirectional Magnetoresistance

In the previous section, we have seen that, according to the Edelstein effect, in certain nonmagnetic materials a charge current can generate a spin polarization. A simple way to study this charge to spin conversion mechanism and to infer the spin texture of a material is to analyze the so-called unidirectional magnetoresistance (UMR) [253].

In general, a magnetoresistive effect occur when the resistivity of a material is modified by the application of an external magnetic field $\boldsymbol{B}$, giving rise to a magnetoresistance ($MR = (R(\boldsymbol{B}) - R(0))/R(0)$). A typical example is the anisotropic magnetoresistance (AMR) in FMs [254,255], where MR depends on the direction of an in-plane applied field. A characteristic measurement of this effect is done applying a current $\boldsymbol{J}$ in the material, while rotating the external magnetic field $\boldsymbol{B}_{ext}$ (α being the angle between $\boldsymbol{J}$ and $\boldsymbol{B}_{ext}$). In a regular FM, the same resistance state is obtained when α is either at 0° and 180° or at 90° and 270°, meaning that the AMR depends only on the direction of the magnetic field.

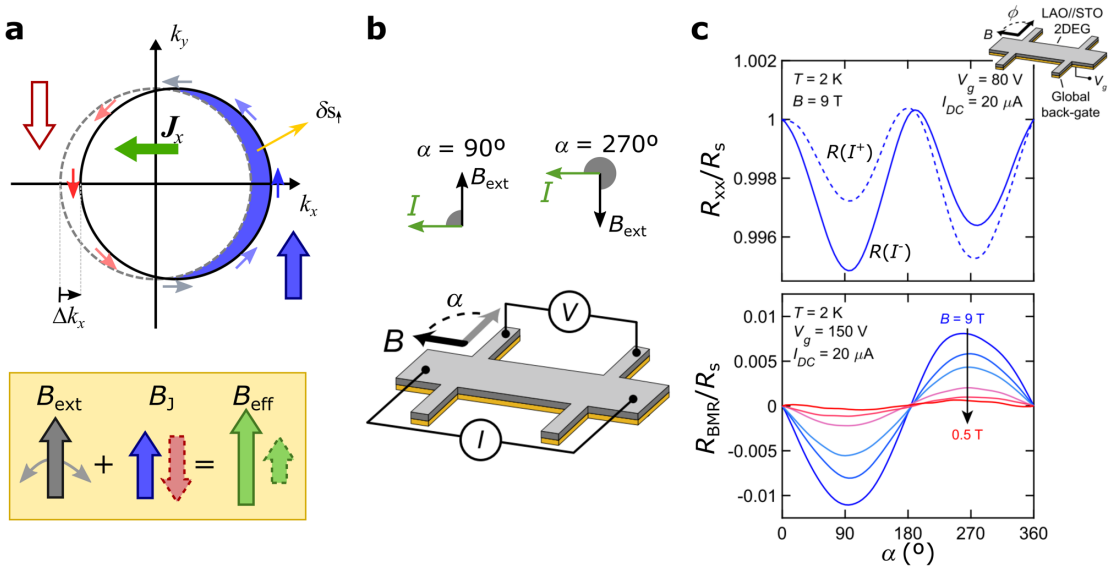

Figure 6.7| Schematic model of UMR and experimental evidence in a Rashba 2DEG. a, The application of a fixed current $\boldsymbol{J}$ along $\pm x$, results in internal field $\boldsymbol{B}_J$ oriented in-plane along $\pm y$ respectively. The effective field $\boldsymbol{B}_{eff}$ experienced by the system, while rotating an external magnetic field $\boldsymbol{B}_{ext}$, is affected by $\boldsymbol{B}_J$, and it leads to a maximum difference in resistance state when the angle between $\boldsymbol{J}$ and $\boldsymbol{B}_{ext}$ is either 90° or 270°. **b**, Schematic of an experiment performed on LAO//STO system. **c**, Experimental results showing the nonreciprocal behavior of the angle dependent resistance with respect to the sign of the current applied (R_{xx} is the longitudinal resistance measured in the Hall bar and R_s the sheet resistance through which the signal is normalized), and the resultant UMR curve (here called BMR due the linear dependence with current and field, $R_{BMR} = R(I^+) - R(I^-)$). Figure adapted from Ref. [256].

However, in a Rashba system, when an AMR-like effect is present [257], the aforementioned equality doesn't hold, and a unidirectional component in the magnetoresistance is observed. As discussed in section 6.5.3, when a charge current $\boldsymbol{J}$ is applied to a Rashba system, electrons moving in the confining electric field can get spin polarized. For the electrons, this is the equivalent of experiencing an effective magnetic field $\boldsymbol{B}_J$ dependent on their momentum k. Naively, one may assume that this static $\boldsymbol{B}_J$ (dependent on the direction of the applied $\boldsymbol{J}$) may interfere with $\boldsymbol{B}_{ext}$ **(see** Figure 6.7a). Consequently, in an experiment like the one discussed for AMR (Figure 6.7b), the effective magnetic field experienced by the material would be different at $\alpha = 90°$ and $\alpha = 270°$, resulting in different resistance states. Repeating the same experiment, with $\boldsymbol{J}$ applied in the opposite direction, and extracting the difference between the two resultant curves, one can obtain the UMR amplitude (Figure 6.7c). From the simple model in Figure 6.7a, one can understand that the

UMR can be used as a powerful probe to map the spin texture of a system, and as a measurement of the charge to spin conversion.

While sometimes it is also called bilinear magnetoresistance (BMR) or even nonreciprocal charge transport, these effects share the same fundamental behavior, and studies on UMR effects have been reported recently in 2DEG [256,258], topological insulators [252], and in other types of Rashba systems [250,259]. Note that, the name BMR comes from the fact that in some these experiments UMR has been observed to show a linear dependence as a function of both current and external magnetic field. Whereas the linear dependence with the current is consistent with the Edelstein mechanism, since increasing the current leads to a larger shift of the Fermi circles in k (thus of the spin polarization and of the $\boldsymbol{B}_J$), the simple model reported above fails to explain the dependence with $\boldsymbol{B}_{ext}$. The magnetic field dependence is more complex and difficult to visualize with an intuitive model. Nevertheless, for the case of 2DEG [256] and topological insulators [260], it has been explained in terms of a purely transport effect involving the spin- and field-dependent scattering of charge carriers at spin-orbit defects.

7 Gate-tunable and Chirality-dependent Edelstein effect in Tellurium nanowires

Chiral materials are the ideal playground for exploring the relation between symmetry, electronic transport and spin dependent phenomena. For instance, chiral organic molecules have been intensively studied to electrically generate spin-polarized currents in the last decade [261–264], but their poor electronic conductivity limits their potential for applications. Conversely, chiral inorganic materials, such as Tellurium, are excellent electrical transport materials but have not been explored to enable the electrical control of spin polarization in devices [42]. Here, we demonstrate the all-electrical generation, manipulation, and detection of spin polarization in chiral single-crystalline Tellurium nanowires. By recording a large (up to 7%) and chirality-dependent unidirectional magnetoresistance, we show that the orientation of the electrically generated spin polarization is determined by the nanowire handedness and uniquely follows the current direction, while its magnitude can be manipulated by an electrostatic gate. The effect is explained in an Edelstein framework that connects the spin texture of Te, to the generated spin density. These results represent a step forward in the understanding of the interplay between structural properties and spin transport phenomena, showing that chiral compounds can be of great interest for a next generation of spintronic devices.

7.1 Tellurium: a prototypical chiral material

As explained in the previous chapter, the lack of symmetries in crystals lead to a number of effects strictly correlated to the electronic properties of the material, including the appearance of spin dependent phenomena. In this regard, chiral materials are the ultimate expression of broken symmetry, lacking inversion and mirror symmetry. Tellurium (Te), is the simplest chiral material that one can think of, since it is composed by helical periodic 1D chains made solely of Te atoms, and kept together by van der Waals forces to form the 3D structure [265,266]. The lack of inversion and mirror symmetries, brought by the chiral structure, and the presence of strong SOC, due to the heavy Te

atoms, make this system an ideal candidate to study unconventional and chirality related charge to spin conversion phenomena (see Chapter 6). So far, signs of current-induced spin polarization have been reported only in impractical bulk Te crystals, through optical [267,268] and nuclear magnetic resonance (NMR) [269,270] measurements. However, it has been shown that Te can be synthesized [271] in nanowires (NWs) or flakes with excellent electronic conductivity [42,272]. In the following sections, a study on the structural and magneto transport properties of such NWs will be presented.

7.1.1 Band structure and spin texture of Te

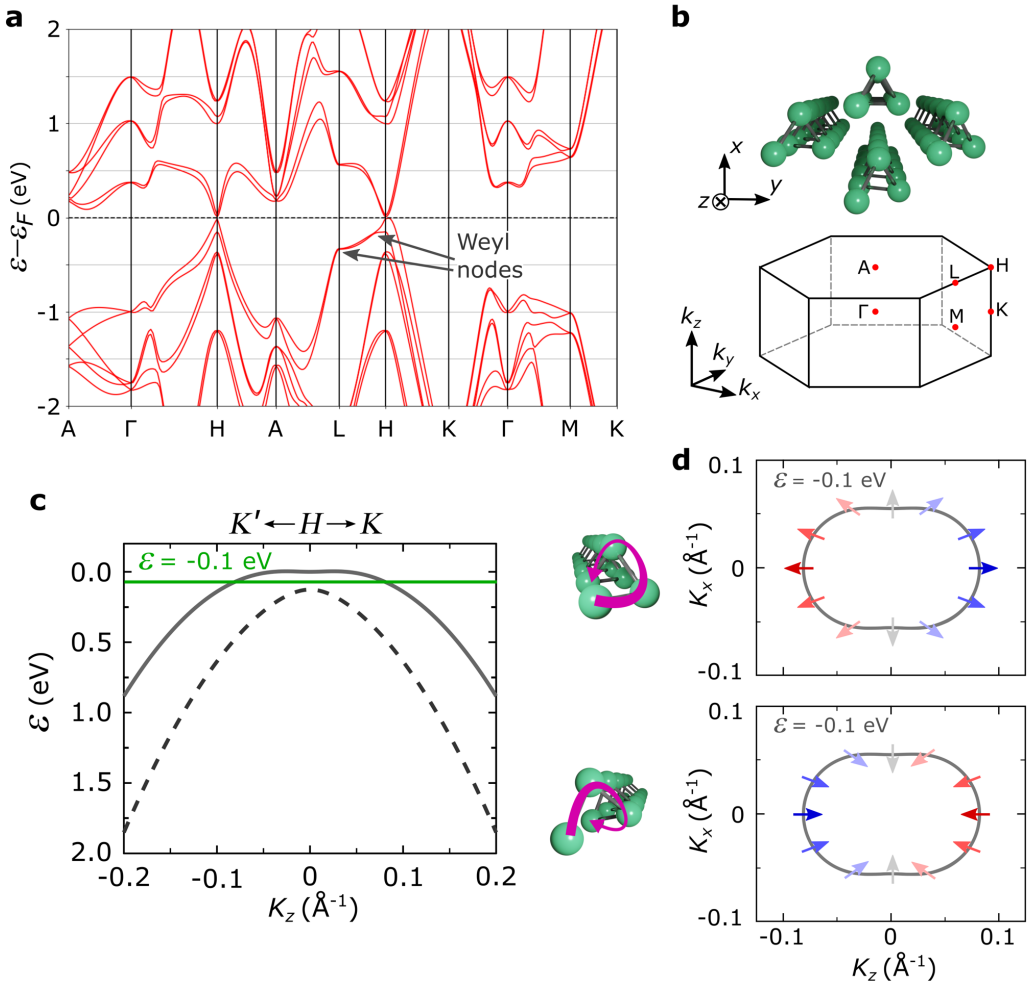

Figure 7.1|Electronic band structure and spin texture of Te. a, Extended band structure of Te obtained by ab initio methods. Two Weyl points are indicated. **b**, Sketch of the crystal structure and of the Brillouin zone. **c**, Zoom of the Te band structure (valence bands) around the H point, obtained from an effective model Hamiltonian [268] with SOC included. Here the z-coordinate is set to be in the same direction of the c-chiral axis. **d**, Iso-energy contours of right- and left-handed Te at $\varepsilon = -0.1$ eV, showing the characteristic radial spin texture. The red/blue colors illustrate the $(+/-)$ z-component of the expectation value of the spin operator.

The band structure of Te has been intensively studied using ab-initio methods [243,244,273–277]. Te is a semiconductor with a small band gap separating the conduction and valence bands of approximately 380 meV [273]. In Figure 7.1a, the extended band structure of Te, calculated by collaborators I. V. Maznichenko and S. Ostanin, shows how the lack inversion symmetry, deriving from the chiral nature of Te, in combination with a high SOC, result in a complex band structure characterized by non-degenerate spin bands at highly symmetric k-points (see Figure 7.1b for a sketch of the Brillouin zone). It is well established that Te is getting self p-doped by the presence of vacancies in the crystal structures [273,278–280], which brings additional holes contributing to the transport properties. For this reason, the Fermi level lies within the band gap in almost the whole Brillouin zone, besides in the vicinity of the H point where, depending on the doping level, the highest valence band might intersect the Fermi level. Moreover, one can observe that at approximately 200 meV and 350 meV below the Fermi level, Weyl points occur along the LH direction (see Figure 7.1a), which is agreement with the band structure calculations in [273].

Since only the states around the H point are near the Fermi level, we use an effective model Hamiltonian proposed in Ref. [268] to remodel the band structure features which are mostly relevant for the electronic transport:

$$H(\mathbf{k}) = -\Delta - \mathrm{A}k_z^2 - \mathrm{B}\sqrt{k_x^2 + k_y^2} + \chi \left[\frac{\Delta}{\sqrt{k_x^2 + k_y^2}} (k_x \hat{\sigma}_x + k_y \hat{\sigma}_y) + \beta k_z \hat{\sigma}_z \right] \tag{7.1}$$

Here, k_z is along the H-K direction and the Pauli spin vector $\hat{\sigma}$ represents the spin degree of freedom. The parameters used were proposed in Ref. [268], $\Delta = 63$ meV , $\mathrm{A} = 3.64 \times 10^{-19}$ eV m^2 , $\mathrm{B} = 3.26 \times 10^{-19}$ eV m^2 , $\beta = 2.4 \times 10^{-10}$ eV m. χ corresponds to the chirality with $\chi = 1$ (left-handed) and $\chi = -1$ (right-handed), respectively. The corresponding effective band structure is shown in Figure 7.1c, and it is composed by two non-degenerate branches of the valence band, separated by 126 meV. The iso-energy contour corresponding to a cut of the valence band at $\varepsilon = 0.1$ eV below the band edge is characterized by a radial spin texture with spins pointing inward/outward in right-/left-handed crystals, as pictured in Figure 7.1d, and as confirmed by recent spectroscopic experiments (see Chapter 6). This is analogous to the spin momentum locking observed in bulk Rashba systems, but with a chirality-de-

pendent radial spin texture (caused by the additional breaking of mirror symmetry), instead of the conventional helical configuration. The effective Hamiltonian model was adapted by Dr. A. Johansson and Professor I. Mertig.

7.1.2 Tellurium nanowires

A hydrothermal process in the presence of a reducing agent was employed to grow single crystalline Te NWs (see Appendix A). The produced NWs are displayed in Figure 7.2a, and they have typical dimensions of 1 - 50 μm in length and 50 nm - 2 μm in width. Figure 7.2b illustrates a 3D sketch of Te 1D chains arranged in their characteristic helical structure that twists around the chiral *c*-axis. Van der Waals forces keep together adjacent atomic chains, which possess the same helicity, providing a defined chirality to the Te crystal structure. From a scanning transmission electron microscopy (STEM) image (Figure 7.2c) of a NW cross section perpendicular to the *c*-axis, it is possible to appreciate the quality of our single crystal NWs. The individual chains forming the crystal appear as triangles stemming from the projection of superimposed Te atoms. This atomic arrangement indicates that the long axis of the Te NWs is oriented along the chain direction (*c*-axis).

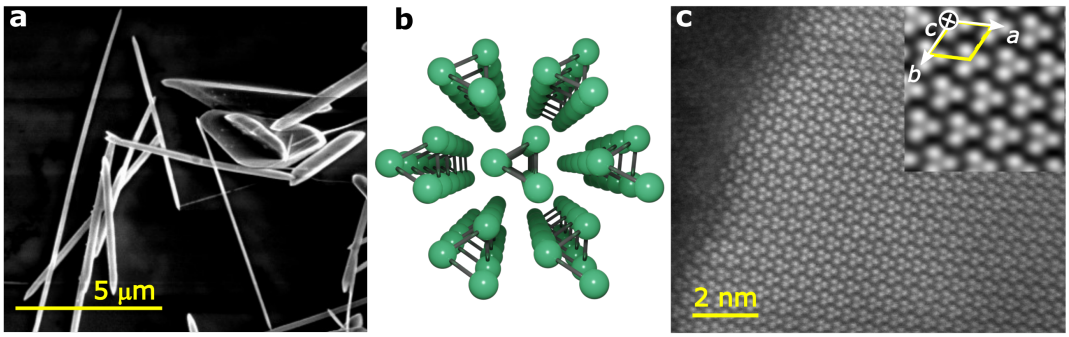

Figure 7.2| Tellurium nanowires. a, SEM image of Te NWs drop-casted on a TEM grid. **b**, 3D sketch of the crystal structure of a Te NW. **c**, STEM image of a Te lamella obtained cutting the NW perpendicularly to the *c*-axis.

As already mentioned, chiral materials can exist in two enantiomeric structures, namely right- and left-handed. STEM was also employed to verify that this was true for our NWs and moreover to identify the two enantiomorphic chiral space groups, $P3_121$ and $P3_221$. While the image in Figure 7.2c shows the high quality of the NW, it cannot be used to identify its chirality. Due to the projection nature of STEM images, neither a single image taken in along another direction could help for this purpose. However, it is possible to unambiguously distinguish between right- and left-handed crystals through a comparison between the atomic arrangement in different crystalline planes

[265,266]. In particular, recording STEM images of different NWs, along proper zone axes, in a tilt series is sufficient to determine the handedness of a chiral crystal by observing the chirality-dependent patterns appearing due to atoms projections. In Figure 7.3, the STEM images of two NWs with opposite handedness match with the models for the space groups $P3_121$ and $P3_221$ (for more details see Appendix B).

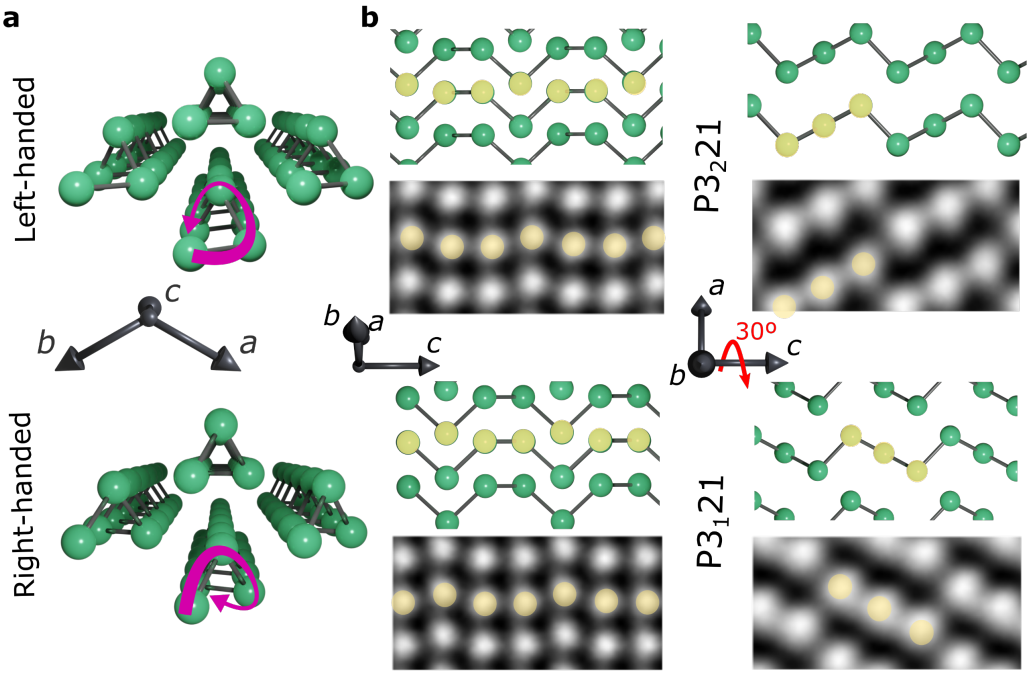

Figure 7.3| Handedness identification via STEM. a, 3D sketches of the right- and left-handed crystal structure of trigonal Te. **d,** Crystal structure sketch and STEM image of two Te NWs with opposite chirality, imaged at [–110] orientation and after a 30° rotation around the *c*-axis ([010]).

7.2 Magnetoelectrical characterization

For the electrical characterization, Te NWs were transferred onto Si/SiO_2 substrates using a Langmuir-Schaefer approach. Individual NWs were subsequently selected through an optical microscope and contacted with Pt contacts defined by standard EBL lithography (see Chapter 2). Figure 7.4a shows the optical image of a contacted Te NW, with a sketch of the four-probe configuration used for the transport experiments. We redefine a cartesian coordinate system to describe the directions of currents and magnetic fields applied, where z is in the same direction as the c crystallographic axis and x (y) are orthogonal to z and directed in (out) of the device plane (see Appendix B for more details).

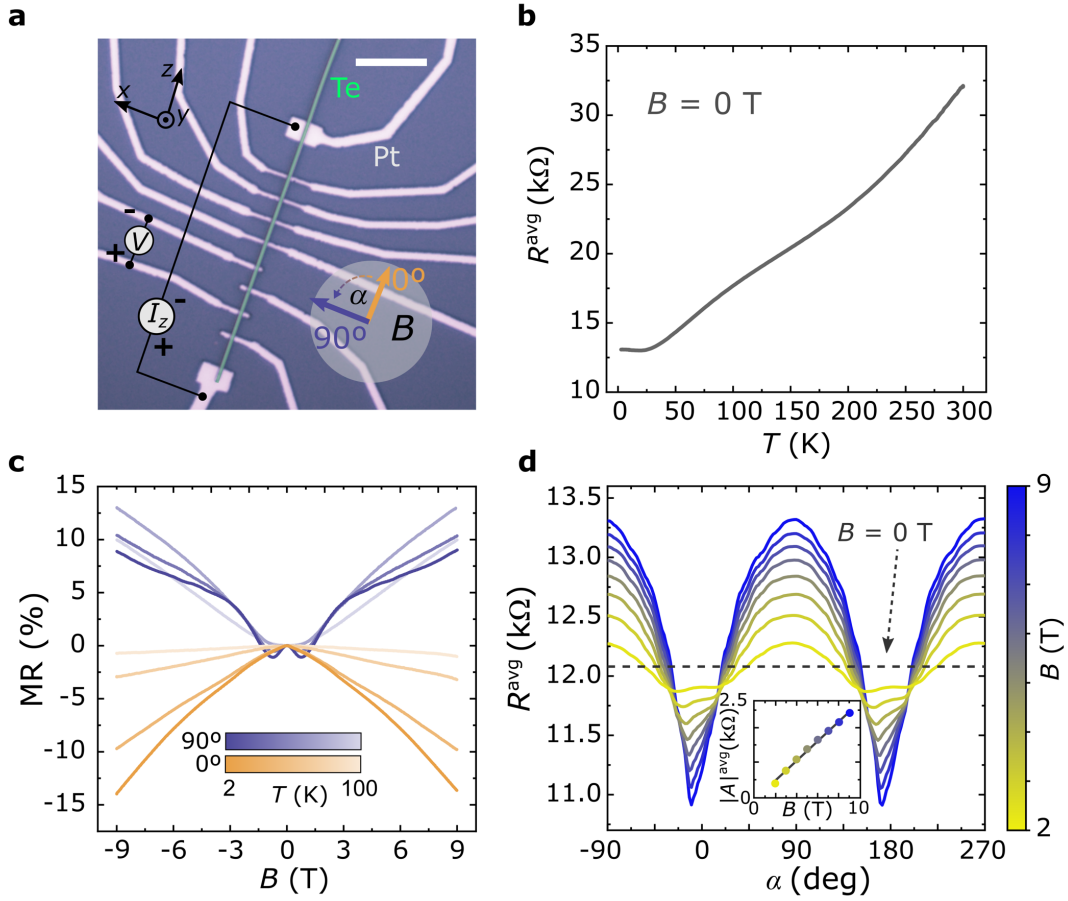

Figure 7.4| Magnetoelectrical characterization of a Te NW. a, Optical image of a typical Te NW contacted with Pt contacts (the scale bar corresponds to 10 μm), illustrating the scheme of the four-probe measurement configuration. The angle α defining the orientation between the magnetic field and the NW is also drawn. **b**, Temperature dependence of the four-probe resistance $R^{avg} = [R(+I_z) + R(-I_z)]/2$ at $B = 0$ T. **c**, Te Magnetoresistance ($MR = [R^{avg}(B) - R^{avg}(0)]/R^{avg}(0)$) measured along ($\alpha = 0°$) and transversally ($\alpha = 90°$) to the chiral z-axis at different temperatures (T = 2, 10, 50 and 100 K). **d**, Angular dependence of R^{avg} at different magnetic fields and $T = 10$ K. The dashed line indicates the resistance at zero field. Small shifts in angle are caused by misalignments introduced when mounting the sample on the chip carrier. Inset: the variation of the angular-dependent MR amplitude ($|A^{avg}| = |R^{avg}(90°) - R^{avg}(0°)|$) with the field applied.

Figure 7.4b-d display the magnetotransport characterization of a typical Te NW. For these measurements, we plot the average resistance $R^{avg} = [R(+I_z) + R(-I_z)]/2$, where $R(+I_z)$ and $R(-I_z)$ are the resistances measured with a d.c. positive and negative current, respectively (see Chapter 2 for details). This way, we obtain the equivalent of the 1st harmonic response in a.c. transport measurements, excluding current-dependent contributions to the resistance [252]. The temperature (T) dependence of the four-probe resistance shows a monotonic decrease of R with decreasing T (Figure 7.4b), indicating

that the Te NWs are degenerately doped. From the transfer characteristics, we observed that the Te NWs are hole-doped, with a field effect mobility that ranges from ~ 500 cm^2/Vs at 300 K to ~ 2500 cm^2/Vs at $T = 10$ K (see Appendix C). This is in agreement with previous reports highlighting that Te vacancies cause hole-doping [273]. As a consequence of this self-doping, the resistivity at room temperature is $\rho = 0.02\ \Omega$ cm, one order of magnitude lower than the value reported for undoped bulk crystals [281].

Figure 7.4c displays the magnetoresistance curves for in-plane magnetic fields B parallel (0°) or perpendicular (90°) to the applied current I_z, at T ranging from 2 to 100 K. When B is parallel to I_z (orange curves in Figure 7.4c), we observe a monotonical decrease of the resistance when increasing the magnetic field. The negative longitudinal magnetoresistance (NLMR), which is unusual for non-magnetic materials, in our Te NWs reaches a maximum value of 15% at $T = 2$ K and $B = 9$ T. This peculiar behavior was already reported for bulk Te [273], and it has been attributed to the presence of Weyl Fermions contributing to the transport, although other effects may also be responsible for such MR [282]. In particular, the trend of our NLMR is different from the one reported in Ref. [273], and we were not able to fit the MR curves with the same functions used to justify the presence of chiral anomaly. This discrepancy does not necessarily rule out the possibly of the presence of a Weyl node, that according to our calculations, should be located at about −200 meV from the band edge, but it does not provide enough evidence to support a claim on the role of this Weyl node on the magnetotransport.

In the case of B perpendicular to I_z (purple curves in Figure 7.4c), the magnetoresistance at low T changes from negative to positive when increasing the field, showing a relative maximum at $B = 0$ T and two minima around $B = \pm\ 1$ T, followed by a change of slope at around $B = 3$ T. The minima slowly flatten out with increasing T, up to $T = 50\ K$, where they disappear. Competing MRs that we were not able to disentangle may contribute to the change of tendency in the transversal MR, that pass from negative at lower fields to positive at higher fields. To avoid further complications, we focus our attention at $B > 3$ T, where the transversal MR is positive and does not reveal other signs of competing effects.

The angular dependence of the magnetoresistance at $T = 10$ K as a function of different magnetic fields is displayed in Figure 7.4d. Here and in the following experiments, we set the angle between the magnetic field and the NWs to be $\alpha = 90°$, when the field is orthogonal to the NW's z-axis and to the current applied, and at $\alpha = 0°$, when the field is parallel to the NW's z-axis and to the

positive current direction (Figure 7.4a). The curves are characterized by sharp minima at around $\alpha = 0°$ and $\alpha = 180°$, i.e., for $B \parallel I_z$, and maxima at around $\alpha = \pm 90°$, for $B \perp I_z$. Note that, for this study, focusing our attention on the regime at $B > 3$ T means that for every field, the resistance measured at $\pm 90°$ ($0°$ and $180°$) is higher (lower) than the resistance measured at $B = 0$ T, which is depicted as a dashed line. The appearance of the maxima and minima is a direct consequence of the MR curves shown in Figure 7.4c, which transit from positive to negative when the field is rotated in the plane of the sample. Additionally, at $T = 10$ K and for $B > 3$ T, the dependence of the resistance on the field is almost linear for both the transverse and the longitudinal MR, but with an opposite slope (Figure 7.4c). Consequently, the difference between the maximum and the minimum value in the angular dependence ($|A^{\mathrm{avg}}|$) increases linearly with the applied field (see inset in Figure 7.4d).

7.3 Chirality dependent Unidirectional Magnetoresistance (UMR)

We now focus on the detection of the chirality-dependent current-induced spin polarization in the Te NWs. Figure 7.5a,b displays a simplified sketch of the radial spin texture of Te for left- and right-handed crystals. As explained in Chapter 6, and according to the Edelstein mechanism, an electric field applied along the z-direction generates a current density j_z and causes a redistribution of states along the k_z direction, which is depicted as a Δk_z shift of the Fermi contour. Due to the radial spin texture of Te, Δk_z induces a homogeneous spin density that is parallel or antiparallel to j_z, depending on the chirality of the NWs. Unlike Rashba systems, the electrical current in Te is expected to acquire a net spin polarization oriented along j_z, which is a peculiar manifestation of the Te symmetries. The current-induced spin polarization can be detected in magnetotransport measurements since it introduces a dependence of the resistance on the mutual orientation of current and magnetic field. This effect, also known as UMR or non-reciprocal charge transport, allows to map the spin texture of a material (see Chapter 6 for details). Using the configurations of current and magnetic field illustrated in the insets of Figure 7.5c,d, we analyzed the angle-dependent magnetoresistance of the NWs, measured for opposite current directions along z ($\pm I_z$). By changing the current direction and varying the angle α between the NWs at a fixed magnetic field, the mutual orientation of I_z and B is reversed. A parallel alignment between field and current is obtained at $0°$ for $+I_z$ and at $180°$ for $-I_z$.

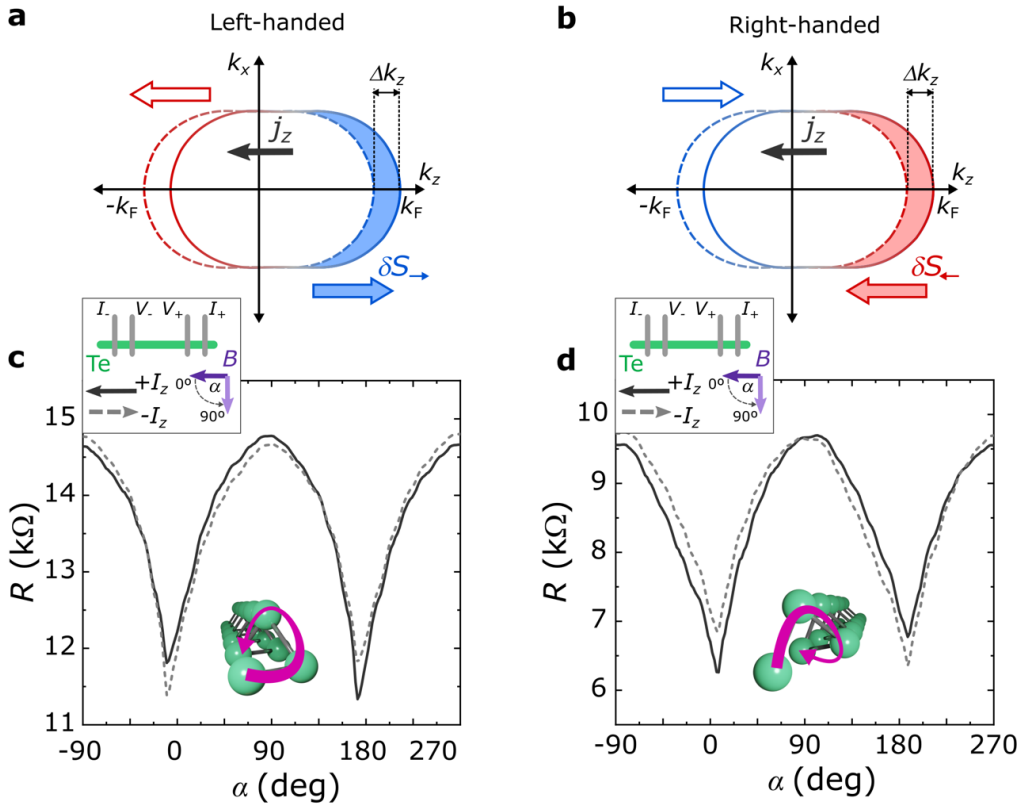

Figure 7.5| Chirality dependent Edelstein effect detected via UMR. a,**b**, Sketch representing the Edelstein mechanism responsible for the UMR. The shift in k_z of the Fermi contours translates in the formation of spin densities oriented in opposite direction, due to the chirality-dependent spin texture. Empty arrows mean depletion of states, filled arrows mean higher occupation of states. **c**,**d** Angular dependences of the magnetoresistance measured at 9 T and 10 K for two Te NWs with opposites handedness (confirmed by STEM analysis). Solid and dashed lines indicate the signals obtained from opposite current directions ($\pm I_z = \pm 1$ μA in **c**, and $\pm I_z = \pm 0.7$ μA in **d**). In inset: schematic of the measurement configuration defining the angle of the magnetic field with respect to the current directions.

Figure 7.5c,d show the resistance measured for $+I_z$ and $-I_z$ as a function of the angle α between the NW and a magnetic field ($B = 9$ T), for the two NWs with opposite chirality (the handedness identification reported in Figure 7.3 was obtained from cross-sections of these two same devices). For both the right- and left-handed NW, we find a strong dependence of the resistance on the relative alignment between I_z and B, which is the hallmark of UMR, and which demonstrates the presence of a net spin polarization in the Te NWs induced by the current. In particular, the left-handed NW is characterized by a significantly higher (lower) resistance when the current is parallel (antiparallel) to the external magnetic field (Figure 7.5c). This non-reciprocal effect can also be observed as a shift in the MR traces measured for opposite current

directions (see Appendix D). Conversely, the right-handed NW displays lower (higher) resistance for I_z parallel (antiparallel) to B (Figure 7.5d), indicating that the UMR of Te is mirrored in NWs with opposite chirality. Hence, the current induced spin polarization is reversed for opposite NW handedness.

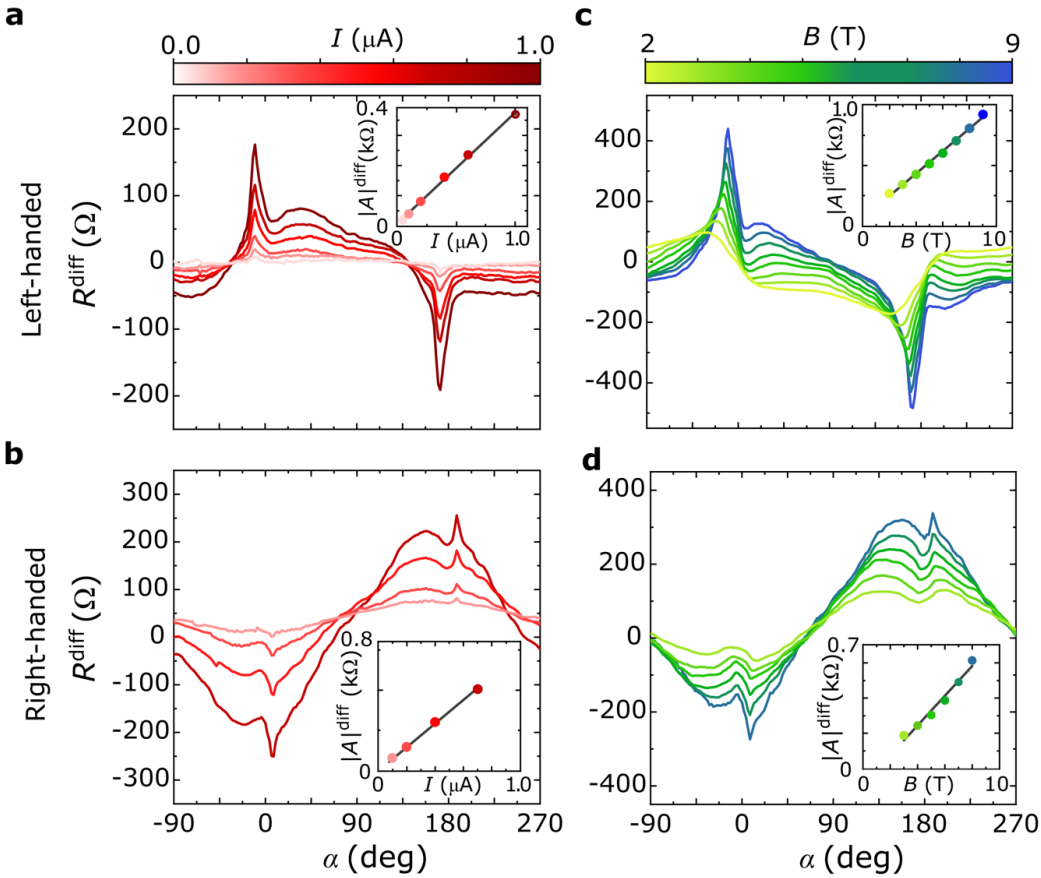

Figure 7.6| UMR dependence on current and magnetic field. a-d, Angle-dependent UMR as a function of the applied current (**a**,**b**, $B = 9$ T); and as function of the magnetic fields (**c**, $\pm I_z = \pm 5$ μA and **d**, $\pm I_z = \pm 1$ μA). The signal $R^{\text{diff}} = [R(+I_z) - R(-I_z)]/2$ shows a UMR with specular features between left- (**a**,**c**) and right- (**b**,**d**) handed NWs. In the insets, the amplitude $|A|^{\text{diff}} = |R(0°) - R(180°)|$ is represented as a function of magnetic field and current, presenting in both cases a linear behaviour.

To analyze these data, we calculate the half difference between the resistance measured applying $+I_z$ and $-I_z$ ($R^{\text{diff}} = [R(+I_z) - R(-I_z)]/2$), obtaining the equivalent of the 2$^{\text{nd}}$ harmonic signal in a.c. transport measurements [252], which provides for a direct signature of UMR. In Figure 7.6, the angular dependence $R^{\text{diff}}(\alpha)$ presents sharp peaks for collinear current and magnetic field (at 0° and 180°), corresponding to the asymmetries in Figure 7.5c,d. This indicates that, in agreement with the Edelstein mechanism (Figure

7.5a,b), the spin polarization is oriented along the direction of the current, parallel to the chiral axis z.

The deviation of $R^{\text{diff}}(\alpha)$ from the sin dependence typically observed for UMR signals can be explained by analysing the presence of additional UMR components not related to the chirality and the dependence of UMR on the peculiar MR recorded in our Te NWs (see Appendix D). Moreover, the trend of the magnetoresponse measured in right- and left-handed NWs is specular since it is directly related to the chirality of the NWs. In this regard, the orientation of spin polarization is determined by the Te handedness, in a similar way the spin polarization in a ferromagnetic metal is determined by its magnetization. By matching the transport measurements with the STEM analysis in Figure 7.3, we can distinguish the NWs handedness through their magnetotransport behaviour.

Figure 7.6a,c show the variation of $R^{\text{diff}}(\alpha)$ measured at $B = 9$ T and different current I_z. A larger magnetoresponse is measured at higher currents, with the signal amplitude $|A|^{\text{diff}} = |R(0°)–R(180°)|$ increasing linearly with I (see insets). This dependence can be understood considering that the spin density generated by the Edelstein effect increases linearly with the displacement Δk_z induced by the current. According to the model in Figure 7.5, a higher current induces a larger spin density, resulting in more spins coupling to the magnetic field (see Chapter 6 for more details).

Figure 7.6b,d display $R^{\text{diff}}(\alpha)$ measured for fixed current and different magnetic fields. Even in this case, we observe a linear increase of $|A|^{\text{diff}}$ with B, which indicates that the UMR recorded in our Te NWs possesses a bilinear response to current and magnetic field. This bilinearity, which has been observed in spin-momentum locked states in Rashba systems [256] and in TIs [252], cannot be simply explained by the model presented above, but it has been explained for these systems only in terms B dependent relaxation processes at scalar and spin-orbit defects, respectively [256,260].

Besides the fundamental connection between the chirality of Te and its magnetotransport, one should note that the UMR amplitude in our NWs is very substantial. In the case of the NW displayed in Figure 7.6a,b, the maximum $|A|^{\text{diff}}$ measured at 9 T and 5 μA amounts to 800 Ω, which corresponds to a 7% variation with respect to the current-averaged resistance measured at the same field and at the same angle, $R^{\text{avg}}(0°,\ 9\text{T}) = 10.8$ kΩ. To the best of our knowledge, in previous reports of UMR, the relative variation in resistance was always $< 1\%$ (Ref. [250,252,256,258,259]). To further compare our results with previous works, we use the figure of merit η defined in Ref. [259], as $\eta =$

$R_{\mathrm{UMR}}/(R_0 jB)$, where in our case due to the different symmetries of Te, we use $|A|^{\mathrm{diff}}/2$ as R_{UMR} and $R(B = 0\ \mathrm{T})$ as R_0, while j is the current density ($j \sim 10^7\ \mathrm{A/m^2}$, see Appendix B) and B the magnetic field applied. As a result, we obtained an $\eta \sim 5 \times 10^{-6}\ \mathrm{cm^2/(AT)}$, which is one order of magnitude larger than the highest value reported for Ge(111) at 15 K ($\eta \sim 4.2 \times 10^{-7}\ \mathrm{cm^2/(AT)}$) in ref. [259] and at least three orders of magnitude larger than what observed in $SrTiO_3$ (ref. [258]), Bi_2Se_3 (ref. [252]) and α-GeTe (ref. [250]). The large UMR magnitude can be explained by the strong Edelstein effect, as detailed below.

7.4 Electrical modulation of UMR

Finally, we focus on the control of the UMR by a gate voltage (V_{G}), which shifts in energy the Fermi level (ε_{F}) of the Te NWs, leading to the tuning of the Edelstein effect. In Figure 7.7a,b, the magnetoresponse evolution is displayed under changes of carrier density, driven by V_{G} modulation. To account for the variation of resistance with the gate, we normalize $R^{\mathrm{diff}}(\alpha)$ measured at different V_{G} with respect to the value $R^{\mathrm{avg}}(90°)$. For negative V_{G}, i.e., lowering the Fermi level and increasing the hole concentration, the magnetoresponse trend is relatively flat except for the two prominent features at $\alpha = 0°$ and $\alpha = 180°$, indicating that the electrical current induces a significant spin polarization only in the z-direction. Increasing V_{G}, i.e., decreasing the hole concentration and bringing the Fermi level closer to the band gap, we observe an increase in the amplitude of the UMR (up to a factor of 6, see Figure 7.7c) and the appearance of shoulders close to the peaks at $\alpha = 0°$ and $\alpha = 180°$. Similar shoulders were observed for $V_G = 0$ V in some NWs, including those shown in Figure 7.6b,d. Their relative intensity was found to change from sample to sample (see Appendix E), probably due to the slightly different doping in different NWs.

The increase of the magnetoresponse at positive V_{G} can be correlated with the Te band structure. Looking at the band structure at different energies, a change of the Fermi contour in k-space is expected to cause a variation of the Edelstein effect efficiency [283] and, consequently, a variation of the magnetoresponse. In Figure 7.7c,d, we compare the gate dependence of the UMR amplitude, $|A^{\mathrm{norm}}| = [R^{\mathrm{diff}}(0°) – R^{\mathrm{diff}}(180°)]/R^{\mathrm{avg}}(90°)$, with the calculated spins per unit cell (S_z), generated by the Edelstein effect at different ε_{F} and a constant charge current density of $10^7\ \mathrm{A/m^2}$ (see Appendix F).

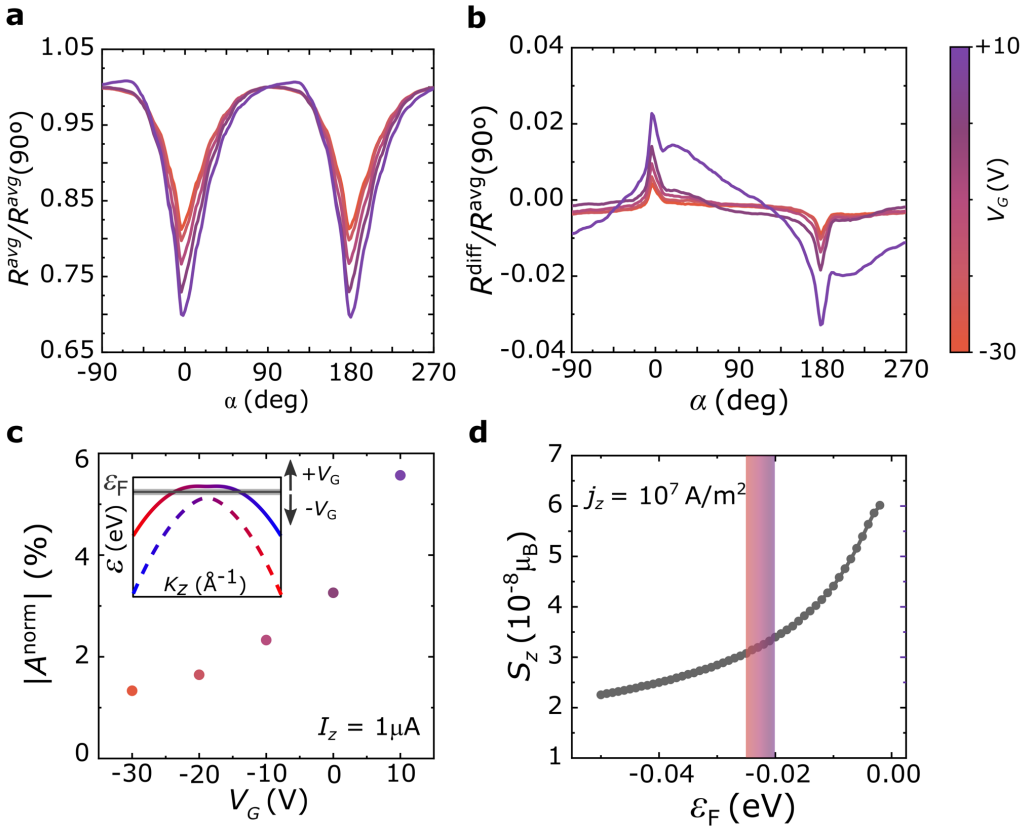

Figure 7.7| Electrical modulation of UMR and comparison with theory. **a**,**b**, Normalized **a**, R^{avg} and **b**, R^{diff} angular dependences measured at $B = 9$ T, $T = 10$ K, and $\pm I_z = \pm 1$ μA, for a left-handed Te NW applying different gate voltages V_{G}. **c**, Gate voltage dependence of the normalized signals' amplitude $|A^{\mathrm{norm}}| = [R^{\mathrm{diff}}(0°) - R^{\mathrm{diff}}(180°)]/R^{\mathrm{avg}}(90°)$, in inset is shown the shift of ε_{F} induced by the gate with respect to the Te band structure (the colors display the spins projection to the z-axis). **d**, Spin per unit cell (S_z) induced by a current density $j_z = 10^7$ A/m^2 through the Edelstein effect for different Fermi energy positions. The zero energy corresponds approximately to the valence band edge, and the highlighted region represents the energy range scanned with applied gate voltages.

In order to compare experiments and calculations, we measured the carrier density of a Te NW through ordinary Hall measurements to estimate the position of ε_{F} in the band structure illustrated in Figure 7.1c. We measured the Hall voltage (V_{H}) created by the injected current I_z in the presence of an out-of-plane magnetic field B_y (Figure 7.8a,b). The carrier density p was obtained from the following relation:

$$p = \frac{B_y}{etR_{\mathrm{H}}}\,, \tag{7.2}$$

where e is the electron charge, t is the thickness of the NW, $R_{\mathrm{H}} = V_{\mathrm{H}}/I_z$, and B_y is the out of plane magnetic field. Therefore, from the slope of the R_{H}

versus B_y curve (inset in Figure 7.8b), the carrier density in the Te NWs is determined. The extracted hole density was $p = 7.4 \times 10^{17}$ cm^{-3} at $V_G = 0$ V and it could be varied in the range $\sim 7 - 8 \times 10^{17}$ cm^{-3} using the back-gate voltage. Interestingly, the rather small modulation in p induces significant changes on the recorded UMR signals, highlighting that it is possible to finely tune the Edelstein effect in Te by acting on its band structure through standard electrostatic gating.

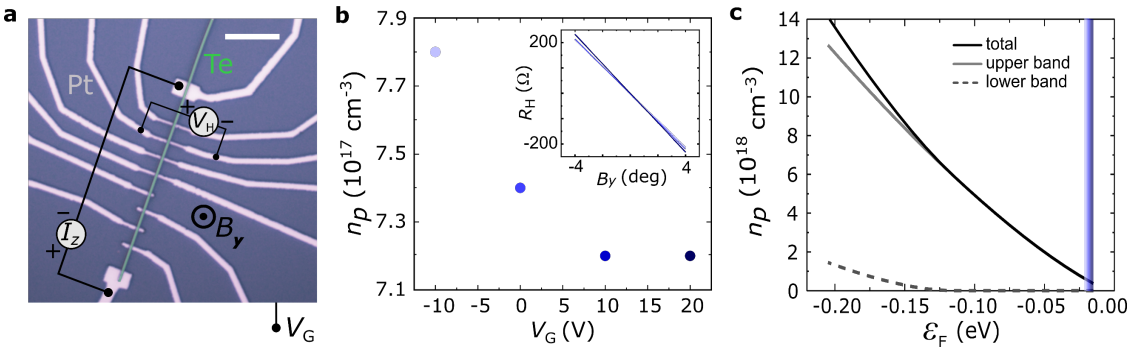

Figure 7.8| Relation between carrier density and band occupancy (D3). **a**, Optical image of a Te NW contacted with Pt electrodes (the scale bar corresponds to 10 μm), illustrating the Hall measurement configuration. **b**, Carrier density extracted from the Hall measurements at different applied gate voltage and at $T = 10$ K. The inset shows the four Hall traces measured at different V_G from which we extracted the carrier densities plotted in the main panel. **c**, Carrier density as function of the Fermi energy position. The grey lines indicate the occupancy of the two valence bands below the gap and their contribution to the total carrier density. The zero energy corresponds to the upper valence band edge, and the highlighted zone represents the energy range accessible with the applied gate voltage.

Our calculations on the charge carrier density reveal that the extracted p corresponds to an ε_F approximately 20 meV below the band edge, which can be tuned in a 5 meV energy window by gating. Figure 7.7d shows that S_z, which is associated to the efficiency of the Edelstein effect creating the spin polarization, increases when ε_F is moved towards the valence band edge, in good agreement with the increase of $|A^{\text{norm}}|$ with V_G displayed in Figure 7.7c. Moreover, we highlight that the calculated ε_F position implies a single band occupancy, since the band which lies closest in energy is populated at energies 130 meV below the valence band edge (see Figure 7.8c). This situation is ideal to maximize the Edelstein effect and thus the UMR, since the occupation of the lower band, with opposite radial spin texture, would partially compensate the induced spin density (see Appendix F for more details on the calculations).

7.5 Conclusions

In conclusion, we demonstrated all-electrical generation, manipulation and detection of chirality dependent spin polarization in single crystalline Te NWs. The spin polarization from chiral origin gives rise to a UMR that is one-to-several orders of magnitude larger than the reported in other non-chiral systems. The UMR is also tunable with electrical gating, providing us with an extra knob for controlling the spin polarization. These effects are induced by an Edelstein effect emerging from the Te radial spin texture. Unlike conventional Rashba systems, and similarly to the CISS observed in organic molecules, the induced spin polarization is oriented along the current direction. We think that our description this phenomenon on the basis of the Edelstein effect might be extended to other chiral systems characterized by translational symmetry. Our results put on a firm ground the fundamental interplay between structural chirality and electron spin in inorganic chiral Te NWs, enabling the design of unconventional all-electrical spintronic devices in which the spin polarization is not determined by the direction of a magnetization, but by the handedness of the crystal.

7.6 Appendices

A. Chemical Synthesis of Te NWs

The synthesis of Te NWs was carried on by Dr. Beatriz Martín-García, and it consists of a high-temperature reduction of a tellurium oxide in presence of hydrazine (N_2H_4) in a basic aqueous medium [42,271,272,284]. We followed the hydrothermal growth recipes proposed in literature [42,272]. Na_2TeO_3 (104 mg) and polyvinylpyrrolidone (average Mw 360,000 – PVP360, 547.9 mg) were mixed in 33 mL of MilliQ® water by magnetic stirring up to achieve a clear solution at room temperature. Then, NH_4OH solution (3.65 mL, 25%w in water) and hydrazine hydrate (1.94 mL, 80%, w/w%) were added while stirring. The mixture is transferred to an autoclave that was sealed and heated at 180°C for 23 h. The resulting material was washed by successive centrifuge-assisted precipitation (5000 rpm – 5 min) and redispersion with MilliQ® water (10 steps of 4 mL water each). At this stage, it is still not possible to selectively produce one or the other enantiomer and the distribution of left- and right-handed NWs is random.

B. Additional crystallographic analysis

From the seven devices fabricated and analysed (D1-D7), two of them, showing opposite magneto responses, were sectioned by FIB for STEM chirality characterisation. Two lamellae were prepared from every device: one perpendicular to the wire at the electrode area to validate the quality of electrical contact, and one along the wire for measuring the chirality (see Figure 7.9a). Helios 600 DualBeam™ (ThermoFisher, USA) was used for lamellae preparation and SEM imaging, TitanG2 60-300 operated at 300kV without STEM corrector was used for STEM imaging. From Figure 7.9b, it is possible, not only to appreciate the quality of the contacts and of the crystal, but also to determine the NW's area (A) and thus the current density (j_z) for a given current (I_z), $j_z = I_z/A$. For chirality determination samples were imaged in either of <010> zones and then tilted ±30° resulting in mirrored images. The handedness was determined by comparison to the atomic models of the known chirality $P3_121$ and $P3_221$. The absence of the mirror plane between the sample and digital image has been ruled out by imaging alphanumeric grid. The STEM analysis was performed by Professor Andrey Chuvilin, after the samples were already measured electrically.

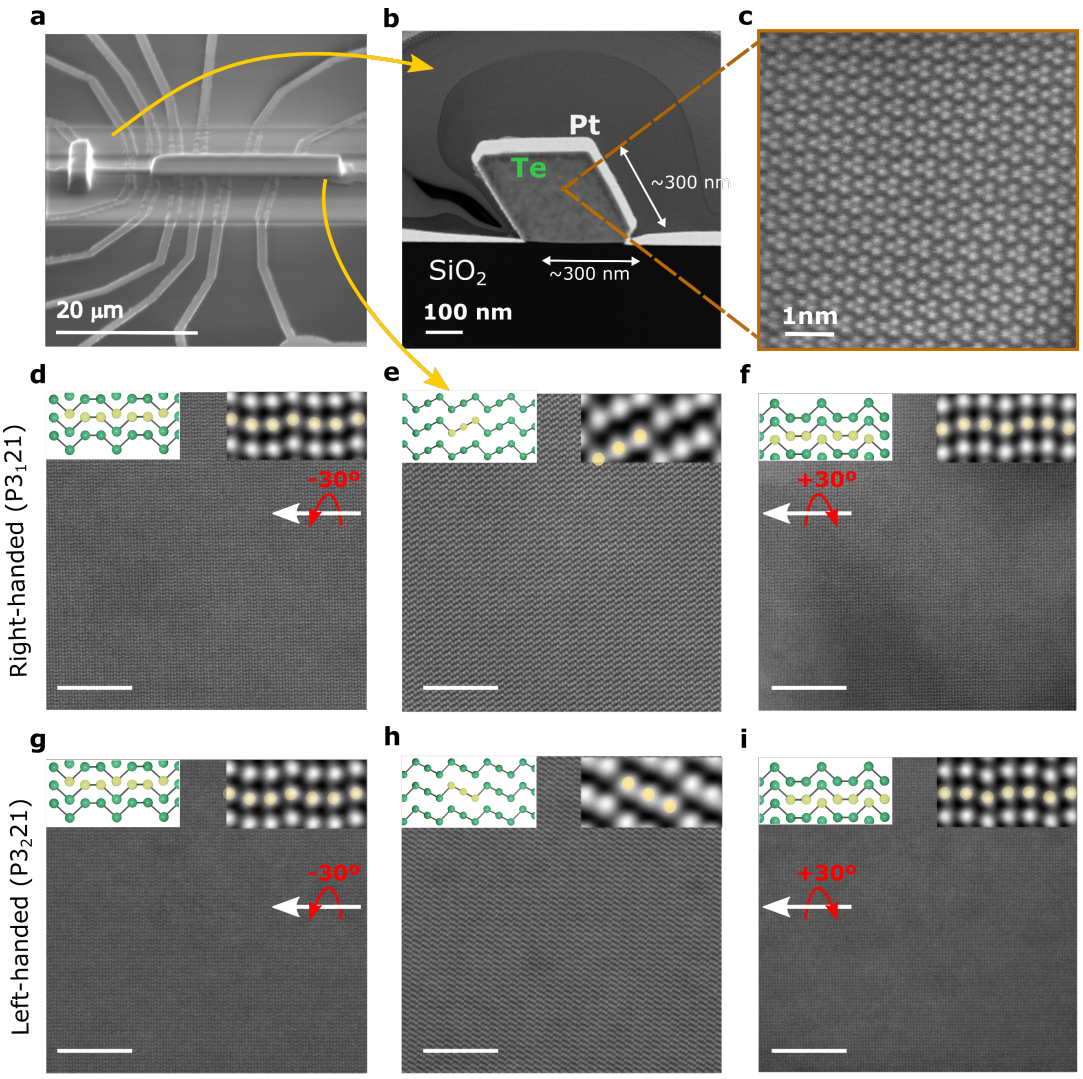

Figure 7.9| Scanning transmission electron microscopy (STEM) characterization. a, Scanning electron microscope image of D3 prepared for STEM analysis, showing the two areas from where the lamellae were taken (similar preparation was applied to each device). **b**,**c**, STEM images, with different magnifications, obtained from the lamella perpendicular to the NW at the contact area. **d-i**, STEM images obtained from the lamellae cut along the two NWs presented in Figure 7.6 (D1, D3) of section 7.3, used for the determination of the handedness. The scale bars correspond to 5 nm. The large area images show the high quality of the synthesized single-crystalline Te NWs. Images **e**,**h**, are taken at <010> zones of the right- and left-handed NWs, respectively. For the chirality determination, the lamellae were rotated by 30^{o} (**d**,**g**) and $+30^{o}$ (**f**,**i**) and compared to the atomic models of the known chirality ($P3_{1}21$ for right- and $P3_{2}21$ for left-handed Te). Insets: crystal structure sketch (left) and zoom-in of the corresponding STEM image (right).

A laboratory Cartesian system was redefined to indicate the direction of the magnetic field in our setup. While it is straightforward to associate the chiral axes c to the z-directions, one may wonder on the orientation of magnetic field with respect to the crystallographic axes a and b of the Te NWs. From the

shape of the cross section in Figure 7.10a, resembling the unit cell, it is reasonable to assume that whenever a NW is deposited on the substrate, one of the crystalline faces, or equivalently a crystallographic direction, is adjacent to the plane of the substrate and perpendicular to c. The direction of the second crystallographic direction is more difficult to predict a priori, as two different orientations of the rhomboidal NW are equally likely, as shown in Figure 7.10b. We note that when scanning the angle α as presented in the experiments of the previous sections, the magnetic field rotates in-plane from c ($\alpha = 0°$) to either a or b ($\alpha = 90°$). This also means that a magnetic field perpendicular to the plane ($\phi = \pm 90°$) is not aligned along a nor b, independently on how the NW is oriented (see Figure 7.10b).

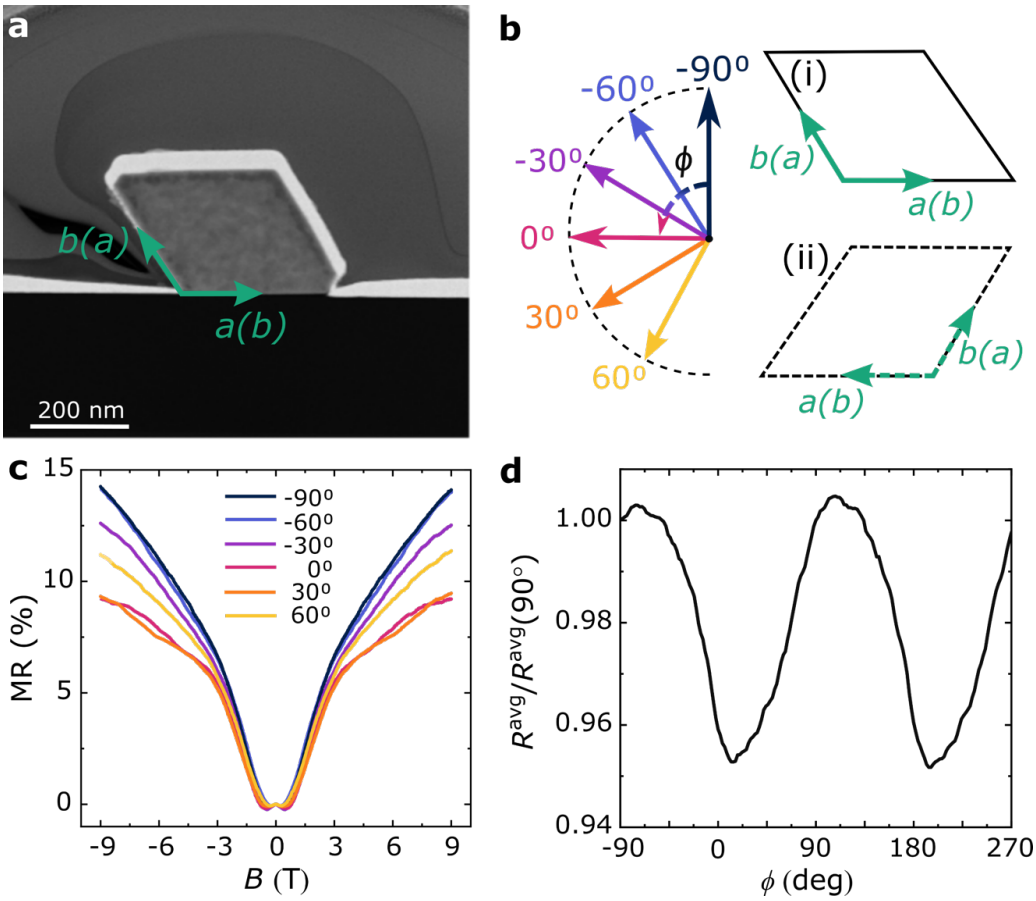

Figure 7.10| Evaluation of crystal directions a,b and their influence on the MR. a, STEM cross section showing the macroscopical shape of the NWs resembling the shape of the Te unit cell and **b**, scheme of the possible orientation of the NWs when laying on the substrate (example taken from D3). **c**, Magnetoresistance measurement at different fixed angles. **d**, angular dependence of R^{avg} scanning the field in the ϕ-plane (measured on D7).

To evaluate the effect of the magnetic field applied along the crystallographic directions, we performed R vs B measurements applying B in the azimuthal plane every 30° from the in-plane direction on device D7. In this way, we are sure to apply the magnetic field parallel to the crystallographic directions, independently on how the NW was lying on the substrate (see Figure 7.10b). From the graphs in Figure 7.10c, we can see that the magnetoresistance does not have a particular relation to the crystallographic orientations. Moreover, from the angular dependence in Figure 7.10d, we observe a periodicity of 90°, that again is not connected to the orientation of the magnetic field along the crystallographic directions. So, while we can speculate on the directions of a and b, they do not seem to have major implications on the magnetoresistive properties, when the current is applied along c.

C. Field-effect mobility

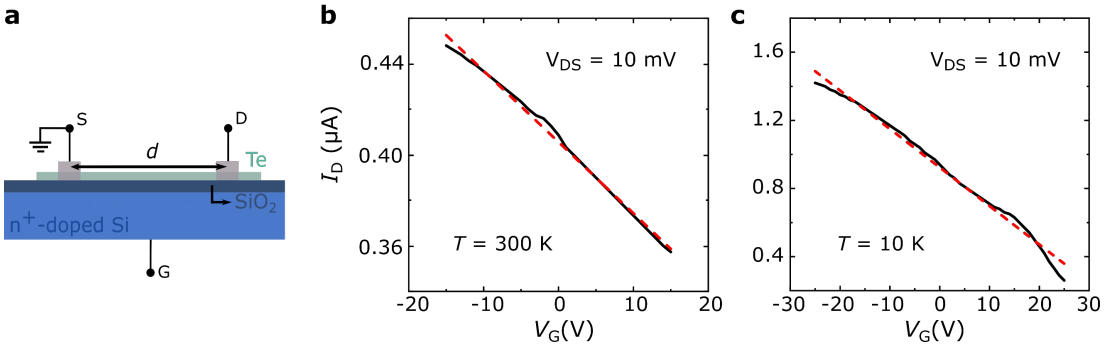

Figure 7.11| Transfer characteristics for field-effect mobility of device D7. **a**, Sketch of the field-effect transistor configuration employed for the measurement. **b**,**c** Back-gate voltage (V_G) dependence of the current (I_D) flowing along a Te NW (D7), at $V_{DS} = 10$ mV and **b**, $T = 300$ K, **c**, $T = 10$ K. The dashed line represents the linear fit used to extract the mobility.

Te NWs deposited on Si(n+)/SiO_2 substrates and contacted with Pt contacts can be measured in a field-effect transistor configuration (Figure 7.11). In the linear regime, the field-effect mobility (μ) can be obtained from the gate voltage (V_G) dependence of the current (I_D) flowing along the Te NW:

$$I_D = \mu \cdot \frac{w}{d} \cdot V_{DS} \cdot C_i \cdot V_G \ , \tag{7.3}$$

where V_{DS} is the voltage between the two electrodes acting as source and drain, d is the distance between these contacts, w is the width of the Te NW, C_i is the capacitance of SiO_2. By using $C_i = 1.15 \times 10^8$ F cm^2, which corresponds to a 300 nm thick layer of SiO_2, and the slope of the transfer curve (Figure 7.10b,c), the field-effect mobility in the Te crystals at 300 K were

obtained from Eq. (7.3). The extracted mobility for device D7 is $\mu \sim 500$ cm^2/(Vs) at 300K and it increases reducing the temperature, reaching a value of $\mu \sim 2500$ cm^2/(Vs) at 10K. The conductivity in the Te crystals decreases for positive V_G, indicating that holes are the majority carriers. This confirms that our synthesized Te NWs are p-type semiconductors.

Here, we would like to point out that, even if the Te NW are generally p-doped and they show a metallic behaviour in the R vs T, the hole doping is not very high ($\sim 7 \times 10^{17}$ cm^{-3}, as obtained by Hall measurements), and that the Fermi energy lies very close to the edge of the valence band. For this reason, even though the field-effect induced by the gate does not switch off the transistor, it does modulate (slightly) the current – and the field-effect mobility can be extracted.

D. Additional magnetoelectrical characterizations

Extended magnetoresistance measurements

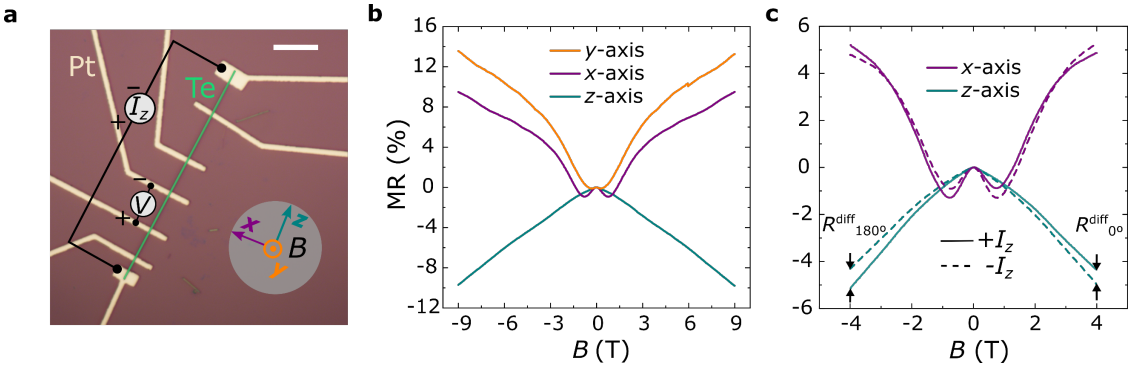

Figure 7.12| Extended magnetoresistance measurements of a Te NW (D1). a, Optical image of a Te NW contacted with Pt electrodes (the scale bar corresponds to 10 μm), illustrating the four-probe measurement configuration and the magnetic field directions. **b**, Current-independent magnetoresistance ($MR = [R^{avg}(B) - R^{avg}(0)]/R^{avg}(0)$) measured on the Te NW with an external field applied along x, y, and z, at $T = 10$ K. **c**, Magnetoresistance traces (continuous line: $MR = [R(+I_z, B) - R(+I_z, 0)]/R(+I_z, 0)$; dashed line: $MR = [R(-I_z, B) - R(-I_z, 0)]/R(-I_z, 0)$) at positive and negative currents measured at $T = 2$ K and with magnetic field applied along the in-plane directions (x and z). Continuous and dashed lines display the MR obtained from $+Iz = +1\ \mu A$ and $-Iz = -1\ \mu A$, respectively. The equivalence between these data and the R^{diff} signals measured in the angular-dependent measurements at 0 and 180 degrees is also indicated.

Performing $R(B)$ in the three cartesian directions that we redefined for our laboratory system (Figure 7.12a,b), one can observe two very different behaviors in the MR, a negative magnetoresistance when the external magnetic field is parallel to the chiral z-axis, and a positive one when it is perpendicular to z

(x- and y-axis). Consistently with the UMR measurements presented, also in the MR traces is possible to observe the current induced spin polarization effect that cause the UMR. In Figure 7.12c, MR curves resolved in current, display how the current direction influences the MR, which in turn gives the UMR presented in the angular dependences. In particular, the equivalence between these data and the R^{diff} signal obtained in the angular-dependent measurements can be understood from the shift of the curves in Figure 7.12c. Interestingly, also the MR traces obtained with the field perpendicular to the chiral axes, are dependent on the direction of the current, indicating that some UMR contribution independent from the chirality may be present in Te.

Evaluation on the presence of UMR extra components

To evaluate this possibility, in Figure 7.13, we present a comparison of the angular dependences of R^{avg} and R^{diff} when scanning B in the three relevant planes ϕ (Figure 7.13a-c), γ (Figure 7.13d-f) and α (Figure 7.13g-i). The angular dependences recorded in the $\alpha-$ and $\gamma-$ planes present a similar behavior, characterized by sharp peaked features recorded at approximately 0° and 180°. This is expected, as these angles correspond to the same physical direction, with the field applied parallel to the crystal c-axis. As a consequence, the values of R^{diff} measured for $\alpha = \gamma = 0°$ and 180° should be exactly the same. Conversely, we find that in $\gamma-$ plane the UMR is smaller for approximately a factor 2. This is likely related to a misalignment of the NW direction with respect to the magnetic field, which reduces the actual magnitude of B applied along the c-axes. Moreover, in both the $\alpha-$ and $\gamma-$ planes R^{diff} decreases rapidly a few degrees away from the maxima/minima, but it does not vanish at $\alpha = \gamma = 90°$ and 270°, where broad shoulders appear, and which are maximum at $V_{\mathrm{G}} = +10$ V.

In the $\phi-$ plane, the peaky features are not observed, since they are related to the UMR measured for the field parallel to the NW c-axis, whereas in the $\phi-$ plane the field is always applied perpendicular to it. R^{diff} does not show any substantial UMR at $V_{\mathrm{G}} = 0$ V, but a small yet clearly detectable signal appears when a gate voltage $V_{\mathrm{G}} = +10$ V is applied. This result is consistent with the measurements in the $\alpha-$ and $\gamma-$planes at 90° and 270° (Figure 7.13d-i). In particular, the UMR amplitude in the direction orthogonal to the c-axis is gate dependent, and it is maximum at $V_{\mathrm{G}} = +10$ V. This "transversal" UMR indicates that the current along the c-axis induces a spin polarization not only in a direction parallel to the NW c-axis, but also orthogonal to it. Such a component is not directly related to the chirality – in the sense that it would not be allowed by the chiral crystal symmetry.

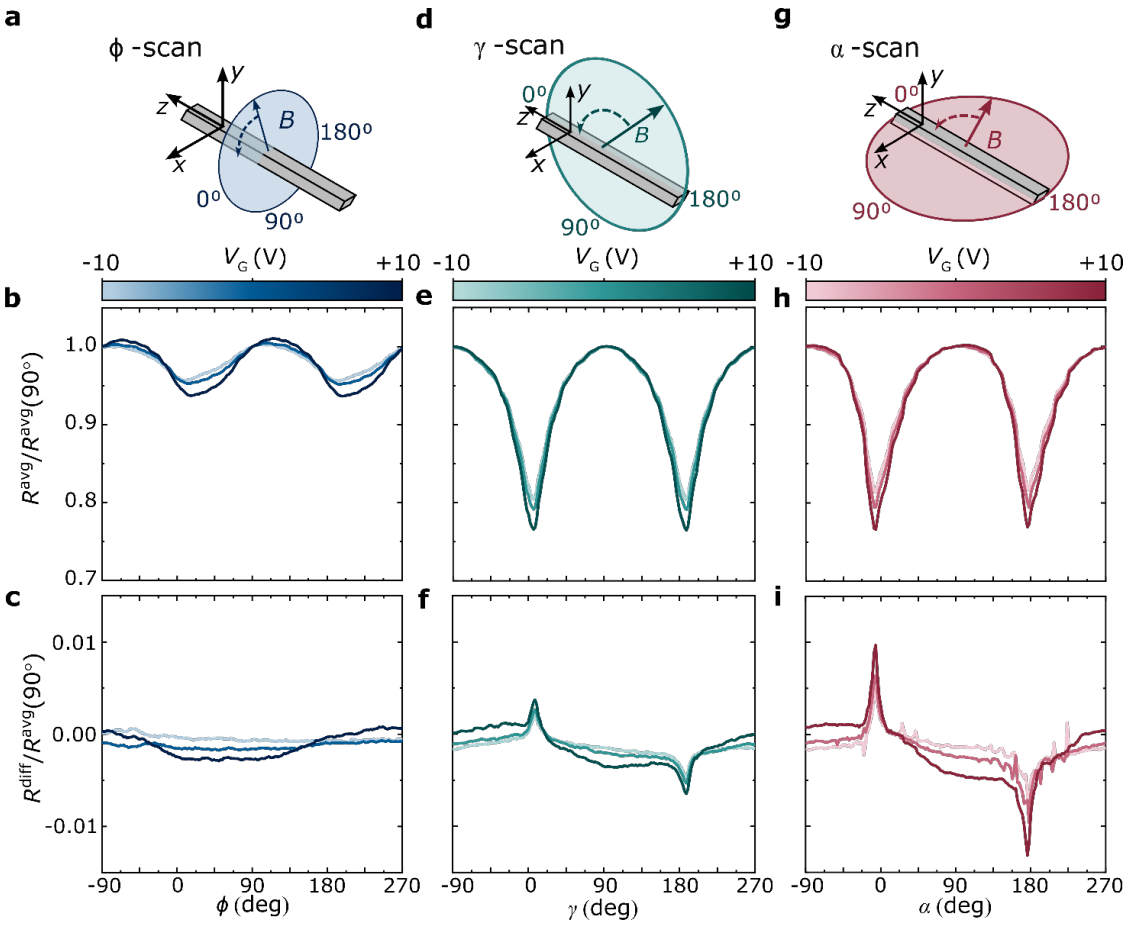

Figure 7.13| Angular dependences of R^{avg} and R^{diff} with magnetic field scanned in the three different planes (device D7). a,**d**,**g**, Definition of the $\phi-$, $\gamma-$, and $\alpha-$ planes, in which the angular dependences was measured. **b**,**e**,**h**, Normalized R^{avg} measured in the three planes at three different gate voltages V_{G} = -10 V, 0 V, and +10 V. **c**, **f**, **i**, Normalized R^{diff} measured in the three planes at three different gate voltages V_{G} = -10 V, 0 V, and +10 V.

In particular, in absence of an external magnetic field, the symmetries of the chiral space groups, $P3_121$ and $P3_221$ (three-fold screw axis (c) and two-fold rotation axis (a)), allow only the diagonal tensor elements of the Edelstein susceptibility $\boldsymbol{\kappa}$ to be nonzero (where in an element κ_{ij}, i would represent the direction of spin polarization and j the one of the electric field, or equivalently the one of the current). In our experiments, the charge current is always applied along the chiral axis (c-axis which is along the z-axis). In the absence of an external magnetic field, this charge current along the chiral axis induces a spin density (anti)parallel to the charge current.

However, the applied magnetic field breaks the crystal symmetries: a magnetic field along the c-axis breaks time-reversal symmetry and the two-fold rotation symmetry. Hence, the tensor elements $\kappa_{ac}, \kappa_{dc}, \kappa_{ca}$ and κ_{cd} are allowed now (here, a is the 2-fold rotation axis in the unperturbed crystal, and

d is the direction perpendicular to a and c). In this case, the current-induced spin density is not aligned perfectly parallel or antiparallel to the charge current anymore. Therefore, the magnetoresistance can become nonzero if B is perpendicular to z. Similarly, when the magnetic field is not along the chiral axis, it can additionally break the threefold screw symmetry and generally allow all tensor elements of $\boldsymbol{\kappa}$ to be nonzero. Thus, when B is rotated, a current in z direction generates a spin density which has x, y, and z components (see section 6 for further symmetry considerations). These additional tensor elements due to the applied magnetic field could explain additional asymmetries.

Nevertheless, we note that the transversal UMR is approximately one order of magnitude smaller than the chirality induced longitudinal UMR. This indicates that the charge to spin conversion along the c-axis is significantly more efficient.

On the origin of the unusual UMR angular dependence

As mentioned in section 7.3, the UMR curves reported in this study deviates from the more typical sin curves usually associated to UMR (e.g., showing the peaky features when $I \parallel B$). The appearance of this extra peaks is strictly connected to the peculiar magnetoresistance behaviors shown in Figure 7.4. While in typical Rashba-Edelstein systems the $R^{\mathrm{avg}}(B)$ follows a similar positive parabolic trend when B is applied along the two axes under probe, in the case of Te we have a strong negative magnetoresistance when the magnetic field is oriented along the chiral axes and a positive one when B is perpendicular to it. This makes the angular dependence of R^{avg} to deviate from a typical $\cos^2$ function (sharp minima at $\alpha \sim 0°$ and 180°). Since R^{diff} is obtained from the difference between the contribution to R^{avg} of positive and negative currents the resultant shape is affected as well.

To better understand the situation, one can think about the simple model explaining the UMR effect, presented in section 6.6 (see here Figure 7.14). This simple model implies the current-induced spin polarization gives rise to UMR only if the material is characterized by a finite MR, which serves as a self-contained sensing element [256]. Moreover, considering the MR as the internal sensing tool, it is immediate to visualize that a steeper MR provides higher sensitivity (Figure 7.14g), or a larger resistance change for a given magnetic field. Therefore, the UMR and the MR are deeply intertwined, and it should be expected that the peculiar MR of Te affects R^{diff}.

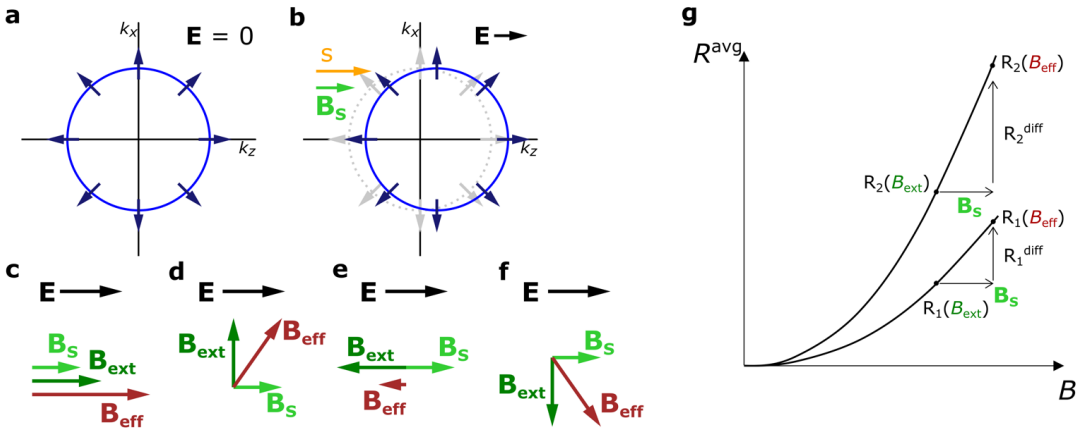

Figure 7.14| Self-sensing mechanism involved in the UMR. a,b, A charge current in Te NWs generates a spin polarization which has the same effect on the transport properties of a magnetic field. **c-f**, The so-generated $\mathbf{B}_S$ adds up to the external field resulting in a $\mathbf{B}_{eff}$ that **g**, generates a change in resistance R^{diff} which depends on the materials magnetoresistance, so that a steeper MR generates a larger R^{diff}.

The use of the MR as an internal sensing element can explain the measured features, at least at a qualitative level. The angular dependence of the R^{avg} at 9 T is a map of the MR at the different angles, and it can be employed as a rough estimate of the sensitivity to a magnetic field at each angle. In principle, the sensitivity of the measurement should be given by the slope of the $R^{avg}(B)$ at the various angles, and not by the MR value itself. For Te, MR transits from positive with the field perpendicular to the NW to negative with the field parallel to the NW. The angles for which MR is maximum in absolute value correspond to the directions with highest sensitivity to the magnetic field, either internal as $\mathbf{B}_S$ or external as $\mathbf{B}_{ext}$. Between these values, the sensitivity decreases quickly, as MR decreases and becomes exactly zero at the angles where it crosses the dashed line in Figure 7.15a. At these angles, the system is not sensitive to the presence of a magnetic field, so that even if there is a current-induced spin polarization with a component in that direction, the system does not have the sensitivity to detect it. As a consequence, R^{diff} decreases rapidly from its value to almost zero, as the sensitivity of R^{avg}.

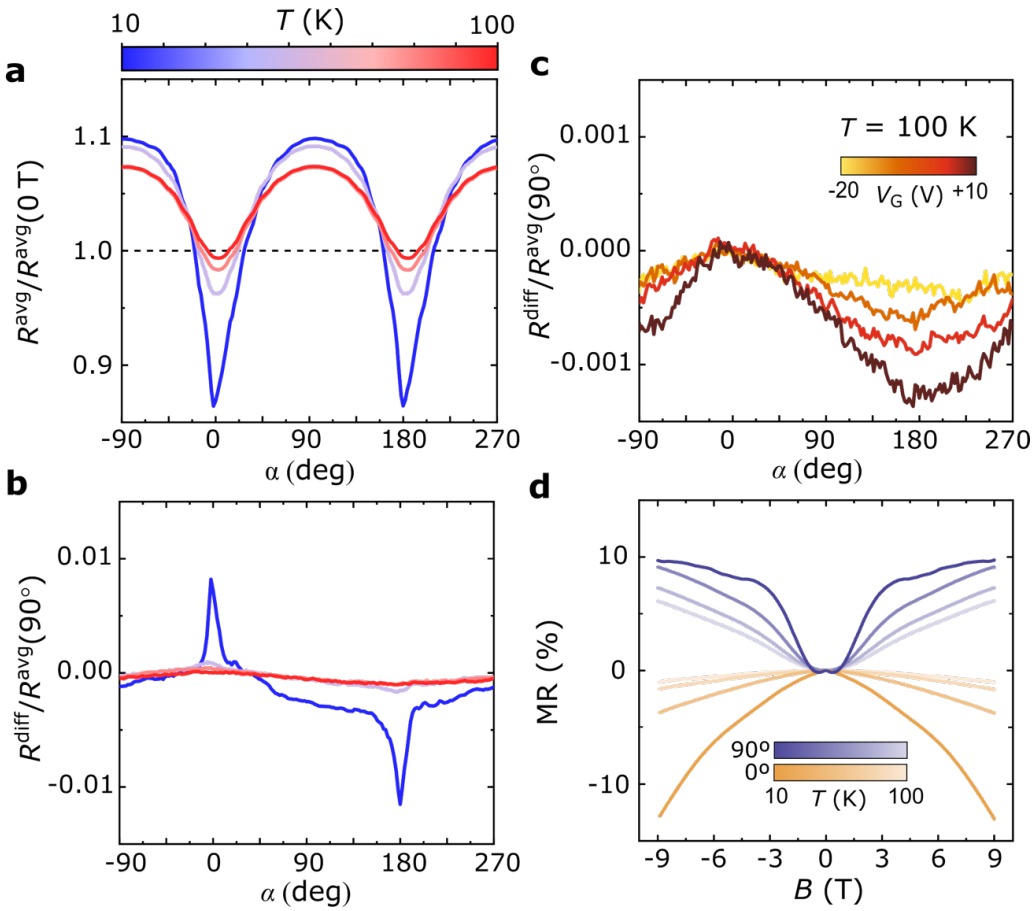

Figure 7.15| Temperature influence in the magnetoresistances measured at α −plane. Angular dependence of normalized **a**, R^{avg} (dashed line represent MR = 0%) **b**, R^{diff} at different temperatures (10, 50, 80 and 100 K). **c**, Angular dependence of normalized R^{diff} at $T = 100$ K applying different gate voltages (-20, -10, 0 and +10 V). **d,** Magnetoresistance measured along ($\alpha = 0°$) and transversally ($\alpha = 90°$) to the chiral *c*-axis at different temperatures (10, 50, 80 and 100 K).

Strong evidence that R^{diff} is strictly connected to the peculiar MR of Te NWs emerges by inspecting Figure 7.15. The sharp features in R^{diff} are reminiscent of the minima in R^{avg}, which in turn are related to the NLMR (compare Figure 7.15a and b). The connection between the features in R^{avg} and R^{diff} is even more clear in Figure 7.15c, which shows R^{diff} measured at $T =$ 100 K. At this temperature, R^{avg} shows a more conventional $\cos^2$ dependence (Figure 7.15a), and R^{diff} also displays an angular dependence without sharp features (Figure 7.15c). Moreover, even the amplitude of R^{diff} displays a T dependence similar to the one of NLMR. At 100 K, the NLMR is much reduced, and R^{diff} is also much lower than at low temperature (see Figure 7.15d).

E. Reproducibility of UMR in different samples

To further verify the reproducibility of our findings, in Figure 7.16 we present the magnetoresponse measured in six different devices (D1-D6). Among these devices, it has been observed a proportion between left- and right-handed NWs of four to two, in agreement with the fact that our synthesis process is not enantio-selective. Maxima and minima are observed respectively around $\alpha = 0°$ and $\alpha = 180°$, in all left-handed NWs, while the opposite trend is shown in the right-handed NWs. The appearance of wide shoulders close to the sharp peaks and dips, are most likely related to small carrier density variations from NW to NW; since similar features are observed in Figure 7.6 when applying a gate voltage that modulates the carrier density of device D2.

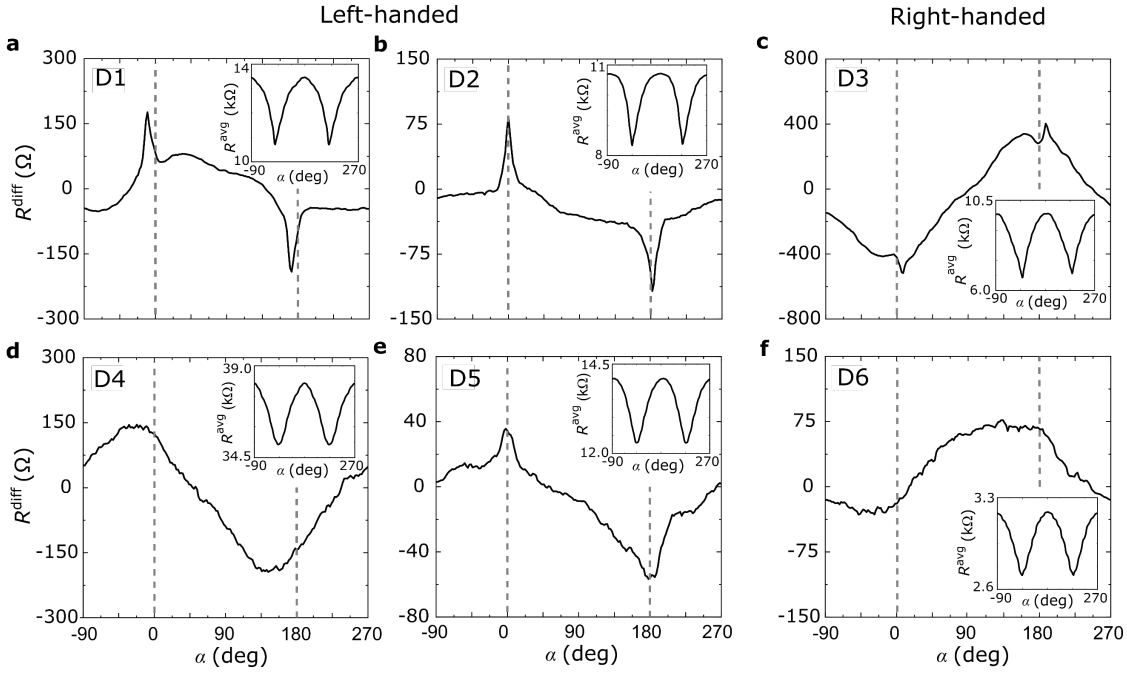

Figure 7.16| Unidirectional magnetoresistance of different Te NWs. Angle-dependent UMR $R^{\text{diff}} = [R(+I_z) - R(-I_z)]/2$ measured in different samples (D1-D6) at $|I_z| =$ 1 μA, $T = 10$ K and $B = 9$ T. The signal shows specular curves between left- (**a**,**b**,**d**,**e**) and right- (**c**,**f**) handed NWs. D1-D3 are the samples reported in the main text, while D4-D6 are additional samples fabricated to reproduce the specular handedness-dependent behaviour of UMR. Insets: Angular-dependent magnetoresistance $R^{\text{avg}} = [R(+I_z) + R(-I_z)]/2$ for the corresponded Te NW measured in the same conditions.

F. Theoretical Calculations on the Edelstein effect

We calculate the charge current density $\mathbf{j}$ as well as the spin density $\mathbf{S}$ response to an external electric field $\mathbf{E}$ (here bold letters represents vectors):

$$\mathbf{j} = -\frac{e}{\mathrm{V}} \sum_{\mathbf{k}} \mathbf{v}_{\mathbf{k}} f_{\mathbf{k}} \ , \tag{7.4}$$

$$\mathbf{S} = \sum_{\mathbf{k}} \langle \mathbf{s} \rangle_{\mathbf{k}} f_{\mathbf{k}} \tag{7.5}$$

Here, e is the absolute value of the elementary charge, V is the sample volume, $\mathbf{v}_{\mathbf{k}} = \frac{\partial \varepsilon}{\hbar \partial \mathbf{k}}$ is the group velocity, $\langle \mathbf{s} \rangle_{\mathbf{k}}$ is the spin expectation value, ε the energy dispersion, and $f_{\mathbf{k}}$ is the distribution function. Its evolution under the influence of an external electric field $\mathbf{E}$ as well as scattering is described by the Boltzmann equation:

$$-\frac{e}{\hbar} \mathbf{E} \frac{\partial f_{\mathbf{k}}}{\partial \mathbf{k}} = \left. \frac{\partial f_{\mathbf{k}}}{\partial t} \right|_{\mathrm{scatt}} \ , \tag{7.6}$$

where we have assumed the system to be stationary and spatially homogeneous. $|\partial f_{\mathbf{k}} / \partial t|_{scatt}$ is the scattering term which we approximate by the relaxation time approximation:

$$\left. \frac{\partial f_{\mathbf{k}}}{\partial t} \right|_{\mathrm{scatt}} = -\frac{1}{\tau_{\mathbf{k}}} g_{\mathbf{k}} \tag{7.7}$$

Here $g_{\mathbf{k}} = f_{\mathbf{k}} - f^0_{\mathbf{k}}$ is the nonequilibrium part of the distribution function, $f^0_{\mathbf{k}}$ is the Fermi Dirac distribution function and $\tau_{\mathbf{k}}$ is the momentum relaxation time. The Boltzmann Equation (7.6) is solved by

$$f_{\mathbf{k}} = f^0_{\mathbf{k}} + \frac{\partial f^0_{\mathbf{k}}}{\partial \varepsilon} e \tau_{\mathbf{k}} \mathbf{v}_{\mathbf{k}} \cdot \mathbf{E} \tag{7.8}$$

Thus, the electric field $\mathbf{E}$ leads to a reoccupation of states, depending on their group velocity and momentum relaxation time. In a simplified picture, this can be understood as a "shift" of the Fermi contour in k-space. Inserting Eq. (7.8) into Eqs. (7.4) and (7.3) yields

$$\mathbf{j}_c = -\frac{e^2}{\mathrm{V}} \sum_{\mathbf{k}} \frac{\partial f_{\mathbf{k}}}{\partial \varepsilon} \tau_{\boldsymbol{k}} \mathbf{v}_{\mathbf{k}} (\mathbf{v}_{\mathbf{k}} \cdot \mathbf{E}) =: \sigma \mathbf{E} \ , \tag{7.9}$$

$$\mathbf{S} = e \sum_{\mathbf{k}} \frac{\partial f_{\mathbf{k}}}{\partial \varepsilon} \tau_{\boldsymbol{k}} \langle \mathbf{s} \rangle_{\mathbf{k}} (\mathbf{v}_{\mathbf{k}} \cdot \mathbf{E}) =: \kappa \mathbf{E} \tag{7.10}$$

In our calculations, we assume $T = 0$ and a constant relaxation time τ_0. Hence, only states at the Fermi level contribute to the transport. Using Eqs. (7.9) and (7.10), we calculate the charge current as well as the current-induced spin density in bulk Te, which is shown as a function of the Fermi level in Figure 7.7c.

The Edelstein effect is defined as the spin density response to an external electric field. Hence, the nonequilibrium spin $\mathbf{S}$ per unit cell is conventionally calculated using Eq. (7.10), and the Edelstein efficiency is expressed via the susceptiblilty tensor κ, $\mathbf{S} = \kappa \mathbf{E}$. However, in our experiment, a constant charge current $\mathbf{j}_c$ is applied, and the gate voltage is modified. Therefore, we express the current-induced spin as a response to a constant charge current. Since in the semiclassical Boltzmann transport theory the electric response to external fields is discussed, we calculate first the charge current as well as the spin density response to the electric field using Eqs. (7.9) and (7.10). Second, we write the internal electric field by transforming Eq. (7.9), $\mathbf{E}^{int} = \sigma^{-1}\, \mathbf{j}_c$. Finally, we express the induced spin per unit cell as a response to this internal electric field, $\mathbf{S} = \kappa \mathbf{E}^{int} = \kappa \sigma^{-1} \mathbf{j}_c$.

In the considered model the charge conductivity tensor is diagonal, and in the absence of a magnetic field the Edelstein susceptibility tensor is also diagonal. Hence, the current-induced spin density can be expressed as $S_z = \kappa_{zz} j_z / \sigma_{zz}$. The tensor elements κ_{zz} and σ_{zz} are calculated using Eqs. (7.10) and (7.9), respectively.

Finally, it is worthed to comment on the role of symmetries in the generation of the spin densities responsible for the appearance of the UMR signals. In Te, inversion symmetry is broken, which allows for the existence of the Edelstein effect. In a system with inversion symmetry, Eq. (7.10) would be zero, since k-dependent spin and velocity expectation values transform under inversion $(k \to -k)$ as $s \to s$ and $v \to -v$. In addition, mirror symmetry is broken. A radial spin texture, as sketched in Fig. 1f, would be forbidden by

mirror symmetry: for example, a mirror operation with the yz mirror plane would force the spin expectation value at (0, 0, k_z) to be oriented along the x direction. A current-induced spin polarization (anti-)parallel to the applied electric field is a signature of broken mirror symmetry: consider for example the spin polarization in z direction induced by an electric field in z direction. According to Eq. (7.10), one needs to sum up over s_z, v_z of all states at the Fermi surface. An yz mirror symmetry would transform $k_x \rightarrow -k_x$, $k_y \rightarrow k_y$, $k_z \rightarrow -k_z$, $v_z \rightarrow v_z$ and $s_z \rightarrow -s_z$. Hence, Eq. (7.10) would vanish (more precisely, the zz component of κ would be zero). These calculations were performed by Dr. Annika Johansson.

Conclusions and future perspectives

In this thesis, we have presented a transversal study on the electronic transport properties of advanced low dimensional van der Waals materials. In the endless research of new materials and effects which could help the technological progress, we took two different paths: modulation of state-of-the-art vdW materials with the use of molecular compounds, and investigation on the electronic transport properties of a chiral system for the study the relationship between symmetry breakings and charge to spin conversion phenomena.

In the first part of this work, using hybrid vdW heterostructures, we demonstrated that by coupling opportune molecules with vdW materials it is possible to manipulate efficiently even physical properties like superconductivity and magnetism of two prototypical vdW materials ($NbSe_2$ and Fe_3GeTe_2).

In the first case, with the choice of the right functional group and self-assembly, we can decide if to strengthen or suppress the superconductivity of $NbSe_2$ producing a dipole induced doping. With our functionalization process, we also observe a stability improvement of the material, which may help to have a new starting platform to further study the role of carrier density variations on the 2D correlated electronic phases of $NbSe_2$. This similar approach could also be used with the 2D ferromagnet FGT in order to increase its Curie temperature, otherwise too low for practical applications. Some failed attempts revealed that the doping induced by the molecules on the thinnest, functioning FGT samples (~ 5 layers) which we were able to isolate, it was not sufficient to significantly displace its Curie temperature. To achieve an efficient modulation of its magnetism, more work must be done to improve the exfoliation process and to isolate single or double layers FGT, such that screening effects may be reduced and the doping could be more effective.

Nevertheless, the work on FGT returned interesting results when we decided to couple the 2D ferromagnet with metalorganic molecules (phthalocyanines) bearing uncompensated spins. An antiferromagnetic coupling, already studied in previous works based on traditional ferromagnetic substrates, establishes between the 2D ferromagnet and the few molecular layers, leading to magnetic hardening and a significant exchange bias with remarkable reproducibility. These results demonstrate that, in general, it should be possible to pin the magnetization of 2D magnets with stable, commercial, and easy to grow molecules. Thus, this molecular approach can be employed to tune the

operating conditions of FGT based vertical MTJ, or even to pin the magnetization of 2D magnetic insulators which could be used to proximitize the graphene channels used in graphene-based spin valves. In this way, the use of molecules could enter in the design of a whole vdW based device, determining some of its operational properties.

In the second part of the work presented in this thesis, we investigated the role of chirality on the electronic transport properties of Tellurium nanowires. Electrically tunable and chirality dependent unidirectional magnetoresistance was detected in several nanowires, suggesting that due to the symmetry breakings related to the chiral structure of Te, a charge current applied to the nanowires induces a significant spin polarization along the chiral axis. The orientation of such spins is defined by the spin texture at the Fermi surface and reverses depending on the handedness of the crystal. These findings add a piece of knowledge about the relationship between charge to spin conversion phenomena and symmetries, paving the way for the use of chiral media in the design of new spintronic devices. In particular, the unusual charge to spin conversion directions may be useful to exploit different geometries in the design of spintronic devices. For instance, if one would be able to grow nanopillars of Te on top of FGT, a current passing through the whole structure would induce the right orientation of spin polarization to induce a torque on the FGT magnetization and eventually flip it. In the same structure, rectification should be observed when passing a lower current density (spin polarized by the ferromagnet), with rectification direction dependent on, handedness of Te and on the FGT magnetization. Such proposal would definitely require a more quantitative study on each component of the device and the optimization of several fabrication processes, which may take more than another full PhD.

Bibliography

[1] Feynmann, R. 'There's plenty of room at the bottom'. *Engineering and Science* vol. 23 (1960)

[2] Ajayan, P., Kim, P. & Banerjee, K. Two-dimensional van der Waals materials. *Phys. Today* **69**, 38–44 (2016)

[3] Wallace, P. R. The Band Theory of Graphite. *Phys. Rev.* **71**, (1947)

[4] Slonczewski, J. C. & Weiss, P. R. Band Structure of Graphite. *Phys. Rev.* **109**, 272 (1958)

[5] Semenoff, G. W. Condensed-Matter Simulation of a Three-Dimensional Anomaly. *Phys. Rev. Lett.* **53**, 2449 (1984)

[6] Haldane, F. D. M. Model for a Quantum Hall Effect without Landau Levels: Condensed-Matter Realization of the 'Parity Anomaly'. *Phys. Rev. Lett.* **61**, 2015 (1988)

[7] Mermin, N. D. Crystalline Order in Two Dimensions. *Phys. Rev.* **176**, 250 (1968)

[8] Fradkin, E. Critical behavior of disordered degenerate semiconductors. II. Spectrum and transport properties in mean-field theory. *Phys. Rev. B* **33**, 3263 (1986)

[9] Novoselov, K. S. *et al.* Electric Field Effect in Atomically Thin Carbon Films. *Science* **306**, 666–669 (2004)

[10] Novoselov, K. S. *et al.* Two-dimensional atomic crystals. *Proc. Natl. Acad. Sci.* **102**, 10451–10453 (2005)

[11] Geim, A. K. & Novoselov, K. S. The rise of graphene. *Nat. Mater.* **6**, 183–191 (2007)

[12] Neto, A. H. C., Guinea, F., Peres, N. M. R., Novoselov, K. S. & Geim, A. K. The electronic properties of graphene. *Rev. Mod. Phys.* **81**, 109 (2009)

[13] Roche, S. *et al.* Graphene spintronics: the European Flagship perspective. *2D Mater.* **2**, 030202 (2015)

[14] Mak, K. F. *et al.* Measurement of the Optical Conductivity of

Graphene. *Phys. Rev. Lett.* **101**, 196405 (2008)

[15] Balandin, A. A. *et al.* Superior Thermal Conductivity of Single-Layer Graphene. *Nano Lett.* **8**, 902–907 (2008)

[16] Lee, C., Wei, X., Kysar, J. W. & Hone, J. Measurement of the elastic properties and intrinsic strength of monolayer graphene. *Science* **321**, 385–388 (2008)

[17] Novoselov, K. S. *et al.* Two-dimensional gas of massless Dirac fermions in graphene. *Nature* **438**, 197–200 (2005)

[18] Zhang, Y., Tan, Y.-W., Stormer, H. L. & Kim, P. Experimental observation of the quantum Hall effect and Berry's phase in graphene. *Nature* **438**, 201–204 (2005)

[19] Novoselov, K. S. *et al.* Room-temperature quantum hall effect in graphene. *Science* **315**, 1379 (2007)

[20] Du, X., Skachko, I., Duerr, F., Luican, A. & Andrei, E. Y. Fractional quantum Hall effect and insulating phase of Dirac electrons in graphene. *Nature* **462**, 192–195 (2009)

[21] Bolotin, K. I., Ghahari, F., Shulman, M. D., Stormer, H. L. & Kim, P. Observation of the fractional quantum Hall effect in graphene. *Nature* **462**, 196–199 (2009)

[22] Dickinson, R. G. & Pauling, L. THE CRYSTAL STRUCTURE OF MOLYBDENITE. *J. Am. Chem. Soc.* **45**, 1466–1471 (2002)

[23] Wilson, J. A. & Yoffe, A. D. The transition metal dichalcogenides discussion and interpretation of the observed optical, electrical and structural properties. *Adv. Phys.* **18**, 193–335 (1969)

[24] Frindt, R. F. & Yoffe, A. D. Physical properties of layer structures : optical properties and photoconductivity of thin crystals of molybdenum disulphide. *Proc. R. Soc. London. Ser. A. Math. Phys. Sci.* **273**, 69–83 (1963)

[25] Joensen, P., Frindt, R. F. & Morrison, S. R. Single-layer MoS_2. *Mater. Res. Bull.* **21**, 457–461 (1986)

[26] Manzeli, S., Ovchinnikov, D., Pasquier, D., Yazyev, O. V. & Kis, A. 2D transition metal dichalcogenides. *Nat. Rev. Mater.* **2**, 17033 (2017)

[27] Mak, K. F., Lee, C., Hone, J., Shan, J. & Heinz, T. F. Atomically thin MoS_2: A new direct-gap semiconductor. *Phys. Rev. Lett.* **105**, 136805 (2010)

[28] Splendiani, A. *et al.* Emerging Photoluminescence in Monolayer MoS_2. *Nano Lett.* **10**, 1271–1275 (2010)

[29] Radisavljevic, B., Radenovic, A., Brivio, J., Giacometti, V. & Kis, A. Single-layer MoS_2 transistors. *Nat. Nanotechnol.* **6**, 147–150 (2011)

[30] Xu, X., Yao, W., Xiao, D. & Heinz, T. F. Spin and pseudospins in layered transition metal dichalcogenides. *Nat. Phys.* **10**, 343–350 (2014)

[31] Koppens, F. H. L. *et al.* Photodetectors based on graphene, other two-dimensional materials and hybrid systems. *Nat. Nanotechnol.* **9**, 780–793 (2014)

[32] Mak, K. F. & Shan, J. Photonics and optoelectronics of 2D semiconductor transition metal dichalcogenides. *Nat. Photonics* **10**, 216–226 (2016)

[33] Mounet, N. *et al.* Two-dimensional materials from high-throughput computational exfoliation of experimentally known compounds. *Nat. Nanotechnol.* **13**, 246–252 (2018)

[34] Dean, C. R. *et al.* Boron nitride substrates for high-quality graphene electronics. *Nat. Nanotechnol.* **5**, 722–726 (2010)

[35] Liu, H. *et al.* Phosphorene: An Unexplored 2D Semiconductor with a High Hole Mobility. *ACS Nano* **8**, 4033–4041 (2014)

[36] Fei, Z. *et al.* Two-dimensional itinerant ferromagnetism in atomically thin Fe_3GeTe_2. *Nat. Mater.* **17**, 778–782 (2018)

[37] Gong, C. *et al.* Discovery of intrinsic ferromagnetism in two-dimensional van der Waals crystals. *Nature* **546**, 265–269 (2017)

[38] Huang, B. *et al.* Layer-dependent ferromagnetism in a van der Waals crystal down to the monolayer limit. *Nature* **546**, 270–273 (2017)

[39] Pan, D. *et al.* Free-Standing Two-Dimensional Single-Crystalline InSb Nanosheets. *Nano Lett.* **16**, 834–841 (2016)

[40] Chiatti, O. *et al.* 2D layered transport properties from topological

insulator Bi_2Se_3 single crystals and micro flakes. *Sci. Rep.* **6**, 27483 (2016)

[41] Lee, J.-U. *et al.* Ising-Type Magnetic Ordering in Atomically Thin $FePS_3$. *Nano Lett.* **16**, 7433–7438 (2016)

[42] Wang, Y. *et al.* Field-effect transistors made from solution-grown two-dimensional tellurene. *Nat. Electron.* **1**, 228–236 (2018)

[43] Geim, A. K. & Grigorieva, I. V. Van der Waals heterostructures. *Nature* **499**, 419–425 (2013)

[44] Jariwala, D., Marks, T. J. & Hersam, M. C. Mixed-dimensional van der Waals heterostructures. *Nat. Mater.* **16**, 170–181 (2017)

[45] Ponomarenko, L. A. *et al.* Tunable metal–insulator transition in double-layer graphene heterostructures. *Nat. Phys.* **7**, 958–961 (2011)

[46] Cheng, R. *et al.* Few-layer molybdenum disulfide transistors and circuits for high-speed flexible electronics. *Nat. Commun.* **5**, 5143 (2014)

[47] Hong, X. *et al.* Ultrafast charge transfer in atomically thin MoS_2/WS_2 heterostructures. *Nat. Nanotechnol.* **9**, 682–686 (2014)

[48] Rivera, P. *et al.* Observation of long-lived interlayer excitons in monolayer $MoSe_2$–WSe_2 heterostructures. *Nat. Commun.* **6**, 6242 (2015)

[49] Ceballos, F., Bellus, M. Z., Chiu, H.-Y. & Zhao, H. Probing charge transfer excitons in a $MoSe_2$–WS_2 van der Waals heterostructure. *Nanoscale* **7**, 17523–17528 (2015)

[50] Bellus, M. Z., Ceballos, F., Chiu, H.-Y. & Zhao, H. Tightly Bound Trions in Transition Metal Dichalcogenide Heterostructures. *ACS Nano* **9**, 6459–6464 (2015)

[51] Žutić, I., Matos-Abiague, A., Scharf, B., Dery, H. & Belashchenko, K. Proximitized materials. *Mater. Today* **22**, 85–107 (2019)

[52] Luo, Y. K. *et al.* Opto-Valleytronic Spin Injection in Monolayer MoS_2 /Few-Layer Graphene Hybrid Spin Valves. *Nano Lett.* **17**, 3877–3883 (2017)

[53] Safeer, C. K. *et al.* Room-Temperature Spin Hall Effect in

Graphene/MoS_2 van der Waals Heterostructures. *Nano Lett.* **19**, 1074–1082 (2019)

[54] Benítez, L. A. *et al.* Tunable room-temperature spin galvanic and spin Hall effects in van der Waals heterostructures. *Nat. Mater.* **19**, 170–175 (2020)

[55] Ghiasi, T. S. *et al.* Electrical and thermal generation of spin currents by magnetic bilayer graphene. *Nat. Nanotechnol.* **16**, 788–794 (2021)

[56] Zhong, D. *et al.* Layer-resolved magnetic proximity effect in van der Waals heterostructures. *Nat. Nanotechnol.* **15**, 187–191 (2020)

[57] Sun, Z. *et al.* Giant nonreciprocal second-harmonic generation from antiferromagnetic bilayer CrI_3. *Nature* **572**, 497–501 (2019)

[58] Zhang, Y. J. *et al.* Enhanced intrinsic photovoltaic effect in tungsten disulfide nanotubes. *Nature* **570**, 349–353 (2019)

[59] Akamatsu, T. *et al.* A van der Waals interface that creates in-plane polarization and a spontaneous photovoltaic effect. *Science* **372**, 68–72 (2021)

[60] Ma, Q. *et al.* Observation of the nonlinear Hall effect under time-reversal-symmetric conditions. *Nature* **565**, 337–342 (2019)

[61] Kang, K., Li, T., Sohn, E., Shan, J. & Mak, K. F. Nonlinear anomalous Hall effect in few-layer WTe_2. *Nat. Mater.* **18**, 324–328 (2019)

[62] Mak, K. F., McGill, K. L., Park, J. & McEuen, P. L. The valley Hall effect in MoS_2 transistors. *Science* **344**, 1489–1492 (2014)

[63] Langer, F. *et al.* Lightwave valleytronics in a monolayer of tungsten diselenide. *Nature* **557**, 76–80 (2018)

[64] Wu, S. *et al.* Observation of the quantum spin Hall effect up to 100 kelvin in a monolayer crystal. *Science* **359**, 76–79 (2018)

[65] Safeer, C. K. *et al.* Large Multidirectional Spin-to-Charge Conversion in Low-Symmetry Semimetal $MoTe_2$ at Room Temperature. *Nano Lett.* **19**, 8758–8766 (2019)

[66] Song, P. *et al.* Coexistence of large conventional and planar spin Hall effect with long spin diffusion length in a low-symmetry semimetal at room temperature. *Nat. Mater.* **19**, 292–298 (2020)

[67] Zhu, H. *et al.* Observation of chiral phonons. *Science* **359**, 579–582 (2018)

[68] Wu, W. *et al.* Piezoelectricity of single-atomic-layer MoS_2 for energy conversion and piezotronics. *Nature* **514**, 470–474 (2014)

[69] Xi, X. *et al.* Ising pairing in superconducting $NbSe_2$ atomic layers. *Nat. Phys.* **12**, 139–143 (2016)

[70] Cao, Y. *et al.* Unconventional superconductivity in magic-angle graphene superlattices. *Nature* **556**, 43–50 (2018)

[71] Du, L. *et al.* Engineering symmetry breaking in 2D layered materials. *Nature Reviews Physics* vol. 3 193–206 (2021)

[72] Manchon, A., Koo, H. C., Nitta, J., Frolov, S. M. & Duine, R. A. New perspectives for Rashba spin–orbit coupling. *Nat. Mater.* **14**, 871–882 (2015)

[73] Castellanos-Gomez, A. *et al.* Deterministic transfer of two-dimensional materials by all-dry viscoelastic stamping. *2D Mater.* **1**, 011002 (2014)

[74] Taghavi, N. S. *et al.* Thickness determination of MoS_2, $MoSe_2$, WS_2 and WSe_2 on transparent stamps used for deterministic transfer of 2D materials. *Nano Res.* **12**, 1691–1695 (2019)

[75] Gómez-Pérez, J. M. Spin transport in magnetic insulator/heavy metal heterostructures. (Universitad del Pais Vasco (UPV), 2020).

[76] *X-ray and Neuron Reflectivity: Principles and Applications. X-ray and Neuron Reflectivity: Principles and Applications* vol. 58 (Springer Berlin Heidelberg, 1999).

[77] Kroemer, H. *Noble Lectures. Physics 1996-2000* (2000).

[78] Novoselov, K. S. *et al.* Electric Field Effect in Atomically Thin Carbon Films Supplementary. *Science* **5**, 1–12 (2004)

[79] Mak, K. F. *et al.* Tightly bound trions in monolayer MoS2. *Nat. Mater.* **12**, 207–211 (2013)

[80] Lien, D. H. *et al.* Electrical suppression of all nonradiative recombination pathways in monolayer semiconductors. *Science* **364**, 468–471 (2019)

[81] Staley, N. E. *et al.* Electric field effect on superconductivity in

atomically thin flakes of $NbSe_2$. *Phys. Rev. B* **80**, 184505 (2009)

[82] Xi, X., Berger, H., Forró, L., Shan, J. & Mak, K. F. Gate Tuning of Electronic Phase Transitions in Two-Dimensional $NbSe_2$. *Phys. Rev. Lett.* **117**, 106801 (2016)

[83] Deng, Y. *et al.* Gate-tunable room-temperature ferromagnetism in two-dimensional Fe_3GeTe_2. *Nature* **563**, 94–99 (2018)

[84] Jiang, S., Li, L., Wang, Z., Mak, K. F. & Shan, J. Controlling magnetism in 2D CrI_3 by electrostatic doping. *Nat. Nanotechnol.* **13**, 549–553 (2018)

[85] Jiang, S., Shan, J. & Mak, K. F. Electric-field switching of two-dimensional van der Waals magnets. *Nat. Mater.* **17**, 406–410 (2018)

[86] Gobbi, M., Orgiu, E. & Samorì, P. When 2D Materials Meet Molecules: Opportunities and Challenges of Hybrid Organic/Inorganic van der Waals Heterostructures. *Adv. Mater.* **30**, 1–20 (2018)

[87] Chhowalla, M. *et al.* The chemistry of two-dimensional layered transition metal dichalcogenide nanosheets. *Nat. Chem.* **5**, 263–275 (2013)

[88] Chen, S. *et al.* Oligothiophene-Functionalized Perylene Bisimide System: Synthesis, Characterization, and Electrochemical Polymerization Properties. *Chem. Mater.* **17**, 2208–2215 (2005)

[89] Wu, W., Liu, Y. & Zhu, D. π-Conjugated molecules with fused rings for organic field-effect transistors: design, synthesis and applications. *Chem. Soc. Rev.* **39**, 1489–1502 (2010)

[90] Beaujuge, P. M. & Fréchet, J. M. J. Molecular Design and Ordering Effects in π-Functional Materials for Transistor and Solar Cell Applications. *J. Am. Chem. Soc.* **133**, 20009–20029 (2011)

[91] Stepanow, S. *et al.* Steering molecular organization and host–guest interactions using two-dimensional nanoporous coordination systems. *Nat. Mater.* **3**, 229–233 (2004)

[92] Barth, J. V., Costantini, G. & Kern, K. Engineering atomic and molecular nanostructures at surfaces. *Nature* **437**, 671–679 (2005)

[93] Champness, N. R. Building with molecules. *Nat. Nanotechnol.* **2**, 671–672 (2007)

[94] Palma, C.-A., Cecchini, M. & Samorì, P. Predicting self-assembly: from empirism to determinism. *Chem. Soc. Rev.* **41**, 3713 (2012)

[95] Lehn, J.-M. From supramolecular chemistry towards constitutional dynamic chemistry and adaptive chemistry. *Chem. Soc. Rev.* **36**, 151–160 (2007)

[96] Kudernac, T., Lei, S., Elemans, J. A. A. W. & Feyter, S. De. Two-dimensional supramolecular self-assembly: nanoporous networks on surfaces. *Chem. Soc. Rev.* **38**, 402–421 (2009)

[97] Wang, Q. H. & Hersam, M. C. Room-temperature molecular-resolution characterization of self-assembled organic monolayers on epitaxial graphene. *Nat. Chem.* **1**, 206–211 (2009)

[98] Lu, J. *et al.* Using the Graphene Moiré Pattern for the Trapping of C60 and Homoepitaxy of Graphene. *ACS Nano* **6**, 944–950 (2011)

[99] Mali, K. S., Greenwood, J., Adisoejoso, J., Phillipson, R. & Feyter, S. De. Nanostructuring graphene for controlled and reproducible functionalization. *Nanoscale* **7**, 1566–1585 (2015)

[100] Gobbi, M. *et al.* Periodic potentials in hybrid van der Waals heterostructures formed by supramolecular lattices on graphene. *Nat. Commun.* **8**, 14767 (2017)

[101] Assies, L. *et al.* Dynamic covalent conjugated polymer epitaxy on graphene. *J. Mater. Chem. C* **7**, 12240–12247 (2019)

[102] Schedin, F. *et al.* Detection of individual gas molecules adsorbed on graphene. *Nat. Mater.* **6**, 652–655 (2007)

[103] Wehling, T. O. *et al.* Molecular Doping of Graphene. *Nano Lett.* **8**, 173–177 (2008)

[104] Liu, H., Liu, Y. & Zhu, D. Chemical doping of graphene. *J. Mater. Chem.* **21**, 3335–3345 (2011)

[105] Kim, K. K. *et al.* Enhancing the conductivity of transparent graphene films via doping. *Nanotechnology* **21**, 285205 (2010)

[106] Coletti, C. *et al.* Charge neutrality and band-gap tuning of epitaxial graphene on SiC by molecular doping. *Phys. Rev. B* **81**, 235401 (2010)

[107] Shi, Y. *et al.* Work Function Engineering of Graphene Electrode via

Chemical Doping. *ACS Nano* **4**, 2689–2694 (2010)

[108] Christodoulou, C. *et al.* Tuning the Work Function of Graphene-on-Quartz with a High Weight Molecular Acceptor. *J. Phys. Chem. C* **118**, 4784–4790 (2014)

[109] Tarasov, A. *et al.* Controlled Doping of Large-Area Trilayer MoS_2 with Molecular Reductants and Oxidants. *Adv. Mater.* **27**, 1175–1181 (2015)

[110] Mouri, S., Miyauchi, Y. & Matsuda, K. Tunable Photoluminescence of Monolayer MoS_2 via Chemical Doping. *Nano Lett.* **13**, 5944–5948 (2013)

[111] Pham, V. P. & Yeom, G. Y. Recent Advances in Doping of Molybdenum Disulfide: Industrial Applications and Future Prospects. *Adv. Mater.* **28**, 9024–9059 (2016)

[112] Yang, L. *et al.* Chloride Molecular Doping Technique on 2D Materials: WS_2 and MoS_2. *Nano Lett.* **14**, 6275–6280 (2014)

[113] Kang, D.-H. *et al.* Controllable Nondegenerate p-Type Doping of Tungsten Diselenide by Octadecyltrichlorosilane. *ACS Nano* **9**, 1099–1107 (2015)

[114] Kang, D.-H. *et al.* High-Performance Transition Metal Dichalcogenide Photodetectors Enhanced by Self-Assembled Monolayer Doping. *Adv. Funct. Mater.* **25**, 4219–4227 (2015)

[115] Zhao, Y. *et al.* Doping, Contact and Interface Engineering of Two-Dimensional Layered Transition Metal Dichalcogenides Transistors. *Adv. Funct. Mater.* **27**, 1603484 (2017)

[116] Kang, D.-H. *et al.* Self-Assembled Layer (SAL)-Based Doping on Black Phosphorus (BP) Transistor and Photodetector. *ACS Photonics* **4**, 1822–1830 (2017)

[117] Kiriya, D., Tosun, M., Zhao, P., Kang, J. S. & Javey, A. Air-stable surface charge transfer doping of MoS_2 by benzyl viologen. *J. Am. Chem. Soc.* **136**, 7853–7856 (2014)

[118] Wehling, T. O., Lichtenstein, A. I. & Katsnelson, M. I. First-principles studies of water adsorption on graphene: The role of the substrate. *Appl. Phys. Lett.* **93**, 202110 (2008)

[119] Li, Y., Xu, C.-Y., Hu, P. & Zhen, L. Carrier Control of MoS2

Nanoflakes by Functional Self-Assembled Monolayers. *ACS Nano* **7**, 7795–7804 (2013)

[120] Bertolazzi, S., Gobbi, M., Zhao, Y., Backes, C. & Samorì, P. Molecular chemistry approaches for tuning the properties of two-dimensional transition metal dichalcogenides. *Chem. Soc. Rev.* **47**, 6845–6888 (2018)

[121] Ohta, T., Bostwick, A., Seyller, T., Horn, K. & Rotenberg, E. Controlling the electronic structure of bilayer graphene. *Science* **313**, 951–954 (2006)

[122] Castro, E. V. *et al.* Biased Bilayer Graphene: Semiconductor with a Gap Tunable by the Electric Field Effect. *Phys. Rev. Lett.* **99**, 216802 (2007)

[123] Gobbi, M. *et al.* Periodic potentials in hybrid van der Waals heterostructures formed by supramolecular lattices on graphene. *Nat. Commun.* **8**, 14767 (2017)

[124] Yu, W. J., Liao, L., Chae, S. H., Lee, Y. H. & Duan, X. Toward Tunable Band Gap and Tunable Dirac Point in Bilayer Graphene with Molecular Doping. *Nano Lett.* **11**, 4759–4763 (2011)

[125] Samuels, A. J. & Carey, J. D. Molecular Doping and Band-Gap Opening of Bilayer Graphene. *ACS Nano* **7**, 2790–2799 (2013)

[126] Park, J. *et al.* Single-Gate Bandgap Opening of Bilayer Graphene by Dual Molecular Doping. *Adv. Mater.* **24**, 407–411 (2012)

[127] Yoshizawa, S. *et al.* Controlled Modification of Superconductivity in Epitaxial Atomic Layer–Organic Molecule Heterostructures. *Nano Lett.* **17**, 2287–2293 (2017)

[128] Kezilebieke, S., Dvorak, M., Ojanen, T. & Liljeroth, P. Coupled Yu-Shiba-Rusinov States in Molecular Dimers on $NbSe_2$. *Nano Lett.* **18**, 2311–2315 (2018)

[129] Kim, M., Safron, N. S., Huang, C., Arnold, M. S. & Gopalan, P. Light-Driven Reversible Modulation of Doping in Graphene. *Nano Lett.* **12**, 182–187 (2011)

[130] Jang, A.-R. *et al.* Reversibly Light-Modulated Dirac Point of Graphene Functionalized with Spiropyran. *ACS Nano* **6**, 9207–9213 (2012)

[131] Li, J. *et al.* Tuning the optical emission of MoS_2 nanosheets using proximal photoswitchable azobenzene molecules. *Appl. Phys. Lett.* **105**, 241116 (2014)

[132] Margapoti, E. *et al.* A 2D Semiconductor–Self-Assembled Monolayer Photoswitchable Diode. *Adv. Mater.* **27**, 1426–1431 (2015)

[133] Dugay, J. *et al.* Phase Transitions in Spin-Crossover Thin Films Probed by Graphene Transport Measurements. *Nano Lett.* **17**, 186–193 (2016)

[134] Datta, S. *et al.* Tuning magnetoresistance in molybdenum disulphide and graphene using a molecular spin transition. *Nat. Commun.* **8**, 677 (2017)

[135] Gobbi, M. *et al.* Collective molecular switching in hybrid superlattices for light-modulated two-dimensional electronics. *Nat. Commun.* **9**, 2661 (2018)

[136] Wang, Q. H. & Hersam, M. C. Room-temperature molecular-resolution characterization of self-assembled organic monolayers on epitaxial graphene. *Nat. Chem.* **1**, 206–211 (2009)

[137] Garnica, M. *et al.* Long-range magnetic order in a purely organic 2D layer adsorbed on epitaxial graphene. *Nat. Phys.* **9**, 368–374 (2013)

[138] Järvinen, P. *et al.* Molecular Self-Assembly on Graphene on SiO_2 and h-BN Substrates. *Nano Lett.* **13**, 3199–3204 (2013)

[139] Rosa, C. J. L. de la *et al.* Molecular doping of MoS_2 transistors by self-assembled oleylamine networks. *Appl. Phys. Lett.* **109**, 253112 (2016)

[140] Zheng, Y. J. *et al.* Heterointerface Screening Effects between Organic Monolayers and Monolayer Transition Metal Dichalcogenides. *ACS Nano* **10**, 2476–2484 (2016)

[141] Wang, J. *et al.* Probing the crystallographic orientation of two-dimensional atomic crystals with supramolecular self-assembly. *Nat. Commun. 2017 81* **8**, 1–8 (2017)

[142] Feyter, S. De & Schryver, F. C. De. Two-dimensional supramolecular self-assembly probed by scanning tunneling microscopy. *Chem. Soc. Rev.* **32**, 139–150 (2003)

[143] Stoeckel, M.-A. *et al.* Boosting and Balancing Electron and Hole

Mobility in Single- and Bilayer WSe_2 Devices via Tailored Molecular Functionalization. *ACS Nano* **13**, 11613–11622 (2019)

[144] Barja, S. *et al.* Identifying substitutional oxygen as a prolific point defect in monolayer transition metal dichalcogenides. *Nat. Commun.* **10**, 3382 (2019)

[145] Zhao, P. *et al.* Air Stable p-Doping of WSe_2 by Covalent Functionalization. *ACS Nano* **8**, 10808–10814 (2014)

[146] Ta, T. K. H. *et al.* Surface Functionalization of WO_3 Thin Films with (3-Aminopropyl)triethoxysilane and Succinic Anhydride. *J. Electron. Mater.* **46**, 3345–3352 (2017)

[147] Lee, B. *et al.* Modification of Electronic Properties of Graphene with Self-Assembled Monolayers. *Nano Lett.* **10**, 2427–2432 (2010)

[148] Barraud, C. *et al.* Unravelling the role of the interface for spin injection into organic semiconductors. *Nat. Phys.* **6**, 615–620 (2010)

[149] Raman, K. V. *et al.* Interface-engineered templates for molecular spin memory devices. *Nature* **493**, 509–513 (2013)

[150] Ma'Mari, F. Al *et al.* Beating the Stoner criterion using molecular interfaces. *Nature* **524**, 69–73 (2015)

[151] Bairagi, K. *et al.* Tuning the Magnetic Anisotropy at a Molecule-Metal Interface. *Phys. Rev. Lett.* **114**, 247203 (2015)

[152] Gambardella, P. *et al.* Supramolecular control of the magnetic anisotropy in two-dimensional high-spin Fe arrays at a metal interface. *Nat. Mater.* **8**, 189–193 (2009)

[153] Lodi Rizzini, A. *et al.* Coupling single molecule magnets to ferromagnetic substrates. *Phys. Rev. Lett.* **107**, 177205 (2011)

[154] Atxabal, A. *et al.* Spin doping using transition metal phthalocyanine molecules. *Nat. Commun.* **7**, 13751 (2016)

[155] Jo, J. *et al.* Molecular Tunability of Magnetic Exchange Bias and Asymmetrical Magnetotransport in Metalloporphyrin/Co Hybrid Bilayers. *ACS Nano* **13**, 894–903 (2018)

[156] Liang, L. *et al.* Inducing ferromagnetism and Kondo effect in platinum by paramagnetic ionic gating. *Sci. Adv.* **4**, eaar2030 (2018)

[157] Zhu, X. *et al.* Signature of coexistence of superconductivity and ferromagnetism in two-dimensional $NbSe_2$ triggered by surface molecular adsorption. *Nat. Commun.* **7**, 11210 (2016)

[158] Cinchetti, M., Dediu, V. A. & Hueso, L. E. Activating the molecular spinterface. *Nat. Mater.* **16**, 507–515 (2017)

[159] Schmaus, S. *et al.* Giant magnetoresistance through a single molecule. *Nat. Nanotechnol.* **6**, 185–189 (2011)

[160] Wende, H. *et al.* Substrate-induced magnetic ordering and switching of iron porphyrin molecules. *Nat. Mater.* **6**, 516–520 (2007)

[161] Lodi Rizzini, A. *et al.* Exchange biasing single molecule magnets: Coupling of $TbPc_2$ to antiferromagnetic layers. *Nano Lett.* **12**, 5703–5707 (2012)

[162] Lodi Rizzini, A. *et al.* Coupling Single Molecule Magnets to Ferromagnetic Substrates. *Phys. Rev. Lett.* **107**, 177205 (2011)

[163] Frindt, R. F. Superconductivity in ultrathin $NbSe_2$ layers. *Phys. Rev. Lett.* **28**, 299–301 (1972)

[164] Cao, Y. *et al.* Quality Heterostructures from Two-Dimensional Crystals Unstable in Air by Their Assembly in Inert Atmosphere. *Nano Lett.* **15**, 4914–4921 (2015)

[165] Ugeda, M. M. *et al.* Characterization of collective ground states in single-layer $NbSe_2$. *Nat. Phys.* **12**, 92–97 (2016)

[166] Zhao, K. *et al.* Disorder-induced multifractal superconductivity in monolayer niobium dichalcogenides. *Nat. Phys.* **15**, 904–910 (2019)

[167] Hamill, A. *et al.* Two-fold symmetric superconductivity in few-layer $NbSe_2$. *Nat. Phys.* **17**, 949–954 (2021)

[168] Rubio-Verdú, C. *et al.* Visualization of Multifractal Superconductivity in a Two-Dimensional Transition Metal Dichalcogenide in the Weak-Disorder Regime. *Nano Lett.* **20**, 5111–5118 (2020)

[169] Kezilebieke, S., Žitko, R., Dvorak, M., Ojanen, T. & Liljeroth, P. Observation of Coexistence of Yu-Shiba-Rusinov States and Spin-Flip Excitations. *Nano Lett.* **19**, 4614–4619 (2019)

[170] Alpern, H. *et al.* Magnetic-related States and Order Parameter Induced

in a Conventional Superconductor by Nonmagnetic Chiral Molecules. *Nano Lett.* **19**, 5167–5175 (2019)

[171] Artel, V. *et al.* Protective molecular passivation of black phosphorus. *npj 2D Mater. Appl.* **1**, 6 (2017)

[172] Calavalle, F. *et al.* Tailoring Superconductivity in Large-Area Single-Layer $NbSe_2$ via Self-Assembled Molecular Adlayers. *Nano Lett.* **21**, 136–143 (2021)

[173] Ahmad, H. M. N. *et al.* Effects of Impurities on the Electrochemical Characterization of Liquid-Phase Exfoliated Niobium Diselenide Nanosheets. *J. Phys. Chem. C* **123**, 8671–8680 (2019)

[174] Wang, H. *et al.* High-quality monolayer superconductor $NbSe_2$ grown by chemical vapour deposition. *Nat. Commun.* **8**, 394 (2017)

[175] Sugimura, H., Hayashi, K., Saito, N., Nakagiri, N. & Takai, O. Surface potential microscopy for organized molecular systems. *Appl. Surf. Sci.* **188**, 403–410 (2002)

[176] Braun, S., Salaneck, W. R. & Fahlman, M. Energy-level alignment at organic/metal and organic/organic interfaces. *Adv. Mater.* **21**, 1450–1472 (2009)

[177] Yu, Y.-J. *et al.* Tuning the Graphene Work Function by Electric Field Effect. *Nano Lett.* **9**, 3430–3434 (2009)

[178] Romaner, L., Heimel, G., Ambrosch-Draxl, C. & Zojer, E. The dielectric constant of self-assembled monolayers. *Adv. Funct. Mater.* **18**, 3999–4006 (2008)

[179] Zojer, E., Taucher, T. C. & Hofmann, O. T. The Impact of Dipolar Layers on the Electronic Properties of Organic/Inorganic Hybrid Interfaces. *Adv. Mater. Interfaces* **6**, 1900581 (2019)

[180] Xing, Y. *et al.* Ising Superconductivity and Quantum Phase Transition in Macro-Size Monolayer $NbSe_2$. *Nano Lett.* **17**, 6802–6807 (2017)

[181] Gibertini, M., Koperski, M., Morpurgo, A. F. & Novoselov, K. S. Magnetic 2D materials and heterostructures. *Nat. Nanotechnol.* **14**, 408–419 (2019)

[182] Gong, C. & Zhang, X. Two-dimensional magnetic crystals and emergent heterostructure devices. *Science* **363**, (2019)

[183] León-Brito, N., Bauer, E. D., Ronning, F., Thompson, J. D. & Movshovich, R. Magnetic microstructure and magnetic properties of uniaxial itinerant ferromagnet Fe_3GeTe_2. *J. Appl. Phys.* **120**, 083903 (2016)

[184] Tan, C. *et al.* Hard magnetic properties in nanoflake van der Waals Fe_3GeTe_2. *Nat. Commun.* **9**, 1554 (2018)

[185] Sinova, J., Valenzuela, S. O., Wunderlich, J., Back, C. H. & Jungwirth, T. Spin Hall effects. *Rev. Mod. Phys.* **87**, 1213–1260 (2015)

[186] Claessens, C. G., Hahn, U. & Torres, T. Phthalocyanines: From outstanding electronic properties to emerging applications. *Chem. Rec.* **8**, 75–97 (2008)

[187] Mugarza, A. *et al.* Electronic and magnetic properties of molecule-metal interfaces: Transition-metal phthalocyanines adsorbed on Ag(100). *Phys. Rev. B - Condens. Matter Mater. Phys.* **85**, 155437 (2012)

[188] Stepanow, S. *et al.* Mixed-valence behavior and strong correlation effects of metal phthalocyanines adsorbed on metals. *Phys. Rev. B* **83**, 220401 (2011)

[189] Wu, W., Harrison, N. M. & Fisher, A. J. Electronic structure and exchange interactions in cobalt-phthalocyanine chains. *Phys. Rev. B - Condens. Matter Mater. Phys.* **88**, 024426 (2013)

[190] Serri, M. *et al.* High-temperature antiferromagnetism in molecular semiconductor thin films and nanostructures. *Nat. Commun.* **5**, 3079 (2014)

[191] Gruber, M. *et al.* Exchange bias and room-temperature magnetic order in molecular layers. *Nat. Mater.* **14**, 981–984 (2015)

[192] Basova, T. V., Kiselev, V. G., Schuster, B. E., Peisert, H. & Chassé, T. Experimental and theoretical investigation of vibrational spectra of copper phthalocyanine: polarized single-crystal Raman spectra, isotope effect and DFT calculations. *J. Raman Spectrosc.* **40**, 2080–2087 (2009)

[193] Du, L. *et al.* Lattice Dynamics, Phonon Chirality, and Spin–Phonon Coupling in 2D Itinerant Ferromagnet Fe_3GeTe_2. *Adv. Funct. Mater.* **29**, 1904734 (2019)

[194] Gweon, H. K. *et al.* Exchange bias in weakly interlayer-coupled van der Waals magnet Fe_3GeTe_2. *Nano Lett.* **21**, 1672–1678 (2021)

[195] Boukari, S. *et al.* Disentangling Magnetic Hardening and Molecular Spin Chain Contributions to Exchange Bias in Ferromagnet/Molecule Bilayers. *Nano Lett.* **18**, 4659–4663 (2018)

[196] Nogués, J. & Schuller, I. K. Exchange bias. *J. Magn. Magn. Mater.* **192**, 203–232 (1999)

[197] Stiles, M. D. & McMichael, R. D. Coercivity in exchange-bias bilayers. *Phys. Rev. B* **63**, 064405 (2001)

[198] O'Grady, K., Fernandez-Outon, L. E. & Vallejo-Fernandez, G. A new paradigm for exchange bias in polycrystalline thin films. *J. Magn. Magn. Mater.* **322**, 883–899 (2010)

[199] Hu, G. *et al.* Antisymmetric Magnetoresistance in a van der Waals Antiferromagnetic/Ferromagnetic Layered $MnPS_3/Fe_3GeTe_2$ Stacking Heterostructure. *ACS Nano* **14**, 12037–12044 (2020)

[200] Zhang, L. *et al.* Proximity-Coupling-Induced Significant Enhancement of Coercive Field and Curie Temperature in 2D van der Waals Heterostructures. *Adv. Mater.* **32**, 2002032 (2020)

[201] Zhu, R. *et al.* Exchange Bias in van der Waals $CrCl_3/Fe_3GeTe_2$ Heterostructures. *Nano Lett.* **20**, 5030–5035 (2020)

[202] Dai, H. *et al.* Enhancement of the Coercive Field and Exchange Bias Effect in $Fe_3GeTe_2/MnPX_3$ (X = S and Se) van der Waals Heterostructures. *ACS Appl. Mater. Interfaces* **13**, 24314–24320 (2021)

[203] Zhang, Y. *et al.* Exchange bias and spin–orbit torque in the Fe_3GeTe_2-based heterostructures prepared by vacuum exfoliation approach. *Appl. Phys. Lett.* **118**, 262406 (2021)

[204] Binasch, G., Grünberg, P., Saurenbach, F. & Zinn, W. Enhanced magnetoresistance in layered magnetic structures with antiferromagnetic interlayer exchange. *Phys. Rev. B* **39**, 4828 (1989)

[205] Baibich, M. N. *et al.* Giant magnetoresistance of (001)Fe/(001)Cr magnetic superlattices. *Phys. Rev. Lett.* **61**, 2472–2475 (1988)

[206] Chappert, C., Fert, A. & Van Dau, F. N. The emergence of spin electronics in data storage. *Nat. Mater.* **6**, 813–823 (2007)

[207] Waldrop, M. M. The chips are down for Moore's law. *Nature* **530**, 144–147 (2016)

[208] Barla, P., Kumar Joshi, V., Somashekara Bhat, · & Joshi, V. K. Spintronic devices: a promising alternative to CMOS devices. *J. Comput. Electron.* **20**, 805–837 (2021)

[209] Julliere, M. Tunneling between ferromagnetic films. *Phys. Lett. A* **54**, 225–226 (1975)

[210] Wang, D., Nordman, C., Daughton, J. M., Qian, Z. & Fink, J. 70% TMR at room temperature for SDT sandwich junctions with CoFeB as free and reference layers. *IEEE Trans. Magn.* **40**, 2269–2271 (2004)

[211] Ikeda, S. *et al.* Tunnel magnetoresistance of 604% at 300K by suppression of Ta diffusion in CoFeB/MgO/CoFeB pseudo-spin-valves annealed at high temperature. *Appl. Phys. Lett.* **93**, 082508 (2008)

[212] Slonczewski, J. C. Current-driven excitation of magnetic multilayers. *J. Magn. Magn. Mater.* **159**, L1–L7 (1996)

[213] Berger, L. Emission of spin waves by a magnetic multilayer traversed by a current. *Phys. Rev. B* **54**, 9353 (1996)

[214] D'Yakonov, M. I. & Perel', V. I. Possibility of Orienting Electron Spins with Current. *JETPL* **13**, 467 (1971)

[215] Hirsch, J. E. Spin Hall Effect. *Phys. Rev. Lett.* **83**, 1834–1837 (1999)

[216] Saitoh, E., Ueda, M., Miyajima, H. & Tatara, G. Conversion of spin current into charge current at room temperature: Inverse spin-Hall effect. *Appl. Phys. Lett.* **88**, 182509 (2006)

[217] Miron, I. M. *et al.* Perpendicular switching of a single ferromagnetic layer induced by in-plane current injection. *Nature* **476**, 189–193 (2011)

[218] Liu, L. *et al.* Spin-torque switching with the giant spin hall effect of tantalum. *Science* **336**, 555–558 (2012)

[219] Miron, I. M. *et al.* Current-driven spin torque induced by the Rashba effect in a ferromagnetic metal layer. *Nat. Mater.* **9**, 230–234 (2010)

[220] Prenat, G. *et al.* Ultra-Fast and High-Reliability SOT-MRAM: From Cache Replacement to Normally-Off Computing. *IEEE Trans. Multi-*

Scale Comput. Syst. **2**, 49–60 (2016)

[221] Cubukcu, M. *et al.* Ultra-Fast Perpendicular Spin-Orbit Torque MRAM. *IEEE Trans. Magn.* **54**, (2018)

[222] Sinova, J. *et al.* Universal intrinsic spin Hall effect. *Phys. Rev. Lett.* **92**, 126603 (2004)

[223] Edelstein, V. M. Spin polarization of conduction electrons induced by electric current in two-dimensional asymmetric electron systems. *Solid State Commun.* **73**, 233–235 (1990)

[224] Sánchez, J. C. R. *et al.* Spin-to-charge conversion using Rashba coupling at the interface between non-magnetic materials. *Nat. Commun.* **4**, 2944 (2013)

[225] Rojas-Sánchez, J.-C. *et al.* Spin to Charge Conversion at Room Temperature by Spin Pumping into a New Type of Topological Insulator: α-Sn Films. *Phys. Rev. Lett.* **116**, 096602 (2016)

[226] Lee, J., Wang, Z., Xie, H., Mak, K. F. & Shan, J. Valley magnetoelectricity in single-layer MoS_2. *Nat. Mater.* **16**, 887–891 (2017)

[227] Rikken, G. L. J. A., Fölling, J. & Wyder, P. Electrical Magnetochiral Anisotropy. *Phys. Rev. Lett.* **87**, 236602 (2001)

[228] Lan, S. *et al.* Observation of strong excitonic magneto-chiral anisotropy in twisted bilayer van der Waals crystals. *Nat. Commun.* **12**, 2088 (2021)

[229] Behin-Aein, B., Datta, D., Salahuddin, S. & Datta, S. Proposal for an all-spin logic device with built-in memory. *Nat. Nanotechnol.* **5**, 266–270 (2010)

[230] Feynmann, R., Leighton, R. & Sands, M. *The Feynman Lectures on Physics, Vol. III.* (Caltech Basic Books, 2011).

[231] Shi, J., Zhang, P., Xiao, D. & Niu, Q. Proper definition of spin current in spin-orbit coupled systems. *Phys. Rev. Lett.* **96**, 076604 (2006)

[232] Vernes, A., Györffy, B. L. & Weinberger, P. Spin currents, spin-transfer torque, and spin-Hall effects in relativistic quantum mechanics. *Phys. Rev. B* **76**, 012408 (2007)

[233] Mott, N. F. The electrical conductivity of transition metals. *Proc. R. Soc. London. Ser. A - Math. Phys. Sci.* **153**, 699–717 (1936)

[234] Vaz, D. C. Spin-to-charge current conversion in $SrTiO_3$-based two-dimensional electron gases. (Sorbonne Université, 2018).

[235] Vas'ko, F. Spin splitting in the spectrum of two-dimensional electrons due to the surface potential. *JETP Lett.* **30**, 541 (1979)

[236] Bychkov, Y. A. & Rashba, E. I. Oscillatory effects and the magnetic susceptibility of carriers in inversion layers. *J. Phys. C Solid State Phys.* **17**, 6039 (1984)

[237] Johansson, A. Spin-orbit driven transport: Edelstein effect and chiral anomaly. (Martin-Luther-Universität Halle-Wittenberg).

[238] Nechaev, I. A. *et al.* Hole dynamics in a two-dimensional spin-orbit coupled electron system: Theoretical and experimental study of the Au(111) surface state. *Phys. Rev. B - Condens. Matter Mater. Phys.* **80**, 113402 (2009)

[239] Datta, S. & Das, B. Electronic analog of the electro-optic modulator. *Appl. Phys. Lett.* **56**, 665–667 (1990)

[240] Dresselhaus, G. Spin-Orbit Coupling Effects in Zinc Blende Structures. *Phys. Rev.* **100**, 580 (1955)

[241] D'Yakonov, M. I. & Perel', V. I. Spin orientation of electrons associated with the interband absorption of light in semiconductors. *Sov. Phys. JETP* **33**, 1053 (1971)

[242] Yoda, T., Yokoyama, T. & Murakami, S. Current-induced Orbital and Spin Magnetizations in Crystals with Helical Structure. *Sci. Rep.* **5**, 12024 (2015)

[243] Sakano, M. *et al.* Radial Spin Texture in Elemental Tellurium with Chiral Crystal Structure. *Phys. Rev. Lett.* **124**, 136404 (2020)

[244] Gatti, G. *et al.* Radial Spin Texture of the Weyl Fermions in Chiral Tellurium. *Phys. Rev. Lett.* **125**, 216402 (2020)

[245] Ganichev, S. D. *et al.* Spin-galvanic effect. *Nature* **417**, 153–156 (2002)

[246] Ziman, J. M. *Electrons and Phonons.* (Oxford University Press, 2001). doi:10.1093/acprof:oso/9780198507796.001.0001

[247] Zhang, W., Jungfleisch, M. B., Jiang, W., Pearson, J. E. & Hoffmann, A. Spin pumping and inverse Rashba-Edelstein effect in NiFe/Ag/Bi and NiFe/Ag/Sb. *J. Appl. Phys.* **117**, 17C727 (2015)

[248] Isasa, M. *et al.* Origin of inverse Rashba-Edelstein effect detected at the Cu/Bi interface using lateral spin valves. *Phys. Rev. B* **93**, 014420 (2016)

[249] Lesne, E. *et al.* Highly efficient and tunable spin-to-charge conversion through Rashba coupling at oxide interfaces. *Nat. Mater.* **15**, 1261–1266 (2016)

[250] Li, Y. *et al.* Nonreciprocal charge transport up to room temperature in bulk Rashba semiconductor α-GeTe. *Nat. Commun.* **12**, 540 (2021)

[251] Kondou, K. *et al.* Fermi-level-dependent charge-to-spin current conversion by Dirac surface states of topological insulators. *Nat. Phys.* **12**, 1027–1031 (2016)

[252] He, P. *et al.* Bilinear magnetoelectric resistance as a probe of three-dimensional spin texture in topological surface states. *Nat. Phys.* **14**, 495–499 (2018)

[253] Avci, C. O. *et al.* Unidirectional spin Hall magnetoresistance in ferromagnet/normal metal bilayers. *Nat. Phys.* **11**, 570–575 (2015)

[254] Thomson, W. On the electro-dynamic qualities of metals:—Effects of magnetization on the electric conductivity of nickel and of iron. *Proc. R. Soc. London* **8**, 546–550 (1857)

[255] Campbell, I. A., Fert, A. & Jaoul, O. The spontaneous resistivity anisotropy in Ni-based alloys. *J. Phys. C Solid State Phys.* **3**, S95 (1970)

[256] Vaz, D. C. *et al.* Determining the Rashba parameter from the bilinear magnetoresistance response in a two-dimensional electron gas. *Phys. Rev. Mater.* **4**, 071001 (2020)

[257] Ben Shalom, M. *et al.* Anisotropic magnetotransport at the $SrTiO_3/LaAlO_3$ interface. *Phys. Rev. B - Condens. Matter Mater. Phys.* **80**, 140403 (2009)

[258] He, P. *et al.* Observation of Out-of-Plane Spin Texture in a $SrTiO_3$ (111) Two-Dimensional Electron Gas. *Phys. Rev. Lett.* **120**, 266802

(2018)

[259] Guillet, T. *et al.* Observation of Large Unidirectional Rashba Magnetoresistance in Ge(111). *Phys. Rev. Lett.* **124**, 027201 (2020)

[260] Dyrdał, A., Barnaś, J. & Fert, A. Spin-Momentum-Locking Inhomogeneities as a Source of Bilinear Magnetoresistance in Topological Insulators. *Phys. Rev. Lett.* **124**, 046802 (2020)

[261] Ray, K., Ananthavel, S. P., Waldeck, D. H. & Naaman, R. Asymmetric scattering of polarized electrons by organized organic films of chiral molecules. *Science* **283**, 814–816 (1999)

[262] Liu, Y., Xiao, J., Koo, J. & Yan, B. Chirality-driven topological electronic structure of DNA-like materials. *Nat. Mater.* **20**, 638–644 (2021)

[263] Yang, S.-H., Naaman, R., Paltiel, Y. & Parkin, S. S. P. Chiral spintronics. *Nat. Rev. Phys.* **3**, 328–343 (2021)

[264] Suda, M. *et al.* Light-driven molecular switch for reconfigurable spin filters. *Nat. Commun.* **10**, 2455 (2019)

[265] Dong, Z. & Ma, Y. Atomic-level handedness determination of chiral crystals using aberration-corrected scanning transmission electron microscopy. *Nat. Commun.* **11**, 1588 (2020)

[266] Ben-moshe, A. *et al.* The chain of chirality transfer in tellurium nanocrystals. *Science* **733**, 729–733 (2021)

[267] Vorob'ev, L. E. *et al.* Optical activity in tellurium induced by a current. *Sov. J. Exp. Theor. Phys. Lett.* **29**, 441 (1979)

[268] Shalygin, V. A., Sofronov, A. N., Vorob'ev, L. E. & Farbshtein, I. I. Current-induced spin polarization of holes in tellurium. *Phys. Solid State* **54**, 2362–2373 (2012)

[269] Furukawa, T., Shimokawa, Y., Kobayashi, K. & Itou, T. Observation of current-induced bulk magnetization in elemental tellurium. *Nat. Commun.* **8**, 954 (2017)

[270] Furukawa, T., Watanabe, Y., Ogasawara, N., Kobayashi, K. & Itou, T. Current-induced magnetization caused by crystal chirality in nonmagnetic elemental tellurium. *Phys. Rev. Res.* **3**, 023111 (2021)

[271] Mayers, B. & Xia, Y. One-dimensional nanostructures of trigonal tellurium with various morphologies can be synthesized using a solution-phase approach. *J. Mater. Chem.* **12**, 1875–1881 (2002)

[272] Qiu, G. *et al.* Quantum Hall effect of Weyl fermions in n-type semiconducting tellurene. *Nat. Nanotechnol.* **15**, 585–591 (2020)

[273] Zhang, N. *et al.* Magnetotransport signatures of Weyl physics and discrete scale invariance in the elemental semiconductor tellurium. *Proc. Natl. Acad. Sci.* **117**, 11337–11343 (2020)

[274] Agapito, L. A., Kioussis, N., Goddard, W. A. & Ong, N. P. Novel family of chiral-based topological insulators: Elemental tellurium under strain. *Phys. Rev. Lett.* **110**, 176401 (2013)

[275] Hirayama, M., Okugawa, R., Ishibashi, S., Murakami, S. & Miyake, T. Weyl Node and Spin Texture in Trigonal Tellurium and Selenium. *Phys. Rev. Lett.* **114**, 206401 (2015)

[276] Li, J. *et al.* Non-orthogonal tight-binding model for tellurium and selenium. *Philos. Mag.* **93**, 3216–3230 (2013)

[277] Nakayama, K. *et al.* Band splitting and Weyl nodes in trigonal tellurium studied by angle-resolved photoemission spectroscopy and density functional theory. *Phys. Rev. B* **95**, 125204 (2017)

[278] Tanuma, S. The Effect of Thermally Produced Lattice Defects on the Electrical Properties of Tellurium. *Sci. reports Res. Institutes, Tohoku Univ. Ser. A, Physics, Chem. Metall.* **6**, 159–171 (1954)

[279] Martin, R. M., Lucovsky, G. & Helliwell, K. Intermolecular bonding and lattice dynamics of Se and Te. *Phys. Rev. B* **13**, 1383 (1976)

[280] Wang, Y. *et al.* Enhanced thermoelectric performance of van der Waals Tellurium via vacancy engineering. *Mater. Today Phys.* **18**, 100379 (2021)

[281] Epstein, A. S., Fritzsche, H. & Lark-Horovitz, K. Electrical properties of tellurium at the melting point and in the liquid state. *Phys. Rev.* **107**, 412–419 (1957)

[282] Ong, N. P. & Liang, S. Experimental signatures of the chiral anomaly in Dirac–Weyl semimetals. *Nat. Rev. Phys.* **3**, 394–404 (2021)

[283] Vaz, D. C. *et al.* Mapping spin–charge conversion to the band structure

in a topological oxide two-dimensional electron gas. *Nat. Mater.* **18**, 1187–1193 (2019)

[284] Roy, M., Sen, S., Gupta, S. K. & Tyagi, A. K. Comment on high-quality luminescent tellurium nanowires of several nanometers in diameter and high aspect ratio synthesized by a poly (vinyl pyrrolidone)-assisted hydrothermal process. *Langmuir* **23**, 10873 (2007)

List of Publications and Contributions

Publications:

This Thesis is based on the following publications:

- *Tailoring Superconductivity in Large-Area Single-Layer $NbSe_2$ via Self-Assembled Molecular Adlayers*
  F. Calavalle, P. Dreher, A. P. Surendran, W. Wan, M. Timpel, R. Verucchi, C. Rogero, T. Bauch, F. Lombardi, F. Casanova, M. V. Nardi, M. M. Ugeda, L. E. Hueso, M. Gobbi
  Nano Letters, 21, 136-143 (2021)

- *Exchange bias in molecule/Fe_3TeGe_2 van der Waals heterostructures via spinterface effects*
  Junhyeon Jo, F. Calavalle, B. Martín-García, F. Casanova, A. Chuvilin, L. E. Hueso*, and M. Gobbi*
  Submitted

- *Gate-tuneable and chirality-dependent charge-to-spin conversion in Tellurium nanowires*
  F. Calavalle, M. Suárez-Rodríguez, B. Martín-García, A. Johansson, D. C. Vaz, H. Yang, I. V. Maznichenko, S. Ostanin A. Mateo-Alonso, A. Chuvilin, I. Mertig, M. Gobbi, F. Casanova and L. E. Hueso
  Nature Materials, (2022 accepted)
  https://arxiv.org/abs/2201.00359

Other publications:

- *Top dielectric induced ambipolarity in an n-channel dual-gated organic field effect transistor*
  K. Bairagi, E. Zuccatti, F. Calavalle, S. Catalano, S. Parui, R. Llopis, F. Ortmann, F. Casanova, L. E. Hueso
  Journal of material Chemistry C, 7, 10389-10393 (2019)

- *Tuning ambipolarity in a polymer field effect transistor using graphene electrodes*
  K. Bairagi, S. Catalano, F. Calavalle, E. Zuccatti, R. Llopis, F. Casanova, L. E. Hueso

Journal of material Chemistry C, 8, 8120-8124 (2020)

- *Room-Temperature Operation of a p-Type Molecular Spin Photovoltaic Device on a Transparent Substrate*
  K. Bairagi, D. G. Romero, F. Calavalle, S. Catalano, E. Zuccatti, R. Llopis, F. Casanova, L. E. Hueso
  Advanced Materials, 32, 1906908 (2020)

- *Strong interfacial exchange field in a heavy metal/ferromagnetic insulator system determined by spin Hall magnetoresistance*
  J. M. Gomez-Perez, X.-P. Zhang, F. Calavalle, M. Ilyn, C. González-Orellana, M. Gobbi, C. Rogero, A. Chuvilin, V. N. Golovach, L. E. Hueso, F. S. Bergeret, F. Casanova
  Nano Letters, 20, 6815-6823 (2020)

- *Real-space observation of vibrational strong coupling between propagating phonon polaritons and organic molecules*
  A. Bylinkin, M. Schnell, M. Autore, F. Calavalle, P. Li, J. Taboada-Gutièrrez, S. Liu, J. H. Edgar, F. Casanova, L. E. Hueso, P. Alonso-Gonzalez, A. Y. Nikitin, R. Hillenbrand
  Nature Photonics, 15, 197-202 (2021)

- *Tuning the magnetic properties of NiPS3 through organic-ion intercalation*
  D. Tezze, J. M. Pereira, Y. Asensio, M. Ipatov, F. Calavalle, F. Casanova, A. M. Bittner, M. Ormaza, B. Martín-García, L. E. Hueso, M. Gobbi
  Nanoscale (2022), DOI: 10.1039/D1NR07281A

Invited Talks

- (2022) **MMM Intermag 2022**, Gate tuneable and chirality-dependent Edelstein effect in Tellurium nanowires. *New Orleans, LA, USA*

Contributed Talks

- (2020) **CMD GEFES 2020**, Tailoring superconductivity in large-area monolayer $NbSe_2$ via self-assembled molecular adlayers. *Madrid, Spain [ONLINE].*
- (2021) **5th Graphene Workshop**, Tailoring Superconductivity in Large-Area Single-Layer $NbSe_2$ via Self-Assembled Molecular Adlayers. *Basel, Switzerland*
- (2021) **QuESTech Final Conference**, Tailoring Superconductivity in Large-Area Single-Layer $NbSe_2$ via Self-Assembled Molecular Adlayers. *Gothenburg, Sweden*

Posters

- (2018) **European School on Nanosciences and Nanotechnologies (ESONN)**, In-device Molecular Spectroscopy of Metal/Organic Semiconductor Interfaces. *Grenoble, France*